Applicability of Graphene Oxide-based Membranes in Separation Processes: A Molecular Dynamics Simulation Study

by

Pilli Rajasekhar Reddy

Registration No: 186107010

A thesis submitted in partial fulfillment of the requirements for the degree of

Doctor of Philosophy

under the supervision of

Prof. Anki Reddy Katha & Prof. Amit Kumar

Department of Chemical Engineering

Indian Institute of Technology, Guwahati

Guwahati - 781039, India

December, 2024

Abstract

In the past decade, multilayered graphene oxide (GO) membranes have emerged as promising candidates for desalination and wastewater treatment applications. Despite their potential, a comprehensive understanding of separation mechanisms remains elusive due to the intricate morphology and structural arrangement of interlayer galleries. This thesis addresses these challenges by constructing two distinct structural configurations, namely lamellar and non-lamellar, to investigate separation mechanisms at the atomistic level. Moreover, one major issue with layered GO membranes is their tendency to swell in an aqueous environment. Recognizing the tendency of layered GO membranes to swell in aqueous environments, this thesis explores cation intercalation within interlayer galleries as a promising solution to mitigate this problem. The applicability of lamellar, non-lamellar, and cation-intercalated GO membranes as forward osmosis (FO) and reverse osmosis (RO) membranes in separation and purification applications is studied using non-equilibrium molecular dynamics (MD) simulations. Real-life scenarios, including seawater, pharmaceutical industrial wastewater, shale gas wastewater, and human urine, are considered to assess the performance of GO membranes. These GO membranes exhibit an improved trade-off between water permeance and selectivity compared to conventional polymeric membranes. This enhanced performance is attributed to the inherent structural characteristics of GO membranes, such as nanosized 2D channels and open edges, which enable the rapid movement of water molecules across membrane layers while efficiently retaining undesired species. The nanosized GO nanosheets have abundant oxygen-containing functional groups (OFGs), i.e., hydroxyl, epoxy, and carboxyl, enhancing their mechanical strength and chemical stability.

In particular, the separation of one of the most consumed antibiotics, amoxicillin (AMX), from the pharmaceutical industrial wastewater with a non-lamellar GO membrane has been investigated using non-equilibrium MD simulations by considering three different membranes, which differ in the number of OFGs on the GO nanosheets. This study reveals that the water and ion permeance depend on the number of OFGs and pore sizes of the membranes. Reducing the number of OFGs in the membranes leads to smaller pore sizes and lower water permeance. The retention and dynamics of AMX molecules reveal that the AMX molecules are likely to be retained on the basal plane of the membrane. This can be attributed to a strong interaction between hydroxyl and epoxy functional groups of the GO nanosheets with AMX molecules.

As mentioned earlier, cation intercalation inside the interlayer gallery of layered GO membranes is a promising solution to mitigate GO membranes' swelling tendency in aqueous environments. However, the effect of cationic concentration inside membrane channels on the mechanism of water permeance and salt rejection is yet to be investigated in detail. This study investigates shale gas wastewater (NaCl, $CaCl_2$, and crude oil) treatment via nonequilibrium MD simulations with cation (K^+, Mg^{2+}) intercalated GO membranes. This study reveals that the presence of a higher concentration of cations inside the GO membrane induces higher water resistance in the membrane. In addition to the concentration of intercalated ions, interlayer distance also plays a significant role in determining water permeance. We observed that Mg^{2+} ion intercalated GO membranes exhibit superior water permeance than K^+ ion intercalated GO membranes due to their higher interlayer distance. We also observed a difference in the crude oil aggregate formation (a composition of alkanes, cycloalkanes, and aromatics) in the two systems (more stable aggregate in K^+ ion intercalated GO membrane system as compared to Mg^{2+} ion intercalated GO membrane system) during the FO process. This can be attributed to weaker interactions of K^+ ions with the crude oil and lower water permeance of K^+ ion intercalated GO membranes than Mg^{2+} ion intercalated GO membranes. This aggregate formation is an important factor for crude oil rejection. On the other hand, more cations inside the GO membrane layers result in better Na^+ rejection but decreased Cl^- rejection.

Specifically, GO membranes, known for their efficacy in rejecting smaller molecules, face limitations due to undesirable swelling in aqueous environments. In this aspect, the potential of cation-intercalated GO membranes as RO membranes is investigated in boron removal via nonequilibrium MD simulations. In the aquatic environment, boron can exist in the form of boric acid or borate ion, depending on the pH of the solution. This study reveals that the GO membranes effectively reject negatively charged borate ions due to their bigger hydration shell and stronger electrostatic repulsion with the membrane than neutral boric acid molecules. Moreover, K^+ ion intercalated GO membranes showed higher boron rejection than Mg^{2+} ion intercalated GO membranes owing to weaker electrostatic attraction of K^+ ions with the boric acid (or borate ions). Additionally, a summary of the effects of OFGs of the GO membrane on boron rejection is provided. Since the hydroxyl and epoxy functional groups interact with boric acid molecules more strongly, these molecules are prevented from permeating through the membrane. On the other hand, the permeation rate of borate ions declines because of their stronger interactions with the carboxyl functional groups.

Likewise, human urine, a rich source of valuable smaller compounds such as urea and ammonia (essential feedstock for urea production), requires efficient recovery methods to meet the increasing global demand for urea. Thus, this study aimed to investigate the recovery of urea and ammonia from human urine through the FO separation technique with cationic-controlled GO membranes via nonequilibrium MD simulations. Human urine, existing in fresh and hydrolyzed states, presents distinct nitrogen forms for recovery—dominantly urea in fresh urine and ammonia (NH_3) in hydrolyzed urine. Results demonstrate that GO membranes exhibit superior urea rejection than ammonia, attributed to factors such as larger urea hydration size, stronger interaction with GO nanosheets, and the formation of small urea aggregates. Furthermore, NH_3 converts into ammonium ions (NH_4^+) depending on the pH of hydrolyzed human urine. To enhance understanding of ammonia recovery, the study investigates two more distinct feed solutions, one containing NH_3 and the other NH_4^+. Positively charged NH_4^+ ions demonstrate greater rejection due to a stable hydration shell, stronger attraction with GO nanosheets, and electrostatic repulsion with intercalated cations (Mg^{2+}) compared to neutral NH_3 molecules. Additionally, the study highlights that hydroxyl and epoxy functional groups of GO nanosheets play a crucial role in impeding the permeation rates of both urea and NH_4^+, leading to significant recovery. The study also highlights that GO membranes achieved higher water permeance with fresh human urine compared to hydrolyzed urine, attributed to a higher osmotic pressure gradient and salt rejection exceeding 94%.

Although cation intercalation inside the GO membranes has emerged as a promising strategy to control the swelling tendency of GO membranes in aqueous environments, there is a need to address the longevity of the intercalated cations within the GO laminates, as the stability of membranes relies on the interactions between these intercalated cations and GO nanosheets. Moreover, the retention of intercalated cations inside the interlayer gallery of GO membranes depends on the morphology and structural arrangement of interlayer galleries. Thus, this study has constructed two distinct structural configurations, namely lamellar and non-lamellar, to address these challenges at the atomistic level. In addition, this study performed nonequilibrium MD simulations to explain how the structural geometry influences water permeance, salt rejection mechanism, and mobility of intercalated cations in the RO process using cation-intercalated GO membranes. This research findings highlight that lamellar GO membranes exhibit higher water permeance, attributed to their well-defined interlayer gallery structure. On the other hand, non-lamellar GO membranes display superior salt rejection due to their

complex interlayer gallery structure that impedes salt permeation. Moreover, the structural complexity of non-lamellar GO membranes contributes to greater stability by retention of the more intercalated cations for a longer time within the layers. Furthermore, a higher percentage of Mg^{2+} cations remained inside the GO laminates as compared to K^{+} cations due to their slower mobility and larger hydration shell.

Declaration

I, hereby declare that the work contained in this thesis entitled "**Applicability of Graphene Oxide-based Membranes in Separation Processes: A Molecular Dynamics Simulation Study**" is original and has been done by me at the Department of Chemical Engineering, Indian Institute of Technology Guwahati, Guwahati, India, under the supervision of **Prof. Anki Reddy Katha and Prof. Amit Kumar**. The work has not been submitted to any other Institute for any degree or diploma. I have followed the guidelines provided by the Institute in preparing the thesis. I have confirmed to the norms and guidelines given in the Ethical Code of Conduct of the Institute.

Pilli Rajasekhar Reddy
Registration No: 186107010
Department of Chemical Engineering
Indian Institute of Technology, Guwahati
Guwahati-781039, Assam, India.

Certificate

It is certified that the work described in this thesis entitled "**Applicability of Graphene Oxide-based Membranes in Separation Processes: A Molecular Dynamics Simulation Study**" by **Mr. Pilli Rajasekhar Reddy** for the award of degree of Doctor of Philosophy is an authentic record of the results obtained from the research work carried out under our supervision at the Department of Chemical Engineering, Indian Institute of Technology Guwahati, Guwahati, India, and this work has not been submitted elsewhere for a degree.

Dr. Anki Reddy Katha
Professor
Chemical Engineering
Indian Institute of Technology, Tirupati
Tirupati-517619, Andhra Pradesh, India

Dr. Amit Kumar
Associate Professor
Chemical Engineering
Indian Institute of Technology, Guwahati
Guwahati-781039, Assam, India.

Acknowledgements

This doctoral thesis would not be completed without the help and extended hands of several people. I take this opportunity to express my sincere thankfulness to all of them.

Firstly, my sincere gratitude to my supervisors, Prof. Anki Reddy Katha and Prof. Amit Kumar for their continuous support, motivation and guidance throughout my Ph.D. thesis work. I would also like to acknowledge my doctoral committee members: Prof. Ashok Kumar Dasmahapatra, Prof. Animes K Golder, and Prof. Kalyan Raidongia. Their valuable suggestions and critical comments shaped the presented thesis work. Besides, I would also like to thank all the Chemical Engineering office, Academic office, Student Affair, and Finance staff members. They were always available whenever I required.

I would also like to thank IITG and the Government of India for providing HPC facility (Param-Ishan and Param-Kamrupa) for conducting the simulations, which would have taken a long time otherwise. I want to extend my sincere gratitude to the Ministry of Human Resource Development for providing financial assistance, making the Ph.D. journey much more manageable.

I want to extend my gratitude to all my fellow friends: Dr. Abhijit Gogoi, Dr. Shivam Tiwari, Dr. Bitang Kwrung Tripura, Dr. Vamsi Krishna Reddy, Mr. Kranthi Kumar, Mr. Nagendra Prasad, and Mr. Adupa Vasistha, for their contributions towards my Ph.D. work directly or indirectly. Lastly, I would like to thank my family for the unconditional love and support they showered on me.

Contents

List of Figures **13**

List of Tables **25**

1 Introduction **26**

1.1 Overview . . . 26

1.2 Why membrane technologies? . . . 27

1.2.1 Reverse Osmosis (RO) process . . . 28

1.2.2 Forward osmosis (FO) process . . . 30

1.3 Motivation: Why graphene oxide (GO) as a membrane material? . . . 31

1.3.1 GO membrane and its challenges . . . 31

1.3.2 Cation intercalated GO membrane . . . 34

1.4 Necessity of pharmaceutical industrial wastewater treatment . . . 36

1.5 Need of boron removal from wastewater . . . 37

1.6 Essential of Human urine treatment . . . 39

1.7 Objectives . . . 41

1.8 Thesis strategy and organization . . . 42

2 Simulation Methodology **43**

2.1 Essence of Computational Modeling . . . 43

2.2 Theory behind the Molecular Dynamics . . . 44

2.2.1 Force Fields . . . 44

2.3 Integration of Equations of Motion . . . 46

2.3.1 Verlet Algorithm . . . 46

2.3.2 Velocity Verlet Algorithm . . . 48

2.4 Periodic Boundary Conditions . . . 49
2.5 Neighbour Searching Methods . . . 52
2.6 Ewald Summation . . . 53
2.7 Ensemble . . . 54
2.7.1 Temperature control or Thermostats . . . 56
2.7.2 Pressure control or Barostats . . . 59
2.8 Water Models . . . 60
2.8.1 Three Point Models . . . 61
2.8.2 Four point water models . . . 61
2.9 A brief discussion on MD codes . . . 62

3 Effect of oxygen-containing functional groups of layered graphene oxide membrane on the removal of amoxicillin: a molecular dynamics study 65
3.1 Objective . . . 65
3.2 Methodology . . . 66
3.2.1 Non lamellar membrane . . . 66
3.2.2 FO Simulation system . . . 68
3.2.3 Simulation Methodology . . . 68
3.3 Results and discussion . . . 69
3.3.1 Membrane Performance . . . 69
3.3.2 AMX Retention . . . 74
3.4 Conclusions . . . 77

4 Cationic stabilized layered graphene oxide (GO) membrane for shale gas wastewater treatment: An atomistic insight 79
4.1 Objective . . . 79
4.2 Methodology . . . 80
4.2.1 Cation intercalated membrane . . . 80
4.2.2 FO simulation system . . . 81
4.2.3 Simulation Methodology . . . 82
4.3 Results and discussion . . . 83
4.3.1 Water permeance . . . 83
4.3.2 Crude oil aggregation and rejection . . . 90

4.3.3 Salt rejection . . . 93
4.3.4 Effect of the pore width (P) . . . 95
4.3.5 Draw solute rejection . . . 98
4.3.6 Comparative water permeance of polymeric FO membranes in oil-water separation . . . 98
4.4 Conclusions . . . 99

5 Understanding the boron rejection of cation intercalated multilayered graphene oxide (GO) membrane in reverse osmosis (RO) process: A Molecular Dynamics study 102
5.1 Objective . . . 102
5.2 Methodology . . . 103
5.2.1 Cation-intercalated GO membrane . . . 103
5.2.2 RO Simulation system . . . 104
5.2.3 Simulation Methodology . . . 105
5.3 Results and discussion . . . 107
5.3.1 Rejection mechanisms of Boric acid and Borate ion . . . 107
5.3.2 Water permeance and salt rejection . . . 113
5.3.3 Intercalated ions distribution . . . 117
5.4 Conclusions . . . 119

6 Urea and ammonia recovery from human urine by forward osmosis (FO) process using cation intercalated graphene oxide (GO) membrane: A molecular dynamics study 120
6.1 Objective . . . 120
6.2 Methodology . . . 122
6.2.1 Cation-intercalated GO membrane . . . 122
6.2.2 FO Simulation system . . . 122
6.2.3 Simulation Methodology . . . 123
6.3 Results and discussion . . . 123
6.3.1 Rejection and Transport mechanisms of Urea and Ammonia (NH_3) . . . 123
6.3.2 Rejection and Transport mechanisms of Ammonia (NH_3) and Ammonium (NH_4^+) ion . . . 127

6.3.3 Water permeance and salt rejection . . . 131
6.4 Conclusions . . . 132

7 Comparative retention analysis of intercalated cations inside the interlayer gallery of lamellar and non-lamellar graphene oxide (GO) membranes in a reverse osmosis (RO) process: A molecular dynamics 133
7.1 Objective . . . 133
7.2 Methodology . . . 134
7.2.1 Non-lamellar cation intercalated GO membrane . . . 134
7.2.2 Lamellar cation intercalated GO membrane . . . 137
7.2.3 RO simulation setup . . . 138
7.2.4 Simulation Methodology . . . 138
7.3 Results and discussion . . . 139
7.3.1 Water permeance . . . 139
7.3.2 Membrane stability . . . 142
7.3.3 Salt rejection . . . 145
7.4 Conclusions . . . 146

8 Conclusions and Future Scope 147
8.1 Conclusions . . . 147
8.2 Scope for Future Investigations . . . 150

A Research Output 153

B Supplementary Information for Specific Chapters 155
B.1 Supplementary information for Chapter 3 . . . 155
B.2 Supplementary information for Chapter 4 . . . 158
B.3 Supplementary information for Chapter 5 . . . 179

Bibliography 187

List of Figures

1.1 A simple membrane separation process. 28

1.2 Description of RO process. 29

1.3 Description of FO process. 30

2.1 Flowchart of pseudocode of (a) Verlet Algorithm and (b) Velocity Verlet Algorithm. 49

2.2 A schematic representation of two dimensional periodic boundary condition. The highlighted box in the center is the original simulation box and all other boxes are images of it. 50

2.3 Different approaches for calculating interactions between particles in molecular dynamics: (a) Cell list and (b) Verlet list. 52

3.1 Stages associated with the construction of non-lamellar GO membrane. (a) Random distribution of GO nanosheets and water in a simulation box. (b) Pulling the center of mass of GO sheets towards the graphene sheet. (c) Relaxation and equilibration to remove the vacuum gap. The blue color is for hydrogen atoms, the red color is for oxygen atoms and cyan color is for carbon atoms. 67

3.2 (a) Amoxicillin molecule. (b) GO membrane. (c) Draw solution. (d) Feed solution. (e) Simulation system. Cyan color is for carbon atoms, red color is for oxygen atoms, blue color is for hydrogen atoms, black color is for Mg^{2+} ions, green color is for Cl^{1-} ions, magenta color is for Al^{3+} ions, yellow color is for sulphur atoms and orange color is for nitrogen atoms. 69

3.3 (a) Water permeance through the membranes. (b) Water permeance through the membranes as a function of oxygen containing functional groups. (c) Pore size distribution of the membranes. (d) RDF of water molecules around the membranes. 70

3.4 (a) Maximum pore size and (b) thickness of the membranes as a function of oxygen containing functional groups. 71

3.5 The variation in the density of the ions along Z direction for (a) GO membrane, (b) rGO membrane and (c) ErGO membrane. The dotted lines indicate the membrane position. 72

3.6 Intercalation of ions inside the interlayer gallery of the membranes. (a) GO membrane. (b) rGO membrane. (c) ErGO membrane. Cyan color is for carbon atoms, red color is for oxygen atoms, blue color is for hydrogen atoms, black color is for Mg^{2+} ions, green color is for Cl^{1-} ions, magenta color is for Al^{3+} ions, yellow color is for sulphur atoms and orange color is for nitrogen atoms. 73

3.7 Variation in the density of AMX molecules along the Z direction for (a) GO membrane (b) rGO membrane and (c) ErGO membrane. Dotted lines indicate the membrane position. 73

3.8 The snapshots of the retained AMX molecules on the membrane surface (top view) for (a) GO membrane (b) rGO membrane and (c) ErGO membrane. The AMX molecule is shown in orange color. Cyan color is for carbon atoms, red color is for oxygen atoms and blue color is for hydrogen atoms. O1, O2, O3 and O4 atoms are shown in red, yellow, purple and black colors respectively. 74

3.9 The van der Waals (vdW) interaction energy between the oxygen atoms of the GO nanosheets and the AMX molecule for (a) GO Membrane (b) rGO Membrane (c) ErGO Membrane. 74

3.10 RDF between the oxygen atoms of the GO nanosheets and the AMX molecule for (a) GO membrane (b) rGO membrane and (c) ErGO membrane. 75

3.11 (a) RDF between the oxygen atoms of the GO nanosheets and the oxygen atom (OH) of the hydroxyl groups and (b) the oxygen atom (OG) of the carbonyl groups of the AMX molecule. (c) The interaction energy of the oxygen-containing functional groups of the GO nanosheets with the oxygen-containing functional groups of the AMX molecule (OH and OG). 75

3.12 The trajectories of AMX molecules for (a) GO membrane (b) rGO membrane and (c) ErGO membrane. Cyan color is for carbon atoms, red color is for oxygen atoms and blue color is for hydrogen atoms. 77

4.1 (a) GO nanosheet. (b) Multilayered GO membrane. (c) Simulation system. Green color is for carbon atoms, red color is for oxygen atoms, blue color is for hydrogen atoms, pink color is for crude oil, yellow color is for Na^+ ions, black color is for Ca^{2+} ions, magenta color is for Cl^- ions, gray color is for K^+ ions, orange color is for choline and lime color is for ethylene glycol. 82

4.2 Water permeane through the (a) K^+ ion intercalated and (b) Mg^{2+} ion intercalated GO membranes. 83

4.3 Variation of the number of water molecules in the draw solution (N_D) as a function of the simulation time. (a) K^+ ion intercalated and (b) Mg^{2+} ion intercalated GO membranes. 84

4.4 Interaction energy of the oxygen-containing functional groups of the GO nanosheets with the intercalated ions. (a) K^+ ion intercalated and (b) Mg^{2+} ion intercalated GO membranes. Here O1, O2, O3, and O4 are the oxygen atoms of a hydroxyl group (-OH), epoxy group (-O-), carboxyl group, which is linked to only C atom (-C=O), and carboxyl group that is bonded to C and H atoms (C-O-H), respectively. 84

4.5 The hydration shells of the K^+ ions of the GO-10-K membrane at different time. The blue color is for hydrogen atoms, the red color is for oxygen atoms and green color is for carbon atoms of the membrane. The gray color is for K^+ ions and magenta color is for water molecules. 85

4.6 The hydration shells of the K^+ ions of the GO-15-K membrane at different time. The blue color is for hydrogen atoms, the red color is for oxygen atoms and green color is for carbon atoms of the membrane. The gray color is for K^+ ions and magenta color is for water molecules. 86

4.7 The hydration shells of the K^+ ions of the GO-20-K membrane at different time. The blue color is for hydrogen atoms, the red color is for oxygen atoms and green color is for carbon atoms of the membrane. The gray color is for K^+ ions and magenta color is for water molecules. 87

4.8 Interaction energy of the oxygen-containing functional groups (OFGs) and aromatic rings (AR) with cations for (a) GO-10-K Membrane and (b) GO-10-M Membrane. (c) Comparative interaction energy (OFGs vs cations) of the GO-10-K and GO-10-M membranes. 88

4.9 Average interlayer distance of the membranes as a function of the simulation time. (a) K^+ ion intercalated and (b) Mg^{2+} ion intercalated GO membranes. . . 89

4.10 The density profiles of the crude oil-water mixture [alkanes (ALK), cycloalkanes (CYALK), aromatics (ARO), and water] along the Z direction for (a) GO-15-K membrane and (b) GO-15-M membrane. Interaction energy of the hydrocarbons with oxygen atom of water (OT) for (c) GO-15-K membrane and (d) GO-15-M membrane. 90

4.11 Snapshot of crude oil aggregation in (a) GO-10-K membrane and (b) GO-10-M membrane. Green color is for carbon atoms, red color is for oxygen atoms, blue color is for hydrogen atoms, gray color is for K^+ ions, black color is for Mg^{2+} ions, yellow color is for alkanes, orange color is for cycloalkanes, and magenta color is for aromatics. 92

4.12 Variation in the density of crude oil along the Z-direction for (a) K^+ ion intercalated and (b) Mg^{2+} ion intercalated GO membranes. The dotted lines indicate the membrane position. 93

4.13 Interaction energy of the crude oil with the intercalated ions (K^+, Mg^{2+}) for GO-15-K and GO-15-M membranes. 93

4.14 Cl^- ion intercalation (in %) for (a) K^+ ion intercalated and (b) Mg^{2+} ion intercalated GO membranes. 94

4.15 Average interaction energy of the K^+ ions with (a) Na^+ and (b) Cl^- ions. 94

4.16 Water permeane through a different pore sizes of the (a) K^+ ion intercalated and (b) Mg^{2+} ion intercalated GO membranes. 96

4.17 Trajectories of the intercalated ions inside the GO laminates during the simulations. (a) K^+ ions, (b) Mg^{2+} ions. Green color is for carbon atoms, red color is for oxygen atoms, blue color is for hydrogen atoms, and remaining colors represent the trajectory of ions. 97

5.1 (a) GO nanosheet. (b) Multilayered GO membrane. (c) RO simulation system. Green color is for carbon atoms, red color is for oxygen atoms, blue color is for hydrogen atoms, yellow color is for Na^+ ions, cyan color is for Cl^- ions, black color is for Mg^{2+} ions, orange color is for K^+ ions, magneta color for boric acid, and violet color for borate ions. 105

5.2 Boric acid (BA) and borate ions (BI) rejections of (a) K^+ ion intercalated GO membranes and (b) Mg^{2+} ion intercalated GO membranes. 107

5.3 The average interaction energies of BA and BI with (a) K^+ ion intercalated GO membranes and (b) Mg^{2+} ion intercalated GO membranes. 108

5.4 Changes in the number of water molecules (N_W) in the hydration shell of both BA and BI along its pathway. Here, dotted lines indicate the membrane position. 109

5.5 The number of water molecules in hydration shells of (a) BA and (b) BI at various positions during the permeation through the membrane. Green color is for carbon atoms, red color is for oxygen atoms, blue color is for hydrogen atoms, and yellow color is for boron atoms. 110

5.6 (a) The radial distribution function (RDF) of water molecules (OT) with BA and oxygen-containing functional groups (OFGs) of the membrane. The RDF (b) and interaction energies (c) of BA with OFGs. (d) The RDF of water molecules (OT) with BI and OFGs. The RDF (e) and interaction energies (f) of BI with OFGs. Here O1, O2, O3, and O4 are the oxygen atoms of a hydroxyl group (-OH), epoxy group (-O-), carboxyl group, which is linked to only C atom (-C=O), and carboxyl group that is bonded to C and H atoms (C-O-H), respectively. 111

5.7 The average interaction energies of intercalated ions (K^+, Mg^{2+}) with (a) BA and (b) BI for GO-K-12P and GO-M-12P membranes. 113

5.8 The water permeance of all membranes. 114

5.9 The 2D mass water density maps in the simulation systems. (a) GO-K-8P, (b) GO-K-10P, (c) GO-K-12P, (d) GO-M-8P, (e) GO-M-10P, and (f) GO-M-12P. . . 115

5.10 Salt rejection percentages of (a) K^+ ion intercalated GO membranes and (b) Mg^{2+} ion intercalated GO membranes. 116

5.11 The average interaction energies of intercalated ions (K^+, Mg^{2+}) with (a) Na^+ and (b) Cl^- ions for GO-K-12P and GO-M-12P membranes. 117

5.12 (a) K^+ and (b) Mg^{2+} ions distribution inside the GO layers as a function of simulation time. (c) The RDF of intercalated ions with water molecules (OT) within the GO laminates. 118

6.1 (a) GO nanosheet. (b) Multilayered GO membrane. (c) FO simulation system. Green color is for carbon atoms, red color is for oxygen atoms, blue color is for hydrogen atoms, magenta color is for urea, yellow color is for Na^+ ions, orange color is for K^+ ions, lime color is for Cl^- ions, black color is for Mg^{2+} ions, and cyan color is for $H_2PO_4^-$. 121

6.2 (a) Relative rejection of urea and NH_3. (b) Radial distribution functions (RDF) of urea and NH_3 with water molecules (OT). Here, UC and UN are carbon and nitrogen atoms of urea, respectively, and AN is the nitrogen atom of NH_3. (c) Number of water molecules in the primary hydration shell, (d) Mass density profiles, and (e) Intercalation percentage of the urea and NH_3. Here, vertical dotted blue lines indicate the membrane position. 124

6.2 continued (f) Electrostatic interactions of GO membranes with urea and NH_3. (g) Electrostatic interactions of individual oxygen-containing functional groups (OFGs) with urea and NH_3. Here, O1, O2, O3, and O4 are the oxygen atoms of a hydroxyl group (-OH), epoxy group (-O-), carboxyl group, which is linked to only C atom (-C=O), and carboxyl group that is bonded to C and H atoms (C-O-H), respectively. (h) RDF of nitrogen-nitrogen atoms for urea (UN-UN) and NH_3 (AN-AN). 125

6.3 Snapshot of (a) Urea and (b) NH_3 molecules within the interlayer gallery of GO membrane. Green color : carbon atoms; red color : oxygen atoms; blue color : hydrogen atoms; magenta color: nitrogen atoms. 126

6.4 a) Relative rejection of NH_3 and NH_4^+. (b) RDF of NH_3 and NH_4^+ with water molecules (OT). Here, AN and ANN are nitrogen atoms of NH_3 and NH_4^+, respectively. Electrostatic interactions of (c) GO membranes and (d) intercalated cations (Mg^{2+}) with NH_3 and NH_4^+. (e) Mass density profiles and (f) Intercalation percentage of NH_3 and NH_4^+. (g) Electrostatic interactions of OFGs with NH_3 and NH_4^+. 128

6.5 (a) Water permeane of Mg^{2+} cation intercalated GO membrane with two different feed solutions, i.e., fresh urine (FS1, nitrogen in the form of urea) and hydrolyzed urine (FS2, nitrogen in the form of NH_3) . (b) Variation of the number of water molecules in the draw solution as a function of the simulation time. (c) Salt rejection percentages. (d) Mg^{2+} cations distribution inside the GO layers as a function of simulation time. 129

7.1 Steps involved in the construction of the non-lamellar graphene oxide (GO) membrane model: (a) Initial random arrangement of GO nanosheets within the water box, (b) pulling the GO sheets onto the rigid graphene sheet, (c) subsequent relaxation and equilibration to remove the vacuum, and (d) a dried non-lamellar GO membrane model. Carbon atoms are depicted in green color, oxygen atoms in red color, hydrogen atoms in blue color, and water molecules in cyan color. . . 135

7.2 (a) Structure of a single graphene oxide (GO) nanosheet. (b) Lamellar arrangement of multilayered GO membrane. (c) Reverse osmosis (RO) simulation system. Green color : Carbon atoms; Red color : Oxygen atoms; Blue color : Hydrogen atoms; Yellow color : Na^+ ions; Magenta color : Cl^- ions; Orange color : K^+ ions. 136

7.3 (a) Water molecules variations in the permeate region with the simulation time and (b) comparative water permeance of all membranes. (c) Pore size distrubution (PSD) of non-lamellar GO membranes. 139

7.4 Two-dimensional (2D) mass density maps of water molecules in the XZ plane. (a) GOL-K, (b) GOL-M, (c) GONL-K, and (d) GONL-M membrane. 140

7.5 (a) The combined average interaction energy of aromatic rings and oxygen-containing functional groups (OFGs) with intercalated cations (K^+, Mg^{2+}) and (b) the percentage of remaining intercalated cations inside the interlayer gallery of all membranes. 142

7.6 (a) The radial distribution function between the intercalated cations (K^+, Mg^{2+}) and water molecules (OT). The coordination number of (b) Mg^{2+} and (c) K^+ cations in their primary and secondary hydration shells along the Z-axis. (d) The average interaction energy between oxygen-containing functional groups (OFGs) and intercalated cations for all membranes. Here, the oxygen atoms of hydroxyl (-OH) and epoxy (-O-) groups are denoted as O1 and O2, respectively, while O3 and O4 represent the oxygen atoms of carboxyl groups (-COOH). 143

7.7 Pathways of four selected (a) K^+ and (b) Mg^{2+} cations within the interlayer gallery of lamellar GO membranes. Green color : carbon atoms; red color : oxygen atoms; blue color : hydrogen atoms, and the remaining colors represent the trajectories of selected intercalated cations. 144

7.8 (a) Salt rejection percentage of all membranes. (b) The radial distribution function between the salt ions (Na^+, Cl^-) and water molecules (OT). (c) The average interaction energy between the salt ions and intercalated cations of all membranes. 145

B.1 Graphene Oxide sheet (50.0×49.0 $Å^2$) with oxygen functional groups. The blue color is for hydrogen atoms, the red color is for oxygen atoms and cyan color is for carbon atoms. 155

B.2 rGO membrane. The blue color is for hydrogen atoms, the red color is for oxygen atoms and cyan color is for carbon atoms. 156

B.3 ErGO membrane. The blue color is for hydrogen atoms, the red color is for oxygen atoms and cyan color is for carbon atoms. 156

B.4 Water permeance as a function of draw solution concentration. 157

B.5 RDF between the oxygen atom (OT) of the water molecule inside the GO membrane and ions of the draw solution. 157

B.6 The hydration shells of the Mg^{2+} ions of the GO-10-M membrane at different time. The blue color is for hydrogen atoms, the red color is for oxygen atoms and green color is for carbon atoms of the membrane. The black color is for Mg^{2+} ions and magenta color is for water molecules. 158

B.7 The hydration shells of the Mg^{2+} ions of the GO-15-M membrane at different time. The blue color is for hydrogen atoms, the red color is for oxygen atoms and green color is for carbon atoms of the membrane. The black color is for Mg^{2+} ions and magenta color is for water molecules. 159

B.8 The hydration shells of the Mg^{2+} ions of the GO-20-M membrane at different time. The blue color is for hydrogen atoms, the red color is for oxygen atoms and green color is for carbon atoms of the membrane. The black color is for Mg^{2+} ions and magenta color is for water molecules. 160

B.9 Water molecule coordination number (w(r)) of the intercalated ions. (a) K^+ ion intercalated and (b) Mg^{2+} ion intercalated GO membranes. 161

B.10 Survival probability (SP) of the water molecules in (a) K^+ ion intercalated and (b) Mg^{2+} ion intercalated GO membrane channels. 161

B.11 Interaction energy of the oxygen-containing functional groups (OFGs) and aromatic rings (AR) with cations for (a) GO-15-K Membrane and (b) GO-15-M Membrane. (c) Comparative interaction energy (OFGs vs cations) of the GO-15-K and GO-15-M membranes. 162

B.12 Interaction energy of the oxygen-containing functional groups (OFGs) and aromatic rings (AR) with cations for (a) GO-20-K Membrane and (b) GO-20-M Membrane. (c) Comparative interaction energy (OFGs vs cations) of the GO-20-K and GO-20-M membranes. 163

B.13 The denisty profiles of the crude oil-water mixture [alkanes (ALK), cycloalkanes (CYALK), aromatics (ARO), water] along the Z direction for (a) GO-10-K membrane and (b) GO-10-M membrane. Interaction energy of the hydrocarbons with oxygen of water (OT) for (c) GO-10-K membrane and (d) GO-10-M membrane. 164

B.14 The denisty profiles of the crude oil-water mixture [alkanes (ALK), cycloalkanes (CYALK), aromatics (ARO), water] along the Z direction for (a) GO-20-K membrane and (b) GO-20-M membrane. Interaction energy of the hydrocarbons with oxygen of water (OT) for (c) GO-20-K membrane and (d) GO-20-M membrane. 165

B.15 Snapshot of crude oil aggregation in (a) GO-15-K membrane and (b) GO-15-M membrane. Green color is for carbon atoms, red color is for oxygen atoms, blue color is for hydrogen atoms, gray color is for K^+ ions, black color is for Mg^{2+} ions, yellow color is for alkanes, orange color is for cycloalkanes, and magenta color is for aromatics. 166

B.16 Snapshot of crude oil aggregation in (a) GO-20-K membrane and (b) GO-20-M membrane. Green color is for carbon atoms, red color is for oxygen atoms, blue color is for hydrogen atoms, gray color is for K^+ ions, black color is for Mg^{2+} ions, yellow color is for alkanes, orange color is for cycloalkanes, and magenta color is for aromatics. 167

B.17 Interaction energy of the crude oil with the intercalated ions (K^+, Mg^{2+}). (a) GO-10-K and GO-10-M membranes. (b) GO-20-K and GO-20-M membranes. . . 168

B.18 Distribution of the Na^+ ions for (a) GO-10-K, (b) GO-15-K, and (c) GO-20-K membranes, at the end of the simulation. Green color is for carbon atoms, red color is for oxygen atoms, blue color is for hydrogen atoms, and yellow color is for Na^+ ions. 168

B.19 Distribution of the Cl^- ions for (a) GO-10-K, (b) GO-15-K, and (c) GO-20-K membranes, at the end of the simulation. Green color is for carbon atoms, red color is for oxygen atoms, blue color is for hydrogen atoms, and orange color is for Cl^- ions. 169

B.20 Distribution of the Na^+ ions for (a) GO-10-M, (b) GO-15-M, and (c) GO-20-M membranes, at the end of the simulation. Green color is for carbon atoms, red color is for oxygen atoms, blue color is for hydrogen atoms, and yellow color is for Na^+ ions. 170

B.21 Distribution of the Cl^- ions for (a) GO-10-M, (b) GO-15-M, and (c) GO-20-M membranes, at the end of the simulation. Green color is for carbon atoms, red color is for oxygen atoms, blue color is for hydrogen atoms, and orange color is for Cl^- ions. 171

B.22 Average interaction energy of the Mg^{2+} ions with (a) Na^+ and (b) Cl^- ions. . . 171

B.23 Distribution of the Na^+ ions for (a) GO-10-K, (b) GO-10-K-10P, and (c) GO-10-K-12P membranes, at the end of the simulation. Green color is for carbon atoms, red color is for oxygen atoms, blue color is for hydrogen atoms, and yellow color is for Na^+ ions. 172

B.24 Distribution of the Cl^- ions for (a) GO-10-K, (b) GO-10-K-10P, and (c) GO-10-K-12P membranes, at the end of the simulation. Green color is for carbon atoms, red color is for oxygen atoms, blue color is for hydrogen atoms, and orange color is for Cl^- ions. 173

B.25 Distribution of the Na^+ ions for (a) GO-10-M, (b) GO-10-M-10P, and (c) GO-10-M-12P membranes, at the end of the simulation. Green color is for carbon atoms, red color is for oxygen atoms, blue color is for hydrogen atoms, and yellow color is for Na^+ ions. 173

B.26 Distribution of the Cl^- ions for (a) GO-10-M, (b) GO-10-M-10P, and (c) GO-10-M-12P membranes, at the end of the simulation. Green color is for carbon atoms, red color is for oxygen atoms, blue color is for hydrogen atoms, and orange color is for Cl^- ions. 174

B.27 Water permeance as a function of the pore offset. 175

B.28 Distribution of the Na^+ ions for membranes with different pore offsets at the end of the simulations. (a) 8 and (b) 16 Å. Green color is for carbon atoms, red color is for oxygen atoms, blue color is for hydrogen atoms, and yellow color is for Na^+ ions. 176

B.29 Distribution of the Cl^- ions for membranes with different pore offsets at the end of the simulations. (a) 8 and (b) 16 Å. Green color is for carbon atoms, red color is for oxygen atoms, blue color is for hydrogen atoms, and orange color is for Cl^- ions. 177

B.30 Radial distribution function (g(r)) of the K^+ and Mg^{2+} ions with the oxygen atoms (OT) of the water inside the layers of the GO membrane. 178

B.31 The density of (a) boric acid (BA) and (b) borate ions (BI) along the Z-axis for K^+ ion intercalated GO membranes. The density of (c) BA and (d) BI along the Z-axis for Mg^{2+} ion intercalated GO membranes. Dotted lines indicate the position of the membrane. 180

B.32 The intercalation percentages of BA and BI for (a) GO-K-10P and (b) GO-M-10P membranes. 180
B.33 Trajectories of (a) BA and (b) BI for feed solution3. Green color is for carbon atoms, red is for oxygen atoms, blue is for hydrogen atoms, and the remaining colors represent the trajectory of BA and BI. 181
B.34 Changes in the number of water molecules (N_P) in the permeate region with the simulation time. (a) K^+ ion intercalated GO membranes and (b) Mg^{2+} ion intercalated GO membranes 182
B.35 Density of water molecules along the Z-axis: (a) K^+ ion intercalated and (b) Mg^{2+} ion intercalated GO membranes. 182
B.36 The 2D mass density maps of Na^+ ions : (a) GO-K-8P , (b) GO-K-10P, and (c) GO-K-12P. The 2D density maps of Cl^- ions : (d) GO-K-8P, (e) GO-K-10P, and (f) GO-K-12P. The 2D density maps of Mg^{2+} ions : (g) GO-K-8P , (h) GO-K-10P, and (i) GO-K-12P. Dotted lines indicate the position of the membrane.184
B.37 The 2D mass density maps of Na^+ ions : (a) GO-M-8P , (b) GO-M-10P, and (c) GO-M-12P. The 2D density maps of Cl^- ions : (d) GO-M-8P, (e) GO-M-10P, and (f) GO-M-12P. The 2D density maps of Mg^{2+} ions : (g) GO-M-8P , (h) GO-M-10P, and (i) GO-M-12P. Dotted lines indicate the position of the membrane. 185
B.38 The density of (a) Na^+ , (b) Cl^- , and (c) Mg^{2+} ions along the Z-axis for K^+ ion intercalated GO membranes. The density of (d) Na^+ , (e) Cl^- , and (f) Mg^{2+} ions along the Z-axis for Mg^{2+} ion intercalated GO membranes. Dotted lines indicate the position of the membrane. 186

List of Tables

2.1 Water model parameters 62

3.1 Number of oxygen containing functional groups on the GO membranes and their corresponding abbreviations 66

3.2 The comparative AMX rejection of different membranes. 78

4.1 Configurations of the GO membranes and their corresponding abbreviations. . . 81

4.2 Percentages of the intercalated chloride ions, choline, and ethylene glycol for all membranes. 99

4.3 The comparative water permeance of polymeric FO membranes in oil-water separation. 100

5.1 Cation-intercalated GO membrane configurations and their corresponding nomenclature. 104

6.1 The comparative rejection of different nitrogen forms by commercial existing polymeric membranes. 130

7.1 Structural arrangements of cation intercalated GO membranes and their respective nomenclature. 137

B.1 The comparative water permeance and boron rejection of a polymeric and graphene based membranes. 183

Chapter 1

Introduction

1.1 Overview

With the growing population, inadequate water resources and increase in environmental pollution, water scarcity become one of the world's most critical challenges. Besides, a significant quantity of the water resources being utilized for industrial development, causing a threat to the remaining water resources due to industrial pollution. Thus, researchers are trying to develop innovative technologies to enhance water recovery (e.g., desalination) and reuse (e.g., wastewater treatment). As the oceans cover nearly 71% of the earth's surface, desalination of saline water is a prominent solution for water scarcity [1, 2]. As a result, the world is advancing towards the desalination of seawater to deliver clean water for all living species. In the past decade, researchers have developed several technologies to draw pure water (or salt removal) from seawater. However, these technologies are ineffective in removing low-concentrated contaminants such as boron [3, 4].

The steady increase in pharmaceuticals consumption from the last few decades because of various diseases [5–7] lead to an increase in their production. A substantial quantity of wastewater present in the ecosystem is mainly due to the discharge of effluents from the pharmaceutical industries[8–10]. They are causing a severe threat to human health as well as to the aquatic environment. Therefore, removal of these effluents from rivers, seas, and groundwater is necessary since water is essential for all living species. On other side, shale gas extraction requires on average 2-7 million gallons of water [11–16]. Thus, the wastewater treatment associated with shale gas needs to be efficient for sustainable production [17–21].

Besides water reuse, there is a growing recognition of the importance of extracting essential nutrients, including nitrogen, phosphorus, and potassium, from wastewater [22–24]. However, the conventional methods for nutrient extraction pose challenges, notably in terms of cost-effectiveness and energy consumption. Thus, efforts to enhance nutrient recovery have emphasized that wastewater streams rich in these nutrients need to be diverted and treated separately rather than being processed at conventional wastewater treatment plants (WWTPs) [25–28]. In particular, the recovery of nitrogen components is crucial for meeting global fertilizer demands.

The overview of this doctoral thesis is an application and understanding the membrane-based technologies, specifically reverse osmosis (RO) and forward osmosis (FO), in the domains of desalination and wastewater treatment, with the overarching goal of ensuring safe water for all living species. The phenomenal progress achieved in computational science plays a crucial role in the design and development of advanced membrane materials, particularly two-dimensional (2D) graphene and its derivative graphene oxide (GO). This research explores their practical applications in real-life scenarios, aiming to understand their underlying mechanisms at an atomistic level.

1.2 Why membrane technologies?

Membrane separation is considered to be the most widely recognized advanced separation technique in recent times and is regarded as a significant breakthrough in separation science and technology. Membrane technology has found its practical applications in various fields of research broadly in sectors such as food and beverages, paper and pulp, metallurgy, textile, automotive, dairy, pharmaceuticals, water treatment, and process industries[29]. It has become an integral part of any separation process. Apart from its wide applications in several fields, it has certain operational advantages such as high flux, high efficiency, ease of operation and cleaning, possible process integration, chemical and thermal stability, high-pressure resistance and cost-effectiveness.

A membrane is a physical, semi-permeable barrier that acts as a specific filter selectively allowing one or more components to pass through it while curbing the flow of other components. The rejected portion is known as the retentate region, while the portion which flows across the membrane is called the permeate region. A membrane, thus, separates the process stream into two regions, the retentate region, and the permeate region. Figure 1.1 illustrates a

simple membrane separation process showing the feed and the permeate region separated by a membrane material. The basic principle of membrane separation is based on the differences in various physical and chemical properties of a system such as size (membrane filtration), charge (electrodialysis, ion exchange), affinity (RO and FO), and vapor pressure (membrane distillation (MD)). Fundamentally, pressure, concentration, and electric potential gradients drive the membrane separation processes[29]. This Ph.D. dissertation focused on understanding, applying, and advancing membrane technologies in real-world scenarios using computational modeling.

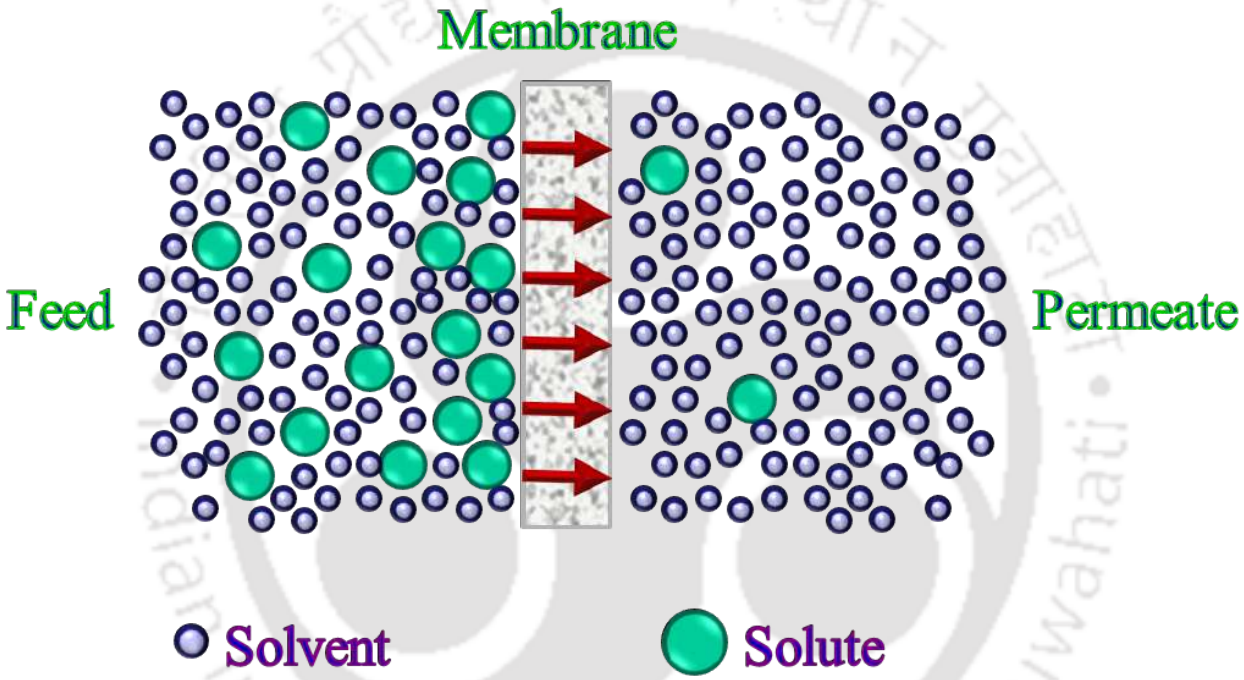

Figure 1.1: A simple membrane separation process.

1.2.1 Reverse Osmosis (RO) process

A typical RO process consists of a feed solution, a permeate region, and a semi-permeable membrane. The RO process uses semi-permeable membranes to separate and remove dissolved solids, organics, submicron colloidal matter, color, and bacteria from water. The progression of the RO process relies on applying external pressure to the feed solution. As shown in Figure 1.2, the feedwater is delivered under pressure through the semi-permeable membrane, where water permeates the minute pores of the membrane and is delivered as purified water called

permeate water. These semi-permeable membranes reject the salt ions while letting the water molecules pass.

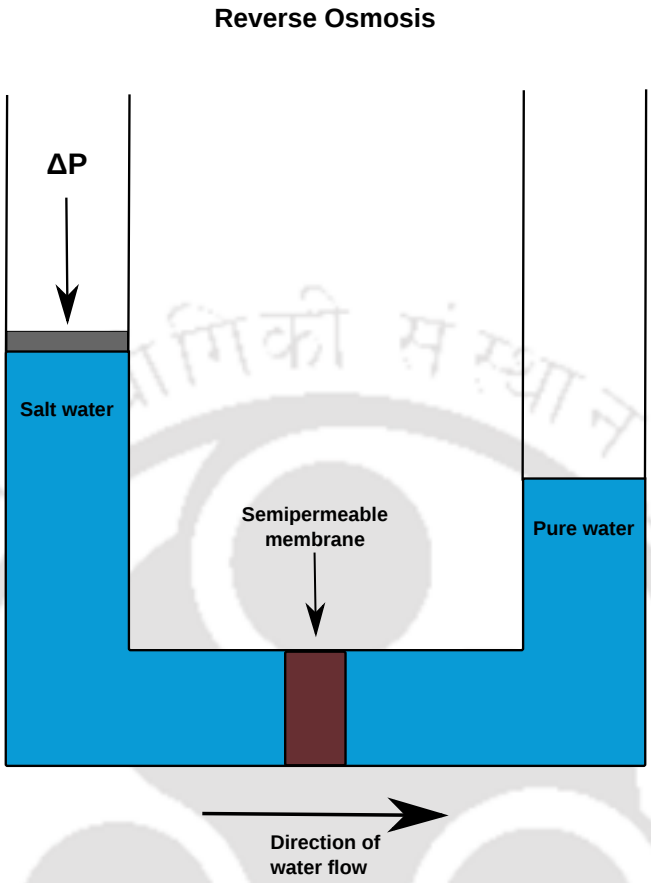

Figure 1.2: Description of RO process.

However, our primary focus is on the membrane system. Membranes, which are used in osmosis (either RO or FO) process, should have the following characteristics.

1. The membrane should be inexpensive, have a long and stable life.
2. The membrane should be easily manufactured with excellent salt rejection.
3. They should have high water flux i.e., highly permeable to water.
4. They should be less susceptible to fouling.
5. The membrane should chemically, physically, and thermally stable in aqueous environments. They need to be strong enough to withstand high pressures and variable feed water quality.

1.2.2 Forward osmosis (FO) process

In the past four decades, membrane development has occurred based on the demand for pressure-driven processes. However, in the last decade, the interest in osmotically driven processes, such as FO, has increased. The process, just like RO, requires a selectively permeable membrane separating two solutions with different osmotic pressures. As shown in Figure 1.3, it works by having two solutions with different different osmotic pressures separated by a selectively permeable membrane. The osmotic pressure of the draw solution should be more than the feed solution. Hence, the selection of the draw solution is very crucial in this process. The process is inherently less prone to fouling than pressure-driven membrane processes.

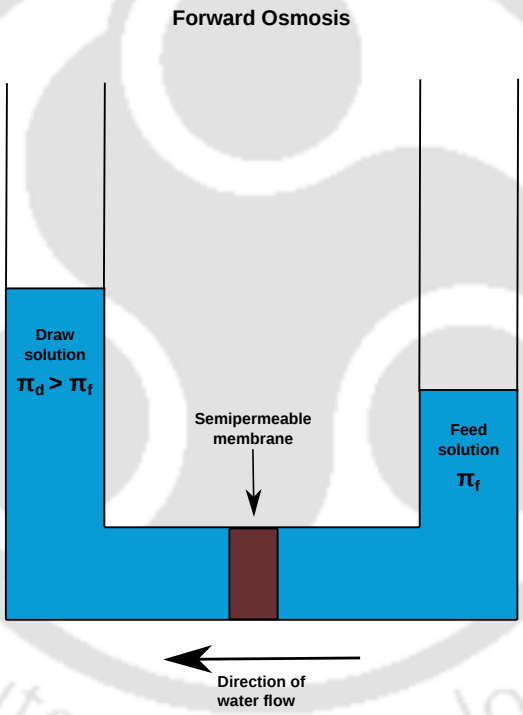

Figure 1.3: Description of FO process.

Fouling is the foremost problem during the usage of a membrane. Cath et al.[30] observed a significant change in the flux decline as a consequence of fouling in the RO process. Further, they identified that fouling in the FO process could be controlled by increasing the cross-flow rate on a membrane sheet which can't be achieved in RO. So, the FO has been growing as an alternative method for the RO in various applications.

1.3 Motivation: Why graphene oxide (GO) as a membrane material?

1.3.1 GO membrane and its challenges

The choice of the membrane material plays a significant role in desalination and wastewater treatment. In the past two decades, substantial efforts have been devoted to developing and applying various commercial polymeric membranes in desalination and wastewater treatment [31–34]. Despite the advancements, challenges persist in the performance of these membranes, encompassing issues such as fouling, filtration efficiency, and the trade-off between water permeance and salt rejection. Specifically, their performance has been suboptimal in rejecting smaller and neutral molecules. In this aspect, the development of advanced membrane materials has emerged as a focal area of interest within academic and industrial research, driven by the need to improve membrane performance and enhance resistance against various fouling agents. Addressing these challenges is particularly critical in applications such as desalination and water treatment, where antifouling properties can significantly improve efficiency and durability. In response, researchers have explored various strategies, including novel materials, surface modifications, and synthesis techniques, to develop antifouling membranes with superior flux and selective separation properties. One promising approach is the integration of nanomaterials in traditional membrane separation applications, offering benefits such as increased antifouling capacity, enhanced flux, improved rejection rates, stability, and even antibacterial properties.

Among these nanomaterials, zeolites, metal-organic frameworks, and carbon-based materials are especially promising due to their unique separation capabilities and adaptability in processing. Carbon nanotubes (CNTs), in particular, have been identified as a potential candidate for next-generation membrane materials, owing to their one-dimensional nanochannels allowing ultra-fast molecular transport and exceptional mechanical strength. Despite their potential, CNT-based membranes are confined mainly to theoretical exploration because of high costs, the technical challenges of achieving high-density, vertically aligned CNTs, and the obstacles associated with scaling up production. Beyond CNTs, advancements in two-dimensional (2D) materials like graphene and its derivatives provide a compelling opportunity to create novel membranes with remarkable separation performance[35–38].

Since the Nobel Prize was awarded in 2010 for groundbreaking experiments on graphene,

research on graphene-based membranes has surged. These membranes, including graphene, graphene oxide (GO), and chemically converted graphene, leverage graphene's unique one-atom-thick, 2D structure, where its sp^2-hybridized carbon atoms form a honeycomb lattice, resulting in exceptional mechanical strength, chemical stability, and scalable production potential[39–41]. The nearly frictionless, ultra-thin surfaces of graphene membranes reduce transport resistance, enabling significant increases in permeate flux and creating vast opportunities in the field of separation science. Particularily, GO have delivered the most promising results in desalination and wastewater treatment [42–52]. Modified Hummers' [53] method is commonly used for synthesizing the GO flakes. The usual synthesis routes for a GO membrane are vacuum filtration[54], spin coating[55], and layer-by-layer (LBL) self-assembly[56].

In contrast to conventional polymeric membranes, GO membranes have the ability to self-assemble into layered structures via the arrangement of neighboring GO nanosheets[35, 42, 57–59]. The resulting microstructure of stacked GO-based membranes manifests as a 2D interlayer gallery containing nanochannels and tunable interlayer spaces (and open edges) between adjoining GO nanosheets. The inherent structural features of GO membranes (i.e., nanosized 2D channels and open edges) have the potential to facilitate the movement of water molecules rapidly across membrane layers while effectively retaining undesired species[35, 42, 43, 57–63]. Furthermore, the nanosized GO nanosheets have abundant oxygen-containing functional groups (OFGs), contributing to their mechanical strength and chemical stability. The epoxy, and hydroxyl oxygen groups are located on the basal plane of the GO nanosheet, and carboxyl groups are located at the edges. In addition, the presence of OFGs enhances the efficacy of the salt rejection mechanism due to the electrostatic interaction of OFGs with salt ions[57, 58, 60, 64, 65]. As water permeability and separation mechanisms depend on the microstructures of GO membranes, understanding the microstructure formation and its consequential impact on membrane performance is highly necessary.

Hence, as a crucial derivative of graphene, GO provides additional functionality with oxygen-containing groups on its edges and basal planes, offering the flexibility to modify its physicochemical properties for targeted applications. As a result, GO, and its derivatives have emerged as valuable materials for improving water flux, rejection, and membrane fouling resistance. Given its accessibility, chemical resilience, and tunable properties, GO has been integrated into various applications, including membranes and their applications in pressure-driven separation, adsorption, catalysis, supercapacitors, and sensing applications.

Although GO membranes are renowned for their efficacy in rejecting smaller and neutral molecules, the full potential of these membranes has been hindered by following challenges of GO membranes. The challenges in utilizing GO nanosheets for large-scale applications lie in the controlled preparation and consistent performance optimization of GO membranes. While producing the GO nanosheets, achieving precise control over parameters such as oxidation degree, functional groups, and size remains complex [57, 66]. Yet, these factors are crucial for optimizing separation mechanisms and enhancing the membrane's overall performance. Unlike traditional polymeric membranes, multilayered GO membranes offer potential advantages, such as resistance to fouling and chlorination; however, creating an effective designable structure requires addressing several key challenges in GO membrane fabrication and stability.

The degree of oxidation directly impacts the interlayer spacing in GO-based membranes, a critical factor in separation efficiency. The typical interlayer spacing, measured at approximately 0.83 nm via X-ray diffraction (XRD), can be increased to about 1 nm by adjusting the oxidation degree[67, 68]. The interlayer spacing fluctuates under varying humidity (or when in contact with water) and influences the formation of water channels that enable selective molecular transport[69–72]. Maintaining consistent layer spacing to optimize water flow and achieve size-exclusion of small molecules requires precise control over oxidation, which is difficult in large-scale production. The GO membranes' separation mechanism involves molecular sieving and Donnan exclusion principles, yet fine-tuning these mechanisms to ensure selective water permeation and efficient separation of targeted molecules remains challenging. The unimpeded water flow through multilayered GO membranes depends on well-defined functional groups and minimally oxidized regions that create frictionless spaces within the lamellar structure.

Further, several factors, including thickness adjustment, reduction, modification, crosslinking, and intercalation, must be explored to refine separation performance in GO membranes. However, challenges persist in maintaining consistency across these modifications, especially as the degree of oxidation affects not only thickness but also hydrophilicity, charge, and nanosheet smoothness. These factors, in turn, influence transport properties. Maintaining structural stability and optimal water channels while enhancing permeability and selectivity remains crucial for further research. This thesis aims to study the swelling tendency of GO membranes in the aqueous environment because GO membranes utilized in desalination and wastewater treatment involve aqueous environments.

To address the issue of undesirable aqueous swelling of layered GO membrane various meth-

ods have been proposed over the years such as physical confinement [73], external pressure regulation[74], crosslinking GO nanosheets [61, 75–80], reduction of the GO nanosheets [81]. However, it is still a great challenge to develop GO membranes using these methods to meet the performance and long-term applicability for industrial purposes. Also, it is observed that the water flux increases significantly for crosslinked membranes with large organic molecules, reducing the rejection of small undesirable species[75]. Similarly, reduction of the GO nanosheets results in lower hydrophilicity along with lower water permeance [81, 82]. Another method to mitigate the aqueous swelling of layered GO membrane is to intercalate them with cations such as K^+, Na^+, Mg^{2+} etc. [70, 78, 83–85]. This is an encouraging solution considering the abundance of these cations in sea water.

1.3.2 Cation intercalated GO membrane

As mentioned earlier, the interlayer spacing is one of the most crucial parameters in determining the performance of layered GO membranes. However, undesirable swelling of GO membranes in an aqueous environment causes hardships during practical applications. In this aspect, introducing cations into the membrane layers demonstrates the most promising developments in counteracting the swelling behavior and ensuring stable interlayer spacing at the nanometer scale.

Chen et al.[70] demonstrated the effectiveness of controlling the interlayer distance of GO membranes with angstrom precision using K^+, Na^+, Ca^{2+}, Li^+, and Mg^{2+} ions. They reported that cationic-controlled GO membranes maintain a stable interlayer distance due to the interactions between the cations and aromatic rings of GO nanosheets and the interactions between the cations and oxygen-containing functional groups of the GO nanosheets. Additionally, they reported varying interlayer distances for different cations that are inserted within the GO laminates. Yuan et al.[81] fabricated reduced graphene oxide (rGO) membranes and introduced K^+ ions into their laminates to establish stable membranes. The study revealed that the strong K^+-π interactions stabilized the nanochannels of the rGO membranes, effectively preventing the permeation of other ions into the nanochannels. As a result, these stabilized rGO membranes exhibited significantly improved salt rejection capabilities compared to pristine GO membranes. Moreover, this study highlighted that a decrease in water permeance and an increase in salt rejection with an increase in cationic concentration within the GO laminates.

Cha-Umpong et al.[86] explained the relationship between the interlayer distances of GO membranes and the charge (and hydrated radius) of cations within their channels. The authors employed density functional theory (DFT) to precisely determine the interlayer distances of GO membranes incorporating Na^+, Ca^{2+}, and Mg^{2+} ions. Further, this study emphasized the significance of the binding energy between the intercalated ions and GO membranes in ensuring a stable interlayer distance. Yang et al.[78] also employed DFT to measure the interlayer distances of graphene membranes, including Li^+, Na^+, and K^+ ions. The study reported an order of interlayer distances, with Li^+ exhibiting the largest value, followed by Na^+ and K^+. Notably, the hydrated K^+ ion, being the smallest in size, significantly reduced the interlayer distances. This valuable insight highlights the significant role of the size of the hydrated ion in determining the interlayer distance. Gogoi et al.[83] examined the impact of cation intercalation on the performance of layered GO membranes using molecular dynamics (MD) simulations. The authors demonstrate that cation intercalation significantly enhances the water flux compared to pristine layered GO membranes with the same interlayer spacing. The reason could be that the introduction of cations results in a more tightly packed arrangement of water molecules and improves the stability of the hydrogen bond network among water molecules, causing the reduced water reorientation dynamics within the interlayer gallery. Furthermore, the intercalation of cations such as K^+ and Mg^{2+} enhances the rejection of Na^+ ions, while the rejection of Cl^- ions experiences a slight decrease.

Liu et al.[84] developed a GO membrane for separating methanol (MeOH) and dimethyl carbonate (DMC) solvents via pervaporation. The interlayer distance of the membrane has adjusted, and its structure stabilized by incorporating metal ions between the GO sheets. These introduced cations interacted with the sp^2 region of GO through cation-π interactions and electrostatic attractions with carboxyl, hydroxyl, and epoxy groups on the GO sheets. To optimize the molecular transport channels within the GO membrane, the researchers experimented with different cation species (Na^+, K^+, Zn^{2+}, Ca^{2+}), varied the cation content, and altered the size of the GO flakes. Gurianov et al.[87] studied the pervaporation desalination performance of GO membranes for salt solutions. The researchers found that the water permeance of the GO membranes decreased from 27 $kg.m^{-2}$ h^{-1} for pure water at 80 °C to 4.5 $kg.m^{-2}$ h^{-1} for a 0.6 M NaCl solution. This decrease in water permeance can be attributed to two main factors: an increase in the activation energy required for water molecule transport and a reduction of over 50-80% in the available free volume for diffusion. Overall, the study highlights that dynamic

variations in interlayer distance and the loading of graphene oxide with ions are critical factors in determining the performance of GO membranes for desalination applications. Recently, Rajasekhar et al.[51] specifically investigated the effect of increasing cationic concentrations within the GO layers for K^+ and Mg^{2+} ion intercalated GO membranes through the FO process via nonequilibrium MD simulations. Three different concentration of cations are considered inside the GO laminates. Through their research, the authors concluded that the increase in cationic concentration resulted in lower water permeance and improved salt rejection.

1.4 Necessity of pharmaceutical industrial wastewater treatment

Based on the pharmaceuticals consumption from the last few decades, antibiotics are among the most prevalent pharmaceutical pollutants detected in pharmaceutical industrial wastewater effluents[88, 89]. Amoxicillin (AMX) is among the highly consumed antibiotics detected in pharmaceutical industrial wastewater. The chemical formula of the AMX is $C_{16}H_{19}N_3O_5S$. It is a hazardous pharmaceutical pollutant since its presence, even in small concentrations, causes severe pollution to the ecosystem. Currently, many experimental techniques such as adsorption [90–93], RO[6, 94, 95], FO[30, 96], nanofiltration (NF) [5, 6, 8, 9, 97], and others[98] have widely been used to purify the wastewater. Among these, membrane technologies such as RO and FO have gained substantial research interest over the years due to their significant characteristics, such as high flux, ease of operation, and efficiency.

However, there are only a handful of available literature which addresses the applicability of carbon based materials for the separation of pharmaceutical molecules [99–102]. These includes adsorption of the pharmaceutical drug molecules on the activated carbon surface [90, 103], rejection of pharmaceutical drug molecules in the RO process using a GO membrane [104] etc. Mansouri *et al.* [90] studied the separation of AMX and ibuprofen (IBU) molecules from the aqueous solution by using three different activated carbon adsorbents. They concluded that the amount of adsorption is more for IBU than the AMX due to its high affinity towards the adsorbent. Bahamon and Vega [103] studied the adsorption of two different kinds of pharmaceuticals (total five drugs) from the wastewater by using activated carbon adsorbents through Monto Carlo simulations. They reported that the amount of uptake depends on the affinity

of drug molecules towards the adsorbent. They also reported that the amount of adsorption of the pharmaceuticals follows the order paracetamol > diclofenac; naproxen > IBP > AMX. Chu *et al.* [99] compared the retention percentages of pharmaceuticals, natural organic matter (NOM), and inorganic salts between pristine ceramic and GO coated ceramic membranes. They reported that GO coated ceramic membranes attained better retention efficiencies compared to the pristine membrane. Moarefian *et al.* [100] studied the separation of AMX from the waste water stream through the NF process using a self-made Polyethersulfone membrane. Their membrane showed a AMX rejection rejection of 99.09% at low initial feed conditions (20 ppm). Wang *et al.* [101] studied the removal of pharmaceuticals from wastewater using an integrated membrane system. In their study they combined a membrane bioreactor (MBR) treatment with RO or NF membrane. They had considered 23 different types of pharmaceuticals and personal care products. Their observations suggested that removal efficiencies increased to significant levels after the MBR combines with RO or NF membrane. Bahamon and Vega [104] investigated the separation of phenol and IBU from the wastewater with layered GO membrane using non-equilibrium MD simulations. They reported that the water permeability strongly depends on the thickness of the membrane and the IBU molecules are likely to adsorb on the basal plane of the membrane.

1.5 Need of boron removal from wastewater

Typically, groundwater contains up to 2 mg/L of boron due to wastewater discharge containing traces of customary products like soaps and detergents, and seawater has a boron concentration of 4-6 mg/L [105–108]. However, the acceptable boron concentration in freshwater is less than 0.1 mg/L on average. Although boron is one of the essential nutrients for all living species, an excessive boron concentration in freshwater can be hazardous to human health and plant growth [109]. As a result, born removal is critical from both saline water and groundwater to ensure the safety of living species.

Naturally, boron is present as a boric acid in an aquatic environment at a pH < 9.2 [110, 111]. With an increasing pH of the solution, boric acid reacts with water and produces a borate ion [111]. Researchers have proposed several processes for removing boric acid from saline water and groundwater, such as adsorption [112], electro-deionization [113], coagulation-precipitation [114], solvent extraction [115], and membrane-based methods. The membrane-based processes,

especially RO, are dominant for purifying saline water because of their energy efficiency and easy operation [116–119].

Physical sieving (size exclusion) and electrostatic interactions are the two primary rejection mechanisms of membrane-based separation methods [47, 116, 120, 121]. A few studies explain the mechanism of boron rejection based on physical sieving, size, shape, and type of the pores (hydrophilic or hydrophobic) for membranes[116–119, 122–124]. However, the role of electrostatic interactions in boron removal is not discussed much in the literature.

Wang et al.[116] prepared thin film composite (TFC) membranes using a technique called interfacial polymerization (IP). They utilized m-phenylenediamine (MPD) and 1,3,5-benzene tricarbonyl trichloride (TMC) to create semi-interpenetrating networks within the membranes. To enhance the surface properties of the membranes (hydrophilicity/hydrophobicity and compactness), various concentrations of polyisobutylene (PIB) dispersed in the organic phase of the TMC monomer before IP. Moreover, the modified membranes exhibited an enhanced size exclusion mechanism of boron rejection compared to unmodified polyamide (PA) membranes. The membranes with a PIB concentration of 0.30% (m/v) delivered an optimal performance, i.e., boron rejection of 93.12% and water flux of 44.17 $L.m^{-2}$ h^{-1} (LMH).

Zhang et al.[119] examined the impact of pore characteristics (hydrophilicity, shape, and size) of covalent organic frameworks (COFs) called TpPa-Rs via non-equilibrium molecular dynamics (NEMD) simulations. Authors considered that COFs have varying functional groups but similar diameters of approximately 6.0 Å. The results showed that the hydrophilic pores containing functional groups such as COOH, NH_2, and OH exhibited boric acid rejection of over 90%. In contrast, the hydrophobic pores with functional groups like NO_2, SH, and CH_3 displayed less than 20% boric acid rejection. The findings demonstrated that the hydrophilic nature of pores played a crucial role in enhancing boric acid rejection, primarily by promoting water adsorption and impeding the transport of boric acid molecules. Risplendi et al.[118] explained the mechanism behind boron rejection through size exclusion using single-layered nanoporous graphene membranes using RO process via MD simulations. The investigation focused on three distinct pore sizes of membranes, i.e., 3.60, 6.28, and 8.37 Å, respectively, and reported corresponding boron rejection percentages of 100, >95, and 80. Additionally, the authors reported the hydration sphere diameter of boric acid to be 7.2 Å.

1.6 Essential of Human urine treatment

As mentioned earlier, the recovery of nitrogen components is crucial for meeting global fertilizer demands. Nitrogen, a crucial element for global fertilizer requirements, is abundant in nature but not readily available in desired forms, such as ammonia and urea [23, 28, 125, 126]. Presently, ammonia production relies heavily on the energy-intensive Haber–Bosch process, demanding a substantial 12,000 kWh per ton-NH_3 production, and ammonia is further utilized in the synthesis of urea [127–129]. Both ammonia and urea serve not only as essential fertilizers but also find applications in diverse industries, including plastic and adhesive manufacturing, refrigerant gas production, diesel exhaust fluid, hand creams, deicing agents for streets and airports, and resin fabrication [28, 128, 130, 131]. Considering these border applications and the energy-intensive nature of current production methods, there is a growing focus on exploring wastewater streams containing rich concentrations of ammonia and urea, human urine stands out as a potential source for such valuable compounds.

Human urine is a nitrogen-rich stream constituting 80% nitrogen by mass in the wastewater; however, it accounts for only 1% of the volumetric flow [132–135]. Despite its relatively small volume in wastewater, it is a nutrient-rich stream, that demands significant energy inputs for effective treatment at WWTPs. Therefore, diverting human urine from wastewater streams could significantly reduce the energy demands of WWTPs [136] and concurrently contribute to the recovery of valuable substances such as ammonia and urea. Consequently, this redirection reduces the dependence on conventionally produced ammonia and urea. Moreover, it is essential to comprehensively understand the unique chemistry of human urine before commencing any treatment processes. Human urine exists in two distinct states, fresh and hydrolyzed, depending on the form of nitrogen targeted for recovery. In fresh urine, urea is the predominant nitrogen form, whereas hydrolyzed urine contains either ammonia or ammonium ions, depending on the pH level [125, 137, 138]. Current existing methods for ammonia recovery from human urine encompass ammonia air stripping, ammonium adsorption through ion exchange, and microbial fuel cells [27, 139–144]. Although these methods have demonstrated effective nitrogen recovery, their drawbacks include high energy consumption, greater chemical input, and challenges in scalability, potentially impeding their implementation. Over the last decade, membrane-based technologies such as NF, RO, and FO have demonstrated significant progress in the field of wastewater treatment.

H. Ray et al.[28] investigated the use of RO (Filmtec flat sheet BW30 membrane) and NF (DOW NF90 membrane) for ammonia recovery from hydrolyzed human urine. The study involved quantifying the permeation of ammonia and various other compounds in urine. The findings of the research revealed complete ammonia permeation in both RO and NF membranes, indicating a zero rejection of ammonia. In another study, S. Habib et al.[32] undertook modifications on commercial polyamide RO membranes, specifically Dupont XLE and BW30XFR. Compared with unmodified membranes showed significant improvements in urea rejection for both modified XLE membranes (from 16.8% to 54.9%) and modified BW30XFR membranes (from 48.4% to 64.6%).

In the study conducted by H. Ray et al.[125], an examination was carried out to assess the rejection of urea in fresh urine under varying pH conditions, as well as the rejection of unionized ammonia and ammonium ions in hydrolyzed urine using RO with Filmtec flat sheet BW30 membrane, NF with DOW NF90 membrane, and microfiltration (MF). The results indicated that the average urea rejection for RO and MF was 57% and 3%, respectively, with no significant influence observed due to changes in pH. For NF, the average urea rejection ranged from 42% to 54%, showing a notable decrease in rejection at pH 12.5 compared to pH 5. Examining the rejection of ammonia, the average rejection for both RO and NF at pH 6.5 and 9 was 94% and 80%, respectively. Interestingly, at pH 11.5, where all nitrogen existed in the form of unionized ammonia, RO demonstrated a 36% rejection of ammonia, while NF exhibited a 10% rejection of ammonia. These findings underscore the pH-dependent variations in urea and ammonia rejection, providing valuable insights into the performance of RO, NF, and MF in treating urine for ammonia recovery.

In the study conducted by C. Courtney et al.[145], a comparative analysis presented on urea rejection capabilities of two categories of NF membranes, namely loose and tight membranes. Notably, the tight NF90 membrane demonstrated enhanced urea rejection, reaching 55% for real fresh urine at a volume reduction factor of 1.1, compared to the lower rejection percentage of loose NF270 membrane (<10%). Similarly, L. Crane et al.[126] employed RO (BW30) and NF (NF90 and NF270) membranes to investigate the selective recovery of urea from fresh human urine. Their findings revealed that BW30 exhibited the highest urea rejection of 76%, followed by NF90 with 55%, and NF270 with a rejection percentage ranging from 2% to 4%.

F. Volpin et al.[23] conducted a comprehensive study on the integration of FO and membrane distillation (MD) for treating human urine. Using a 2.5 M NaCl draw solution with a commercial

flat sheet polyamide (PA) thin-film composite (TFC) as the FO membrane, the study achieved urea and NH_3 rejection rates ranging from 80% to 85%, with NH_4^+ rejection exceeding 95%. Likewise, H. Ray et al.[130] employed a two-step process involving FO and MD for the recovery of urea from fresh human urine. A semipermeable FO membrane (Porifera) and 1 M NaCl as a draw solution are used in this investigation. The combined process yields a product solution with an average urea concentration ranging from 45% to 68% of that present in fresh urine. F. Volpin et al.[24] investigated a PA-TFC membrane utilized as a FO membrane for human urine treatment by considering the $MgSO_4$ and $Mg(NO_3)_2$ as draw solutions, achieving a 50% nitrogen recovery in the draw solution. H. Ray et al.[31] employed a novel approach involving strategic pH manipulation in the context of the FO process (PA-TFC FO membrane (Porifera Inc., Ca)). Using a draw solution of 1.5 M KH_2PO_4, the study achieved up to 86% ammonia recovery in the draw solution.

1.7 Objectives

The following objectives addressed in this thesis have been formulated in response to identified gaps presented in the existing literature.

Objective 1: Effect of oxygen-containing functional groups of layered graphene oxide membrane on the removal of amoxicillin: a molecular dynamics study.

Objective 2: Cationic stabilized layered graphene oxide membrane for shale gas wastewater treatment: An atomistic insight

Objective 3: Understanding the boron rejection of cation intercalated multilayered graphene oxide membrane in reverse osmosis process: A molecular dynamics study

Objective 4: Urea and ammonia recovery from human urine by forward osmosis process using cation intercalated graphene oxide membrane: A molecular dynamics study

Objective 5: Comparative retention analysis of intercalated cations inside the interlayer gallery of lamellar and non-lamellar graphene oxide membranes in a reverse osmosis process: A molecular dynamics study

The outcomes of the research have been published in reputed international peer-reviewed journals, including Molecular Simulation (Taylor & Francis), Desalination (Elsevier), the Journal of Molecular Liquids (Elsevier), and the Journal of Physical Chemistry B (ACS). A few more manuscripts are anticipated to be submitted shortly. Further information regarding journal and

conference publications is provided at the end of the thesis.

1.8 Thesis strategy and organization

Chapter 2 provides a brief overview of the simulation technique, molecular dynamics, employed throughout this thesis, explaining its fundamental formalism.

Chapter 3 focuses on the impact of oxygen-containing functional groups of GO membranes on pharmaceutical industrial wastewater treatment. Specifically, the study examines the behavior of Amoxicillin, a widely consumed antibiotic, through realistic structural configurations of the membrane employing the FO process.

Chapter 4 examines a strategy to mitigate the undesirable swelling tendency of GO membranes by introducing cations within their layers. The study evaluates the effect of intercalated cationic concentration on membrane performance, particularly in the context of treating shale gas wastewater, employing two distinct kinds of cations in FO mode.

Chapter 5 addresses the role of two primary rejection mechanisms of membrane technologies, namely physical sieving and electrostatic interactions, using boron as a pollutant in reverse osmosis (RO) mode with two different cation-intercalated GO membranes.

Chapter 6 explores the potential of cation-intercalated GO membranes in the treatment of human urine via FO mode, considering variations in urine composition—fresh and hydrolyzed—and analyzing the rejection of primary nitrogenous compounds, including ammonia and urea.

Chapter 7 presents the comparative retention time analysis of intercalated cations within distinct structural configurations of GO membranes and evaluates their relative performance in RO mode, utilizing seawater as the feed solution.

Chapter 8 contains the conclusions and some ideas for future works.

Chapter 2

Simulation Methodology

2.1 Essence of Computational Modeling

In the realm of scientific investigation, the integration of computer simulations offers invaluable particulars to traditional experimental methods for addressing intricate scientific challenges. A fundamental objective of computer simulations is to emulate the experiments effectively, providing the microscopic details of the mechanism, and facilitating the comprehensive understanding of research outcomes. Simultaneously, these simulations serve as a valuable predictive tool, anticipating experimental outcomes with precision. In the domain of molecular simulations, two widely employed methods are Monte Carlo (MC) and Molecular Dynamics (MD).

The methodology employed in MC simulations is simple, and rooted in stochastic principles that rely on the probability distribution of system properties. The occurrence of events in MC simulations is governed by associated probabilities, where the selection of a particular event is dictated by the use of random numbers. In contrast, the MD simulation method is a deterministic approach, using Newton's law of motion to model the dynamic behavior of the system. Notably, MD simulations offer several advantages over MC simulations, particularly in elucidating system dynamics, exploring temperature effects, and integrating external fields. Consequently, MD simulations find specialized applications in handling complex systems, such as membranes and proteins, where a substantial number of atoms are involved.

2.2 Theory behind the Molecular Dynamics

The core of the classical MD simulation methodology relies on the application of Newton's law of motion, wherein particles are treated as Newtonian entities, ignoring quantum effects on them. This assumption implies that electrons are assumed to remain in their ground states, and their dynamics are promptly adjusted in response to changing atomic positions. Thus, Newton's equation of motion (eqn. 2.1) applies to the particles, where F_i denotes force, m_i represents mass, and a_i signifies particle acceleration. Through the careful determination of positions and velocities for each atom, the state of the system can be predicted, facilitating the calculation of subsequent positions and velocities. This iterative procedure yields a trajectory of atomic motions and interactions of atoms, providing valuable insights into the dynamic behavior of molecular systems.

$$a_i = \frac{d^2 x_i}{dt^2} = \frac{F_i}{m_i} \tag{2.1}$$

2.2.1 Force Fields

The heart of the MD simulations is the utilization of forcefields, which are essential for measuring the atomic interactions and dynamics of any simulation system. A forcefield is conceptually defined as a set of empirical energy functions and associated parameters, helping to precise measurement of the potential energy function for a given system of atoms. This potential energy function is a key to a simulation system that measures different modes of interaction among atoms within the system, expressed as a function of their atomic coordinates. The potential energy function facilitates the calculation of forces acting on the atoms, following the principle that the force ($\vec{F}(\vec{r})$) on the object is the negative derivative of the potential energy function ($U(\vec{r})$) (eqn. 2.2). Consequently, understanding the forces exerted on atoms within the system allows for the computation of their positional changes over time.

$$\vec{F}(\vec{r}) = -\nabla U(\vec{r}) \tag{2.2}$$

$$
\begin{aligned}
U(r_1, ..., r_N) = & \sum_{bonds} \frac{1}{2} K_b (r - r_0)^2 + \sum_{angles} K_\theta (\theta - \theta_0)^2 \\
& + \sum_{Dihedral} V_n [1 + cos(C_n \phi + \delta_n)] + \sum_{Improper} K_\phi (\phi - \phi_0)^2 \\
& + \sum_{i,j \in nb} \left\{ \left[4\epsilon_{ij} \left(\frac{\sigma_{ij}}{r_{ij}} \right)^{12} - \left(\frac{\sigma_{ij}}{r_{ij}} \right)^{6} \right] + \frac{q_i q_j}{r_{ij}} \right\}
\end{aligned} \tag{2.3}
$$

The potential energy function employed in MD simulations contains bonded and non-bonded interaction terms of atoms within the system (eqn. 2.3). The bonded terms of this function account for various interactions, including bond stretching, angle bending, dihedral or torsional rotations, and improper potential terms. The initial term of this function accounts for bond oscillations around the equilibrium bond length (r_0), characterized by a specified bond force constant (K_b). The second term outlines angle oscillations around the equilibrium angle (θ_0), regulated by a specified angle force constant (K_θ). The third term introduces the dihedral potential, incorporating parameters such as amplitude (V_n), dihedral angle (ϕ), periodicity (n), and phase shift (δ). Addressing improper potentials, the fourth term integrates the angle (ϕ) between the plane formed by the central atom and two peripheral atoms and the plane formed by the peripheral atoms. To capture non-bonded interactions, the fifth term employs the 12-6 Lennard-Jones potential, effectively modeling attractive and repulsive forces between atom pairs through equilibrium interatomic van der Waals (vdW) distance (σ_{ij}) and potential well depth (ϵ_{ij}). Lastly, the sixth term accounts for Coulombic potential, expressing electrostatic interactions between atoms represented as point charges (q_i or q_j). To initiate an MD simulation, the precise specification of these parameters is imperative, and quantum-mechanical calculations play a pivotal role in computing these values. Some popular forcefields frequently used in MD simulations are CHARMM[146, 147], OPLS-AA [148], GROMOS[149] and AMBER[150]. Each of these forcefields target to reproduce a specific set of experimental properties, and hence are developed and optimized accordingly. Also, these forcefields differ in the parametrization methodologies and treatment of a particular term. However, the basic skeleton of each of these forcefields is same as eqn. 2.3.

2.3 Integration of Equations of Motion

Obtaining an analytical solution to the Newton's equation of motion is impractical due to the complexity of the potential function and the challenges associated with solving of N-body problem. Consequently, the adoption of a numerical approximation (termed integration) approach becomes compulsory to obtain a precise solution. However, the selection of an integration method for MD simulations requires careful consideration of a few essential factors. Foremost among these considerations, the integrator must be accurate. When dealing with many-body systems, any numerical integrator faces challenges in providing correct trajectories over extended timescales. This challenge arises from the sensitivity to initial conditions, wherein an arbitrarily small difference in the initial condition leads to exponential divergence of trajectories over finite time. Therefore, an effective MD integration algorithm must navigate small time steps (Δt) during simulations to ensure the accuracy of trajectories. Additionally, a proficient MD integration algorithm must prioritize energy conservation, a key factor in the precise calculation of thermodynamic properties. Without energy conservation, simulations may become unstable due to simulation diverging towards infinite energy. Time reversibility is another essential parameter, assuring energy conversation during the simulations. In practical applications, a few methods are available that fulfill these specified necessities. Among them, the most accurate and stable algorithms are the Verlet and Velocity Verlet algorithms.

2.3.1 Verlet Algorithm

The idea behind the Verlet algorithm(VA)[151] is quite simple; it uses Taylor series expansion to generate new positions of the atoms. The Taylor expansion for a position $r_i(t + \Delta t)$ can be written as:

$$r_i(t + \Delta t) \approx r_i(t) + \Delta t \dot{r}_i + \frac{1}{2}\Delta t^2 \ddot{r}_i(t) \tag{2.4}$$

The terms higher than second order in the above Taylor expansion are neglected. Also, as is known, the first derivative of the position is the velocity($\dot{r}_i(t) = v_i(t)$), and the second is acceleration($\ddot{r}_i(t) = a_i(t)$), also using Newton's second law we have $a_i(t) = F_i(t)/m_i$. Hence, we can rewrite the eqn 2.4 as:

$$r_i(t + \Delta t) \approx r_i(t) + \Delta t v_i(t) + \frac{\Delta t^2}{2m_i} F_i(t) \tag{2.5}$$

A similar expression could be written for $r_i(t - \Delta t)$ as:

$$r_i(t - \Delta t) \approx r_i(t) - \Delta t v_i(t) + \frac{\Delta t^2}{2m_i} F_i(t) \tag{2.6}$$

Adding eqns 2.5 and 2.6 and rearranging we get

$$r_i(t + \Delta t) \approx 2r_i(t) - r_i(t - \Delta t) + \frac{\Delta t^2}{2m_i} F_i(t) \tag{2.7}$$

Eqn 2.7 and 2.6 are the most crucial parts of VA. The VA's execution can be elaborated in the following steps:

1. A set of energy-minimized coordinates and initial velocities is provided to the integrator at $t = 0$.

2. The eqn 2.5 is used to kick-start the integrator and obtain the first set of new coordinates $r_1(\Delta t), ..., r_N(\Delta t)$.

3. The eqn 2.7 can now be used to obtain future positions and generate an arbitrary length of the trajectory.

4. The velocities can be computed using the centered difference formula on positions as follows:

$$v_i(t) = \frac{r_i(t + \Delta t) - r_i(t - \Delta t)}{2\Delta t} \tag{2.8}$$

Like any algorithm or a numerical technique, VA is also not perfect and has its share of advantages and drawbacks, which could be enlisted as follows:

Advantages:

- One of the key feature of VA is that it is simple yet accurate and is easy to implement. The memory requirements of VA are also modest.

- The VA uses the force evaluation very optimally(once at each integration step), which makes the integrator quite efficient since the force calculation is computationally the most demanding step in any MD simulation.

- Another critical characteristic of VA is that it is time-reversible, a property of EOM that a good integrator should satisfy.

Drawbacks:

- The velocity evaluation in VA is not straightforward; instead, it is inaccurate and inefficient as it involves another set of iterations with eqn 2.8.
- The VA needs an auxiliary eqn (eqn 2.6) to obtain the first step and then move on with eqn 2.7; hence it is not a self-starting algorithm.

2.3.2 Velocity Verlet Algorithm

Although the VA is an elegant approach to integrating the equation of motion, it suffers a serious drawback. It does not evolve velocities simultaneously with positions, and velocities are required for kinetic energy calculations. To overcome the shortcomings of VA, Swope et al. developed the velocity Verlet algorithm(VVA)[152]. The main idea behind the VVA is the realization that the EOM can evolve backward in time. Considering second-order Taylor expansion for position $r_i(t + \Delta t)$ we have:

$$r_i(t + \Delta t) \approx r_i(t) + \Delta t v_i(t) + \frac{\Delta t^2}{2m_i} F_i(t) \tag{2.9}$$

Now if we want to evolve the system backward in time that is from $t + \Delta t)$ to t the Taylor expansion could be written as:

$$r_i(t) \approx r_i(t + \Delta t) - \Delta t v_i(t + \Delta t) + \frac{\Delta t^2}{2m_i} F_i(t + \Delta t) \tag{2.10}$$

substituting the value of $r_i(t + \Delta t)$ from eqn 2.9 in eqn 2.10 and rearranging yields

$$v_i(t + \Delta t) = v_i(t) + \frac{\Delta t}{2m_i}[F_i(t) + F_i(t + \Delta t)] \tag{2.11}$$

Eqn 2.11 is the equation used to perform velocity evolution in VVA and eqn 2.9 for position evolution. Hence, VVA can perform both velocity and position evolution simultaneously. The VVA can be executed in the following steps:

1. A set of energy-minimized coordinates and initial velocities is provided to the integrator at $t = 0$.
2. New set of coordinates are calculated at $t + \Delta t$ using eqn 2.9.
3. Forces are computed at $t + \Delta t$ using the coordinates obtained in the second step.
4. Finally the velocities are calculated at $t + \Delta t$ using the eqn 2.11

The followings are the advantages and drawbacks of VVA: Advantages:

- The most crucial aspect of VVA is its accurate and efficient evaluation of velocities and positions simultaneously.
- It is an algorithm that is straightforward to implement. A code for VVA will be a simple transcription of eqn 2.9 and 2.11 into the particular language's syntax.
- The VVA is time-reversible, which contributes to its numerical stability.

The only serious drawback of VVA is that it is computationally a little more expensive than VA. However, the accuracy and the ease of velocity evaluation provided by VVA outweigh this little expense.

Additionally, a better understanding of both the VA and VVA algorithms, a flowchart illustrating their pseudocodes, is presented in Figure.2.1.

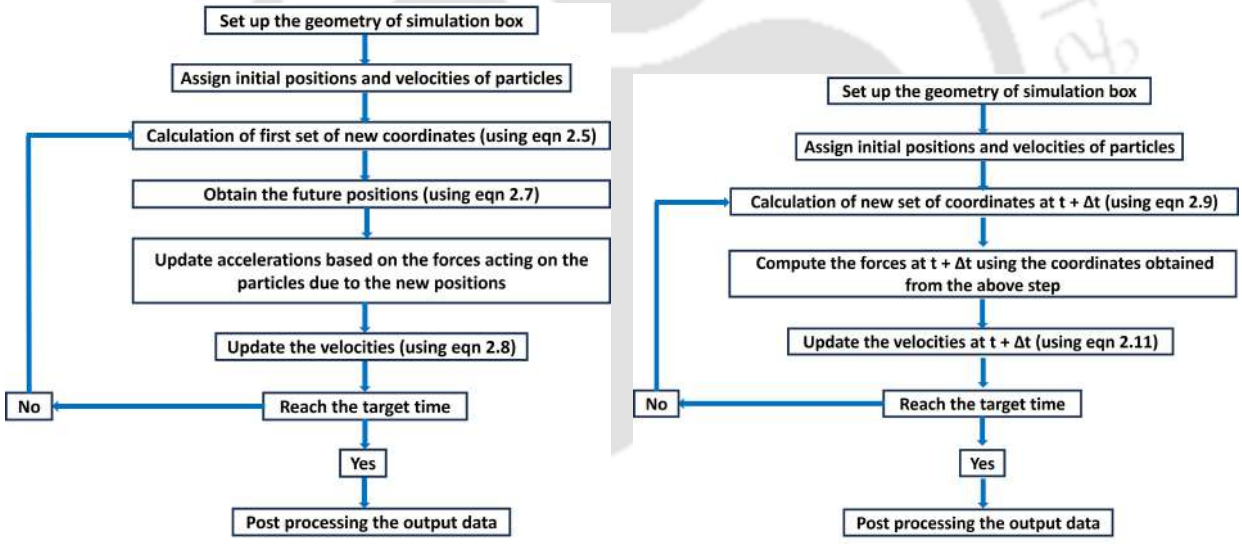

Figure 2.1: Flowchart of pseudocode of (a) Verlet Algorithm and (b) Velocity Verlet Algorithm.

2.4 Periodic Boundary Conditions

The precise treatment of the simulation cell boundary and the shape of the simulation box is of utmost priority, especially when dealing with a limited number of simulated particles in comparison to the extensive scale of a realistic system, typically on the order of 10^{23} particles.

The impact of the boundary becomes particularly pronounced in smaller systems, whereas it is less significant in larger systems where the majority of particles interact extensively, minimizing the effects of confining walls. Moreover, in complex simulation systems, it is crucial to replicate realistic environmental conditions for accurate results. In this aspect, the adoption of periodic boundary conditions (PBC) proves to be an effective strategy, allowing the simulation of an infinite system through the use of a smaller unit cell. The unit cell, a representative of the simulation box, is surrounded by an infinite number of translated copies, in all directions (due to PBC consideration) (Figure 2.2). This setup ensures that when a particle within the unit cell crosses its boundary, it reappears on the opposite side, mimicking an infinite system. Consequently, particles near the boundary interact not only with neighboring particles within the unit cell but also with image particles, essentially replicas of the original unit cell. The implementation of PBC helps minimize the impact of boundaries effectively, ensures a more accurate representation of the simulation environment, and contributes to the reliability of the simulation results.

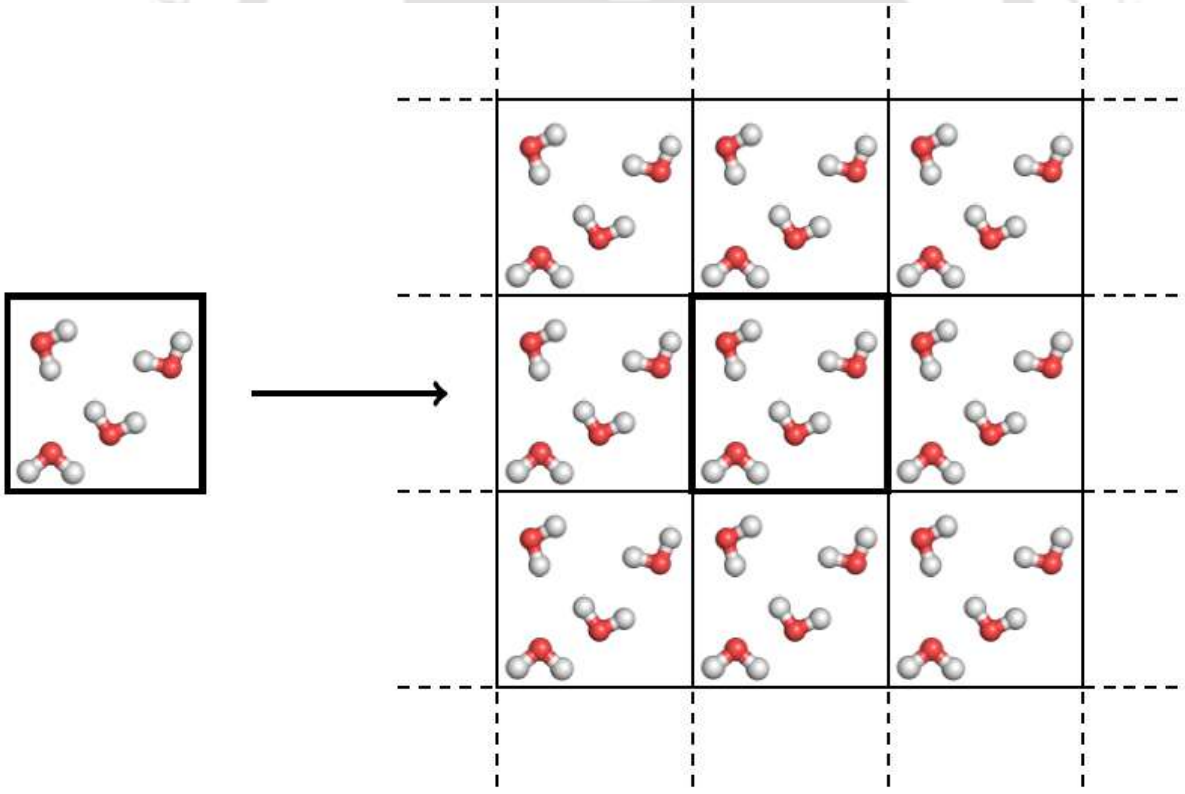

Figure 2.2: A schematic representation of two dimensional periodic boundary condition. The highlighted box in the center is the original simulation box and all other boxes are images of it.

Although PBC is widely used to approximate bulk behavior and helps reduce computational time, it introduces certain artifacts or limitations that can affect the accuracy and interpretation of simulation results if not handled correctly. Understanding these artifacts is crucial for selecting appropriate system sizes and ensuring reliable simulations. Here, we will discuss some cases where artifacts influence the simulation results and introduce two concepts, minimum image convention, and cutoff distance, to minimize these issues.

One common artifact happens because of finite-size effects. This means that when the simulation cell is too small, interactions between a particle and its periodic images may occur. This can result in artificial correlations and distort properties like diffusion, especially for long-range interactions (e.g., electrostatics). In this aspect, the simulation box should be large enough to ensure that particles do not interact significantly with their own periodic images so that we can minimize these effects during the simulations. This concept is known as the minimum image convention. This concept ensures that each particle only interacts with the closest copy of another particle, not with any distant replicas. By doing this, unnecessary interactions are avoided, and the simulation remains more accurate.

Furthermore, the minimum image convention alone isn't enough for systems with long-range electrostatic interactions (such as interactions between charged particles). In these cases, methods like Ewald summation or Particle Mesh Ewald (PME) are used to calculate the long-range interactions correctly. These methods separate the calculations into short and long-range parts, ensuring the results are accurate even with PBC.

Another artifact comes from how we choose the cutoff distance for particle interactions. If the cutoff distance is too small, some important interactions will be missed, making the results inaccurate. On the other hand, if the cutoff distance is too large, the simulation becomes more computationally expensive, and periodic images might interfere with the results. Hence, choosing a cutoff distance is crucial, typically less than half the length of the simulation box. Using the minimum image convention alongside this helps ensure the interactions are correctly calculated. Thus, using the minimum image convention, carefully choosing cutoff distances, and applying special techniques for long-range interactions effectively reduce artifacts in simulations with PBC, ensuring accurate and meaningful results.

2.5 Neighbour Searching Methods

During MD simulations, computational power is significantly demanded during the calculation of non-bonded terms of the potential energy function. This computational demand arises from evaluating non-bonded energy interactions among every pair of atoms, and the number of calculations increases as the square of the number of atoms. To mitigate this computational burden and enhance computational efficiency, a strategic approach is employed, wherein interactions between atoms beyond a predefined cutoff distance are excluded from consideration. The optimization of computation crucially relies on the implementation of efficient methods for excluding atom pairs separated by significant distances, collectively known as "neighbor-searching methods." Two prominent methodologies for determining particle neighbors are Cell lists and Verlet lists methods (Figure 2.3).

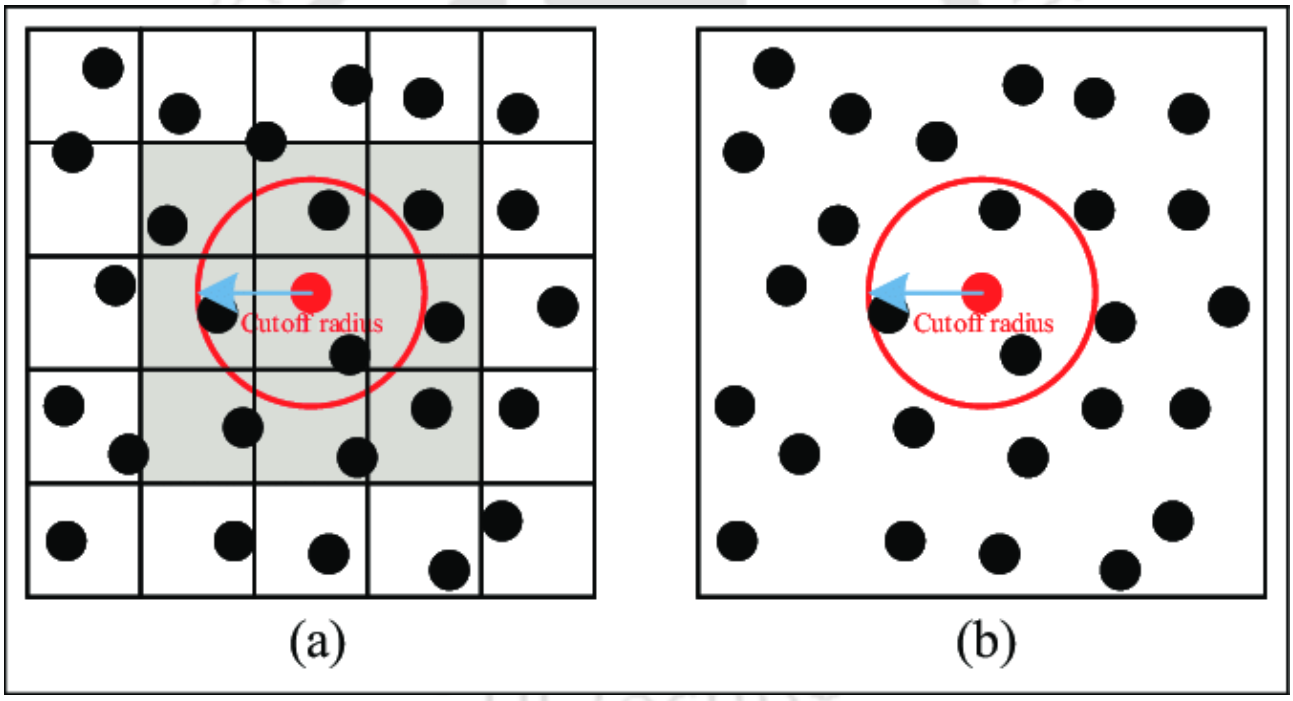

Figure 2.3: Different approaches for calculating interactions between particles in molecular dynamics: (a) Cell list and (b) Verlet list.

The cell lists method involves dividing the simulation domain into n cells, each possessing edge lengths greater than or equal to the cutoff radius of the interaction under consideration. Within this cell size, all particles within the cutoff radius are considered. The interaction potential for each particle is then computed by summing the pairwise interactions with particles

in the same cell, along with those in neighboring cells. On the other hand, the verlet list method maintains a list of particles within the cutoff distance of each particle, with an additional buffer distance. Although constructing the verlet list involves evaluating all pairwise distances initially, it can be utilized for multiple consecutive time steps until any particle moves more than half of the buffer distance. At this point, the list becomes invalid, initiating the construction of a new list. In practice, the verlet list method proves to be more computationally efficient for evaluating pairwise interactions, particularly in measuring short-range interactions such as vdW interactions.

2.6 Ewald Summation

In the previous section, we discussed the idea of measuring vdW interactions through a appropriate choice of cutoff distance. However, the evaluation of electrostatic interactions is trickier due to the long-range nature of the Coulombic interactions. The relationship between vdW and Coulombic interactions with the length scale is evident from the eqn. 2.12.

$$U_{NB}(r_1, ..., r_N) = \sum_{i,j \in nb} \left\{ \left[4\epsilon_{ij} \left(\frac{\sigma_{ij}}{r_{ij}} \right)^{12} - \left(\frac{\sigma_{ij}}{r_{ij}} \right)^{6} \right] + \frac{q_i q_j}{r_{ij}} \right\} \tag{2.12}$$

To tackle the long-range nature of the Columbic interactions, Ewald introduced a technique now known as Ewald summation[153]. The basic idea of the Ewald summation is that a function that is long-range in real space is short-range in the reciprocal or Fourier space. Hence, if the Columbic term could be transformed into a Fourier representation, it could be evaluated efficiently. We write the reciprocal term in the Columbic contribution of eqn to achieve this. 2.12 as :

$$\frac{1}{r} = \frac{erf(\alpha r)}{r} + \frac{erfc(\alpha r)}{r} \tag{2.13}$$

where the $erf(\alpha r)$ is the error function and $erfc(\alpha r)$ is its complement, both are defined as:

$$erf(x) = \frac{2}{\sqrt{\pi}} \int_0^x dt\, e^{-t^2} \tag{2.14}$$

$$erfc(x) = 1 - erf(x) = \frac{2}{\sqrt{\pi}} \int_x^\infty dt\, e^{-t^2} \tag{2.15}$$

It can be noted that, based on the definitions given above, the first term of the eqn. 2.13 is long-range while the second is short-range. Hence, the short-range term can be evaluated along with the vdW term in the real space, while the long-range term can be computed in the Fourier space. Thus using eqn. 2.13 the Coulombic term can be written as a sum of two terms as follows:

$$U_{Coloumbic} = \underbrace{\frac{q_i q_j erf(\alpha r_{ij})}{r_{ij}}}_{\text{long}} + \underbrace{\frac{q_i q_j erfc(\alpha r_{ij})}{r_{ij}}}_{\text{short}} \tag{2.16}$$

As explained, the short-range term can be evaluated along with the vdW term. The α in the above equations is used to tune in an appropriate cutoff distance for the short-range Coulombic interactions. The long-range part is computed using the Poisson summation rule leading to a Fourier series expansion of the error function. The final equation obtained is as follows:

$$U_{long} = \frac{1}{V} \sum \frac{4\pi}{|g|^2} exp\left(\frac{|g|^2}{4\alpha^2}\right) \left|\sum q_i exp(ig.r_i)\right|^2 - \frac{\alpha}{\sqrt{\pi}} \sum_i q_i^2 \tag{2.17}$$

The eqn. 2.17 is called Ewald sum. The V and g are the volume of the simulation cell and the reciprocal space vectors, respectively. Although eqn. 2.17 tackled the calculation of long-range Coulombic interactions ingeniously; direct implementation of it is still computationally expensive, particularly for large systems. Essman et al. introduced the smooth particle mesh Ewald (SPME) method[154] for efficient evaluation of Ewald sum. In SPME, the space is divided into grids, and the charges are uniformly distributed across its nodes; this is achieved using an interpolation scheme with a B-spline function.

2.7 Ensemble

Statistical mechanics predict macroscopic properties, such as pressure (P), temperature (T), and volume (V), using microscopic details of a system. Herein, the concept of ensemble is introduced to establish a connection between the microscopic characteristics of individual particles and the macroscopic properties of the system. An ensemble is defined as a collection of microstates that share an identical macrostate. The concept of the ensemble could be summarized mathematically as follows:

$$M = \frac{1}{\mathcal{Z}} \sum_{i=1}^{\mathcal{Z}} m(X_i) \tag{2.18}$$

Where M is a macroscopic observable, $\mathcal{Z}$ is the number of members in the ensemble, $m(X)$ represents a microscopic phase space function, and X denotes a coordinate on the phase space.

Ensembles provide a systematic approach to derive the thermodynamic properties of a system through the application of classical and quantum mechanics. While these derivations involve complex mathematical equations, the focus of this dissertation is to provide a comprehensive overview of existing ensembles, explaining the specific type of system they aim to simulate. In practical terms, ensembles are conceptualized and categorized based on the control and fixation of particular properties, such as T, P, V, total number of particles (N), total energy (E), or chemical potential (μ). The choice of ensemble depends on the specific problem and the desired conditions for simulating the system. MD simulations usually simulate one of the following thermodynamic ensembles:

1. The microcanonical (or NVE) ensemble, where N, V, and E are maintained constant during the simulation.

2. The canonical (or NVT) ensemble, where N, V, and T are held constant.

3. The isothermal-isobaric (or NPT) ensemble, where N, P, and T are kept constant.

Simulating the NVE ensemble is straightforward, provided the MD code effectively conserves the system's energy. In practical terms, the NVE ensemble represents an isolated system that cannot exchange heat or matter with its outer environment. This isolation ensures the conservation of total energy while allowing fluctuations in potential and kinetic energy. The typical MD simulation begins with an unstable initial structure having high potential energies, requiring minimization. Thus, as total energy conservation is essential, a decrease in volume corresponds to an increase in kinetic energy, leading to high temperatures. As a result of abrupt temperature increases can pose challenges in simulations; consequently, the NVE ensemble may not always appropriate choice to conduct MD simulations.

Whereas, the NVT ensemble holds greater practical relevance, considering that controlling the temperature of a system is more feasible in real-world scenarios than controlling its energy. In this ensemble, the system is permitted to exchange heat with its surroundings to maintain a constant temperature. To implement this feature in simulations, the use of a temperature control algorithm, commonly known as a thermostat, is essential. This involves scaling the

velocities of the system to adjust kinetic energy and, consequently, maintain a stable temperature. Given that many experimental conditions in laboratories involve constant ambient pressure rather than fixed volumes, the NPT ensemble is widely employed in simulations. In the NPT ensemble, the system can exchange heat, and simultaneously, adjustments can be made to the volume to keep the pressure constant. Achieving this involves constant rescaling of one or more dimensions of the simulation box, effectively manipulating the pressure. Alongside a thermostat for temperature control, a pressure control algorithm, termed a barostat, becomes essential in the NPT ensemble.

2.7.1 Temperature control or Thermostats

Velocity Rescaling: In statistical mechanics, the temperature of an unconstrained system connects with the time-averaged kinetic energy (eqn. 2.19). To maintain the system's temperature ensuring a constant average kinetic energy while permitting fluctuations in instantaneous kinetic energy (eqn. 2.20).

$$\langle K \rangle = \frac{3}{2} N k_B T \tag{2.19}$$

$$K = \sum_i \frac{1}{2} m_i {v_i}^2 \tag{2.20}$$

One viable approach to modulating and maintaining temperature is velocity rescaling. In essence, to implement a mathematical thermostat, it is important to ensure that velocities can produce a consistent average kinetic energy over a specific time interval. During each timestep, computational analysis detects the atomic motion, and scaling velocities by a factor (λ) to achieve the desired temperature. If atoms move too fast, the velocities are multiplied by a scaling factor less than one; conversely, if the velocities are too low, they are multiplied by a factor greater than one. The specific expression for the scaling factor depends on both the desired temperature ($T_{desired}$) and the current temperature ($T(t)$) of the system at that particular timestep (eqn. 2.22).

$${v_i}^{new} = {v_i}^{old}.\lambda \tag{2.21}$$

$$\lambda = \sqrt{\frac{T_{desired}}{T(t)}} \tag{2.22}$$

When the desired temperature exceeds the actual temperature, the λ becomes greater than one, enhancing the old velocities, causing atoms to move faster and increasing the temperature toward the target. Conversely, if the desired temperature is lower than the actual temperature, the λ becomes less than one, lowering the old velocities and reducing the temperature. Moreover, it is important to underline that this velocity scaling operation happens at every timestep of the simulation. However, this velocity-rescaling approach does not accurately reproduce the canonical ensemble. Because, if velocities are precisely rescaled at a constant value during each timestep, kinetic energy will not exhibit the desired fluctuations. Consequently, this velocity-rescaling algorithm is rarely employed in molecular dynamics.

Berendsen Thermostat: The Berendsen thermostat[155] operates on a similar principle as velocity rescaling but integrates complex equations for defining the scaling factor. Conceptually, this thermostat functions by coupling the simulated system to an imaginary heat bath maintained at a constant temperature. In this analogy, the fictitious heat bath serves as a source of thermal energy, either supplying or extracting heat from the system based on the desired temperature. The temperature change is proportionate to the temperature difference between the bath (T_{Bath}) and the system (T(t)) (eqn. 2.29).

$$\frac{\partial T(t)}{\partial t} = \frac{(T_{Bath} - T(t))}{\tau} \tag{2.23}$$

$$\lambda = \sqrt{1 + \frac{\Delta t}{\tau}\{\frac{T_{desired}}{T(t)} - 1\}} \tag{2.24}$$

One significant advantage of this thermostat is that allowing users to choose the coupling value according to specific requirements. For large values of the coupling time constant (τ), the coupling factor (λ) equals 1, implying that the old velocity remains unaltered by the scaling factor. This indicates that no coupling between the heat bath and the system. Whereas, smaller τ values result in a stronger coupling. The selection of τ requires careful consideration, typically measured in picoseconds (ps), and a default value often set at 1 ps. In this thermostat, the speed of temperature equilibration is controlled by the strength of the coupling, making it a reliably converging and robust thermostat. This attribute proves particularly advantageous during system relaxation, such as at the beginning of an MD simulation following energy

minimization. However, it is essential to mention that this thermostat algorithm is reliable for only relaxation purposes, it does not ensure correct sampling of the canonical ensemble for production runs. Therefore, it is advisable to avoid using the Berendsen thermostat for production MD simulations in most cases.

Andersen Thermostat: The Andersen thermostat[156] operates on the fundamental principle of simulating random collisions that influence the particles within the system, leading to changes in the system's temperature. Conceptually, this can be visualized as a heat bath in contact with the system, emitting random particles that collide with the atoms in our system. Here, the term "collision frequency (ν)" specifies the degree of coupling between the heat bath and the system.

$$P(t) = \nu e^{-\nu t} \tag{2.25}$$

In practical terms, the collisions are achieved in simulations by randomly selecting atoms and assigning them new velocities drawn from a Maxwell-Boltzmann distribution at the desired temperature. The careful selection of the ν value is essential, as low ν value may result in inadequate temperature control and the failure to generate a canonical ensemble. On the other hand, excessively high ν value can overly disturb the system. This thermostat accurately samples the canonical ensemble; however, it has the drawback of not conserving momentum due to velocity randomization. This characteristic can impact correlated motions, potentially slowing down the kinetics of the system. Therefore, this thermostat algorithm is not recommended for studying the kinetics or diffusion properties of a system.

Nosé–Hoover Thermostat: The Nosé–Hoover thermostat belongs to the extended system category of methods, introduced by Nosé and further developed by Hoover[157, 158]. This approach differs from previous methods by directly incorporating the thermal bath into the system. This integration is achieved by introducing an artificial variable associated with a fictional "heat bath mass" into the equations of motion. The modified Lagrangian equation of the motion for Nosé–Hoover method is given by:

$$\mathcal{L}_{N-H} = \sum_{i=1}^{N} \frac{1}{2} m_i (s\dot{r}_i)^2 - U(r^N) + \frac{Q\dot{s}^2}{2} - g k_B T ln s \tag{2.26}$$

Where s is the position of the imaginary heat bath, $\dot{s}$ is the conjugate velocity of the heat bath, and Q is the effective mass of the heat bath.

An essential feature of this thermostat is its capability to regulate temperature without relying on random numbers, conserving correlated motions and providing a more accurate description of kinetics and diffusion properties. The temperature control is executed in this thermostat through a second-order equation, resulting in slightly slower convergence. Despite this, the Nosé–Hoover thermostat is well-suited for reproducing the canonical ensemble and become one of the most widely used thermostats for production runs in classical molecular dynamics.

2.7.2 Pressure control or Barostats

Berendsen Barostat: The Berendsen barostat[159] operates on a similar concept to the Berendsen thermostat. In this approach, instead of adjusting velocities, the barostat modulates pressure by dynamically scaling the volume of the simulation box. When the box size decreases, atoms experience compression, leading to an overall increase in system pressure. On the other hand, increasing the box size allows atoms to expand in a larger volume, resulting in a decrease in pressure. Similar to the Berendsen thermostat, this algorithm visualizes the system as weakly coupled to a pressure bath, achieving volume (V) scaling through a scaling factor (λ).

$$V_i^{new} = V_i^{old}.\lambda \tag{2.27}$$

$$r_i{}^{new} = r_i{}^{old}.\lambda^{1/3} \tag{2.28}$$

$$\frac{\partial P(t)}{\partial t} = \frac{(P_{Bath} - P(t))}{\tau} \tag{2.29}$$

$$\lambda = 1 - \frac{\beta \Delta t}{3\tau}(P_{Bath} - P(t)) \tag{2.30}$$

In practical terms, this involves scaling the coordinates of each atom (r) based on our requirements, where scaling the volume by λ corresponds to scaling atomic coordinates by $\lambda^{1/3}$. The rate of pressure change over time is proportional to the pressure difference between the bath (P_{bath}) and the system (P(t)). The coupling constant (τ) governs the interaction between the two subsystems, with adjustments necessary for the desired coupling strength. The constant β signifies the isothermal compressibility of the substance, with larger values for

easily compressible ones. While the Berendsen barostat efficiently equilibrates the system, it deviates from precisely sampling the NPT statistical ensemble. Pressure fluctuations tend to be smaller than expected, making it less suitable for production MD simulations. As a result, it is generally recommended to refrain from using the Berendsen barostat in such scenarios.

Andersen Barostat: Andersen[156] introduced a pressure control method employing an extended system variable, similar to the Nosé–Hoover thermostat. In this approach, the system is coupled to a pressure bath, and the coupling is established by incorporating an additional degree of freedom in the equations of motion. This additional degree of freedom adjusts itself to equalize the internal and external pressure. The extra degree of freedom acts as a piston, assigned a fictional mass. The equation of motion for such a system is given by:

$$\dot{r} = \frac{p_i}{m_i} + \frac{1}{3}\left(\frac{\dot{V}}{V}\right) r_i \tag{2.31}$$

$$\dot{p} = F_i + \frac{1}{3}\left(\frac{\dot{V}}{V}\right) p_i \tag{2.32}$$

$$\ddot{V} = \frac{P - P_0}{M} \tag{2.33}$$

Here P is the instantaneous pressure, P_0 is the desired pressure, V is the volume, M is the mass of the imaginary piston, and r_i, p_i, m_i and F_i the position, momentum, mass, and force for the ith particle respectively. The choice of the mass of the piston determines the decay time of the volume fluctuations. Additionally, Nosé and Klein[160] proposed a similar method to Andersen's barostat for molecular simulation, further developed by Hoover[161], and it is now commonly known as "Nosé–Hoover barostat." This barostat offers improved performance and greater applicability in MD simulations for pressure control.

2.8 Water Models

Water holds a crucial role in numerous chemical and biological processes, especially in membrane-based wastewater treatment methods, where 70-80% of atoms in simulations represent water molecules. As a result, the choice of water models becomes crucial as it significantly influences the simulation cost. In simulation studies, three-site and four-site water models are widely

utilized. Here, we will provide a brief overview of three popular and efficient water models belonging to the aforementioned categories. Moreover, these water models differ in terms of their accuracy and computational efficiency. Hence, the choice of a particular water model depends on the specific requirements of the simulation, the system being studied, and the available computational resources.

2.8.1 Three Point Models

Three point water models are one of the earliest and simplest models. In this model the water molecule is represented by three point charge for hydrogen and oxygen atoms. Despite their simplicity, three-point water models can provide reasonable approximations of certain properties and behaviors of real water, making them computationally efficient for a wide range of applications. We will discuss two widely used three point models namely TIP3P and SPC/E.

TIP3P (Transferable Intermolecular Potential 3 Points): TIP3P is one of the earliest and most widely used three point model. It was proposed by Jorgensen et al.[162]. In the TIP3P model, each water molecule is represented by three point charges: a negative charge at the oxygen atom (-0.834 e) and two positive charges at the hydrogen atoms (+0.417 e). The atomic charges and Lennard-Jones parameters are fitted to reproduce experimental properties of water, such as the density and heat of vaporization. The O–H bond length and H–O–H bond angle used in TIP3P model are 0.9572 Å and 104.52° respectively.

SPC/E (Extended Simple Point Charge): SPC/E model[163] is very similar to TIP3P, each water molecule is represented as three point charges: one negative charge located at the oxygen atom (-0.8476 e) and two positive charges located at the hydrogen atoms (+0.4238 e). The O–H bond length and H–O–H bond angle used in SPC/E model are 1Å and 109.47° respectively. The target properties of SPC/E are the density and the vaporization enthalpy at room temperature. However, the key difference between TIP3P and SPC/E is the use of a polarization energy correction in case of SPC/E to correctly reproduce the vapourization enthalpy of real water.

2.8.2 Four point water models

Four point water models improve upon the limitations of three-point models by incorporating a Lennard-Jones site for the lone pair electrons on the oxygen atom. This inclusion allows

for better representation of water's structure and dynamics, but it also increases the model's complexity.

TIP4P (Transferable Intermolecular Potential 4 Points): Being a four point model, TIP4P is represented by three point charges and one Lennard-Jones site. However, the key feature of this model is that the site carrying the negative charge is not located at the oxygen atom but on the H–O–H bisector at a distance of 0.15 Å, effectively accounting for the oxygen atom's lone pair electrons. The TIP4P model was proposed by Jorgensen et al.[162]. The addition of the Lennard-Jones site for the oxygen atom's lone pair electrons allows the TIP4P model to more accurately represent hydrogen bonding interactions compared to TIP3P. However, this addition of the Lennard-Jones site makes TIP4P slightly more complex than TIP3P, which may result in slightly longer computation times.

This thesis briefly discussed TIP3P, SPC/E, and TIP4P water models. The corresponding technical parameters of these water models are presented in Table.7.1.

Table 2.1: Water model parameters

Water Model	$\mathbf{r}_{OH}$ **(Å)**	**H-O-H (°)**	σ_{OO} **(Å)**	ϵ_{OO} **(kcal mol^{-1})**	$\mathbf{q}_O$ **(e)**	$\mathbf{q}_h$ **(e)**	$\mathbf{q}_m$ **(e)**	$\mathbf{r}_{OM}$ **(Å)**
TIP3P [162]	0.9572	104.52	3.1506	0.152	-0.834	0.417	-	-
SPC/E [163]	1.0	109.47	3.166	0.1553	-0.8476	0.4238	-	-
TIP4P [162]	0.9572	104.52	3.1540	0.155	-	0.52	-1.04	0.15

r_{OH} indicates the bond length of OH, ∠HOH represents the H-O-H angle, σ_{OO} represents the LJ σ of OO (i.e., σ is the distance at which the LJ potential between two atoms is zero), ϵ_{OO} represents the LJ ϵ of OO (i.e., ϵ is the well depth at the distance of minimum energy), q_O represents the charge on oxygen atom, q_h represents the charge on hydrogen atom, q_m represents the massless point M assosiated with the oxygen atom charge, r_{OM} represents the bond length of OM.

2.9 A brief discussion on MD codes

MD simulations have become invaluable in studying molecular behavior across various scientific domains. The MD platforms, NAMD (Nanoscale Molecular Dynamics), LAMMPS (Large-scale Atomic/Molecular Massively Parallel Simulator), and GROMACS (GROningen MAchine for Chemical Simulations), are particularly renowned in academic and industrial research, each

offering distinct advantages depending on the type of system and simulation. This section explains the comparative strengths of the above-mentioned MD software packages.

NAMD is a popular MD package designed to handle extensive biomolecular simulations efficiently across multiple nodes. Developed with scalability in mind, it utilizes parallel algorithms that allow for efficient computation on high-performance computing (HPC) clusters. NAMD is compatible with the OPLS-AA, CHARMM, and other force fields, which is advantageous when working with complex molecular systems that require detailed force field parametrizations. For systems where accurate biomolecular, surface interactions and interface behavior need to be studied, NAMD offers flexibility and efficiency for handling those large system sizes for long simulation times.

LAMMPS, another popular MD package, is known for its flexibility and versatility in simulating various materials, including polymers, metals, and coarse-grained models. LAMMPS is developed and designed with a modular structure, allowing users to extend its functionality through plugins and custom modules. This adaptability makes it suitable for heterogeneous systems and specialized simulations involving adsorption phenomena, surface interactions, etc. LAMMPS can also scale efficiently across high-performance computing clusters, utilizing CPU and GPU resources and supporting complex interactions involving atomic and continuum scales. This flexibility in handling diverse particle types and interactions makes LAMMPS ideal for simulations that require non-standard boundary conditions or custom force fields.

GROMACS, on the other hand, is highly regarded for its performance in simulating biomolecular systems such as proteins, lipids, and nucleic acids. Initially developed for biophysical applications, it has become a powerful tool for large-scale calculations, especially on single-node and multi-core systems. Critical advantages of GROMACS include its speed and efficiency, user-friendly command-line interface, and built-in trajectory analysis and visualization tools. These features make GROMACS a preferred choice for high-throughput simulations of complex biomolecular systems, where computational efficiency is paramount. Furthermore, GROMACS supports GPU acceleration, which enhances its utility for researchers aiming to simulate large biomolecular systems quickly and accurately.

In this thesis, the simulations have been conducted using NAMD and LAMMPS. The reason for choosing these two MD packages over GROMACS is that they offer unique advantages over GROMACS for researchers dealing with membrane-based systems and large-scale simulations. LAMMPS excels in flexibility and customization, making it ideal for modeling diverse materials

beyond biomolecules, such as membranes, metals, and complex interfaces. Its modular structure allows for custom plugins, non-standard boundary conditions, and multi-scale simulations, which are valuable for material science and surface interactions. NAMD, on the other hand, is optimized for massive parallelization across high-performance clusters, making it a strong choice for large biomolecular and membrane systems where efficient scaling is critical.

Chapter 3

Effect of oxygen-containing functional groups of layered graphene oxide membrane on the removal of amoxicillin: a molecular dynamics study*

3.1 Objective

As discussed in Chapter 1, pharmaceutical consumption has increased in the past couple of decades; as a result, concentration levels of pharmaceuticals, particularly antibiotics, have increased in the groundwater. Therefore, this study aims to investigate removing one of the most consumed antibiotics, amoxicillin (AMX), from pharmaceutical industrial wastewater with a graphene oxide (GO) membrane. Consequently, non-equilibrium molecular dynamics (MD) simulations are performed in FO mode to understand the separation mechanism of AMX molecules from an atomistic point of view. In most of the previous atomistic studies on layered GO membranes, an ideal lamellar structure of the membrane is considered. Contrary

*Rajasekhar reddy, P., Abhijit Gogoi, and K. Anki Reddy. "Effect of oxygen-containing functional groups of layered graphene oxide membrane on the removal of amoxicillin: a molecular dynamics study." Molecular Simulation 48, no. 3 (2022): 185-196.

to this, in this present study, we have adopted a more realistic method [164] to construct a GO membrane with a different number of oxygen-containing functional groups. The effect of these functional groups on the removal of AMX molecules has been reported in detail in the subsequent sections. These functional groups also affect the pore size distribution of the GO membrane. Consequently, it affects the water permeance and salt rejection of the membrane.

3.2 Methodology

3.2.1 Non lamellar membrane

This section explains the methodology for the construction of a realistic (non-lamellar) GO membrane. The lamellar membrane definition is that the geometric parameters of the membrane are predefined, and they are uniform. For non-lamellar membranes, these parameters are not predefined, and they are non-uniform.

Table 3.1: Number of oxygen containing functional groups on the GO membranes and their corresponding abbreviations

Type of the membrane	O1	O2	O3	O4
GO	972	972	486	486
rGO	486	486	243	243
ErGO	234	234	126	126

Here **O1**, **O2**, **O3**, and **O4** are the oxygen atoms of a hydroxyl group (−OH), epoxy group (−O−), carboxyl group which is linked to only C atom (−C=O) and carboxyl group that is bonded to C and H atom (C−O−H), respectively. GO represents graphene oxide membrane, rGO indicates reduced GO, and ErGO means extended reduced GO.

The GO nanosheets are generated by using the model proposed by Lerf and Klinowski [165] with a chemical composition of $C_{10}O_1(OH)_1(COOH)_{0.5}$ [166, 167]. The size of the GO nanosheets considered in this present study is 50.0×49.0 Å^2 (Figure B.1). Using these GO nanosheets three different GO membranes ((GO, rGO, ErGO)) are constructed which differ in the number of oxygen containing functional groups. The number of oxygen-containing func-

tional groups present in each of these membrane are tabulated in Table.3.1.

For the construction of the GO membrane, a multistep procedure is adopted [164] as shown in Figure.3.1. In step 1, eighteen GO nanosheets are randomly distributed inside a simulation cell of volume, V=$150 \times 50 \times 300$ Å^3, and with 15 weight percentage of water. In step 2, the GO nanosheets are pulled on to a surface of graphene sheet placed at the bottom of the simulation cell to replicate the experimental synthesis of the membrane (vacuum filtration process). Here we apply a harmonic force constant of 15 kcal/(mol$\times$Å^2) at a pulling rate of 10 Å/ns on the GO nanosheets. Following this MD simulations are performed for 25 ns in the canonical ensemble (NVT), with periodic boundary conditions (PBC) in X and Y directions at a temperature of 300 K. Finally, in step 3, the graphene sheet at the bottom of the simulation box is removed. A semi-isotropic constant pressure simulation (NPT) with a target pressure of 1 bar in the Z-direction is performed for 20 ns with PBC in three dimensions to release the vacuum and create a GO membrane model. A similar method is followed to construct the rGO (Figure B.2) and ErGO (Figure B.3) membranes.

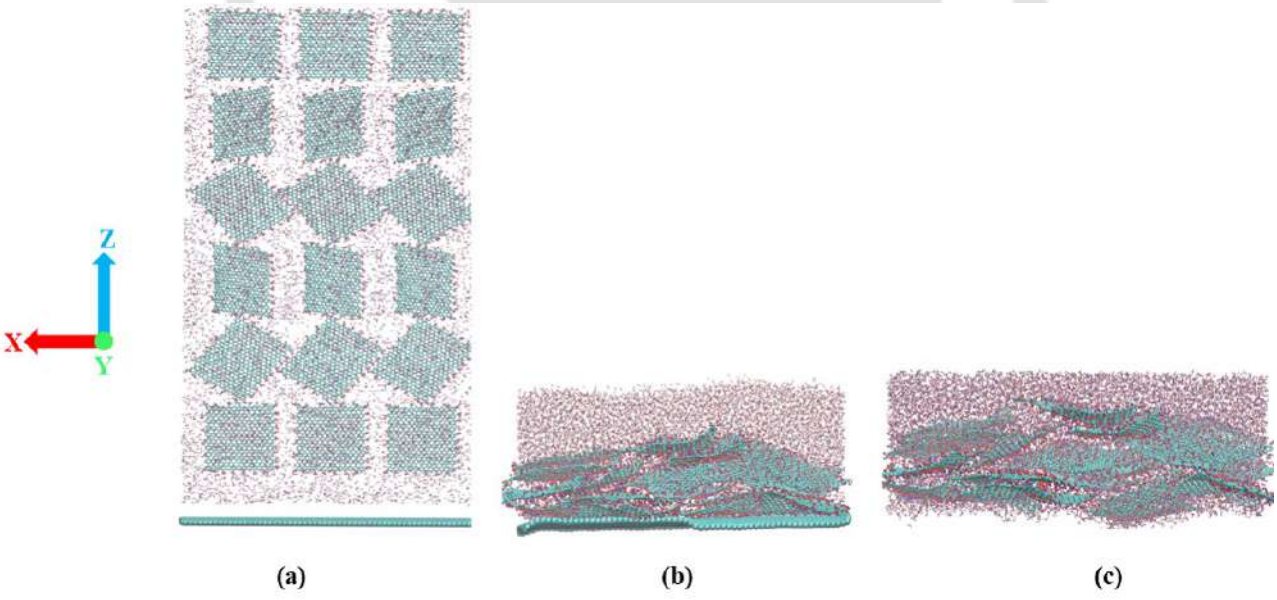

Figure 3.1: Stages associated with the construction of non-lamellar GO membrane. (a) Random distribution of GO nanosheets and water in a simulation box. (b) Pulling the center of mass of GO sheets towards the graphene sheet. (c) Relaxation and equilibration to remove the vacuum gap. The blue color is for hydrogen atoms, the red color is for oxygen atoms and cyan color is for carbon atoms.

3.2.2 FO Simulation system

A typical FO process consists of a draw solution, a semipermeable membrane and a feed solution. The osmotic pressure of the draw solution is higher than the feed solution. Because of this difference in osmotic pressure, water molecules from the feed solution permeate through the membrane towards the draw solution. An aqueous AMX solution (Figure.3.2(d)) is considered as the feed solution which contains 10 AMX molecules and 10000 water molecules. A mixture of 3.0 M $MgCl_2$ and 0.05 M $Al_2(SO_4)_3$ solution (Figure.3.2(c)) is considered as the draw solution . It consists of 652 Mg^{2+}ions, 1304 Cl^- ions, 22 Al^{3+} ions, 33 $(SO_4)^{2-}$ and 11000 water molecules. For each simulation systems, the hydrated GO membrane is placed between the feed solution and the draw solution. At the end of the draw and feed solution a graphene sheet is placed which acts as piston (Figure.3.2(e)). In both of these pistons atmospheric pressure is applied in opposite directions. In addition, 30 Å of the vacuum is placed on top and bottom of the simulation system along the Z direction.

3.2.3 Simulation Methodology

In the current study, all non-equilibrium MD simulations are performed with the NAMD 2.11 package[168] using OPLS-AA forcefield parameters [148]. Water molecules are modeled with TIP3P water model[162]. The van der Waals interactions are computed using Lennard-Jones potential with a cutoff radius of 12 Å. The long-range electrostatic interactions are computed using the Particle Mesh Ewald (PME) method[154].

Once the simulation systems are created, energy minimization steps are performed. Subsequently, the systems are equilibrated at a pressure of 1.0 atm and a temperature of 300.0 K for 1.0 ns. Then, the production runs are performed for 20 ns in an NVT ensemble with periodic boundary conditions in all the directions. These simulations are performed with a time step of 1 fs. The temperature is kept constant throughout the simulations using Langevin dynamics with 5.0 ps^{-1} as a damping factor. The trajectories are saved at every 20.0 ps. During the equilibration, the GO nanosheets are constrained in all three directions. However, only a few selected carbon atoms, which are not bonded to any oxygen-containing functional groups (not the entire GO nanosheet), are fixed during the production simulations. The purpose of fixing the carbon atoms is to maintain the interlayer distance (developed during the membrane construction) between the GO layers during the production simulations. For each membrane, five

independent FO simulations are performed with different initial configurations. The results reported in the subsequent section are averaged over these five simulations.

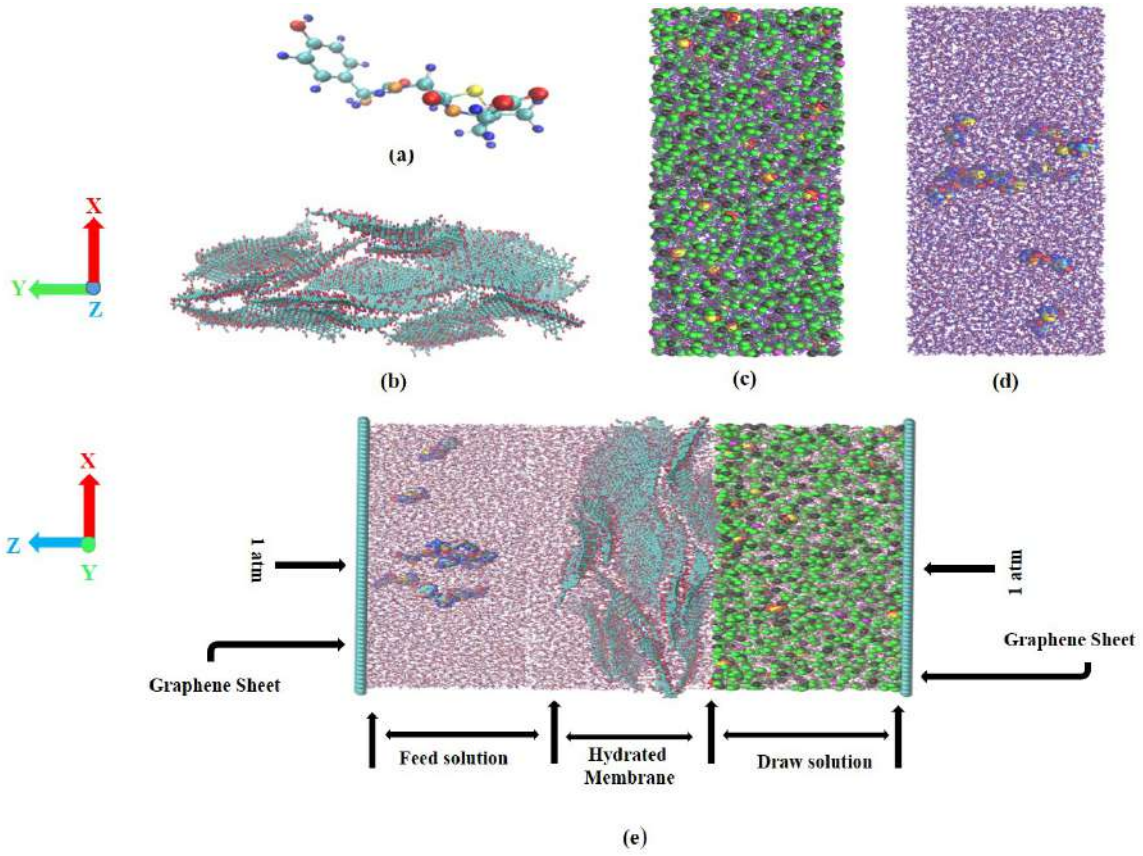

Figure 3.2: (a) Amoxicillin molecule. (b) GO membrane. (c) Draw solution. (d) Feed solution. (e) Simulation system. Cyan color is for carbon atoms, red color is for oxygen atoms, blue color is for hydrogen atoms, black color is for Mg^{2+} ions, green color is for Cl^{1-} ions, magenta color is for Al^{3+} ions, yellow color is for sulphur atoms and orange color is for nitrogen atoms.

3.3 Results and discussion

3.3.1 Membrane Performance

The performance of the membranes are compared with one another in terms of water permeance and salt rejection. Figure.3.3(a) presents the water permeance (in kg m^{-2} h^{-1} bar^{-1}) through membranes. The GO membrane (164.50) exhibits the highest water permeance, followed by the rGO (46.28) and ErGO (15.08) membrane. Figure.3.3(b) shows the water permeance of

the membranes as a function of a number of oxygen containing functional groups. The GO, rGO, and ErGO membranes have 2916, 1458, and 720 oxygen functional groups, respectively. Figure.3.3(b) clearly illustrates that the water permeance decreases with the reduction in the oxygen containing functional groups of the membrane.

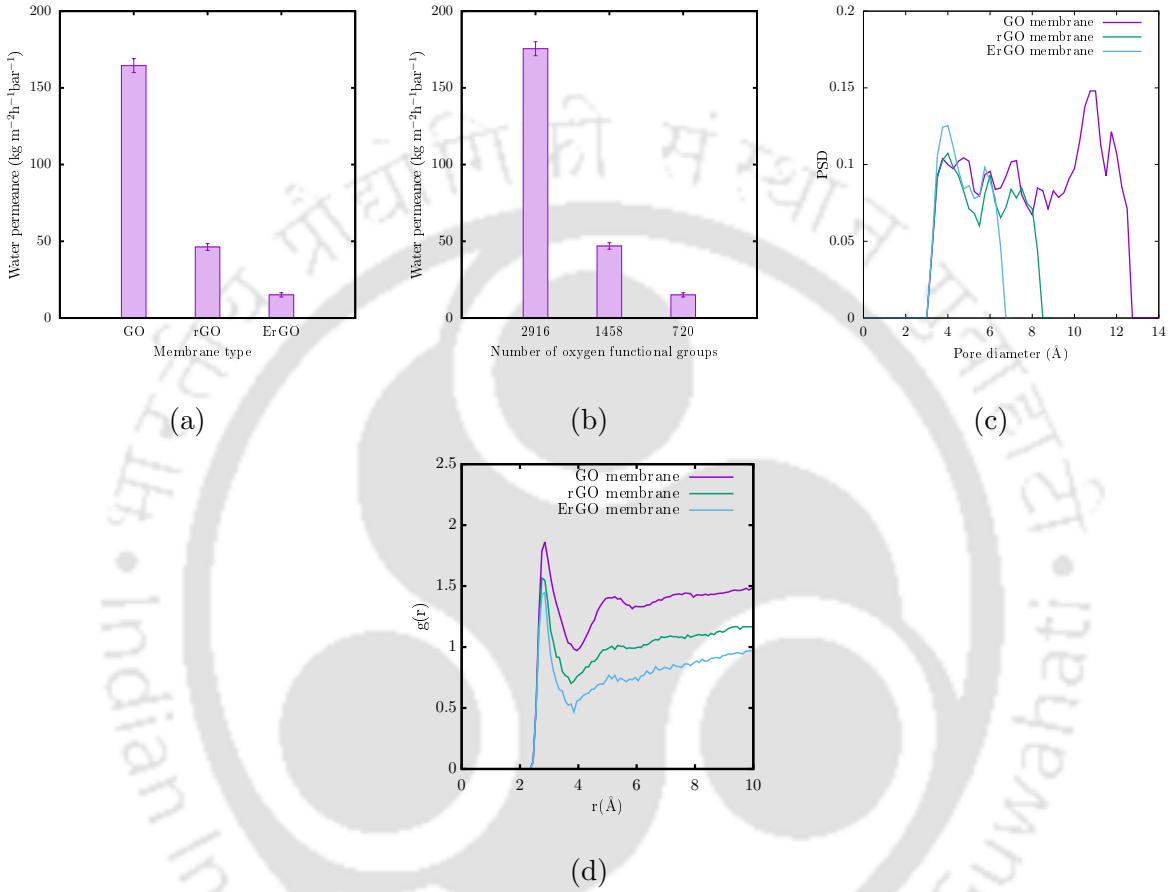

Figure 3.3: (a) Water permeance through the membranes. (b) Water permeance through the membranes as a function of oxygen containing functional groups. (c) Pore size distribution of the membranes. (d) RDF of water molecules around the membranes.

The pore size distribution of all three membranes are shown in Figure.3.3(c). The pore size distribution (PSD) of the GO membrane agrees with the observations reported by Williams et.al.[164]. We utilized the method developed by Bhattacharya and Gubbins[169] to compute the PSD in the non-lamellar GO membrane models. In this method of reference[169], the pore size at a particular point is defined as the largest sphere that can encompass the point without the overlap of the neighboring atoms. This method employs a Monte Carlo integration algorithm to compute PSD. As shown in Figure.3.3(c), the GO membrane has a broader range of pore sizes (or free pore volume) than the rGO and ErGO membranes. The range of pore

diameters (in Å) of the GO, rGO, and ErGO membranes is 3.25-12.5, 3.25-8.25, and 3.25-6.5, respectively. The GO membrane achieved higher water permeance due to the higher free pore volume than the rGO and ErGO membranes. As shown in Figure.3.3(d), the RDF[170, 171] between the membrane and water molecules reveals the affinity of water molecules towards the membrane. As a result, the GO membrane showed a higher affinity, followed by the rGO and ErGO membranes. Moreover, the affinity between the membrane and water molecules strongly depends on the number of oxygen-containing functional groups of the membranes. Consequently, the more oxygen-containing functional groups and broader range of pore sizes of the membranes cause higher water permeance. The RDF (g(r)) is defined,

$$g_{ij}(r) = \frac{P_{ij}(r, r + \Delta r)V}{4\Pi r^2 \Delta r P_i P_j} \tag{3.1}$$

where r is the distance between a pair of particles i and j, V is the total volume of the system, P_{ij}(r,r+Δr) is the number of atoms j around i within a shell from r to r+Δr, P_i and P_j indicates the number of atoms i and j, respectively.

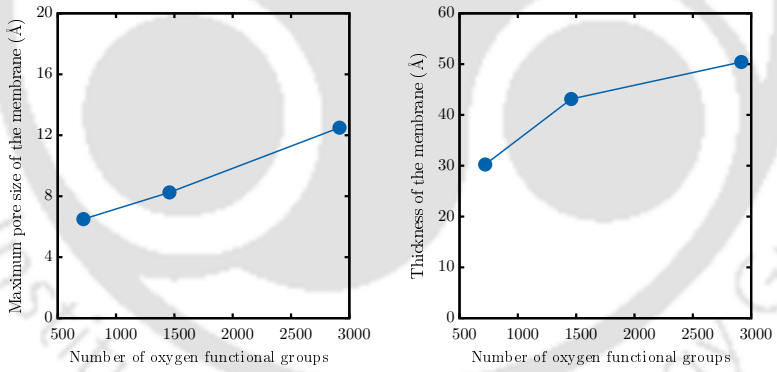

(a) (b)

Figure 3.4: (a) Maximum pore size and (b) thickness of the membranes as a function of oxygen containing functional groups.

Furthermore, the water permeance depends on the geometric parameters of the membrane, such as thickness and pore diameter. In this study, the geometric parameters of the membranes depend on the number of oxygen-containing functional groups of the membrane. Figure.3.4(a) illustrates that reducing the number of oxygen-containing functional groups of the membrane generates the smaller size of the pore diameters. Figure.3.4(b) explains that less oxygen-containing functional groups create a smaller interlayer distance between the GO lay-

ers, leading to a thinner membrane. The thickness of the membrane (in Å) of the GO, rGO, and ErGO membranes is 50.41, 43.14, and 30.24, respectively. Hence, reducing the number of oxygen-containing functional groups can produce a thinner and smaller range pore size of the membranes. Consequently, the GO membrane exhibited higher water permeance than the rGO and ErGO membranes, as shown in Figure.3.3(a).

Additionally, non-equilibrium MD simulations are performed for the GO membrane with different concentrations of the draw solutions [$MgCl_2$ (2M and 5M)] using the same concentration of the feed solution to study the water permeance as a function of an osmotic pressure gradient. As shown in Figure B.4, the water permeance increases with the increase in the concentration of the draw solution[172]. The movies are created to visualize how the water molecules (shown in magenta color) permeate through the membranes, and link is provided (click here).

Figure.3.5 shows the density of ions along the Z direction for the GO, rGO, and ErGO membranes. The dotted lines indicate the position of the membrane. From the density plots it can be seen that no ions have permeated through any of the membranes i.e. all the membranes show 100% salt rejection. However, a few ions get intercalated inside the interlayer gallery of the membrane.

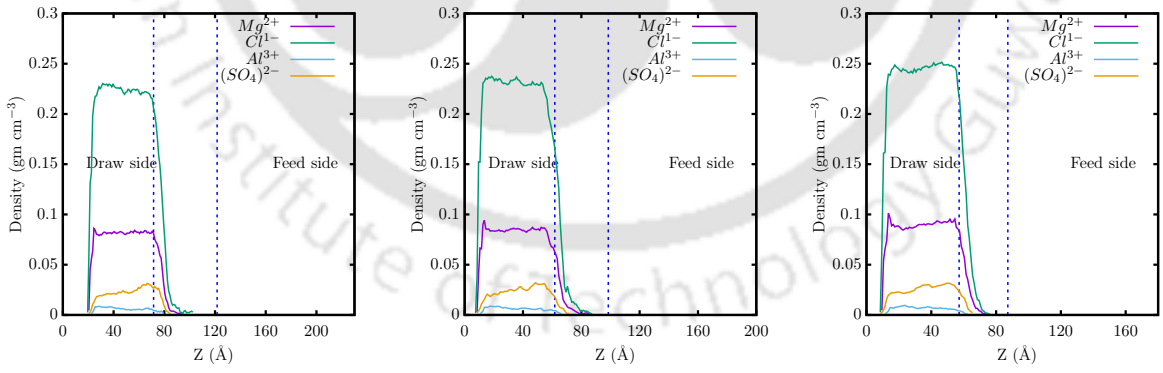

(a) (b) (c)

Figure 3.5: The variation in the density of the ions along Z direction for (a) GO membrane, (b) rGO membrane and (c) ErGO membrane. The dotted lines indicate the membrane position.

Figure.3.6 shows the snapshots of ions intercalated inside the membrane. The number of intercalated ions is more for the GO membrane followed by rGO and ErGO membranes. The higher intercalation of ions inside the interlayer gallery of GO membranes can be attributed to

its larger pore sizes. We also computed the RDF between the ions of the draw solution and the oxygen atoms of water. Figure B.5 shows the RDF between the oxygen atom (OT) of the water inside the GO membrane and ions from the draw solution. These results suggest that Al^{3+} ions have intensive interactions with the water, followed by the Mg^{2+}, Cl^{-} ions. Hence, the permeation rate of Al^{3+} ions is least followed by Mg^{2+}, Cl^{-} ions.

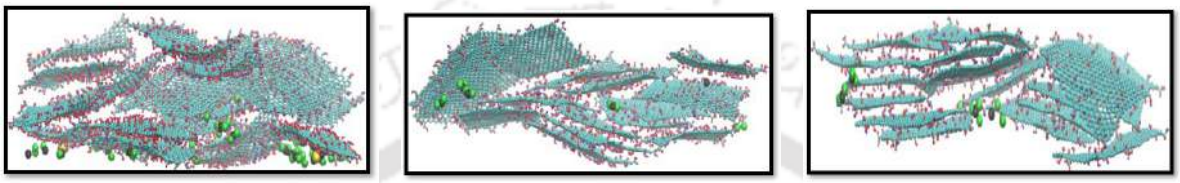

(a) (b) (c)

Figure 3.6: Intercalation of ions inside the interlayer gallery of the membranes. (a) GO membrane. (b) rGO membrane. (c) ErGO membrane. Cyan color is for carbon atoms, red color is for oxygen atoms, blue color is for hydrogen atoms, black color is for Mg^{2+} ions, green color is for Cl^{1-} ions, magenta color is for Al^{3+} ions, yellow color is for sulphur atoms and orange color is for nitrogen atoms.

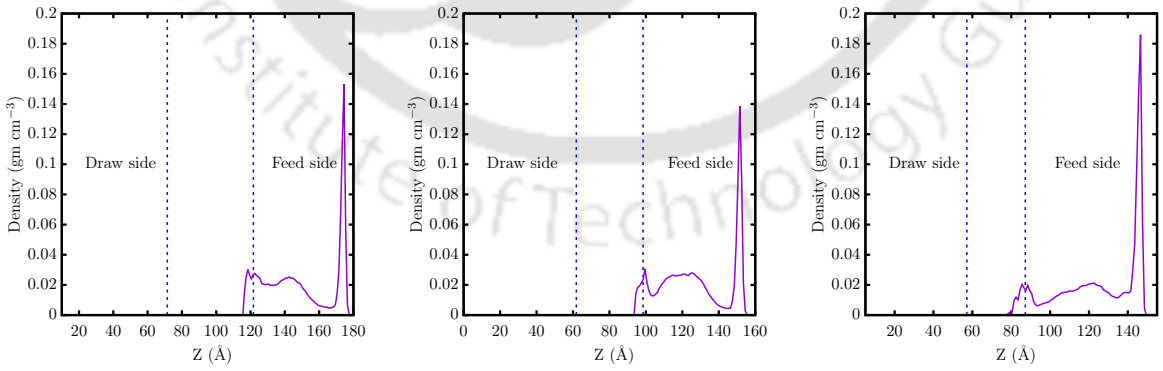

(a) (b) (c)

Figure 3.7: Variation in the density of AMX molecules along the Z direction for (a) GO membrane (b) rGO membrane and (c) ErGO membrane. Dotted lines indicate the membrane position.

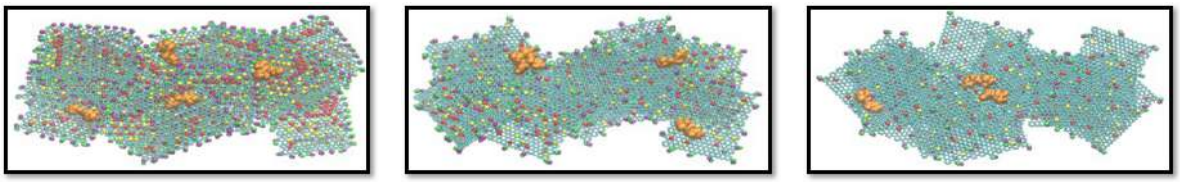

(a) (b) (c)

Figure 3.8: The snapshots of the retained AMX molecules on the membrane surface (top view) for (a) GO membrane (b) rGO membrane and (c) ErGO membrane. The AMX molecule is shown in orange color. Cyan color is for carbon atoms, red color is for oxygen atoms and blue color is for hydrogen atoms. O1, O2, O3 and O4 atoms are shown in red, yellow, purple and black colors respectively.

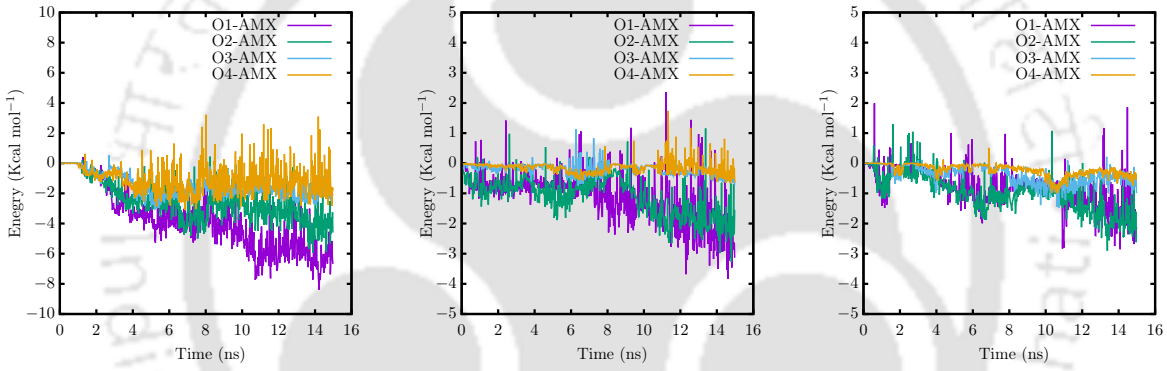

(a) (b) (c)

Figure 3.9: The van der Waals (vdW) interaction energy between the oxygen atoms of the GO nanosheets and the AMX molecule for (a) GO Membrane (b) rGO Membrane (c) ErGO Membrane.

3.3.2 AMX Retention

Figure.3.7 shows the density of the AMX molecules as a function of Z for the GO, rGO, and ErGO membranes. The dotted lines denote the position of the membrane. The first local maxima in all the plots indicate that few AMX molecules are retained on the surface of the membrane. Figure.3.8 shows the snapshots of the retained AMX molecules on the surface of GO, rGO, and ErGO membranes. These snapshots reveal that interactions between the AMX molecules and oxygen-containing functional groups of the membrane predominantly cause the retention of few AMX molecules on the surface of the membrane. To understand the interactions, we calculated the interaction energies between the AMX molecules and the

oxygen-containing functional groups of the membrane.

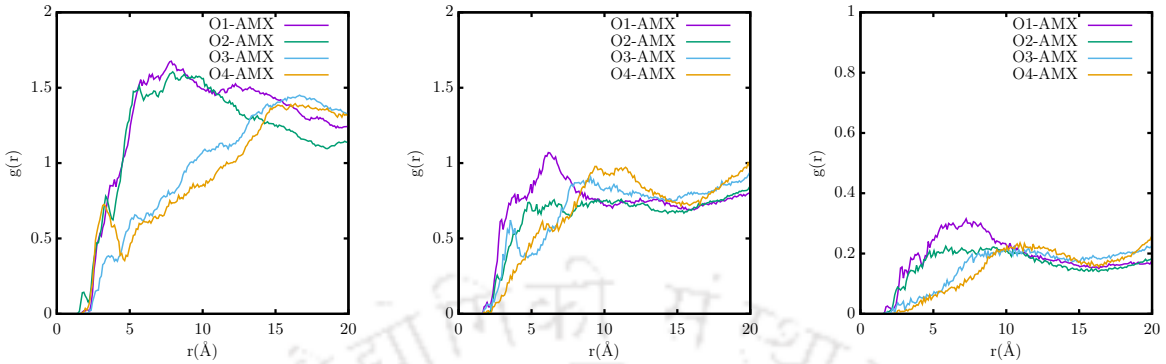

Figure 3.10: RDF between the oxygen atoms of the GO nanosheets and the AMX molecule for (a) GO membrane (b) rGO membrane and (c) ErGO membrane.

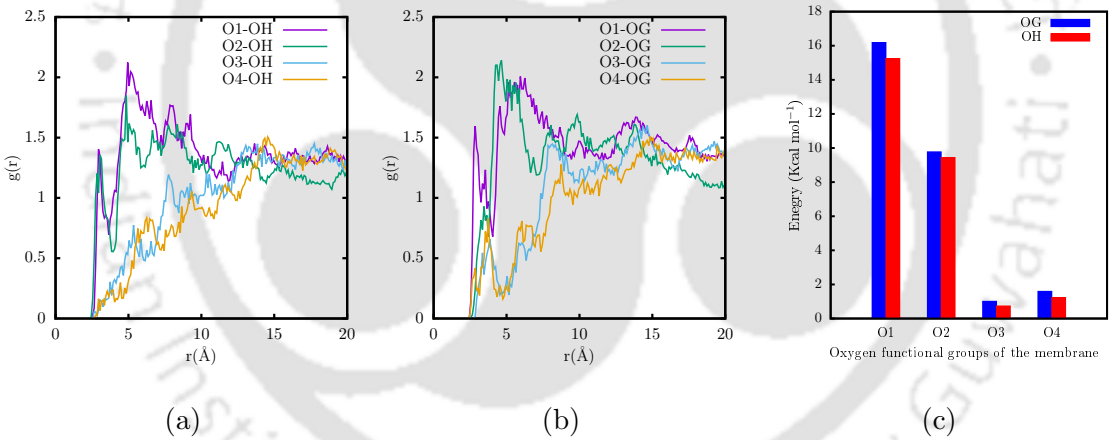

Figure 3.11: (a) RDF between the oxygen atoms of the GO nanosheets and the oxygen atom (OH) of the hydroxyl groups and (b) the oxygen atom (OG) of the carbonyl groups of the AMX molecule. (c) The interaction energy of the oxygen-containing functional groups of the GO nanosheets with the oxygen-containing functional groups of the AMX molecule (OH and OG).

Figure.3.9 shows the van der Waals (vdW) interaction energy between the oxygen atoms of the functional groups on the GO nanosheets and the AMX molecule. This interaction energy follows the order O1-AMX > O2-AMX > O3-AMX $\gtrapprox$ O4-AMX. This indicates that the AMX molecules have stronger interactions with the hydroxyl (O1) and epoxy (O2) functional groups of the GO nanosheets than the carboxyl (O3 and O4) functional groups. These results also

agree with the RDF between the AMX molecule and the oxygen atoms present in functional groups of the GO nanosheet. As shown in Figure.3.10, the AMX molecules have intensive interactions with the hydroxyl functional groups followed by the epoxy and carboxyl functional groups of the GO nanosheets. The carboxyl groups are located at the edges, and the epoxy and hydroxyl groups are located on the basal plane of the GO nanosheets. Consequently, few AMX molecules are retained on the basal plane of the membranes due to their high interactions with the hydroxyl and epoxy functional groups (Figure.3.8). The vdW interaction between the oxygen containing functional groups and AMX molecules is lower for rGO, ErGO membranes as compared to GO membrane. This is because the number of oxygen-containing functional groups is less in rGO and ErGO membranes than the GO membrane (shown in Table.3.1). The number of retained AMX molecules also decreases with decrease in the number of oxygen-containing functional groups (Figure.3.8)). The vdW interaction energy has more impact on the system than the electrostatic interaction energy, as shown in Figure B.6.

The AMX molecule contains a hydroxyl (−OH) and carbonyl groups (−C=O). We plotted the RDF between the membrane's oxygen-containing functional groups (OFGs) and the OFGs of the AMX molecules. Figure.3.11(a) presents the RDF between oxygen atoms on the GO nanosheets and the oxygen atoms (OH) present in hydroxyl functional groups of the AMX molecules. Similarly, Figure.3.11(b) shows the RDF between the oxygen atoms on the GO nanosheets and the oxygen atoms (OG) of the carbonyl functional groups of the AMX molecules. An observation found in Figure.3.11 is that the hydroxyl and carbonyl functional groups of the AMX molecules are more likely to interact with the hydroxyl (O1) and epoxy (O2) functional groups of the GO nanosheets than carboxyl (O3 and O4) functional groups.

Further, to understand which OFGs of AMX molecules have stronger interactions with OFGs of GO membrane, the interaction energies are reported in Figure.3.11(c). These energy values also indicate that OFGs of AMX molecules have stronger interactions with the epoxy and hydroxyl functional groups than carboxyl functional groups of the GO membrane. Furthermore, these values exhibit that the AMX molecule's carbonyl groups have stronger interactions with the GO membrane than with hydroxyl groups.

Figure.3.12 depicts the trajectories of the AMX molecules, which are retained on the surface of the GO membrane. The length of the trajectories of the AMX molecules increases as the number of oxygen containing functional groups on the GO membrane decreases. In other words, because of the reduction in the number of oxygen-containing functional groups, AMX

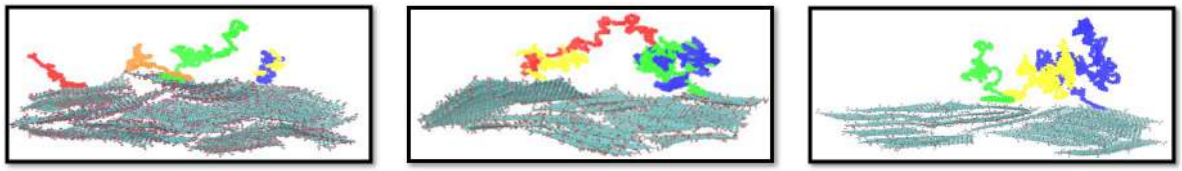

(a) (b) (c)

Figure 3.12: The trajectories of AMX molecules for (a) GO membrane (b) rGO membrane and (c) ErGO membrane. Cyan color is for carbon atoms, red color is for oxygen atoms and blue color is for hydrogen atoms.

molecules take more time to reach the surface of the membrane. The average time taken by AMX molecules to reach the surface of the GO, rGO, and ErGO membranes are 4, 10, and 13.5 ns, respectively. This can be attributed to lower interaction energy between AMX molecules and GO membranes as a consequence of reducing the number of oxygen containing functional groups.

As mentioned in the introduction, a few commercial polymeric and composite membranes have been employed to study the AMX rejection phenomena via different separation techniques, such as Ultrafiltration (UF), Nanofiltration (NF), Adsorption, and Forward Osmosis (FO). The comparative AMX rejection percentages of these membranes are presented in Table.3.2.

3.4 Conclusions

This present study focuses on the applicability of GO membrane for the removal of drug molecules. For this, non-equilibrium MD simulations are performed considering AMX as a model drug molecule. The trajectories of the non-equilibrium MD simulations have been utilized to examine the performance of three different membranes (GO, rGO, and ErGO) as FO membranes. These membranes differ in the number of oxygen-containing functional groups. The water and ion permeance of the membranes are strongly dependent on the number of oxygen-containing functional groups on the membrane. Decreasing the number of oxygen-containing functional groups leads to smaller pore sizes of the membranes, and it tends to lower water permeance. The water permeance through the membrane follows the order: GO membrane > rGO membrane > ErGO membrane. Reducing the number of oxygen-containing functional groups of the membrane also leads to less intercalation of ions inside the interlayer

Table 3.2: The comparative AMX rejection of different membranes.

Name of the membrane	AMX Rejection (%)	Separation Process
Polyethersulfone [PES] [173]	99	NF
PES-PEG [174]	85	NF
Silica composite [175]	90	NF
PES [5]	56.49 - 99.09	NF
Polyacrylonitrile (PAN)- Maleate ferroxane (Mf) [176]	92.3	NF
PAN - Goethite (Goe) [176]	86.3	NF
PSF/PVP/SiO_2 [177]	66.52-89.81	NF
PES/PVP/GO-TiO_2 [178]	97 ± 1.2	UF
PES@R1.Co^{2+} [179]	90	Adsorption
Present study (GO/rGO/ErGO)	100	FO

gallery of the membrane. The interaction of AMX molecules is stronger with hydroxyl and epoxy functional groups than carboxyl functional groups. Consequently, the AMX molecules are more likely to retain on the basal plane of the membrane. Reducing the number of oxygen-containing functional groups of the membrane leads to longer trajectory paths of the AMX molecules. For the smooth functioning of a FO process, the selection of an appropriate draw solution is important. It would be interesting to examine the performance of the membranes reported in this present study against the different draw and feed solution environments. The observations reported in this present study would be helpful in future investigations on the applicability of GO membranes for separation and purification applications.

Chapter 4

Cationic stabilized layered graphene oxide (GO) membrane for shale gas wastewater treatment: An atomistic insight*

4.1 Objective

In recent years, GO membranes have emerged as one of the most promising candidates for wastewater treatment. However, one major issue with layered GO membranes is their tendency to swell in aqueous environments. Cation intercalation inside the interlayer gallery of layered GO membrane emerges as one of the promising solutions to mitigate this problem [70, 78, 83–85]. However, the effect of cationic concentration inside membrane channels on the mechanism of water permeance and salt rejection is yet to be investigated in detail. Moreover, in the past few decades, shale gas extraction has enriched gas production, which has dropped the prices of natural gas and oil. However, shale gas extraction requires, on average, 2-7 million gallons of water [11–16]. Thus, the wastewater treatment associated with shale gas needs to be efficient for sustainable production [17–21]. Also, no atomistic insights are available in the literature on shale gas wastewater treatment using the FO process.

*Reddy, P. Rajasekhar, Abhijit Gogoi, and K. Anki Reddy. "Cationic stabilized layered graphene oxide (GO) membrane for shale gas wastewater treatment: An atomistic insight." Desalination 559 (2023): 116621.

Consequently, this study investigates shale gas wastewater (NaCl, $CaCl_2$, and crude oil) treatment via nonequilibrium molecular dynamics (MD) simulations with cation (K^+, Mg^{2+}) intercalated GO membranes in FO mode. The effect of cationic concentration on water permeance and salt rejection has been presented in detail. This study also demonstrated the crude oil aggregate formation and its stability for two kinds of cation intercalated membranes.

4.2 Methodology

4.2.1 Cation intercalated membrane

Cation intercalated GO membrane is created using the procedure explained below. Firstly, GO nanosheets are built using visual molecular dynamics (VMD) [180] and Avogrado [181] (Fig. 4.1(a)). The chemical composition of the GO nanosheets is $C_{10}O_1(OH)_1(COOH)_{0.5}$ [71, 83, 182, 183]. A multilayered GO membrane (shown in Fig. 4.1(b)) is constructed using these GO nanosheets, considering the geometric parameters of the membrane known as pore width (P), pore offset (O), and interlayer distance (I). In the present study[83], all membranes have the same value of O, which is 8 Å. For the parameter P, three different values are considered which are 8, 10, and 12 Å. The interlayer distance is chosen corresponding to the work of Chen et al.,[70] and it depends on the nature of the intercalated cations. Accordingly, the selected value of I, for K^+ intercalated GO membranes is 11.4 Å, and for Mg^{2+} intercalated GO membranes is 13.6 Å [70].

To investigate the effect of cation concentration inside the membrane, three GO membranes are constructed with P = 8 Å using the same number of GO nanosheets. Then, K^+ ions (10, 15, and 20) are randomly distributed inside the interlayer gallery of the GO membrane. Following that, K^+ ion intercalated GO membranes are equilibrated after merging with an equilibrated water box (overlapped water molecules are removed). Following the same procedure, Mg^{2+} ion (10, 15, and 20) intercalated GO membranes are constructed. Additionally, two more multilayered GO membranes with differing pore widths (10 and 12 Å) are constructed for each K^+ and Mg^{2+} ion intercalated membrane (10 ions within the GO layers). Details of all these membranes are presented in Table. 4.1.

Table 4.1: Configurations of the GO membranes and their corresponding abbreviations.

Name of the membrane	Intercalated ions	Ion type	I(Å)	P(Å)
GO-10-K	10	K^+	11.4	8
GO-15-K	15	K^+	11.4	8
GO-20-K	20	K^+	11.4	8
GO-10-M	10	Mg^{2+}	13.6	8
GO-15-M	15	Mg^{2+}	13.6	8
GO-20-M	20	Mg^{2+}	13.6	8
GO-10-K-10P	10	K^+	11.4	10
GO-10-K-12P	10	K^+	11.4	12
GO-10-M-10P	10	Mg^{2+}	13.6	10
GO-10-M-12P	10	Mg^{2+}	13.6	12

4.2.2 FO simulation system

The feed solution, draw solution, and semi-permeable membrane are the three components of a FO system. The osmotic pressure difference between the draw solution and feed solution act as a driving force for the water molecules to permeate through the membrane. The draw solution in this study is a 1:2 molar ratio of choline chloride and ethylene glycol solution. It contains 536 choline molecules, 536 chloride ions, 1070 ethylene glycol molecules, and 11200 water molecules. In this study, the feed solution is shale gas wastewater whose major components are light crude oil, NaCl, $CaCl_2$ and water [20, 184–189]. Previous theoretical and experimental work considered hexane and heptane mixture as light crude oil [188, 190]. Crude oil, on the other hand, is a complicated mixture of hydrocarbons. Referring to Miranda's work [191–195], this study considered alkanes (four types), cycloalkanes (two types), and aromatics (two types) to be the composition of light crude oil. The feed solution contains 73 sodium ions, 6 calcium ions, 85 chloride ions, alkanes (144 hexane, 132 heptanes, 156 octanes, 180 nonanes), cycloalkane (96 cyclohexane, 156 cyclo heptane), aromatics (60 benzene, 156 toluene), and 18000 water molecules. The hydrated cation intercalated GO membrane is placed between the feed solution

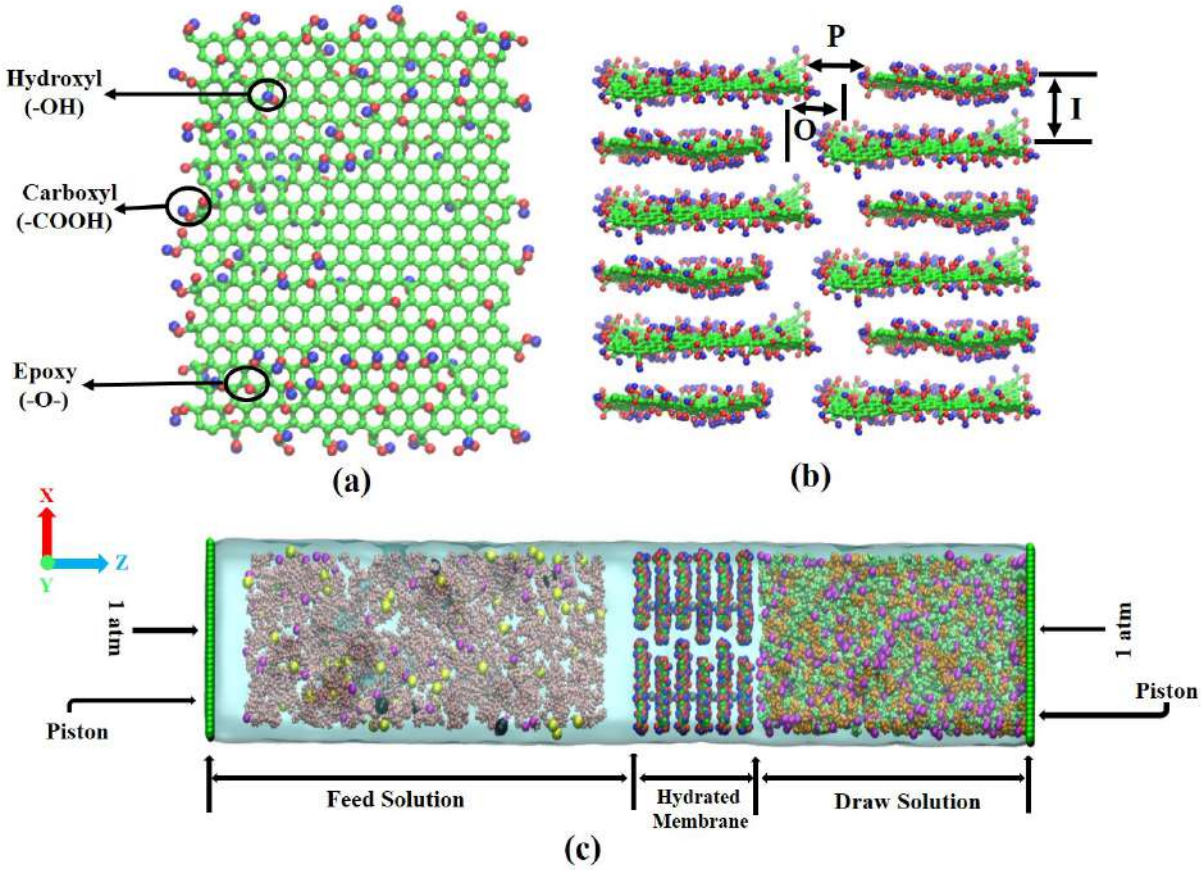

Figure 4.1: (a) GO nanosheet. (b) Multilayered GO membrane. (c) Simulation system. Green color is for carbon atoms, red color is for oxygen atoms, blue color is for hydrogen atoms, pink color is for crude oil, yellow color is for Na^+ ions, black color is for Ca^{2+} ions, magenta color is for Cl^- ions, gray color is for K^+ ions, orange color is for choline and lime color is for ethylene glycol.

and the draw solution in each FO simulation system (Fig. 4.1(c)). A graphene sheet is placed at the end of the draw and feed solution, which acts as a piston. Atmospheric pressure is applied in opposing directions on both of these pistons. In addition, along the Z−axis, vacuum of 30 Å in length is placed on top and bottom of the simulation system.

4.2.3 Simulation Methodology

All the non-equilibrium MD simulations reported in this study are performed using OPLS−AA forcefield parameters[196] with NAMD 2.11 package[197]. The Lennard−Jones potential is employed to compute the van der Waals interactions with a cutoff radius of 12 Å. The Particle

Mesh Ewald (PME) method [154] is used to calculate long−range electrostatic interactions. Water molecules are represented using the TIP3P water model[162]. After constructing the FO simulation systems as explained in the previous section, energy minimization is performed. Following that, a 1.0 ns equilibration run is carried out at 300.0 K with a constant pressure of 1.0 atm. After that, 20 ns of production runs are performed with a time step of 1.0 fs in an NVT ensemble with the periodic boundary conditions in all three directions. Carbon atoms located at the corner of the GO nanosheets are fixed during the production runs to maintain the layered structure of the membrane [198, 199]. Langevin dynamics is used to maintain the constant temperature during the simulations with a damping factor of 5.0 ps^{-1}. The trajectories are saved at every 20 ps. Three independent simulations are performed with different initial configurations for each membrane. The findings presented in the following sections are averaged over these three independent simulations [71, 83].

4.3 Results and discussion

4.3.1 Water permeance

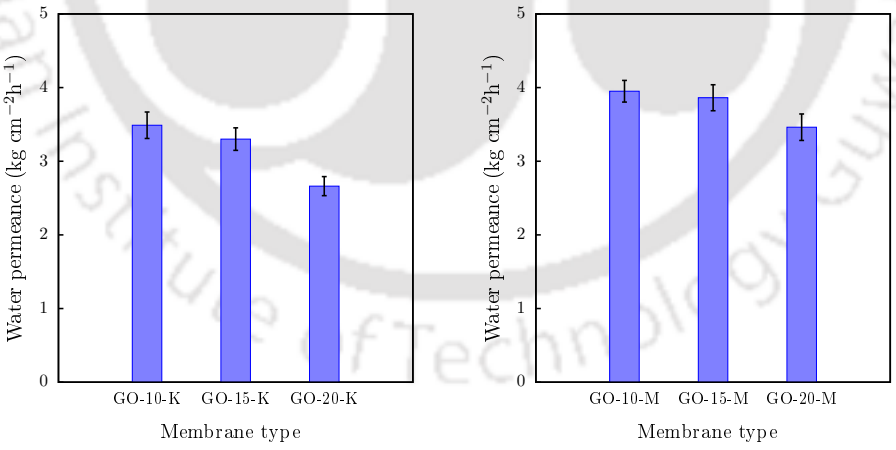

(a) (b)

Figure 4.2: Water permeane through the (a) K^+ ion intercalated and (b) Mg^{2+} ion intercalated GO membranes.

From the MD simulations first we investigated the effect of concentration of intercalated cations on the performance of the membranes. Fig. 4.2(a) shows that the GO-10-K membrane exhibits the highest water permeance, followed by GO-15-K and GO-20-K membranes.

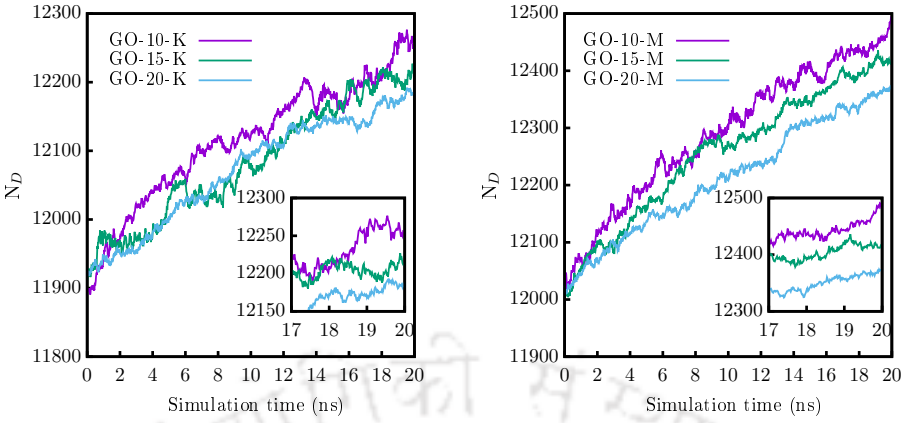

(a) (b)

Figure 4.3: Variation of the number of water molecules in the draw solution (N_D) as a function of the simulation time. (a) K^+ ion intercalated and (b) Mg^{2+} ion intercalated GO membranes.

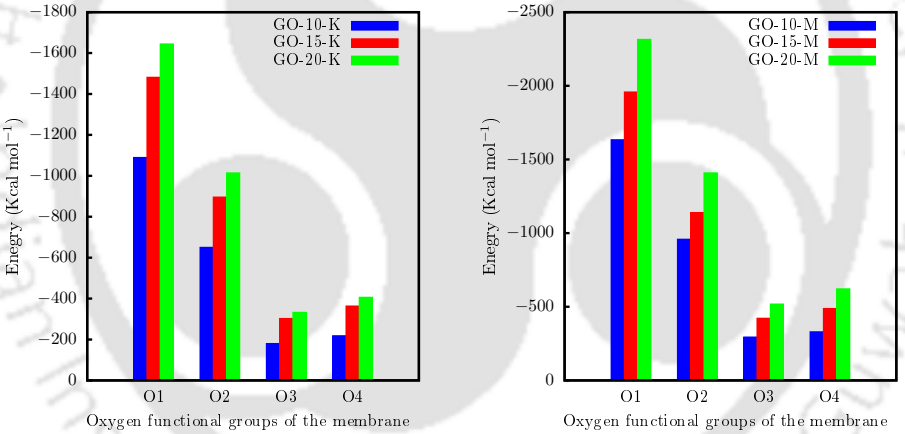

(a) (b)

Figure 4.4: Interaction energy of the oxygen-containing functional groups of the GO nanosheets with the intercalated ions. (a) K^+ ion intercalated and (b) Mg^{2+} ion intercalated GO membranes. Here O1, O2, O3, and O4 are the oxygen atoms of a hydroxyl group (-OH), epoxy group (-O-), carboxyl group, which is linked to only C atom (-C=O), and carboxyl group that is bonded to C and H atoms (C-O-H), respectively.

Likewise, the GO-10-M membrane has the highest water permeance, followed by the GO-15-M and GO-20-M membranes, as shown in Fig. 4.2(b). So with the increase in the number of intercalated cations water permeance decreases. Fig. 4.3 shows the variation of the number of water molecules (N_D) in the draw solution as a function of the simulation time. The N_D of

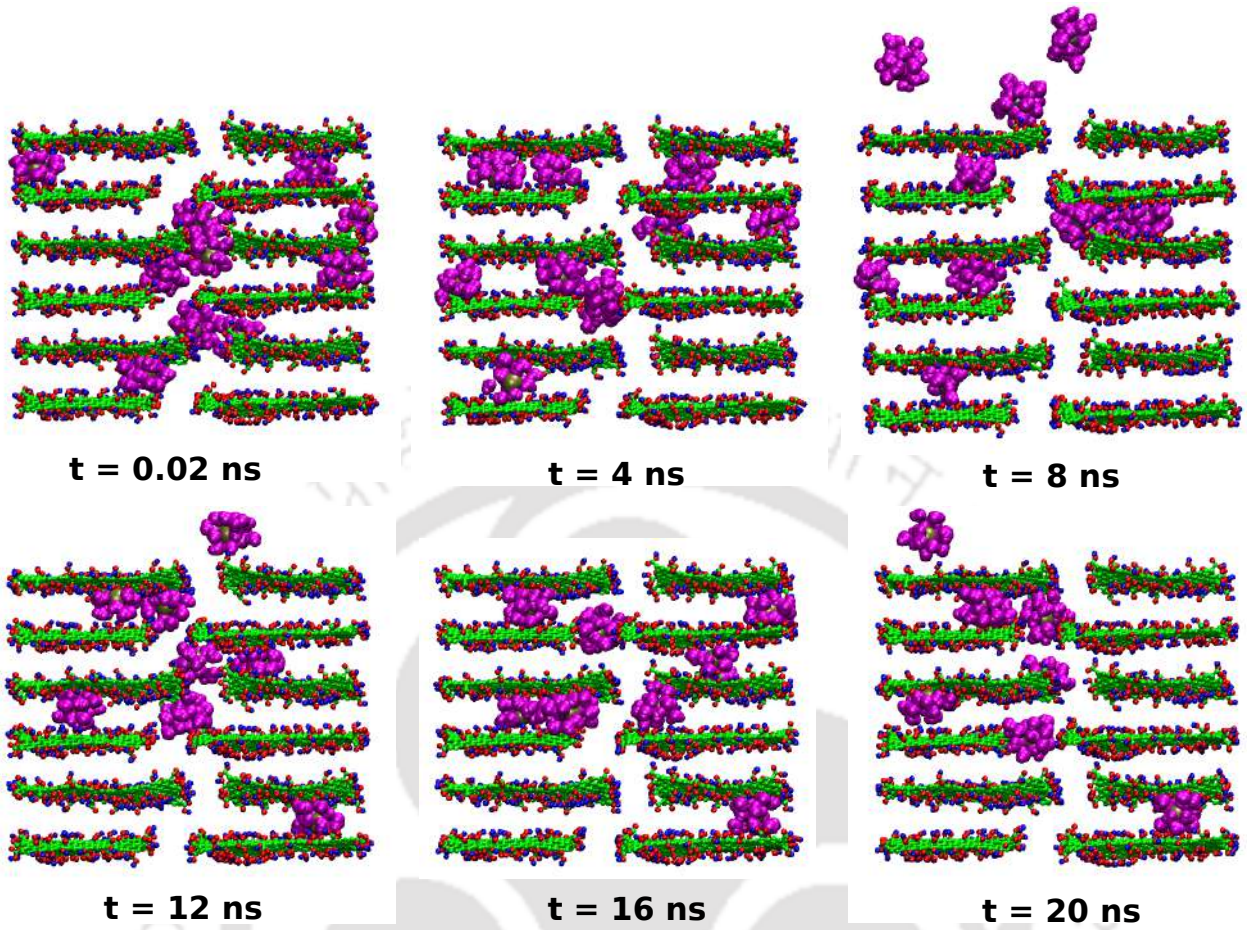

Figure 4.5: The hydration shells of the K^+ ions of the GO-10-K membrane at different time. The blue color is for hydrogen atoms, the red color is for oxygen atoms and green color is for carbon atoms of the membrane. The gray color is for K^+ ions and magenta color is for water molecules.

the K^+ and Mg^{2+} ion intercalated membranes are depicted in Fig. 4.3(a) and (b), respectively. As shown in Fig. 4.3, the rate of increase in water molecules in the draw solution is more in the GO-10-K / GO-10-M membrane, followed by the GO-15-K / GO-15-M and GO-20-K / GO-20-M membranes. Water permeance is calculated as follows:

$$Water\ permeance = \frac{V}{A \times t} \tag{4.1}$$

In the above equation, V is the net volume of permeated water molecules through the membrane, A is the area of the membrane, and t is the simulation time.

This simulation work agrees with the experimental studies of cationic stabilized GO membranes that have examined the relationship between water permeance and cationic concentra-

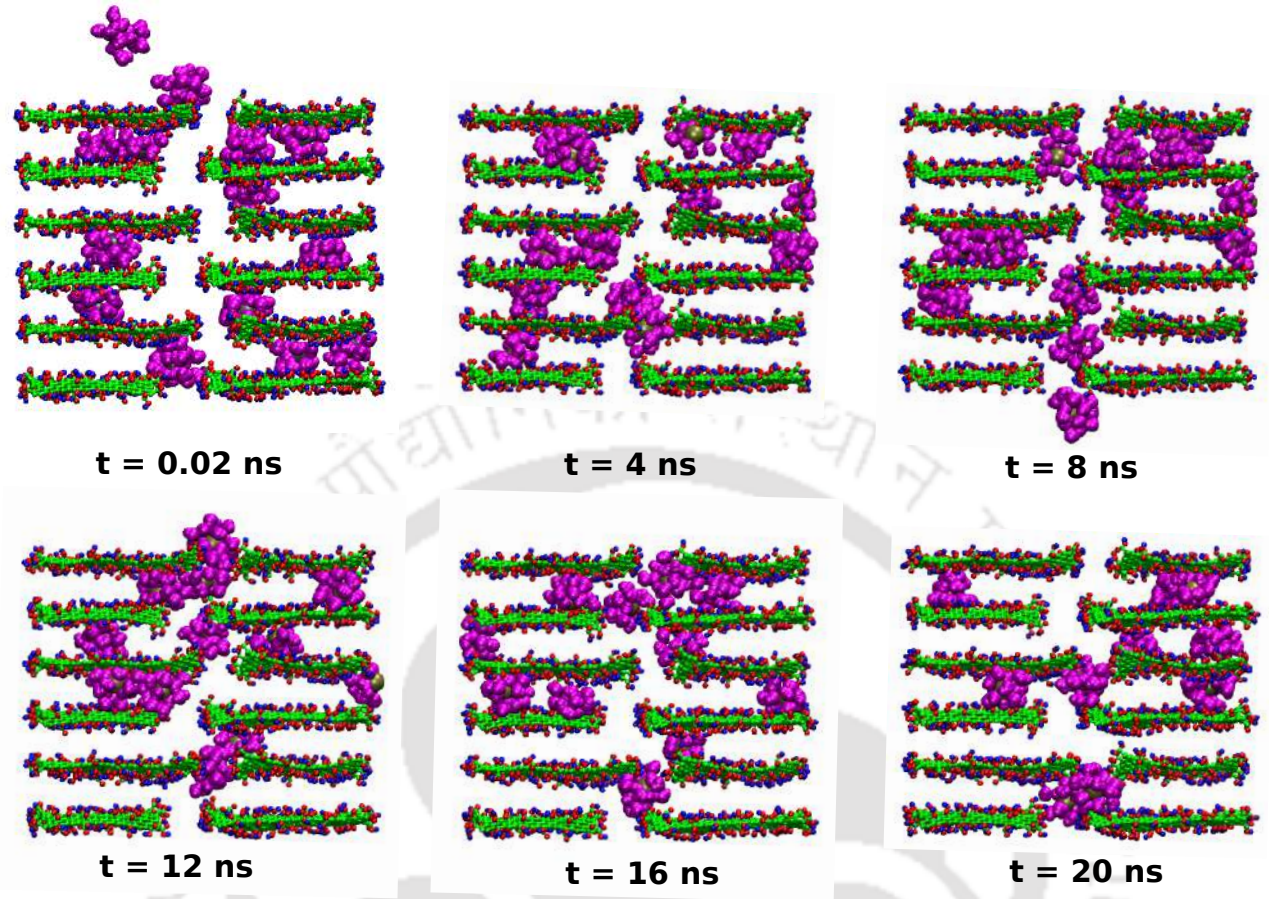

Figure 4.6: The hydration shells of the K^+ ions of the GO-15-K membrane at different time. The blue color is for hydrogen atoms, the red color is for oxygen atoms and green color is for carbon atoms of the membrane. The gray color is for K^+ ions and magenta color is for water molecules.

tion within GO layers [81, 84]. However, these experimental investigations consider several aspects of GO membranes, such as the quantity of oxygen-containing functional groups, size, thickness, and interlayer spacing of the GO flakes. In addition to the characteristics of the GO membrane, the experiments considered other factors, such as the hydrated radius of intercalated cations, the strength of electrostatic interactions of cations with GO nanosheets, and the operating temperature. In order to address the performance of the membranes, this simulation study considers the intensity of electrostatic interactions of the intercalated cations with the GO nanosheets and the hydrated radius of intercalated cations.

The oxygen-containing functional groups (OFGs) of the GO membranes influence water permeance; especially, hydroxyl functional groups promote water permeance, and carboxyl

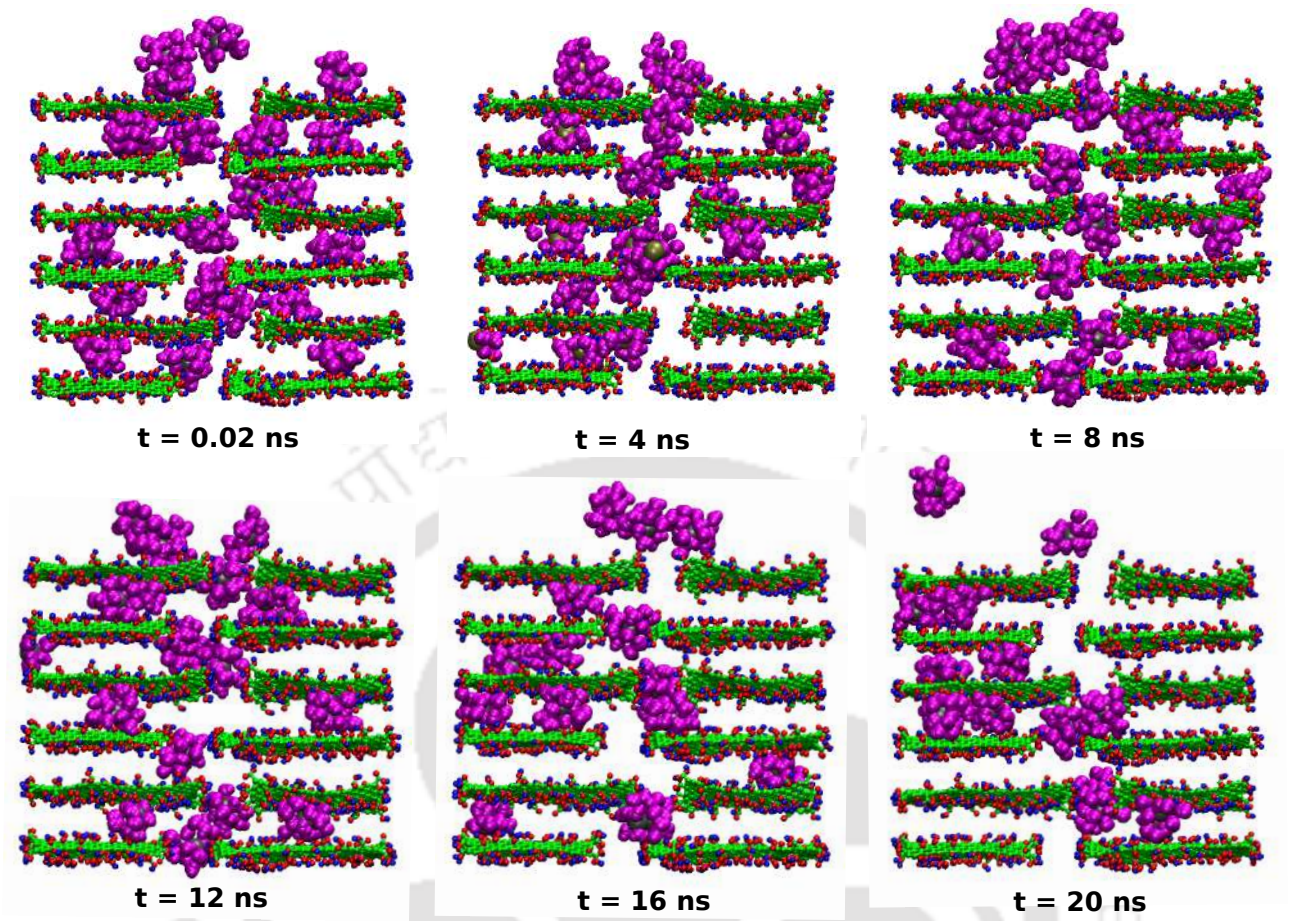

Figure 4.7: The hydration shells of the K^+ ions of the GO-20-K membrane at different time. The blue color is for hydrogen atoms, the red color is for oxygen atoms and green color is for carbon atoms of the membrane. The gray color is for K^+ ions and magenta color is for water molecules.

functional groups induce water resistance [48, 63]. The electrostatic interactions of intercalated cations with OFGs are measured to investigate the role of OFGs in lowering water permeance with an increase in the cationic concentration within GO laminates. According to Fig. 4.4, increasing the ionic concentration within GO channels reduces the accessible free volume of the GO membrane (particularly at the domain of hydroxyl functional groups) for the passage of water molecules because of increasing interactions of cations with hydroxyl functional groups. As a result, the possibility of pulling water molecules into the membrane layers by hydroxyl functional groups decreases with an increase in the cationic concentration. Thus, increasing the cationic concentration inside the GO channels leads to lower water permeance. As seen in Fig. 4.4, interactions of cations with carboxyl groups also increase with increasing cationic content.

It means that the frequency of cations' mobility towards the edges of the membranes increase, which may result in the blockage of pores due to the merging of hydration shells of cations.

The hydration shells of the K^+ ions of the GO-10-K, GO-15-K, and GO-20-K membranes at different time are presented in Fig. 4.5, 4.6, and 4.7, respectively, to investigate the water permeance further. These snapshots indicate that the hydration shells of intercalated ions tend to merge with each other with the increase in the ionic concentration. While ions are translocating inside the GO laminates, their merged hydrated shells cause pore-clogging, leading to lower diffusion of water molecules. We observed identical phenomena in the Mg^{2+} ion intercalated GO membranes. Hydration shells of the Mg^{2+} ions of the GO-10-M, GO-15-M, and GO-20-M membranes are presented in Fig. B.6, B.7, and B.8, respectively. To further investigate the diffusion behavior of water molecules through the membranes, the water molecule coordination number (w(r)) of intercalated ions and survival probability (SP) of water molecules within the membrane region are presented in the supporting information (Fig. B.9 and B.10).

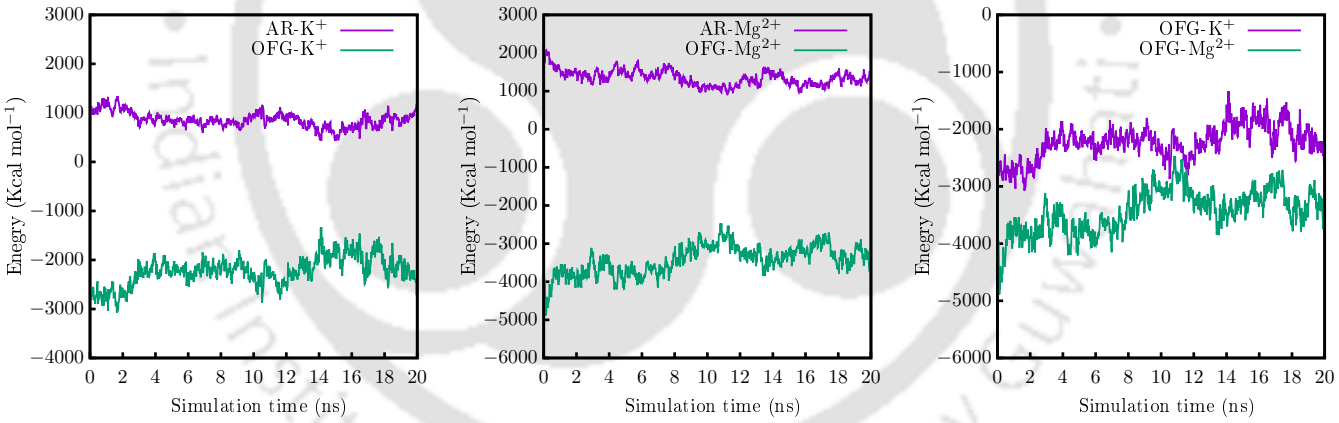

(a) (b) (c)

Figure 4.8: Interaction energy of the oxygen-containing functional groups (OFGs) and aromatic rings (AR) with cations for (a) GO-10-K Membrane and (b) GO-10-M Membrane. (c) Comparative interaction energy (OFGs vs cations) of the GO-10-K and GO-10-M membranes.

The water permeance of Mg^{2+} cation intercalated GO membranes is higher than K^+ cation intercalated GO membranes, as shown in Fig. 4.2. The water permeance depends on the interlayer distance of the membranes. On the other hand, the interlayer distance of the cation intercalated GO membranes depends on the interactions of the oxygen-containing functional groups (OFGs) and aromatic rings (AR) of the GO membranes with the cations. The interaction

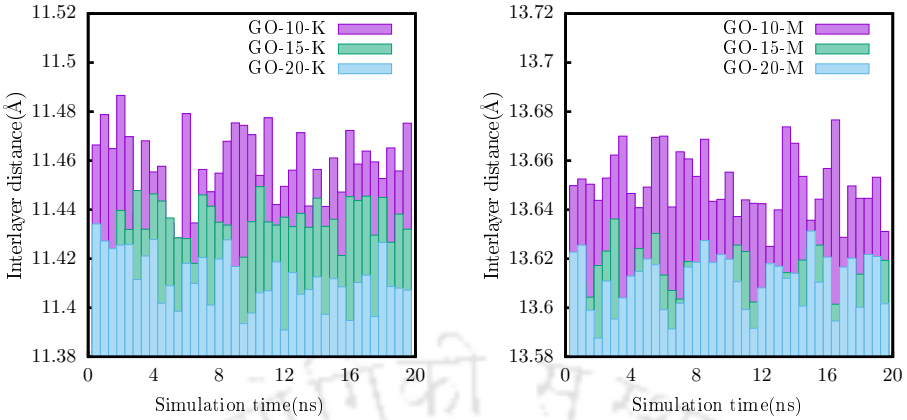

(a) (b)

Figure 4.9: Average interlayer distance of the membranes as a function of the simulation time. (a) K^+ ion intercalated and (b) Mg^{2+} ion intercalated GO membranes.

energies are computed to understand further which interactions are significant in maintaining the interlayer distance. The interaction energy of the cations with the OFGs is stronger than those with the AR, as shown in Fig. 4.8(a) and (b). As a result, the interactions of the cations with OFGs are more significant than AR to maintain the interlayer distance of the membrane. As shown in Fig. 4.8(c), the interaction energy of the OFG with Mg^{2+} ions is stronger than those with K^+ ions[84, 200]. It implies that Mg^{2+} ions keep the interlayer distance between the GO layers more stable than K^+ ions. A similar analysis of the remaining membranes is presented in Fig. B.11, B.12 and results are similar to GO-10-K and GO-10-M membranes.

The average interlayer distance of the membranes during the course of the simulation is displayed in Fig. 4.9. As previously stated, the stability of the interlayer distance depends on the interactions of intercalated ions with OFGs and AR. The interaction energy gets stronger with the increase in the ionic concentration within the GO layers. Accordingly, as the ionic concentration increases, the interlayer distance becomes more stable. Moreover, the Mg^{2+} ion intercalated membranes achieve better stability than the K^+ ion intercalated membranes. Hence, Mg^{2+} ion intercalated GO membranes exhibited higher water permeance than K^+ ion intercalated GO membranes.

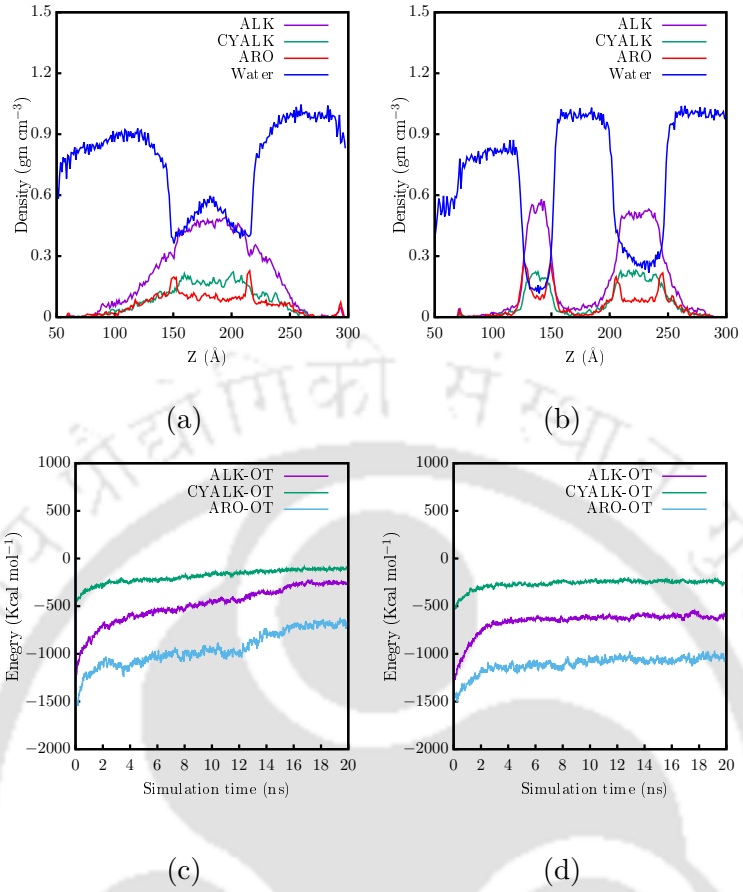

Figure 4.10: The density profiles of the crude oil-water mixture [alkanes (ALK), cycloalkanes (CYALK), aromatics (ARO), and water] along the Z direction for (a) GO-15-K membrane and (b) GO-15-M membrane. Interaction energy of the hydrocarbons with oxygen atom of water (OT) for (c) GO-15-K membrane and (d) GO-15-M membrane.

4.3.2 Crude oil aggregation and rejection

This study considered shale gas wastewater as a feed solution containing NaCl, $CaCl_2$, crude oil, and water. Crude oil contains alkanes (ALK), cycloalkanes (CYALK), and aromatics (ARO). Crude oil is not soluble in water, unlike the salts (NaCl and $CaCl_2$). As a result, crude oil aggregation happens in the feed solution. The stability of the aggregation could be an important factor in separating the crude oil from the shale gas wastewater.

Fig. 4.10(a),(b) shows the density profiles of the crude oil-water mixture for the FO process with GO-15-K and GO-15-M membranes. It observed that for the GO-15-K membrane, crude oil forms one large aggregate. On the other hand, for the GO-15-M membrane, crude oil forms two small aggregates and distributes throughout the feed solution. It implies that crude oil

aggregation is more stable in the the GO-15-K membrane.

Fig. 4.10(a),(b) also shows that aromatics are more concentrated at the crude oil-water interface than other hydrocarbons. The interfacial tension of aromatics-water is lower than other hydrocarbons-water, leading to accumulation at the interface [191]. The interaction energies of hydrocarbons with oxygen atom of water (OT) for the GO-15-K and GO-15-M membranes are shown in Fig. 4.10(c) and (d). They reveal that aromatics interact more strongly with water, which means they are more concentrated at the crude oil-water interface. Fig. 4.11(a),(b) presents the snapshots related to the crude oil aggregation of the GO-10-K and GO-10-M membranes. These snapshots show that for the GO-10-K membrane, crude oil forms one aggregate, whereas the GO-10-M membrane has two small aggregates. Furthermore, one crude oil aggregate is observed in the GO-15-K and GO-20-K membranes, whereas GO-10-M and GO-20-M membranes have two small aggregates. Fig. B.13, B.14, B.15, B.16 present the observations for these membranes.

Fig. 4.12(a), (b) shows the crude oil density profiles of all K^+, Mg^{2+} ion intercalated GO membranes, respectively. Here, dotted lines indicate the position of the membrane. Due to the aggregation nature of the crude oil, all membranes exhibited 100% crude oil rejection. Moreover, crude oil aggregate forms closer to the surface of Mg^{2+} ion intercalated membranes as compared with the K^+ ion intercalated membranes. Fig. 4.11 also shows that crude oil aggregation happens nearer the surface of the Mg^{2+} ion intercalated membrane than the K^+ ion intercalated membrane. The Mg^{2+} ion intercalated membranes have higher water permeance than K^+ ion intercalated membranes, which causes crude oil to push closer to the surface of Mg^{2+} ion intercalated membranes. Furthermore, the van der Waals (vdW) interaction energy of crude oil with intercalated ions is presented in Fig. 4.13. It shows that crude oil's interactions with Mg^{2+} ions are more significant than those with K^+ ions. Hence, the higher permeance of the Mg^{2+} ion intercalated GO membranes and stronger interactions of the Mg^{2+} ions with crude oil result in unstable crude oil aggregate forms closer to the surface of these membranes. A similar analysis of the other membranes is presented in Fig. B.17, and the results are analogous to these membranes.

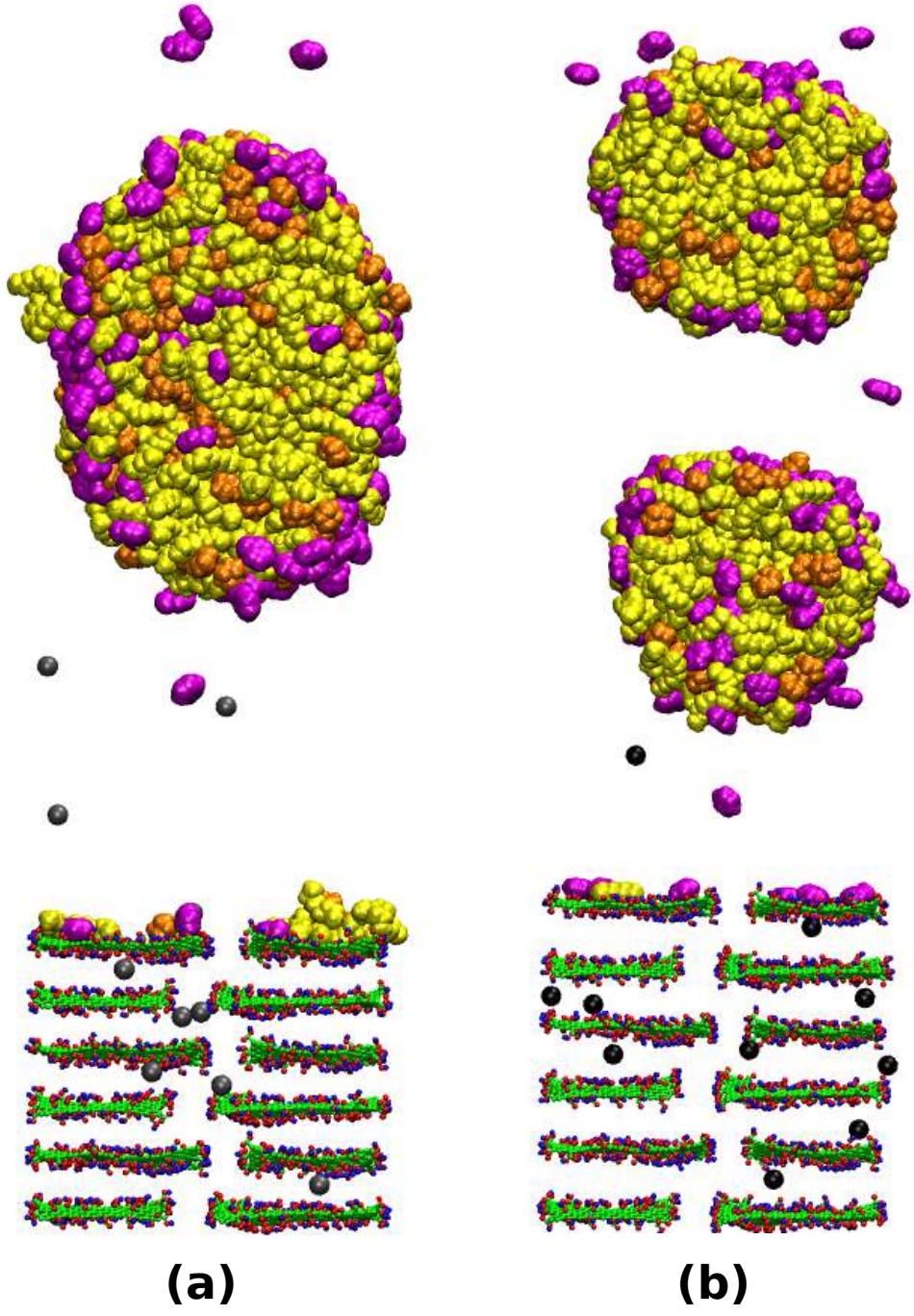

Figure 4.11: Snapshot of crude oil aggregation in (a) GO-10-K membrane and (b) GO-10-M membrane. Green color is for carbon atoms, red color is for oxygen atoms, blue color is for hydrogen atoms, gray color is for K^+ ions, black color is for Mg^{2+} ions, yellow color is for alkanes, orange color is for cycloalkanes, and magenta color is for aromatics.

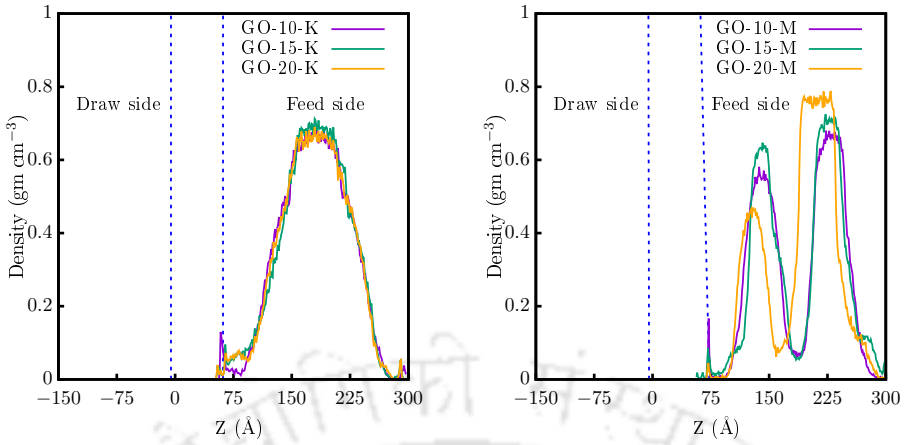

(a) (b)

Figure 4.12: Variation in the density of crude oil along the Z-direction for (a) K^+ ion intercalated and (b) Mg^{2+} ion intercalated GO membranes. The dotted lines indicate the membrane position.

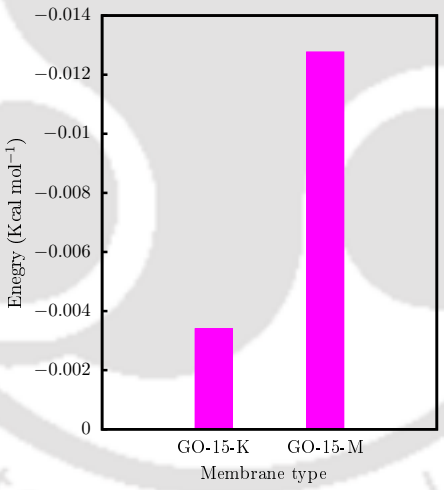

Figure 4.13: Interaction energy of the crude oil with the intercalated ions (K^+, Mg^{2+}) for GO-15-K and GO-15-M membranes.

4.3.3 Salt rejection

Fig. B.18 depicts the distribution of Na^+ ions for K^+ ion intercalated GO membranes at the end of the simulation. One Na^+ ion intercalated inside the layers of the GO-10-K and GO-15-K membranes, but none in the GO-20-K membrane. Moreover, the Na^+ ion travels to the 4^{th} layer in the GO-10-K membrane, whereas the movement is restricted to the 2^{nd} layer in the GO-15-K membrane. The presence of more K^+ ions inside the membrane layers causes stronger

electrostatic repulsion, which inhibits the passage of Na^+ ions, resulting in better Na^+ rejection.

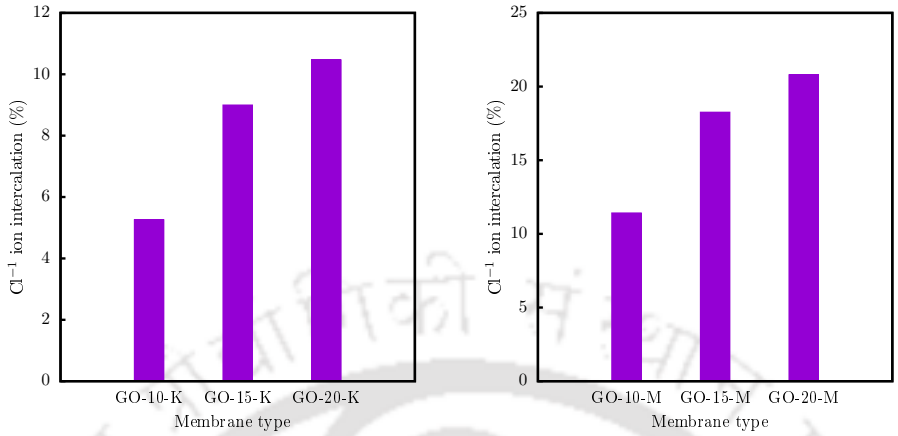

Figure 4.14: Cl^- ion intercalation (in %) for (a) K^+ ion intercalated and (b) Mg^{2+} ion intercalated GO membranes.

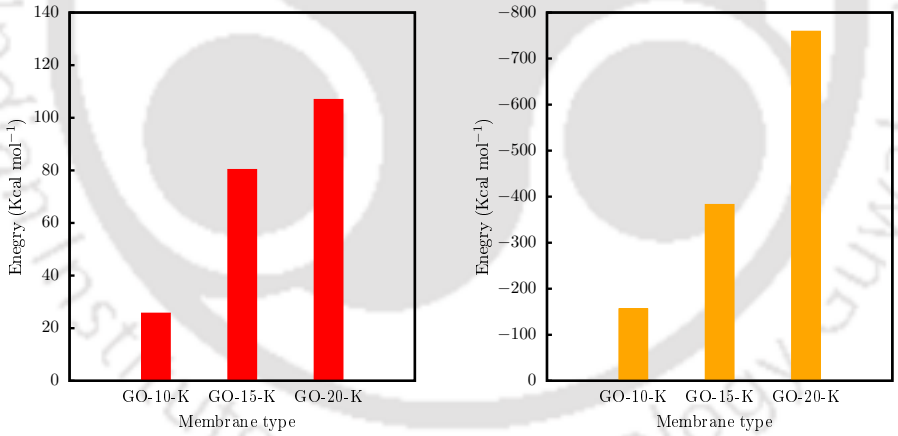

Figure 4.15: Average interaction energy of the K^+ ions with (a) Na^+ and (b) Cl^- ions.

The distribution of the Cl^- ions for K^+ ion intercalated GO membranes at the end of the simulation is shown in Fig. B.19. The GO-10-K, GO-15-K, and GO-20-K membranes have 5.26%, 9.00%, and 10.47% Cl^- ions within their layers, respectively, as shown in Fig. 4.14(a). It means that as the number of K^+ ions increases, so does the penetration of Cl^- ions. Additionally, for GO-10-K and GO-15-K membranes, Cl^- ion transport is restricted to the 3^{rd} and 5^{th} layers, respectively. On the other hand, one Cl^- ion permeated through the

GO-20-K membrane. In contrast to Na^+ transport, the presence of K^+ ions enhances Cl^- ion permeation.

The electrostatic interactions of intercalated ions with salt ions (Na^+ and Cl^-) are measured to investigate the insights of salt rejection. Fig. 4.15(a) and (b) illustrates the electrostatic interaction energies of K^+ ions with Na^+ and Cl^- ions, respectively. Increased ionic concentration within the GO layers causes stronger electrostatic repulsion with Na^+ ions, as shown in Fig. 4.15(a). As a result, the GO-20-K membrane rejected all Na^+ ions. Similarly, as seen in the Fig. 4.15(b), increasing ionic concentration, the electrostatic repulsion of K^+ ions with Cl^- ions reduces and promotes Cl^- ion transport within the GO laminates.

The distribution of Na^+ and Cl^- ions in Mg^{2+} ion intercalated membranes at the end of the simulations are shown in Fig. B.20 and B.21. The results of these membranes are similar to the K^+ ion intercalated membranes. The GO-10-M and GO-15-M membranes have one Na^+ ion within their layers, whereas the GO-20-M membrane has none. Besides, the Na^+ ion travels to the 3^{rd} layer in the GO-10-M membrane, whereas its movement is restricted to the 2^{nd} layer in the GO-15-M membrane.

The GO-10-M, GO-15-M, and GO-20-M membranes have 11.42%, 18.26%, and 20.80% Cl^- ions intercalated within their layers, respectively, as shown Fig. 4.14(b). Moreover, Cl^- ion transport is restricted to the 5^{th} and 6^{th} layers for GO-10-M and GO-15-M membranes, respectively. On the other hand, one Cl^- ion permeated through the GO-20-M membrane. Moreover, Mg^{2+} ion intercalated membranes have more Cl^- ions within the layers than the K^+ ion intercalated membranes due to their higher interlayer distance.

Fig. B.22 depicts the electrostatic interactions of Mg^{2+} ions with salt ions. With the increase in intercalated Mg^{2+} ions, the electrostatic repulsion with Na^+ ions increases. In contrast, when the ionic concentration increases, the electrostatic repulsion with Cl^- ions decreases. As a result, the GO-20-M membrane rejects all Na^+ ions while enhancing Cl^- ion transport.

4.3.4 Effect of the pore width (P)

This section explains the influence of the pore width of the membranes on water permeance and salt rejection. Water permeance of the K^+ and Mg^{2+} ion intercalated membranes with different pore widths is presented in Fig. 4.16(a) and (b), respectively. As shown in Fig. 4.16(a), the GO-10-K-12P membrane exhibited the higher water permeance, followed by the GO-10-K-10P and

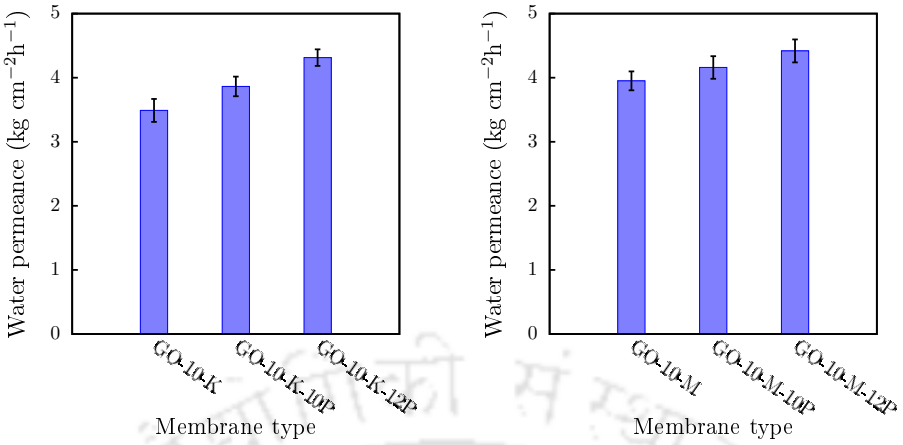

Figure 4.16: Water permeane through a different pore sizes of the (a) K^+ ion intercalated and (b) Mg^{2+} ion intercalated GO membranes.

GO-10-K membranes. Likewise, the GO-10-M-12P membrane has the highest water permeance, followed by the GO-10-M-10P and GO-10-M membranes, as shown in the Fig. 4.16(b). It indicates that increasing the pore width of the membranes enhances water permeance [62].

Fig. B.23 illustrates the distribution of the Na^+ ions for K^+ ion intercalated membranes with different pore widths at the end of the simulations. Unlike the GO-10-K membrane, which has one Na^+ ion within the layers, the GO-10-K-10P and GO-10-K-12P membranes have two Na^+ ions inside the GO laminates. However, the mobility of Na^+ ions is restricted to the 5^{th} layer of the membranes. As shown in Fig. B.24, the GO-10-K, GO-10-K-10P, and GO-10-K-12P membranes have 5.26%, 9.47%, and 9.47% Cl^- ions inside the layers, respectively. Cl^- ion transport is restricted to 2^{nd}, 4^{th}, and 5^{th} layer of the GO-10-K, GO-10-K-10P, and GO-10-K-12P membranes, respectively. In other words, increasing the pore size of the membranes drives a slightly higher number of ions into the layers. Yet, the presence of K^+ ions inhibited ion permeation through the larger pores of the GO laminates.

Fig. B.25 and B.26 illustrate the distribution of Na^+ and Cl^- ions for Mg^{2+} ion intercalated membranes with different pore widths at the end of the simulations, respectively. Observations on the Mg^{2+} ion intercalated membranes are quite similar to the K^+ ion intercalated membranes. The GO-10-M membranes have one Na^+ ion, whereas both GO-10-M-10P and GO-10-M-12P have two Na^+ ions within the layers. The movement of the Na^+ ions is limited to the 3^{rd} layer of the membranes. The presence of the Cl^- ions inside the interlayer gallery of the GO-10-M, GO-

10-M-10P, and GO-10-M-12P membranes are 11.42%, 11.42%, and 18.09% respectively. Cl^- ion transport is restricted to the 5^{th} and 6^{th} layer of the GO-10-M and GO-10-M-10P membranes, respectively. However, one Cl^- ion permeated through the GO-10-M-12P membrane. So, Mg^{2+} ions also restricted the permeation of ions through the larger pores of the GO laminates. Additionally, the effect of the pore offset(O) on the membrane performance (water permeance and salt rejection) is presented in the supporting information (Fig. B.27, B.28, and B.29).

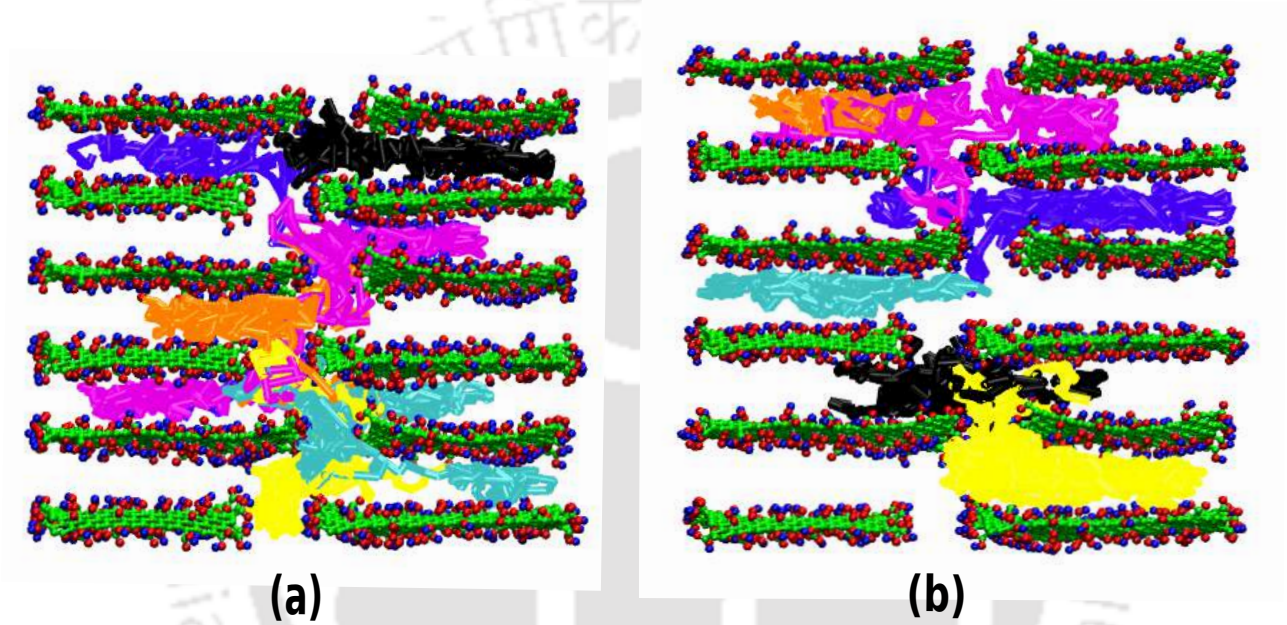

Figure 4.17: Trajectories of the intercalated ions inside the GO laminates during the simulations. (a) K^+ ions, (b) Mg^{2+} ions. Green color is for carbon atoms, red color is for oxygen atoms, blue color is for hydrogen atoms, and remaining colors represent the trajectory of ions.

In addition, to investigate the distribution of K^+ and Mg^{2+} ions inside the membrane layers during the simulations, the radial distribution function (g(r)) is computed between these ions and oxygen atom of water (OT). As shown in Fig. B.30, Mg^{2+} ions have more intense interactions with water than K^+ ions [86, 201]. Consequently, Mg^{2+} ions move at a slower rate than K^+ ions. The trajectories of the remained K^+ and Mg^{2+} ions inside the GO laminates at the end of the simulations are shown in Fig. 4.17. They are helpful to examine ions mobility within the GO layers during the simulations. It shows that K^+ ions have greater mobility than Mg^{2+} ions. As a result, more Mg^{2+} ions remained inside the membrane layers than K^+ ions. At the end of the simulation, 6, 9, 11, 6 and 6 K^+ ions remained within the layers of the GO-10-K, GO-15-K, GO-20-K, GO-10-K-10P and GO-10-K-12P membranes, respectively. Likewise, the

GO-10-M, GO-15-M, GO-20-M, GO-10-M-10P and GO-10-M-12P membranes have 9, 11, 13, 9 and 9 Mg^{2+} ions, respectively. The movies are created to visualize the mobility of intercalated cations within the GO laminates during the simulations, and a link is provided(click here).

4.3.5 Draw solute rejection

The draw solution is a 1:2 molar ratio of choline chloride and ethylene glycol solution. It contains 536 choline molecules, 536 chloride ions, 1070 ethylene glycol molecules, and 11200 water molecules. In the time scale of the simulation, we didn't observe any complete permeation of either choline or ethylene glycol, or chloride ions from the draw solution. This indicates that the present membrane systems are good at draw solute rejection, which is also an important requirement of an ideal FO membrane. However, few ions are intercalated within the GO laminates. The percentages of the intercalated chloride ions, choline, and ethylene glycol for all membranes (at the end of the simulations) are provided in Table.4.2. It indicates that the intercalation of chloride ions increases as quantity of K^+ and Mg^{2+} ions increases. By contrast, the intercalation of the choline and ethylene glycol decreases as quantity of K^+ and Mg^{2+} ions increases. Moreover, the intercalation of choline, chloride ions, and ethylene glycol increases with increasing the membrane's pore width.

4.3.6 Comparative water permeance of polymeric FO membranes in oil-water separation

The water permeance of a few commercial polymeric FO membranes utilized for oil-water separation is presented in Table.4.3. The water permeance reported in Fig.4.2 is higher compared to the water permeance of the experimental FO investigations. Typically, the water permeance obtained in atomistic simulations [71, 82, 83] is higher than the experimental observations [185, 202–204] due to considerations of the physical characteristics of the membrane, such as its thickness. In atomistic simulations, the thickness of the membranes is a few nm, whereas, in experimental studies, it could be a few microns. Typically, the water permeance of the membranes decreases with the increase in thickness of the membranes [205–207]. Consequently, the membranes via atomistic simulations showed higher water permeance due to the ultra-thin membrane structure. After scaling, the water permeance obtained in an atomistic simulation to the micron length scale indicates that the GO membranes as FO membranes exhibited higher

Table 4.2: Percentages of the intercalated chloride ions, choline, and ethylene glycol for all membranes.

Name of the membrane	Chloride ions (%)	Choline (%)	Ethylene glycol (%)
GO-10-K	2.24	3.36	4.29
GO-15-K	2.43	2.61	3.83
GO-20-K	2.98	2.24	3.45
GO-10-M	2.61	3.73	5.60
GO-15-M	2.98	3.17	4.76
GO-20-M	3.73	2.61	3.73
GO-10-K-10P	4.29	4.29	5.89
GO-10-K-12P	5.97	5.78	6.54
GO-10-M-10P	5.41	5.59	6.54
GO-10-M-12P	7.27	7.08	7.75

water permeance than the polymeric FO membranes.

4.4 Conclusions

This study focuses on the effect of cationic concentration on water permeance and the salt rejection mechanism of the cation intercalated GO membranes. In this work, nonequilibrium MD simulations are performed using cation intercalated GO membranes with shale gas wastewater as the feed solution. We observed that the presence of more number of cations inside the GO laminates causes resistance to water mobility, leading to lower water permeance. This study also reveals that Mg^{2+} ions have stronger interactions with the GO nanosheets than K^+ ions. Thus, Mg^{2+} ion intercalated GO membranes maintained a more stable interlayer distance than K^+ ion intercalated GO membranes. In contrast, increasing cation concentration inside the GO layers increases Na^+ rejection but decreases Cl^- rejection.

Although higher concentration of intercalated cations aren't favoring the water permeance,

Table 4.3: The comparative water permeance of polymeric FO membranes in oil-water separation.

Name of the membrane	Water permeance (Kg m^{-2} h^{-1})	Crude oil concentration (ppm)	Draw solution
HTI-TFC [185]	4.8 ± 0.2	100	4.8 M $MgCl_2$
HTI-TFC [185]	2 ± 0.1	100	4.8 M LiCl
HTI-CTA [202]	14	219.7	4.44 M NaCl
HTI-CTA [202]	2	552.4	0.85 M NaCl
PAN-TFC [203]	16.5 ± 1.2	500	1 M NaCl
PAN-TFC [203]	11.8 ± 1.6	200,000	1 M NaCl
TFC-CTA [204]	25.5 ± 2.5	200	2 M NaCl
TFC-CTA [204]	12.5 ± 2.5	200	0.58 M NaCl
TFC-CTA [204]	23 ± 2.0	100,000	2 M NaCl
TFC-CTA [204]	12.5 ± 2.0	100,000	0.58 M NaCl

presence of the cations stabilize the GO laminates. Our simulation results emphasize that the water permeance and salt rejection trade-off of GO-based membranes can be better understood by tuning the concentration of intercalated cations. This study suggests that membranes should maintain an optimum concentration of cations to resolve the water permeance and salt rejection trade-off. Besides the membrane performance, this study also explains the stability of crude oil aggregation, which is significant for shale gas wastewater treatment. The nature of the crude oil aggregation phenomena varies for different cation intercalated GO membranes, and it needs to be investigated further. In this study, crude oil aggregation is stable for K^+ ion intercalated GO membranes due to their weaker interactions of K^+ ions with crude oil. In contrast, crude oil aggregation forms closer to the surface of Mg^{2+} ion intercalated GO membranes owing to their higher water permeance and stronger interactions of Mg^{2+} ion with crude oil. Moreover, Aromatics are more concentrated at the surface of the crude oil-water mixture (for all membranes) due to lower interfacial tension of aromatics-water.

In continuation to this study, it would be interesting to investigate the separation of surfactant stabilized oil water mixtures. Along with this, the performance of this cation intercalated membrane with different draw and feed solution combinations could also be investigated. The observations reported in this study would be crucial in designing layered GO membranes for various separation and purification applications.

Chapter 5

Understanding the boron rejection of cation intercalated multilayered graphene oxide (GO) membrane in reverse osmosis (RO) process: A Molecular Dynamics study*

5.1 Objective

Water scarcity is a severe concern with the growing global population and industrialization. As the oceans cover nearly 71% of the earth's surface, desalination of saline water is a prominent solution for water scarcity [1, 2]. As a result, the world is advancing towards desalinating seawater to deliver clean water for all living species. Researchers have developed several technologies in the past decade to draw pure water (or salt removal) from seawater. However, these technologies are ineffective in removing low-concentrated contaminants such as boron [3, 4]. In the aquatic environment, boron can be present in the form of boric acid or borate ion, depending on the pH of the solution; as a result, this study considers two forms of boron to investigate

*Reddy, P. Rajasekhar, Amit Kumar, and K. Anki Reddy. "Understanding the boron rejection of cation intercalated multilayered graphene oxide (GO) membrane in reverse osmosis (RO) process: A molecular dynamics study." Journal of Molecular Liquids 389 (2023): 122817.

the boron rejection mechanism.

Physical sieving (size exclusion) and electrostatic interactions are the two primary rejection mechanisms of membrane-based separation methods [47, 116, 120, 121]. A few studies explain the mechanism of boron rejection based on physical sieving, size, shape, and type of the pores (hydrophilic or hydrophobic) for membranes[116–119, 122–124]. However, the literature does not discuss the role of electrostatic interactions in boron removal. Moreover, the rejection of boron by GO membranes (as RO membranes) employing non-equilibrium MD simulations hasn't been studied to date. This study provides information on boron rejection from saline water using cation-intercalated GO membranes through the RO separation process via MD simulations, including neutral (boric acid) and negatively charged (borate ion) boron species. Factors governing the relative transport and rejection mechanisms of boric acid and borate ion in the RO separation technique through GO membranes are comprehensively discussed. Further, the effects of the intercalated cations placed within the GO laminates on boron rejection are explained in detail. The article also presents the comparative water permeance and salt rejection of cationic intercalated GO membranes.

5.2 Methodology

5.2.1 Cation-intercalated GO membrane

This study investigated the boron rejection mechanism by using multilayered cation (K^+ or Mg^{2+}) intercalated GO membranes. The cation-intercalated GO membranes are constructed corresponding to the procedure mentioned below. Firstly, two distinct sizes of GO nanosheets (40×48 Å^2 and 31×48 Å^2) are created by considering the Lerf and Klinowski model [182] using a visual molecular dynamics (VMD) [180] and Avogrado [181], where the oxygen-containing functional groups are randomly distributed. According to this model, the basal plane of the GO nanosheets predominantly consists of epoxy and hydroxyl functional groups, while carboxyl functional groups are at the edges (Figure.5.1(a)). The chemical composition of the GO nanosheets is $C_{10}O_1(OH)_1(COOH)_{0.5}$ [82, 83, 183, 208], considering the typical C/O ratio (2.0-4.0) reported in the literature[209–211]. Then, multilayered GO membranes (Figure.5.1(b)) are assembled using these GO nanosheets by taking account of geometric parameters of membranes such as pore width (P), offset (O), and interlayer distance (I). All membranes have the

same value of O, which is 8 Å [83]. Whereas three different P values are considered, and they are 8, 10, and 12 Å. The value of I varies with the intercalated cation within the GO layers, corresponding with Chen et al.'s work [70]. Accordingly, the I value for K^+ and Mg^{2+} ions is 11.4 and 13.9 Å, respectively. In Chen et al.'s work[70], GO membranes are immersed in various salt solutions of a 0.25 M concentration to analyze the stability of interlayer distances in GO membranes under different salt solution environments. We found that the present study requires ten intercalated cations within the interlayer gallery of GO membranes to represent the concentration mentioned in the above experimental study. Hence, we randomly placed ten cations (K^+ or Mg^{2+}) within the interlayer gallery of the multilayered GO membrane to construct the cation-intercalated GO membranes. It is then hydrated with an equilibrated water box, and details of all membranes are provided in table.5.1.

Table 5.1: Cation-intercalated GO membrane configurations and their corresponding nomenclature.

Name of the membrane	Ion type	I(Å)	P(Å)
GO-K-8P	K^+	11.4	8
GO-K-10P	K^+	11.4	10
GO-K-12P	K^+	11.4	12
GO-M-8P	Mg^{2+}	13.6	8
GO-M-10P	Mg^{2+}	13.6	10
GO-M-12P	Mg^{2+}	13.6	12

5.2.2 RO Simulation system

A typical RO simulation system consists of a feed solution, a semi-permeable membrane, and a permeate. This study considered three distinct feed solutions. The feed solution1 comprises 60 Na^+ ions, 15 Mg^{2+} ions, 90 Cl^- ions, 15 Boric acid molecules, and 30000 water molecules. The feed solution2 consists of 65 Na^+ ions, 20 Mg^{2+} ions, 90 Cl^- ions, 15 Borate ions, and 30000 water molecules. The feed solution3 contains 64 Na^+ ions, 17 Mg^{2+} ions, 90 Cl^- ions, 8 Boric acid molecules, 8 Borate ions, and 30000 water molecules. For all RO simulation systems, the

hydrated multilayered GO membrane is positioned between the feed and permeate regions, as shown in the figure.5.1(c). Additionally, graphene sheets are placed at the end of the feed, permeate regions, and act as pistons. Furthermore, a vacuum of 30 Å is provided on the top and bottom of all RO simulation systems in the Z-direction. In addition, feed and permeate pistons are subjected to pressures of 10 MPa and 1 atm, respectively.

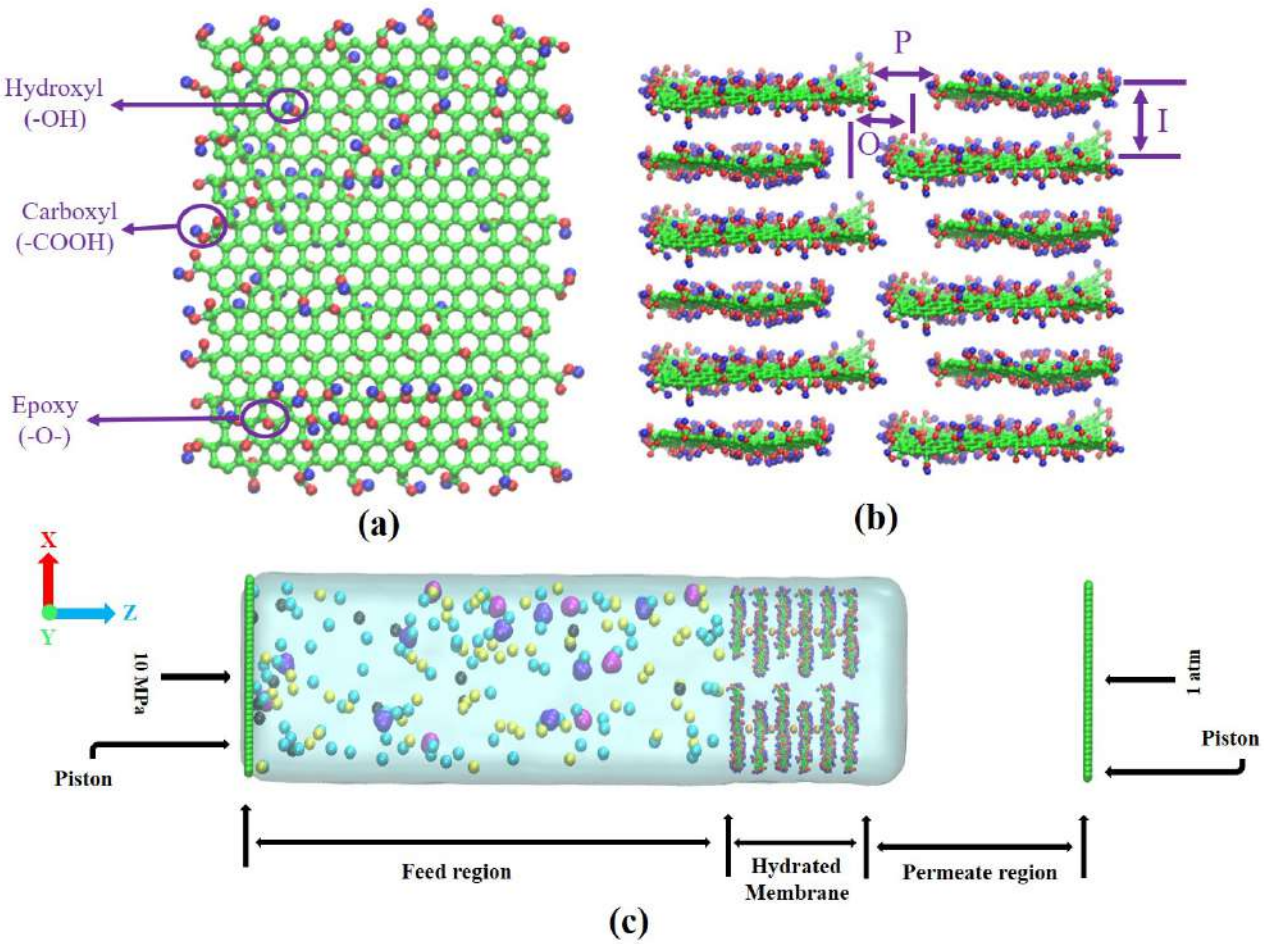

Figure 5.1: (a) GO nanosheet. (b) Multilayered GO membrane. (c) RO simulation system. Green color is for carbon atoms, red color is for oxygen atoms, blue color is for hydrogen atoms, yellow color is for Na^+ ions, cyan color is for Cl^- ions, black color is for Mg^{2+} ions, orange color is for K^+ ions, magneta color for boric acid, and violet color for borate ions.

5.2.3 Simulation Methodology

All MD simulations in this study are carried out using LAMMPS package [212]. The parameters utilized for the GO nanosheets are adapted from an article entitled "Computational Charac-

terisation of Dried and Hydrated Graphene Oxide Membranes," published in Nanoscale[213]. The authors of this study employed the CHARMM forcefield to model bonded and non-bonded interactions of GO flakes[214]. Density functional theory (DFT) calculations were performed using Gaussian 09 at the B3LYP/6-31+G* level of theory to determine partial charges of the GO atoms[215–218]. The partial charges were obtained via geometry optimization and fitting an electrostatic potential, according to the Merz-Singh-Kollman scheme[219, 220]. The parameters utilized for boric acid are adapted from the article [118] "Fundamental Insights on Hydration Environment of Boric Acid and Its Role in Separation from Saline Water." The authors used the Force Field Toolkit (ffTK) in VMD for boric acid parametrization [221]. Molecular mechanics (MM) calculations were performed to replicate quantum mechanics (QM) data obtained at the MP2/6-31G(d) and HF/6-31G(d) levels of theory using Gaussian03 [222]. Bonded parameters [[in CHARMM format]] were derived from the QM Hessian, while dihedral parameters were fitted to QM potential energy scans in 15° increments. Therefore, in the present study, we employed these pre-validated parameters. The CHARMM forcefield parameters are used for the remaining atomic species[214]. The van der Waals interactions are computed using the Lennard-Jones potential with a cutoff distance of 12 Å. The particle-particle particle-mesh method is employed to calculate the long-range electrostatic interactions. Water molecules are represented using the TIP3P water model [162]. After constructing the RO simulation system, we performed an energy minimization followed by equilibration at a constant temperature of 300 K for 0.5 ns. Subsequently, production runs of 30 ns with a timestep of 1 fs are performed with periodic boundary conditions in all three directions. The Nose-Hoover thermostat is employed to maintain a constant temperature in the simulations with a damping factor of 50 fs. All atomic trajectories are saved for every time interval of 20 ps. During the production runs, a few selected carbon atoms positioned at the corner and non-bonded to any oxygen-containing functional groups of GO nanosheets are fixed to maintain a layered structure of the membrane [198, 199]. The reported results in the subsequent section are averaged over three simulations with different initial configurations [71, 83, 119].

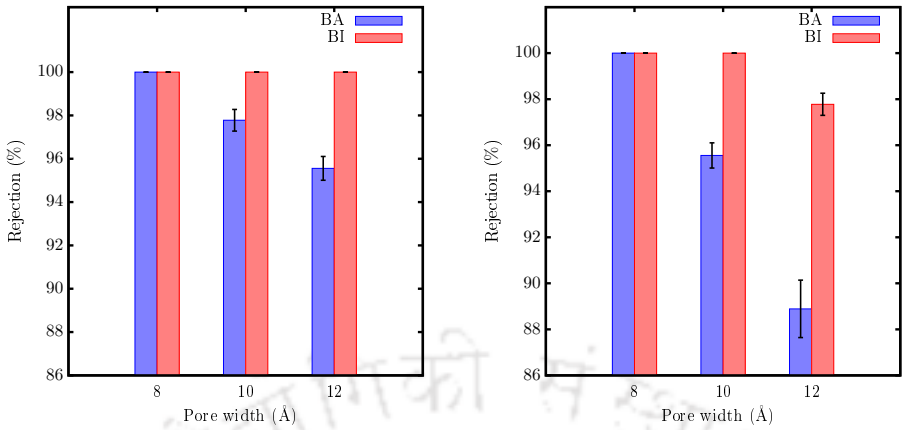

(a) (b)

Figure 5.2: Boric acid (BA) and borate ions (BI) rejections of (a) K^+ ion intercalated GO membranes and (b) Mg^{2+} ion intercalated GO membranes.

5.3 Results and discussion

5.3.1 Rejection mechanisms of Boric acid and Borate ion

Figure.5.2 presents the rejection of the boric acid (BA) and borate ion (BI) of the K^+ and Mg^{2+} ion intercalated GO membranes as a function of their pore width. Rejection (in %) is defined as:

$$Rejection(\%) = \frac{C_f - C_p}{C_f} \times 100 \tag{5.1}$$

In the above equation, C_f is the concentration of species in the feed, and C_p is the concentration of species in the permeate.

As shown in the figure.5.2 (a), K^+ ion intercalated membranes exhibit declining BA rejection and constant BI rejection (100%) with increasing pore width. Besides, the Mg^{2+} ion intercalated membranes also display decreasing BA rejection and changing BI rejection with increasing pore width, as shown in the figure.5.2 (b). In other words, the BI rejection of K^+ and Mg^{2+} ion intercalated membranes is greater than the BA rejection. It can be attributed to the electrostatic interaction of the membranes with BA and BI [124]. Inherently, GO membranes had a slightly negative charge, inducing a stronger electrostatic repulsion with the BI, leading to a better BI rejection.

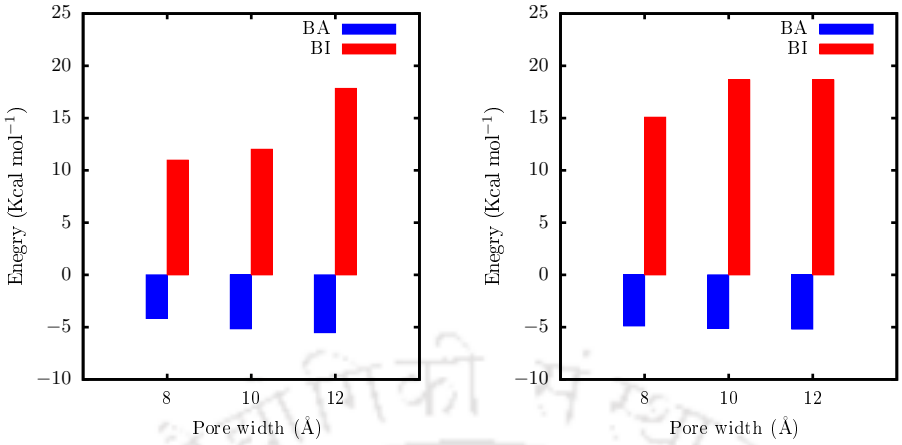

Figure 5.3: The average interaction energies of BA and BI with (a) K^+ ion intercalated GO membranes and (b) Mg^{2+} ion intercalated GO membranes.

The electrostatic interaction energy of both kinds of membranes with BA and BI is presented in figure.5.3. These plots indicate that BI has a stronger electrostatic repulsion than BA due to its negative charge. Moreover, the electrostatic repulsion of BI with membranes gets stronger as the pore width of the membranes increases. The reason could be that with an increase in the pore width, the chances of BI entering the membrane are higher, leading to greater interactions with the membranes. However, 100% BI rejection is attained due to their stronger electrostatic repulsion with the membranes (except for GO-M-12P membrane). BA rejection decreases as its experiences weaker electrostatic repulsion with the membranes.

To further understand the rejection mechanism, the density plots of the BA and BI for all membranes are presented in figure.B.31. According to figures.B.31(a) and (b), a few BA molecules permeated through GO-K-10P and GO-K-12P membranes, but none for the GO-K-8P membrane. However, no BI molecules permeated through K^+ ion intercalated GO membranes. As shown in figures.B.31(c) and (d), a few BA molecules permeated through GO-M-10P and GO-M-12P, but none for the GO-M-8P. Moreover, no BI molecules permeated through the GO-M-8P and GO-M-10P, but one BI molecule permeated through the GO-M-12P membrane. These plots also indicate that BA rejection decreases with increasing the pore width of the membrane. However, BI molecules are greatly rejected by all membranes even though the pore width of the membranes increases, which can be attributed to their greater electrostatic repulsion with the membranes.

These density plots also indicate that the intercalation of both BA and BI molecules inside the GO laminates increases with an increase in the pore width of the membranes. According to Banasiak et al., [223] BA molecules are poorly hydrated than BI molecules. It means that hydrated BA molecules are smaller than hydrated BI molecules in size. As a result, BA molecules can permeate more quickly through the membrane than BI molecules. However, BA molecules have a stronger interactions with the hydroxyl functional groups of the GO membrane (positioned on the basal plane), causing resistance to faster permeation through the GO layers [119, 224]. Therefore, despite membranes having a higher intercalation percentage, the greater interactions of BA molecules with hydroxyl groups of the membranes prevents the permeation through the membrane, causing a superior BA rejection.

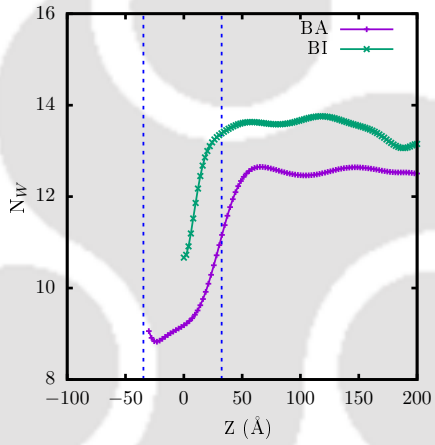

(a)

Figure 5.4: Changes in the number of water molecules (N_W) in the hydration shell of both BA and BI along its pathway. Here, dotted lines indicate the membrane position.

The changes in the number of water molecules (N_W) in the hydration shell of both BA and BI along its pathway are presented in figure.5.4. Here, dotted lines indicate the membrane position. As shown in the figure.5.4, BI has more water molecules than BA at any position during permeation through the membrane. It signifies that hydrated BI is bigger in size than hydrated BA. In addition, the snapshots of these hydration shells at various positions are shown in figure.5.5. Water molecules within the radius of hydration shells from the center of permeating BA and BI are shown in CPK representations (VMD). GO membrane atoms are shown in VDW representations (VMD) within 20 Å from the center of permeating BA and BI. These snapshots also indicate that the hydration shell of BI is bigger than BA. Moreover, the

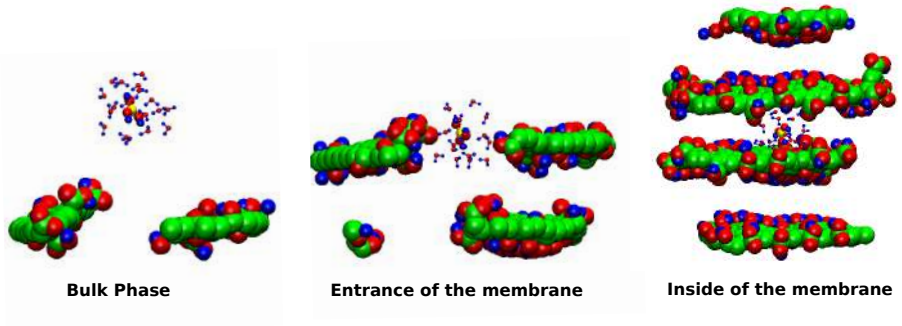

(a)

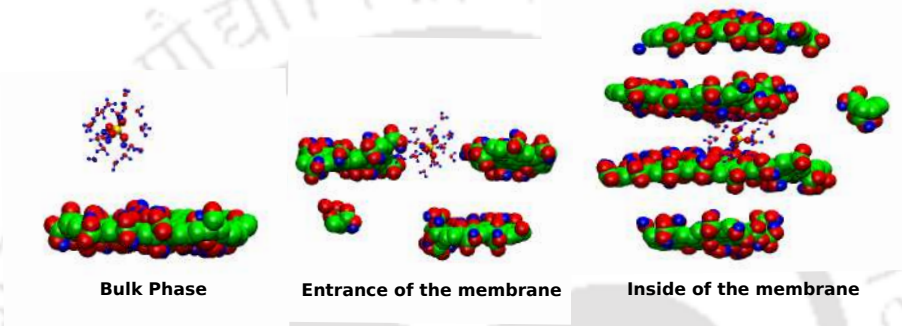

(b)

Figure 5.5: The number of water molecules in hydration shells of (a) BA and (b) BI at various positions during the permeation through the membrane. Green color is for carbon atoms, red color is for oxygen atoms, blue color is for hydrogen atoms, and yellow color is for boron atoms.

hydration shell shrinks at the entrance of the membrane due to stronger interactions of water molecules and oxygen-containing functional groups of the GO membrane and the shrinkage is more for BA molecules, which results in lower BA rejection.

The radial distribution function (RDF) and interaction energies are provided to understand the BA rejection mechanism at the atomistic level. The RDF of water molecules (OT) with BA molecules and oxygen functional groups (OFGs) of the membranes are presented to study the hydration shell of BA molecules while permeating through the membrane. Figure.5.6(a) illustrates that water molecules interact more strongly with carboxyl functional groups (O4-OT) than BA molecules (BA-OT). Due to stronger interactions of water molecules with carboxyl functional groups, the hydration sphere of BA molecules shrinks, resulting from dehydration, and causes it easier for BA molecules to enter the membrane.

Although BA molecules are weakly hydrated, GO membranes exhibited a significant rejection (for a larger pore width) owing to stronger interactions of BA molecules with OFGs. The

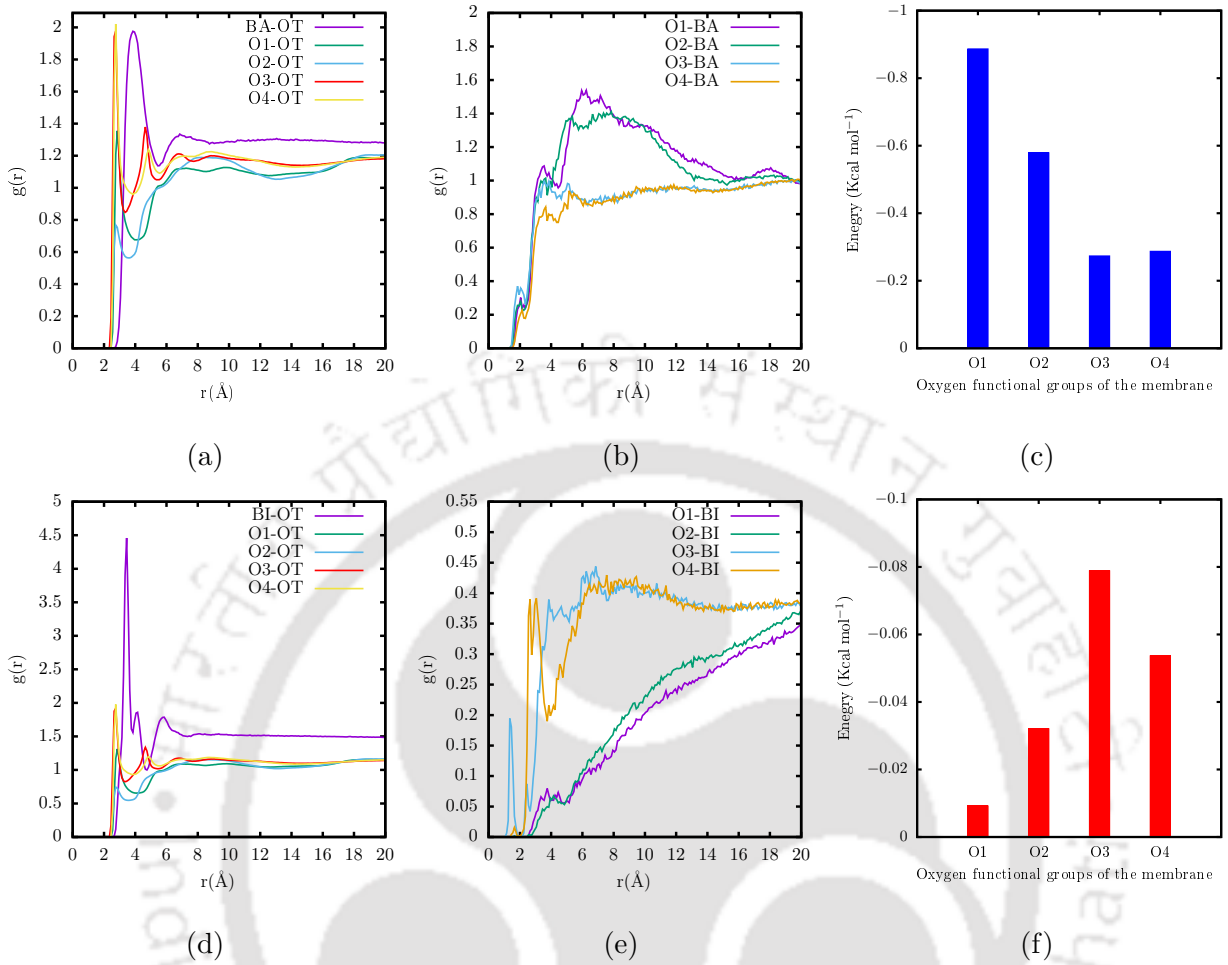

Figure 5.6: (a) The radial distribution function (RDF) of water molecules (OT) with BA and oxygen-containing functional groups (OFGs) of the membrane. The RDF (b) and interaction energies (c) of BA with OFGs. (d) The RDF of water molecules (OT) with BI and OFGs. The RDF (e) and interaction energies (f) of BI with OFGs. Here O1, O2, O3, and O4 are the oxygen atoms of a hydroxyl group (-OH), epoxy group (-O-), carboxyl group, which is linked to only C atom (-C=O), and carboxyl group that is bonded to C and H atoms (C-O-H), respectively.

RDF of BA molecules with OFGs of the GO membrane is represented in figure.5.6(b). The plots show that hydroxyl and epoxy functional groups interact more with BA molecules than carboxyl functional groups. The interaction energies of the BA molecules with OFGs of membranes are also calculated to know which OFGs are preventing BA molecules from permeating through a membrane. As shown in the figure.5.6(c), hydroxyl and epoxy functional groups cause resistance to BA molecule's permeation through the membranes because of their stronger electrostatic interactions with the BA molecules. Therefore, the stronger interactions of BA

molecules with the hydroxyl and epoxy functional groups lead to a better BA rejection despite their poorly hydrated nature.

According to figure.5.2, all membranes achieved higher BI rejection than BA rejection due to the bigger hydrated shell of BI than BA. Figure.5.6(d) shows the RDF of water molecules with BI and OFGs of membranes for analyzing the hydration shell of BI at the atomistic level. The plots signify that water molecules interact more with BI than OFGs of the membrane. It means that the water molecules belonging to the hydration sphere are intact with BI while permeating through the membranes. Thus, all membranes reject BI more effectively than BA.

As shown in figure.B.31, a few BI are intercalated inside the GO layers for the membranes consisting of wider pores. Yet, all membranes attained 100% rejection (expect for GO-M-12P membrane) due to their stronger interactions with the OFGs of the membrane, which are causes for the declining diffusion rate of BI. The RDF and interaction energies of the BI with the OFGs of the membranes are reported to discuss which OFGs are restricting the permeation rate of BI. Figure.5.6(e) displays the RDF of BI with the OFGs of the membrane. These plots reveal that BI interact more strongly with carboxyl functional groups than hydroxyl and epoxy functional groups. Contrary to BA molecules, carboxyl functional groups are responsible for preventing the permeation of BI through the membrane. The interaction energies of the BI with the OFGs are presented in figure.5.6(f). These plots also confirm that BI interact more with the carboxyl functional groups than other functional groups. Therefore, carboxyl functional groups of membranes and the bigger hydrated shell of BI are helping towards better BI rejection.

The influence of intercalated ions (K^+ or Mg^{2+}) on the rejection of BA and BI is reported using their electrostatic interaction energies. As shown in the figure.5.2, K^+ ion intercalated GO membranes exhibited a higher BA rejection than the Mg^{2+} ion intercalated GO membranes. Figure.5.7(a) shows the electrostatic interaction energies of intercalated ions with BA molecules for both types of membranes with a pore width of 12 Å. It implies that the GO-M-12P membrane has stronger electrostatic attraction with BA molecules than the GO-K-12P membrane. Consequently, the GO-M-12P membrane draws the BA molecules into the GO channels, resulting in lower BA rejection than the GO-K-12P membrane. As seen in figure.5.2, all membranes except the GO-M-12P membrane achieved a 100% BI rejection. The electrostatic interaction energies of intercalated ions with the BI for GO-K-12P and GO-M-12P membranes are presented in figure.5.7(b). From this figure, the GO-K-12P membrane has a slightly weaker electrostatic attraction than the GO-M-12P membrane, causing a slight difference in BI rejection. Therefore,

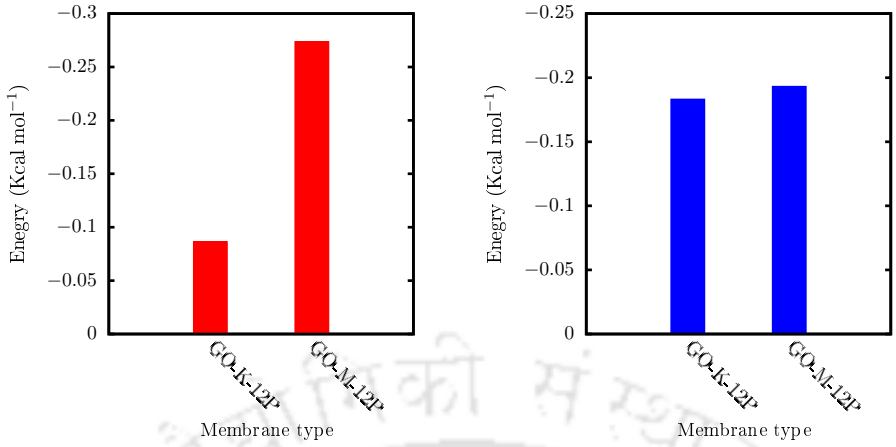

Figure 5.7: The average interaction energies of intercalated ions (K^+, Mg^{2+}) with (a) BA and (b) BI for GO-K-12P and GO-M-12P membranes.

the intercalated ions also have a significant role in rejecting BA and BI.

In addition, we examined the relative rejection of BA and BI (for feed solution3, where both BA and BI are present) for GO-K-10P and GO-M-10P membranes. Neither BA nor BI permeated through either of the membranes during the simulation time. However, few BA and BI intercalated within the membrane layers. The intercalation percentage of BA and BI for GO-K-10P and GO-M-10P membranes is presented in figures.B.32(a) and (b), respectively. According to these figures, the BI intercalation percentage of both membranes does not significantly differ. However, the GO-M-10P membrane has a higher BA intercalation percentage than the GO-K-10P membrane. As explained earlier, K^+ ions have a weaker electrostatic attraction with BA molecules than Mg^{2+} ions. Hence, the GO-M-10P membrane has a higher BA intercalation percentage than the GO-K-10P membrane. Furthermore, the trajectories of a few selected BA and BI are depicted in the figure.B.33(a) and (b), respectively. The trajectory analysis indicates that the BA molecules are more mobile than the BI molecules within the layers of the GO membrane, which could also be a potential reason for lower BA rejection.

5.3.2 Water permeance and salt rejection

The comparative performance of the membranes is explained in this section in terms of water permeance and salt rejection. The water permeance of all membranes is reported in figure.5.8. As expected, the water permeance of the membrane increased with the increasing membrane's

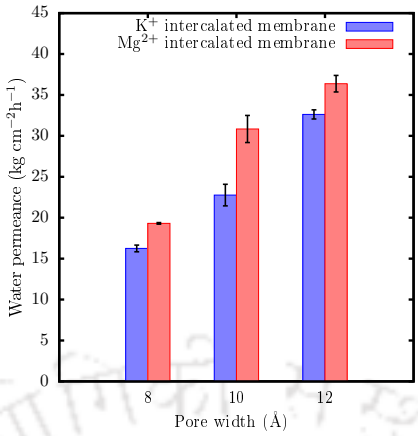

(a)

Figure 5.8: The water permeance of all membranes.

pore width. As a result, GO-K-12P and GO-M-12P membranes exhibited higher water permeance compared to other membranes considered in this study. However, the water permeance of Mg^{2+} ion intercalated GO membranes is higher than K^+ ion intercalated GO membranes due to the larger interlayer distance. The changes in the number of water molecules (N_P) in the permeate with the simulation time are presented in figure.B.34. Water permeance is calculated as follows:

$$Water\ permeance = \frac{V}{A \times t} \tag{5.2}$$

In the above equation, V represents the overall volume of water molecules that have passed through the membrane, A denotes the surface area of the membrane, and t corresponds to the simulation time.

In addition to assessing the water permeance of GO membranes, we investigated the water dynamics within the membranes using two-dimensional (2D) mass density maps of water molecules and water density profiles along the Z-axis. Figure.5.9 illustrates the 2D mass density maps of water molecules for GO membranes intercalated with K^+ (a-c) and Mg^{2+} (d-f) ions. The observed density maps reveal that Mg^{2+} ion intercalated membranes have a higher density of water molecules within the GO layers compared to K^+ ion intercalated membranes. The reason could be the higher interlayer distance in the Mg^{2+} ion intercalated membranes provides a greater free pore volume for water permeation (or lower water resistance) than the K^+ ion intercalated membranes. Consequently, Mg^{2+} ion intercalated membranes draw more

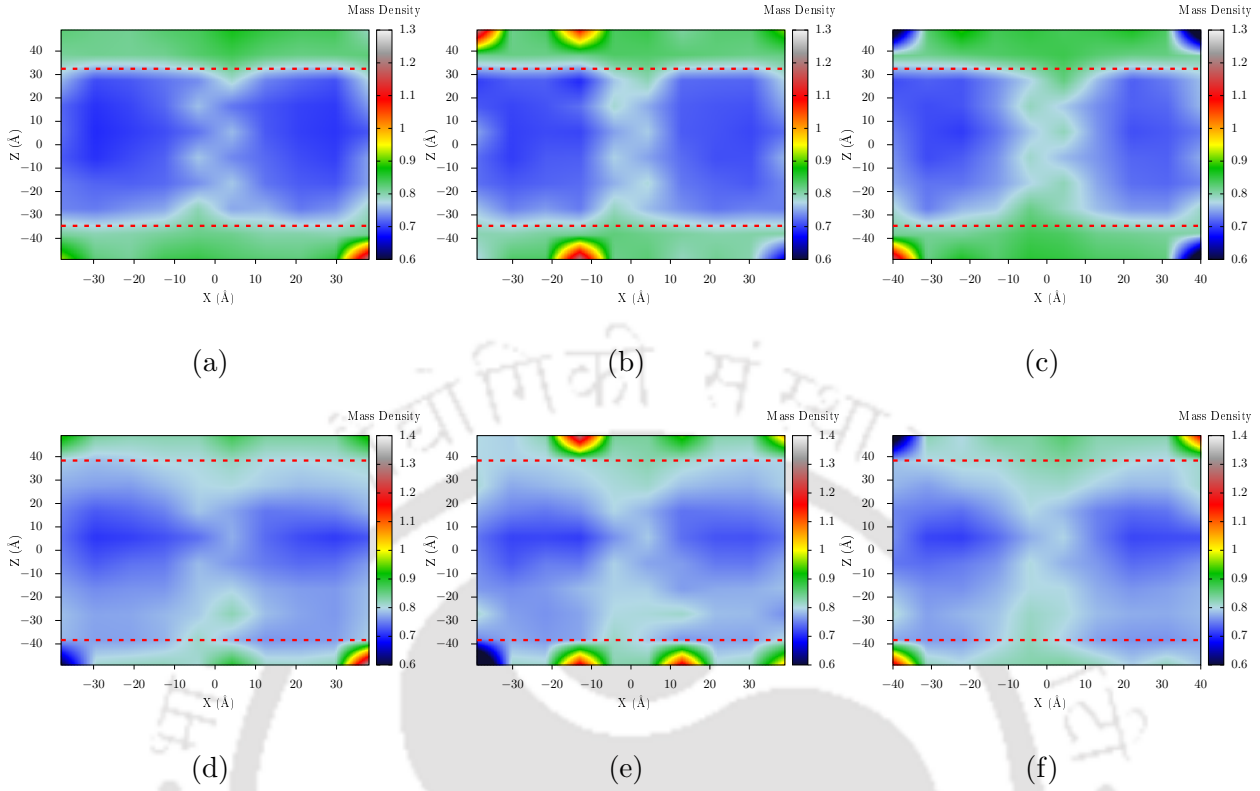

Figure 5.9: The 2D mass water density maps in the simulation systems. (a) GO-K-8P, (b) GO-K-10P, (c) GO-K-12P, (d) GO-M-8P, (e) GO-M-10P, and (f) GO-M-12P.

water molecules into their layers, resulting in higher water permeance than the K^+ ion intercalated membranes. Additionally, the 2D density maps revealed that as the pore width of the membranes increases, the pathway available for water permeation through the membrane layers becomes wider, resulting in higher water permeance. Water density profiles along the Z-axis are presented in Figure.B.35(a) and (b) to further understand the water density variations within the same ion-intercalated membranes. These density plots indicate that an increase in the pore width of the membranes leads to higher water density within the GO laminates, corresponding to an increased free pore volume. As a result, increasing the pore width of both ion-intercalated membranes leads to higher water permeance.

The comparative water permeance and boron rejection of a few commercial polymeric and graphene based membranes are presented in Table.B.1. Comparing one-to-one membranes is difficult due to differences in experimental systems, including varying thicknesses and free pore volumes. Nevertheless, observations indicate that GO membranes completely reject boron within a given simulation time scale while exhibiting reasonably better water permeance when

compared to other membrane systems.

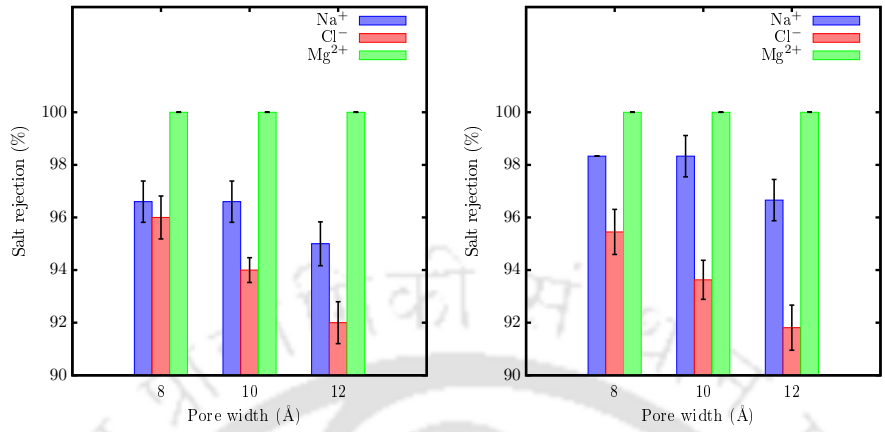

Figure 5.10: Salt rejection percentages of (a) K^+ ion intercalated GO membranes and (b) Mg^{2+} ion intercalated GO membranes.

The salt rejection percentages of K^+ ion and Mg^{2+} ion intercalated GO membranes are shown figure.5.10 (a) and (b), respectively. As seen in figures.5.10(a) and (b), all membranes delivered 100% Mg^{2+} rejection. On the other hand, with an increase in the pore width of the membrane, the rejection of Na^+ and Cl^- ions decreases. In comparison to Mg^{2+} ion intercalated GO membranes, K^+ ion intercalated GO membranes showed poor Na^+ rejection and excellent Cl^- rejection. The 2D mass density maps and density profiles of salt ions of all membranes is presented in figures.B.36, B.37, and B.38. These plots also indicate that all membranes rejected all Mg^{2+} ions, and as membrane pore width increases, the rejection of Na^+ and Cl^- ions decreases.

As explained earlier, K^+ ion intercalated GO membranes delivered lower Na^+ rejection and superior Cl^- rejection over Mg^{2+} ion intercalated GO membranes. It exposes that the intercalated ions within the GO layers influence the salt rejection mechanism of the membrane. To further understand the impact of intercalated ions on salt rejection, the electrostatic interactions of these ions with salt ions are presented in figure.5.11. As shown in figure.5.11(a), the GO-M-12P membrane has a greater electrostatic repulsion with Na^+ ions than the GO-K-12P membrane. It indicates that Mg^{2+} ion intercalated membranes reject more quantity of Na^+ ions than the K^+ ion intercalated membranes. Figure.5.11(b) shows that the GO-K-12P membrane has a weaker electrostatic repulsion with Cl^- ions than the GO-M-12P membranes. It

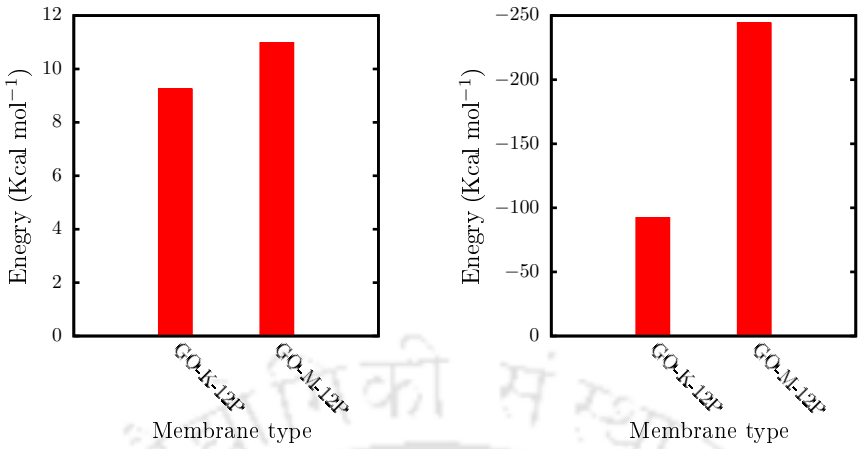

Figure 5.11: The average interaction energies of intercalated ions (K^+, Mg^{2+}) with (a) Na^+ and (b) Cl^- ions for GO-K-12P and GO-M-12P membranes.

signifies that K^+ ion intercalated membranes reject Cl^- ions significantly better than Mg^{2+} ion intercalated membranes.

5.3.3 Intercalated ions distribution

The percentage of intercalated ions within the GO laminates as a function of the simulation time is represented in figures.5.12(a) and (b) for K^+ ion intercalated and Mg^{2+} ion intercalated GO membranes, respectively. As shown in figures.5.11(a) and (b), the percentage of remaining ions within the GO layers decreases with the time scale of the simulation. Figures.5.12 also displays that for both kinds of membranes with pore widths of 8 and 10 Å, there is no substantial percentage difference of resident ions within GO layers. However, this percentage drops significantly for a pore width of 12 Å. Moreover, during the time scale of the simulation, a higher percentage of Mg^{2+} ions stayed within the GO laminates than the K^+ ions. It can be attributed to the mobilitity of intercalated ions within the GO layers. To investigate this further, the RDF of these intercalated ions with the oxygen atom of the water molecules is computed. As shown in figure.5.12(c), Mg^{2+} ions interact more strongly with the water molecules than the K^+ ions. It means that compared to the hydration sphere of K^+ ions, the hydration sphere of Mg^{2+} ions is relatively stable and holds more water molecules. As a result, Mg^{2+} ions move slower across the GO layers than K^+ ions. Accordingly, at the end of the simulation, a higher percentage of the Mg^{2+} ions stayed within the GO laminates than the K^+ ions. The movies depicting the

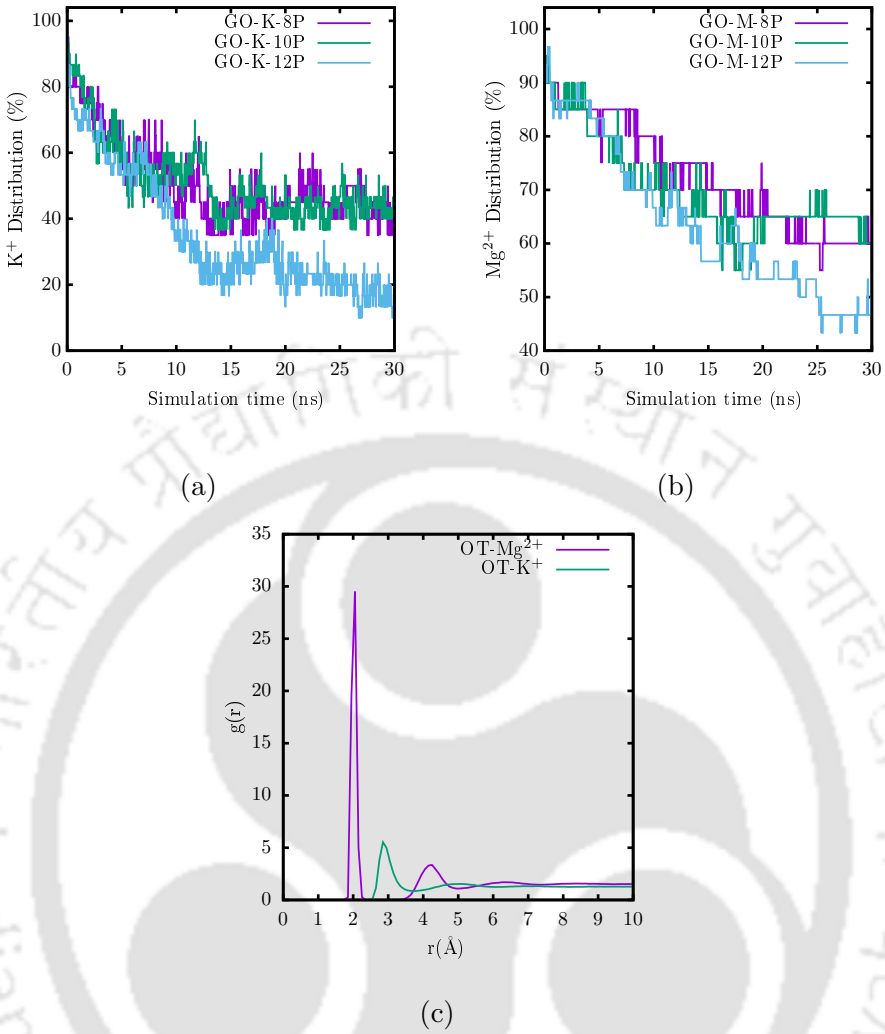

Figure 5.12: (a) K^+ and (b) Mg^{2+} ions distribution inside the GO layers as a function of simulation time. (c) The RDF of intercalated ions with water molecules (OT) within the GO laminates.

motion of cations within the GO channels have been provided (link).

The interlayer distance of a cation-intercalated GO membrane can change as intercalated cations move out of the membrane layers. This problem can be addressed by either preventing the cations from leaving the system or replacing the migrated cations with similar ones from the feed solution. However, the mobility of cations makes it impossible to prevent their migration out of the membrane layers. Therefore, a potential solution for this issue is replacing migrated cations with similar cations. In practical applications, feed solutions (e.g., seawater) contain similar abundant cations that can migrate into the membrane layers and replace the migrating cations. In simulations, as cation substitution is difficult (while a simulation is progressing), we

fixed a few selected carbon atoms of the GO nanosheets to maintain a nearly constant interlayer distance throughout the simulations. In the future, exploring different strategies to extend the retention time of intercalated cations within GO membrane layers will be of great interest in maintaining a consistent interlayer distance.

5.4 Conclusions

In summary, non-equilibrium MD simulations are performed on cationic intercalated GO membranes in RO mode to explore the boron rejection mechanism at the atomistic level. The optimum pore size for boron rejection is proposed by constructing two types of cationic intercalated GO membranes (K^+ or Mg^{2+}) with different pore widths. Boron can be present in the form of boric acid or borate ion, depending on the pH of the solution; as a result, neutral boric acid and negatively charged borate ions are considered in this work to investigate the boron rejection mechanism. This study observed that all membranes reject borate ions effectively when compared to boric acid. The reason is that borate ions hold a bigger hydration shell than boric acid and exhibit stronger electrostatic repulsions with GO membranes. Moreover, K^+ ion intercalated GO membranes favor boron rejection because K^+ ions showed weaker electrostatic attraction with boric acid (or borate ions) than Mg^{2+} ions. Further, the results demonstrated a directly proportional relationship between boron rejection and the intensity of interactions with oxygen-containing functional groups of the GO membrane. Boric acid molecules interact strongly with hydroxyl and epoxy functional groups, whereas borate ions interact strongly with carboxyl functional groups. In addition, boric acid rejection decreases as the pore width of the membrane increases. However, these multilayered cationic intercalated GO membranes delivered better boric acid rejection for wider pores (12 Å) than nanoporous graphene and polymeric membranes. At the same time, all membranes exhibited superior borate ions rejection. Furthermore, compared to Mg^{2+} ion intercalated GO membranes, K^+ ion intercalated GO membranes exhibit greater Cl^- rejection, poor Na^+ rejection, and lower water permeance. The present study provides atomistic insights on boron rejection that can guide experimental study toward a better design of GO-based membranes.

Chapter 6

Urea and ammonia recovery from human urine by forward osmosis (FO) process using cation intercalated graphene oxide (GO) membrane: A molecular dynamics study

6.1 Objective

Human urine, a rich source of valuable compounds such as urea and ammonia (essential feedstock for urea production), requires efficient recovery methods to meet the increasing global demand for urea[23, 28, 125–129, 132–135]. To the best of the author's knowledge, no prior research has explored the application of GO membranes in nitrogen recovery from urine. Moreover, human urine, being a complex solution, prompts an investigation into its treatment via a FO separation technique. Thus, this study aimed to investigate the recovery of urea and ammonia from human urine through the FO separation technique via nonequilibrium MD simulations. Although, GO membranes, known for their efficacy in rejecting smaller molecules, face limitations due to undesirable swelling in aqueous environments. In response, this study uses cationic-controlled GO membranes to mitigate swelling in aqueous environments.

In particular, human urine, existing in fresh and hydrolyzed states, presents distinct nitrogen

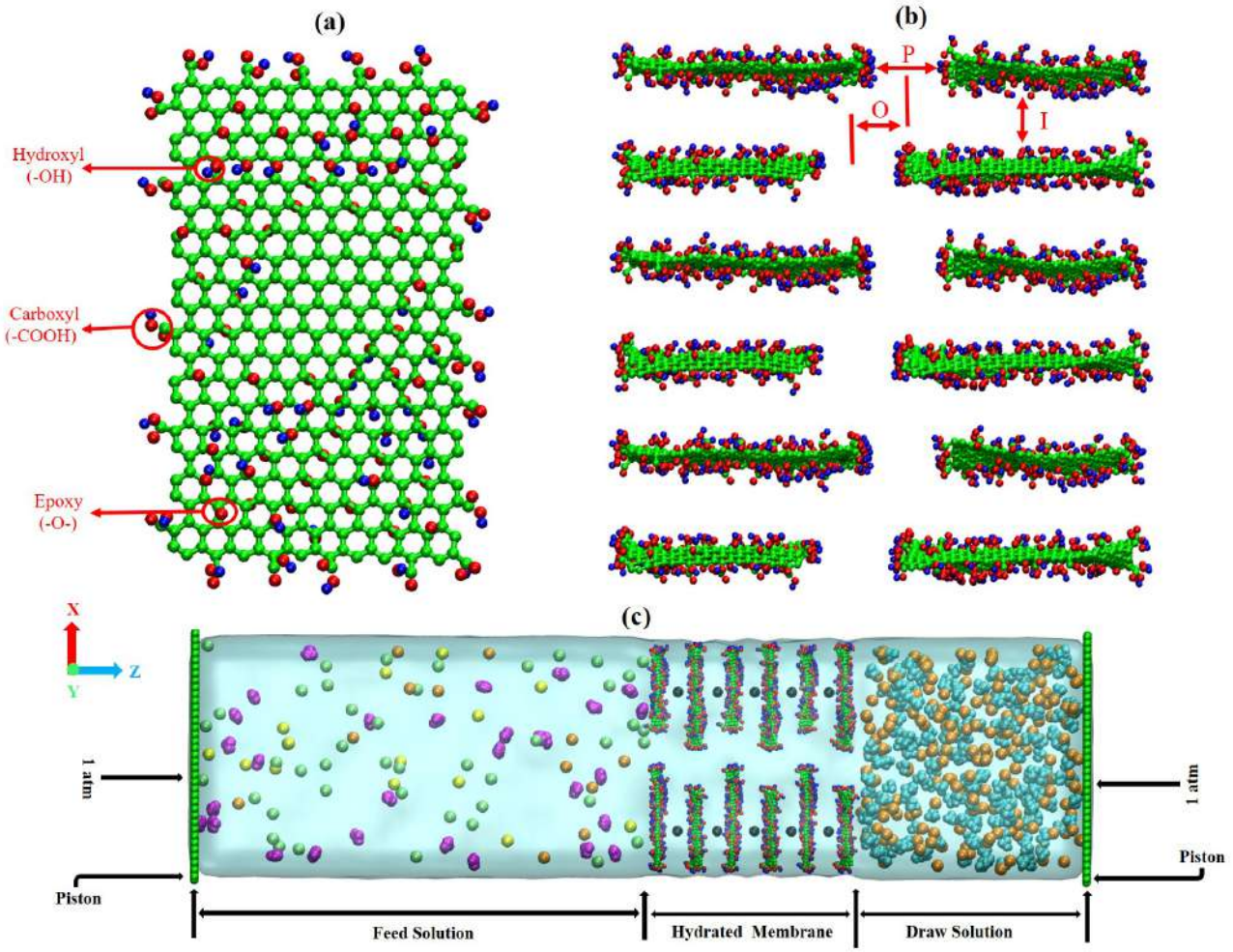

Figure 6.1: (a) GO nanosheet. (b) Multilayered GO membrane. (c) FO simulation system. Green color is for carbon atoms, red color is for oxygen atoms, blue color is for hydrogen atoms, magenta color is for urea, yellow color is for Na^+ ions, orange color is for K^+ ions, lime color is for Cl^- ions, black color is for Mg^{2+} ions, and cyan color is for $H_2PO_4^-$.

forms for recovery. Urea is dominant in fresh urine, and ammonia (NH_3) or ammonium ion (NH_4^+) is dominant in hydrolyzed urine, depending on the pH[125, 137, 138]. Accordingly, this simulation study considers three distinct feed solutions based on nitrogen forms: urea, NH_3, and NH_4^+. Therefore, this study can provide insights into the transport of these nitrogen forms across a GO membrane and the role of size exclusion and electrostatic interactions in the rejection of nitrogen compounds. Further, this study elucidates the role of functional groups presented on the GO membrane and the intercalated cations on the transport and rejection of urea, NH_3, or NH_4^+ ions. The nature of the urine feed solution (either fresh or hydrolyzed)

can also influence the water permeance of GO membranes. Overall, this study provides a comprehensive assessment of a cation-intercalated GO membrane in treating urine solution.

6.2 Methodology

6.2.1 Cation-intercalated GO membrane

A multilayered cation-intercalated GO membrane is constructed with two distinct sizes of GO nanosheets (40×48 Å^2 and 31×48 Å^2). These nanosheets are generated using Visual Molecular Dynamics (VMD) [180] and Avogadro [181] softwares. The renowned Lerf-Klinowski model [182], with a chemical composition of $C_{10}O_1(OH)_1(COOH)_{0.5}$ [51, 52, 82, 83, 183, 208], is employed to achieve a C/O ratio within the typical range of 2.0-4.0 as per literature [209–211]. This model prescribes the random distribution of hydroxyl and epoxy functional groups on the basal plane, while carboxyl functional groups are positioned at the sheet edges. The construction of the multilayered GO membrane (Fig. 6.1(b)) incorporates geometric parameters such as pore width (P), pore offset (O), and interlayer distance (I). The selected values for P and O are 12 Å and 8 Å, respectively. As mentioned earlier, this study aims to construct a cation-intercalated GO membrane, and to achieve this, magnesium ions (Mg^{2+}) are introduced randomly within the membrane layers. Following the approach established by Chen et al.[70], the I value is considered to be 13.6 Å (based on the nature of intercalated cations). Finally, the cation-intercalated GO membrane is hydrated in an equilibrated water box.

6.2.2 FO Simulation system

A typical FO simulation system comprises a feed solution, a draw solution, and a semi-permeable membrane. The driving force for water permeation across the membrane is the osmotic pressure difference between the draw solution and the feed solution. In this study, three different feed solutions are considered: Feed solution1 with 14 Na^+ ions, 12 K^+ ions, 46 Cl^- ions, 30 urea molecules, and 20,000 water molecules; Feed solution2 with 14 Na^+ ions, 12 K^+ ions, 46 Cl^- ions, 60 ammonia molecules, and 20,000 water molecules; and Feed solution 3 with 14 Na^+ ions, 12 K^+ ions, 106 Cl^- ions, 60 ammonium ions, and 20,000 water molecules. A 1.5 M KH_2PO_4 solution is considered as the draw solution, containing 200 K^+ ions, 200 $H_2PO_4^-$ ions, and 10,000 water molecules. For all FO simulation systems, a hydrated cation-intercalated

GO membrane is positioned between the feed and draw solutions, as displayed in Fig. 6.1(c). Furthermore, graphene sheets acted as pistons positioned at the extremities of feed and draw solutions, subjected to one atmospheric pressure in opposing directions on both positions. In addition, a 30 Å vacuum in length is placed above and below the simulation system along the Z-axis.

6.2.3 Simulation Methodology

All non-equilibrium Molecular Dynamics (MD) simulations are performed in this study using the OPLS-AA forcefield parameters [196] and executed with the NAMD 2.11 package [197]. Van der Waals interactions are computed employing the Lennard–Jones potential with a cutoff radius of 12 Å. Long-range electrostatic interactions are calculated using the Particle Mesh Ewald (PME) method [154]. TIP3P water model is used to represent water molecules [162]. Following the construction of FO simulation systems, as described earlier in this section, an energy minimization step is conducted. Subsequently, a 1.0 ns equilibration run is performed at 300.0 K under constant pressure conditions of 1.0 atm. Then, followed by 100 ns production runs are carried out with a time step of 1.0 fs in an NVT ensemble, with periodic boundary conditions in all three directions. During the production runs, a few selected carbon atoms located at the corner of the GO nanosheets are fixed to preserve the layered structure of the membrane [198, 199, 225]. Langevin dynamics, with a damping factor of 5.0 ps^{-1}, is employed to maintain a constant temperature throughout the simulations. Trajectories are saved at 20 ps intervals. Each FO simulation system performs three independent simulations with different initial configurations, and the presented findings in subsequent sections are averaged over these three simulations [51, 52, 71, 83].

6.3 Results and discussion

6.3.1 Rejection and Transport mechanisms of Urea and Ammonia (NH_3)

As mentioned in the previous section, urine exists in two states, i.e., fresh and hydrolyzed. Fresh urine presents nitrogen in the form of urea, whereas hydrolyzed urine has nitrogen in the form of NH_3/NH_4^+. This section explains the relative rejection and transport of two primary

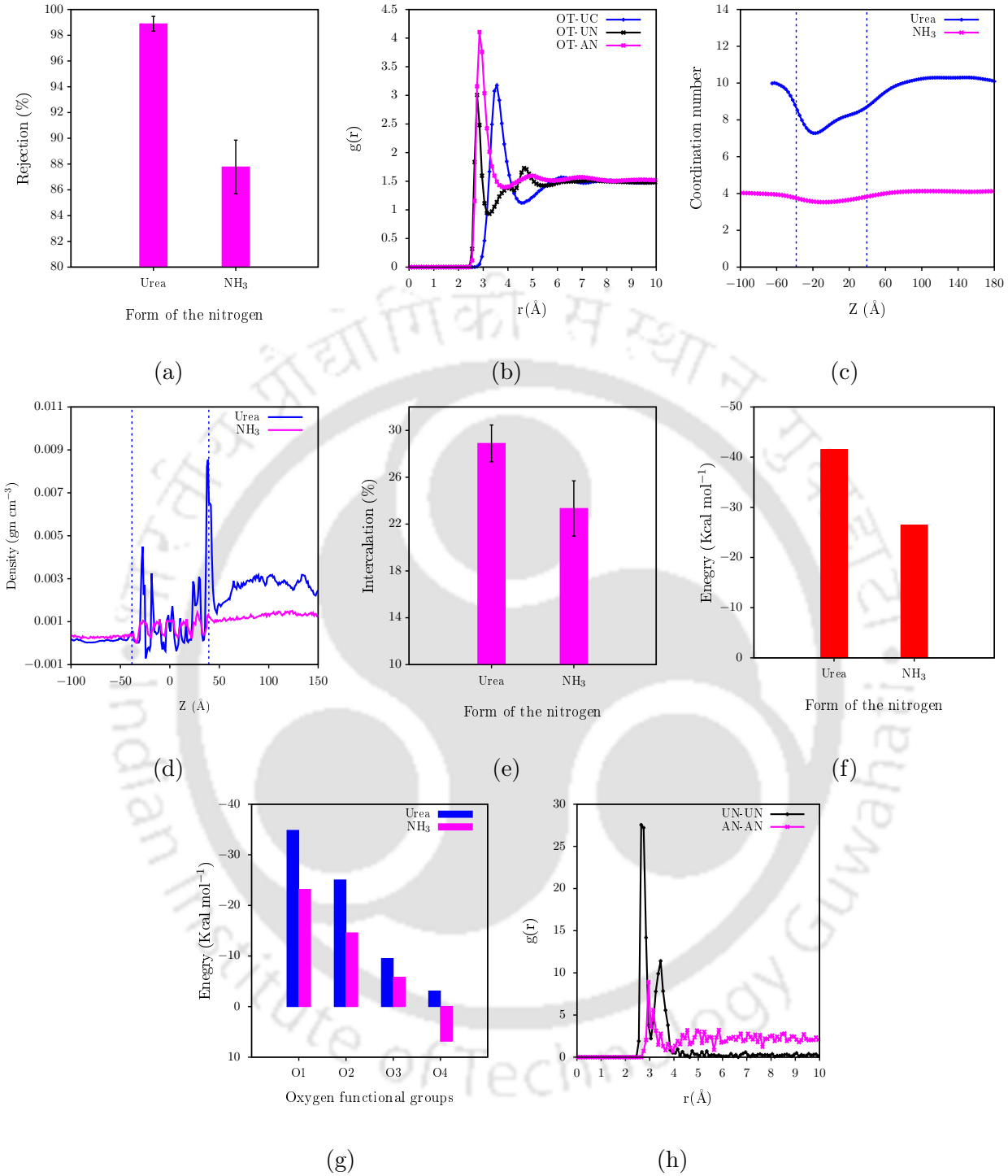

Figure 6.2: (a) Relative rejection of urea and NH_3. (b) Radial distribution functions (RDF) of urea and NH_3 with water molecules (OT). Here, UC and UN are carbon and nitrogen atoms of urea, respectively, and AN is the nitrogen atom of NH_3. (c) Number of water molecules in the primary hydration shell, (d) Mass density profiles, and (e) Intercalation percentage of the urea and NH_3. Here, vertical dotted blue lines indicate the membrane position.

Figure 6.2: continued
(f) Electrostatic interactions of GO membranes with urea and NH_3. (g) Electrostatic interactions of individual oxygen-containing functional groups (OFGs) with urea and NH_3. Here, O1, O2, O3, and O4 are the oxygen atoms of a hydroxyl group (-OH), epoxy group (-O-), carboxyl group, which is linked to only C atom (-C=O), and carboxyl group that is bonded to C and H atoms (C-O-H), respectively. (h) RDF of nitrogen-nitrogen atoms for urea (UN-UN) and NH_3 (AN-AN).

forms of nitrogen (i.e., urea and NH_3) in the urine. The relative rejection of the urea and NH_3 is shown in Fig. 6.2(a), indicating that nitrogen in the form of urea is rejected better than in the form of NH_3. Membrane rejection phenomena primarily depend on size exclusion and electrostatic interactions. As urea and NH_3 are neutral molecules, size exclusion plays a significant role in the rejection. Both these molecules are smaller in size; however, NH_3 is much smaller than the urea (18 g/mol vs. 60 g/mol). This could be a reason for attaining a higher urea rejection as compared to NH_3 rejection. To confirm this, radial distribution functions of urea and NH_3 with water molecules (OT) and the number of water molecules in primary hydration shells of these molecules are presented in Fig. 6.2(b) and (c). Here, UC and UN are carbon and nitrogen atoms of urea, respectively, and AN is the nitrogen atom of NH_3. The change in the number of water molecules in the primary hydration shell of urea and NH_3 is measured at the first maximum of the peaks (UC-OT and AN-OT), shown in Fig. 6.2(b). As shown in Fig. 6.2(c), urea has more water molecules in its primary hydration shell than NH_3. It indicates the urea has a bigger hydration shell than the NH_3, resulting in greater urea rejection. However, while entering into the membrane layers, urea molecules start dehydrating, resulting in the loss of a few water molecules in their hydration shells. The reason could be the interactions of nitrogen atoms and water molecules, and these interactions are stronger for NH_3 as compared to urea, as shown in Fig. 6.2(b). As a result, urea molecules are dehydrated while moving into the membrane layers. However, throughout the pathway, urea molecules have more water molecules in their primary hydration shell than the NH_3 molecules; hence, nitrogen in the form of urea exhibited higher rejection.

To further understand the rejection and transport phenomena, the mass density profiles of the urea and NH_3 are presented in Fig. 6.2(d). Here, vertical dotted blue lines indicate

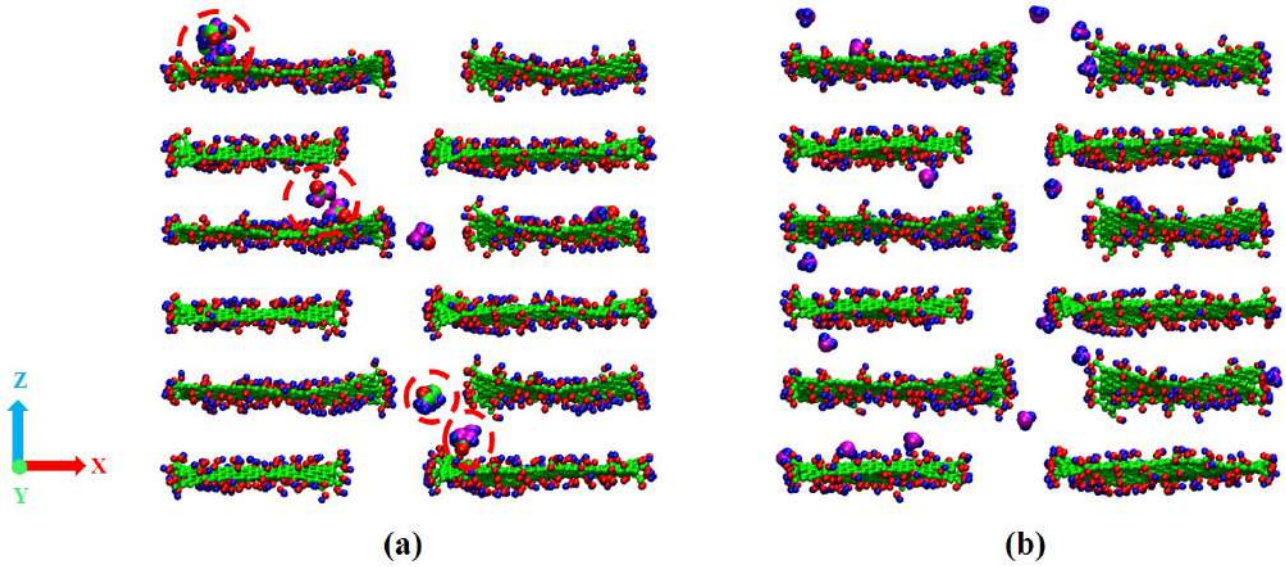

Figure 6.3: Snapshot of (a) Urea and (b) NH_3 molecules within the interlayer gallery of GO membrane. Green color : carbon atoms; red color : oxygen atoms; blue color : hydrogen atoms; magenta color: nitrogen atoms.

the membrane position. These profiles indicate that a higher amount of the urea molecules are intercalated inside the interlayer gallery of GO membranes, whereas a higher amount of NH_3 molecules are permeated through the membrane layers. The intercalation percentage of the urea and NH_3 molecules is presented in Fig. 6.2(e). Although a higher percentage of the urea molecules are intercalated inside the GO membrane layers, a higher percentage of urea rejection is attained. The reasons could be the strength of electrostatic interactions of oxygen-containing functional groups (OFGs) with these molecules and the formation of smaller urea aggregates within the GO layers. The electrostatic interactions of GO membranes with urea and NH_3 are presented in Fig. 6.2(f). Inherently, the GO membrane has a negative charge, and it has stronger electrostatic attractions with urea molecules than NH_3 molecules, as shown in Fig. 6.2(f). As a result, the permeation rate of the urea molecules decreases and results in greater rejection. Particularly, understanding which OFGs of GO membranes are causing resistance to the permeation of urea molecules is necessary. For this, electrostatic interactions of individual OFGs with both urea and NH_3 molecules are presented in Fig. 6.2(g). It implies that hydroxyl and epoxy groups have stronger interactions than the carboxyl groups for both molecules. Moreover, the interaction strength of the hydroxyl and epoxy groups with urea molecules is stronger than with the NH_3 molecules, causing a higher urea rejection. We

observed the formation of smaller urea aggregates during the process, whereas no such NH_3 aggregates (shown in Fig. 6.3). The reason for this difference could be the disparity of nitrogen atom interactions. The RDF of nitrogen-nitrogen atoms for urea (UN-UN) and NH_3 (AN-AN) are presented in Fig. 6.2(h). These plots clearly indicate that interactions of the nitrogen-nitrogen atoms are stronger for urea as compared to NH_3. As a result, urea forms smaller aggregates inside the membrane layers, causing a better rejection.

6.3.2 Rejection and Transport mechanisms of Ammonia (NH_3) and Ammonium (NH_4^+) ion

As mentioned in the introduction, the form of nitrogen changes with changing the pH of the hydrolyzed urine. At pH 11.5, the state of the nitrogen is NH_3, whereas at pH 6.5, the state of the nitrogen is NH_4^+. The rejection of NH_3 is lower than urea, as shown in Fig. 6.2(a). Lower rejection of NH_3 can be made better by changing the pH of the feed solution. In addition, the permeated NH_3 (contains nitrogen (N)) into the draw solution (contains potassium (K) and phosphorous (P)) can be used as a fertilizer (rich N, P, K). This section explains the comparative rejection and transport of NH_3 and NH_4^+. Nitrogen in the form of NH_4^+ exhibits higher rejection than in the form of NH_3, as shown in Fig. 6.4(a). As explained above, size exclusion and electrostatic interactions determine the membrane rejection phenomena. Here, electrostatic interactions play a more crucial role than the size exclusion in rejecting positive-charged NH_4^+ and neutral-charged NH_3. To understand the role of size exclusion, the RDF of NH_3 and NH_4^+ with water molecules (OT) is presented in Fig. 6.4(b). Here, AN and ANN are nitrogen atoms of the NH_3 and NH_4^+, respectively. These profiles imply no significant change in the size of the primary hydration shell, and NH_4^+ has stronger interactions with water molecules than NH_3. In other words, NH_4^+ has a more stable hydration shell than NH_3.

To understand the effect of electrostatic interactions, the interaction energies of the NH_3 and NH_4^+ are presented in Fig. 6.4(c). As shown in Fig. 6.4(c), positively charged NH_4^+ has stronger attractions with the negatively charged GO membrane as compared with the neutral-charged NH_3. Moreover, this study used the Mg^{2+} cation intercalated GO membranes and the impact of these cations on the rejection of both NH_3 and NH_4^+ presented in Fig. 6.4(d). It indicates that positively charged NH_4^+ has a stronger repulsion with Mg^{2+} intercalated cations. As a result, the transport rate of the NH_4^+ decreases and causes a better rejection than NH_3.

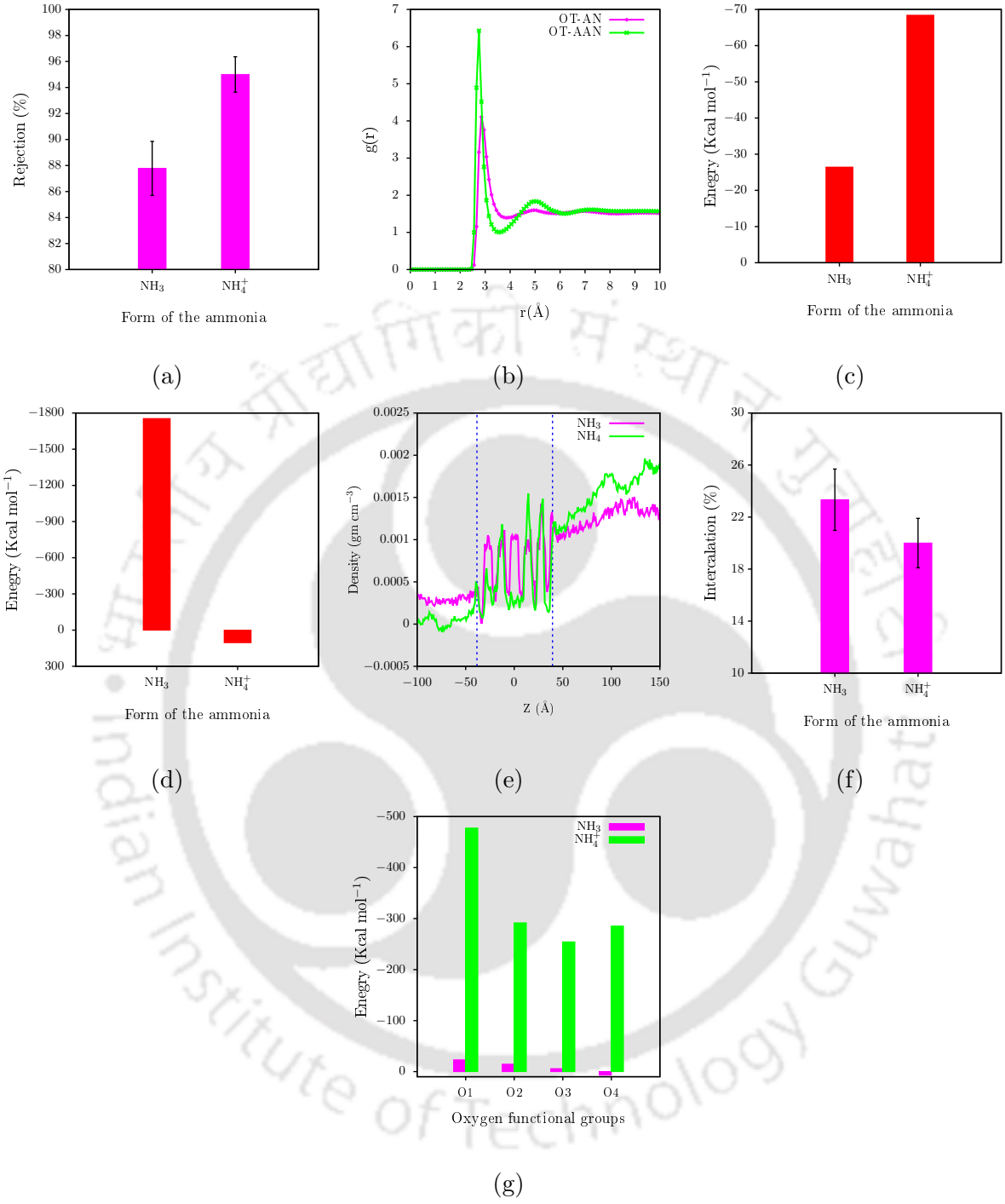

Figure 6.4: a) Relative rejection of NH_3 and NH_4^+. (b) RDF of NH_3 and NH_4^+ with water molecules (OT). Here, AN and ANN are nitrogen atoms of NH_3 and NH_4^+, respectively. Electrostatic interactions of (c) GO membranes and (d) intercalated cations (Mg^{2+}) with NH_3 and NH_4^+. (e) Mass density profiles and (f) Intercalation percentage of NH_3 and NH_4^+. (g) Electrostatic interactions of OFGs with NH_3 and NH_4^+.

Further understanding the transport mechanism of NH_3 and NH_4^+, the mass density profiles are presented in Fig. 6.4(e). These density profiles indicate that a higher amount of the NH_3 molecules are permeated through the membranes, and some of both NH_3 and NH_4^+ are intercalated inside the membrane layers. The intercalation percentage of NH_3 and NH_4^+ is presented in Fig. 6.4(f), which shows that a higher percentage of the NH_3 molecules are intercalated within the layers. As shown in Fig. 6.4(g), the strong interactions of the hydroxyl and epoxy functional groups are causing higher NH_4^+ rejection than the NH_3 molecules.

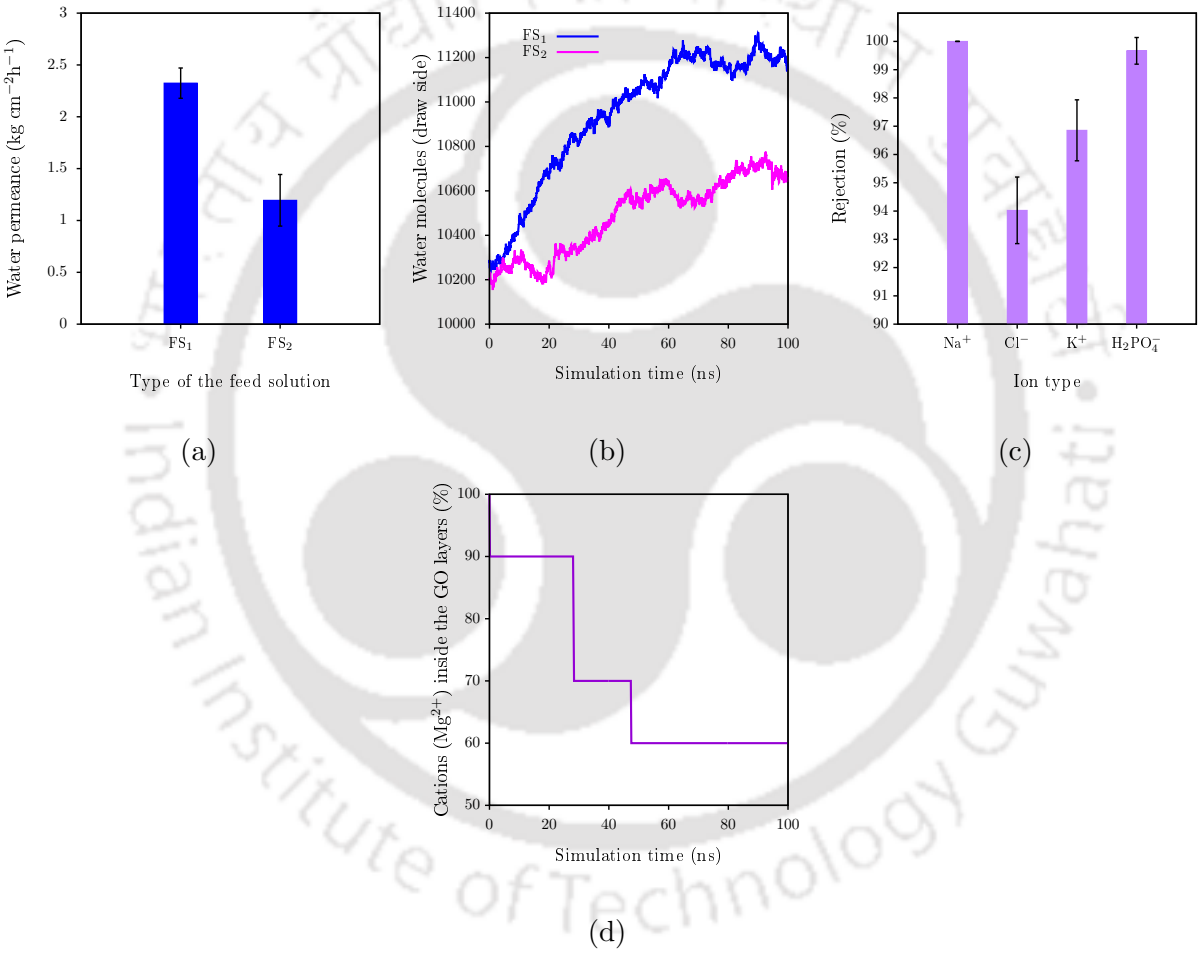

Figure 6.5: (a) Water permeane of Mg^{2+} cation intercalated GO membrane with two different feed solutions, i.e., fresh urine (FS1, nitrogen in the form of urea) and hydrolyzed urine (FS2, nitrogen in the form of NH_3) . (b) Variation of the number of water molecules in the draw solution as a function of the simulation time. (c) Salt rejection percentages. (d) Mg^{2+} cations distribution inside the GO layers as a function of simulation time.

As mentioned in the previous section, to the best of the author's knowledge, no prior research has investigated the use of GO membranes for nitrogen recovery from human urine.

However, some commercially available polymeric membranes are currently employed in treating human urine. A comparative analysis of the rejection performance for different nitrogen forms between these polymeric membranes and the GO membranes explored in this study is presented in Table.6.1.

Table 6.1: The comparative rejection of different nitrogen forms by commercial existing polymeric membranes.

Name of the membrane	Urea Rejection (%)	NH_3 Rejection (%)	NH_4^+ Rejection (%)
Filmtec flat sheet BW30 [28]	-	0	-
DOW NF90 [28]	-	0	-
Modified XLE [32]	54.9	-	-
Modified BW30XFR [32]	64.6	-	-
Filmtec flat sheet BW30 [125]	57	94	-
DOW NF90 [125]	42-54	80	-
Tight NF90 [145]	55	-	-
Loose NF270 [145]	<10	-	-
BW30 [126]	76	-	-
NF90 [126]	55	-	-
NF270 [126]	2-4	-	-
PA-TFC [23]	80-85	80-85	> 95
Porifera [130]	45-68	-	-
PA-TFC [31]	-	86	-
PA-TFC [24]	-	50	-
Present study	98.88 ± 0.57	87.77 ± 2.078	95 ± 1.36

6.3.3 Water permeance and salt rejection

In this section, we explained the membrane performance in terms of water permeance and salt rejection. The water permeance of two different feed solutions, i.e., fresh urine (FS1, nitrogen in the form of urea) and hydrolyzed urine (FS2, nitrogen in the form of NH_3), is reported in Fig. 6.5(a). This displays that the membrane achieved higher water permeance with FS1. It means that water transport via the GO membrane is greater when the FO process has fresh urine as a feed solution. The potential reason could be the difference in osmotic pressure because the osmotic pressure gradient drives the FO process. The osmotic pressure of fresh and hydrolyzed urine is 13.7 and 29.1 bar, respectively [23]. Thus, the osmotic pressure gradient of fresh urine is higher than hydrolyzed urine, resulting in greater water permeance with fresh urine. Furthermore, we monitored the permeation of water molecules from the feed solution to draw solution during the simulation time, as reported in Fig. 6.5(b). These profiles also signify that the current FO membrane delivered higher water permeance with fresh urine as a feed solution. To further assess the membrane performance, the details of various salt ion rejections are presented in Fig. 6.5(c). The current FO system achieved the higher rejection of Na^+, Cl^+, K^+, and $H_2PO_4^-$, which are all greater than 94%. Additionally, we presented the percentage of intercalated cations (Mg^{2+}) inside the interlayer gallery of the GO membrane as a function of a simulation time in Fig. 6.5(d).

As shown in Fig. 6.5(d), it is observed that, over the course of the simulation, a few intercalated cations migrate out of the membrane layers, thereby influencing the interlayer distance. Addressing this issue involves either impeding the movement of cations out of the membrane layers or replacing the migrated cations with similar ones within the membrane layers. Preventing the migration of cations out of the membrane layers is quite challenging due to the inherent movement of cations within the simulation system, making such prevention impractical. Consequently, cation replacement within the membrane layers emerges as a possible solution, particularly feasible in experimental studies. Practical experiments, such as those involving seawater as a feed solution, offer a rich source of abundant cations. During experiments, some of these cations can naturally enter the membrane layers, effectively countering the migration of similar cations. Contrastingly, simulation studies present difficulties in achieving cation substitution during simulation progression. We implemented a strategy of fixing specific corner carbon atoms of GO nanosheets to keep a nearly constant interlayer distance. In this

aspect, future research should focus on exploring innovative strategies to prolong the retention time of intercalated cations within GO membrane layers, thereby ensuring a consistent interlayer distance. Such initiatives are crucial for implementing GO-based membranes in practical applications.

6.4 Conclusions

In summary, this study investigates the recovery of urea and ammonia from human urine using a cation-intercalated GO membrane in FO separation process through non-equilibrium MD simulations. This simulation study considers three distinct feed solutions based on nitrogen forms: urea, NH_3, and NH_4^+. Our findings reveal that GO membranes exhibit superior rejection of urea compared to NH_3 due to factors such as larger hydration size of urea, stronger attraction with GO nanosheets, and the formation of small urea aggregates. Furthermore, this study highlights that nitrogen in the form of NH_4^+ demonstrates greater rejection compared to NH_3, attributed to the stable hydration shell of positively charged NH_4^+ ions, stronger attraction with GO nanosheets, and electrostatic repulsion with intercalated cations in contrast to neutral NH_3 molecules. Additionally, the present study underscores that the hydroxyl and epoxy functional groups of the GO nanosheets significantly inhibit the permeation rates of urea and NH_4^+, resulting in substantial recovery. This research further demonstrates that GO membranes achieved higher water permeance with fresh human urine compared to hydrolyzed urine, attributed to a greater osmotic pressure gradient and salt rejection exceeding 94%. In the context of the FO process, this simulation study incorporates a draw solution enriched with phosphorous (P) and potassium (K). During the FO process, the permeation of nitrogen (N) components into this draw solution (which already contains P & K)) can be utilized as a fertilizer (rich N, P, K) in agricultural applications. The findings presented in this study would offer valuable insights for experimental researchers engaged in the development of FO processes for the recovery of urea and ammonia from human urine.

Chapter 7

Comparative retention analysis of intercalated cations inside the interlayer gallery of lamellar and non-lamellar graphene oxide (GO) membranes in a reverse osmosis (RO) process: A molecular dynamics study*

7.1 Objective

Although cation intercalation inside the GO membranes has emerged as a promising strategy to control the swelling tendency of GO membranes in aqueous environments, there is a need to address the longevity of the intercalated cations within the GO laminates, as the stability of membranes relies on the interactions between these intercalated cations and GO nanosheets. Moreover, the retention of intercalated cations inside the interlayer gallery of GO membranes depends on the morphology and structural arrangement of interlayer galleries. Thus, this study

*Reddy, P. Rajasekhar, K. Anki Reddy, and Amit Kumar. "Comparative Retention Analysis of Intercalated Cations Inside the Interlayer Gallery of Lamellar and Nonlamellar Graphene Oxide Membranes in Reverse Osmosis Process: A Molecular Dynamics Study." The Journal of Physical Chemistry B (2024).

has constructed two distinct structural configurations, namely lamellar and non-lamellar, to address these challenges at the atomistic level. To the best of the author's knowledge, no research has been reported in the literature on the lifetime of intercalated cations within GO layers. To comprehensively explore the dynamics and lifespan of intercalated cations within membrane layers, this study performed nonequilibrium MD simulations on two varieties of intercalated cation membranes, considering both lamellar and non-lamellar configurations. The study employed a realistic simulation approach to create non-lamellar cation intercalated GO membranes. The study focuses on understanding how membrane structure and morphology, including features like 2D nanochannels and pore geometry, impact membrane performance in terms of water permeance and salt rejection through the RO separation technique. The results of the present study provide atomistic-level insights into how membrane morphology influences membrane performance and a relationship between membrane structure and functionality.

7.2 Methodology

7.2.1 Non-lamellar cation intercalated GO membrane

In this study, non-lamellar cation intercalated GO membranes are prepared using the following multistep procedure, as shown in Figure.7.1. Firstly, 12 GO nanosheets of two different sizes are randomly placed in a simulation box with dimensions of 75×50×400 $Å^3$ containing 15 weight percentage of water molecules, and a rigid graphene sheet is positioned at the bottom of the water box. Then, GO nanosheets are pulled onto the surface of the graphene sheet to mimic a vacuum filtration process commonly used in experimental membrane synthesis. This pulling process is carried out at a rate of 100 Å/s with a force constant of 5 kcal/(mol ×$Å^2$), applying periodic boundary conditions (PBC) in X and Y directions in an NVT ensemble. Subsequently, the rigid graphene sheet is removed, and a 20 ns simulation is performed in an NPT ensemble with PBC in all directions to release the vacuum and create a well-relaxed GO membrane model. Afterward, the water molecules are removed from the simulation system. An additional 10 ns of simulations are performed in an NPT ensemble with PBC in all directions to further relax the GO membrane model, resulting in a dried GO membrane. Then, this dried GO membrane is used to construct K^+ cation-intercalated GO membrane. Fifteen K^+ cations are randomly placed within the interlayer gallery of the dried GO membrane and then hydrated

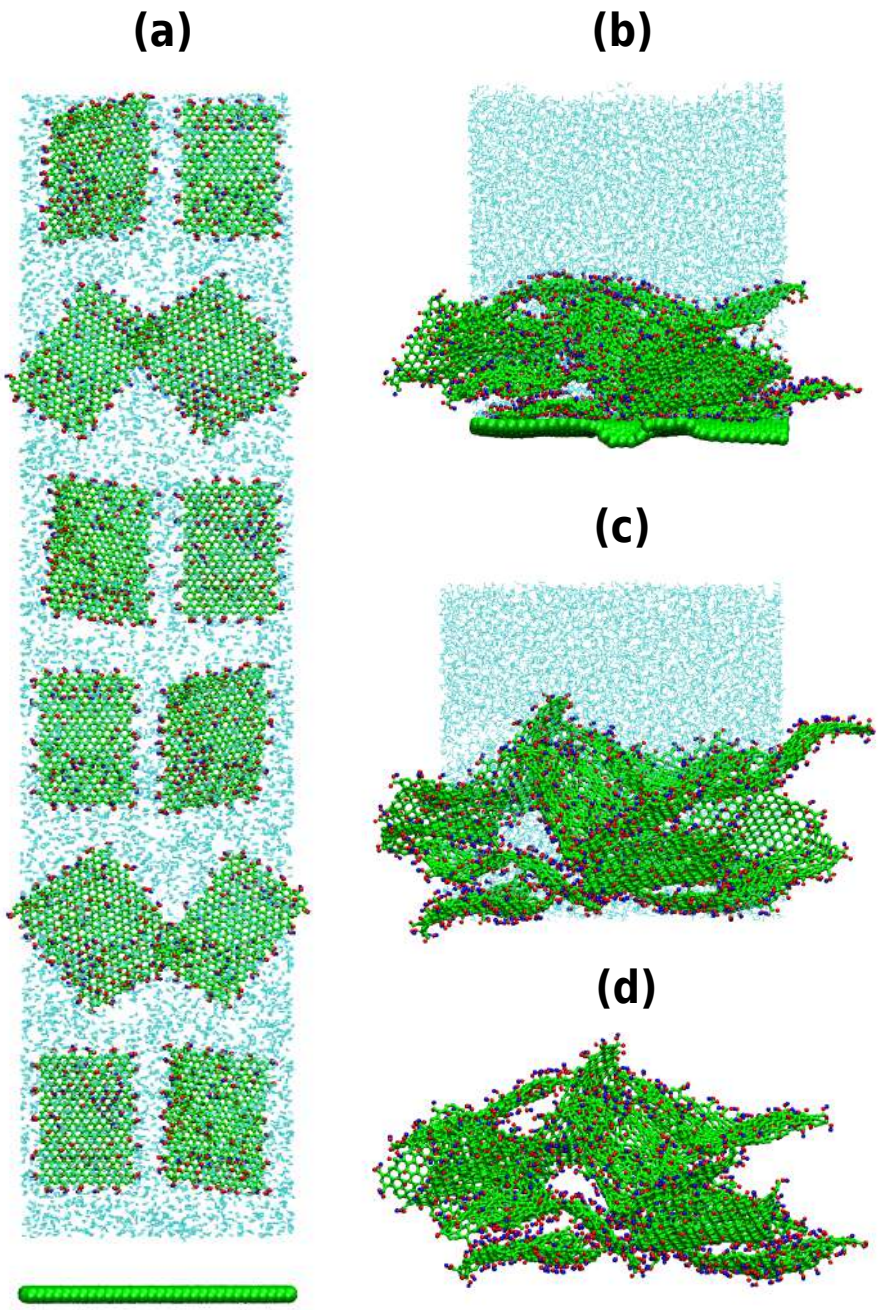

Figure 7.1: Steps involved in the construction of the non-lamellar graphene oxide (GO) membrane model: (a) Initial random arrangement of GO nanosheets within the water box, (b) pulling the GO sheets onto the rigid graphene sheet, (c) subsequent relaxation and equilibration to remove the vacuum, and (d) a dried non-lamellar GO membrane model. Carbon atoms are depicted in green color, oxygen atoms in red color, hydrogen atoms in blue color, and water molecules in cyan color.

with an equilibrated water box. A similar procedure is replicated with a 25 weight percentage of water in the simulation box to build a Mg^{2+} cation-intercalated GO membrane model.

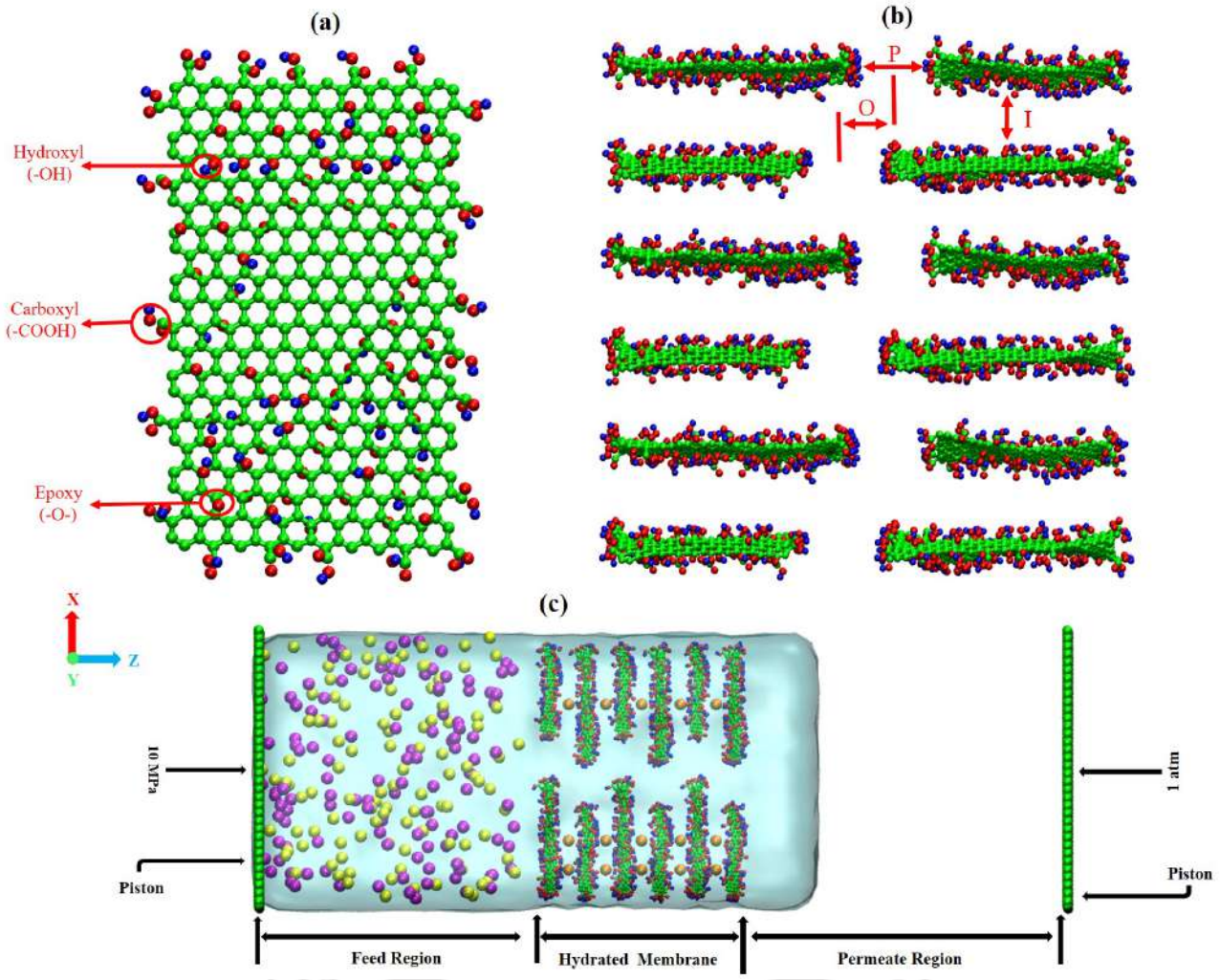

Figure 7.2: (a) Structure of a single graphene oxide (GO) nanosheet. (b) Lamellar arrangement of multilayered GO membrane. (c) Reverse osmosis (RO) simulation system. Green color : Carbon atoms; Red color : Oxygen atoms; Blue color : Hydrogen atoms; Yellow color : Na^+ ions; Magenta color : Cl^- ions; Orange color : K^+ ions.

The structure of the GO nanosheet is illustrated in Figure.7.2 (a). For constructing the GO membrane models in this study, two distinct sizes of GO nanosheets are developed: one with dimensions of 40×48 $Å^2$ and the other one with dimensions of 31×48 $Å^2$. The development of the GO nanosheets followed the well-known Lerf-Klinowski model[182], which suggests that hydroxyl and epoxy functional groups are located on the basal plane of the GO nanosheet, and carboxyl functional groups are at the edges. Accordingly, GO nanosheets are designed with a

chemical composition of $C_{10}O_1(OH)_1(COOH)_{0.5}$[82, 83, 183, 208], considering the C/O ratio of 2.0-4.0 reported in the literature [209–211]. The Visual Molecular Dynamics (VMD)[180] and Avogadro[181] softwares are used to create the GO nanosheets, where the functional groups are randomly distributed throughout the structures.

7.2.2 Lamellar cation intercalated GO membrane

Non-lamellar GO membranes can define as the geometric parameters of the membranes, such as pore width (P), pore offset (O), and interlayer distance (I) are not predefined and non-uniform throughout the membrane structure. Whereas lamellar GO membrane (shown in Figure.7.2 (b)) has uniform geometric parameters throughout the membrane structure, they are predefined. This study assembled multilayered lamellar cation intercalated GO membranes considering the values of P and O are 10 Å and 8 Å, respectively. As mentioned earlier, this study focuses on the K^+ and Mg^{2+} cation intercalated GO membranes. The I value varies depending on the type of intercalated cations, as reported in the work of Chen et al. Moreover, the I values, 11.4 Å and 13.6 Å, correspond to K^+ and Mg^{2+} cations taken from Chen et al.'s work[70]. After constructing the membranes considering the above-mentioned geometric parameters, 15 cations are randomly positioned within the GO layers to create cation-intercalated GO models. Following the membrane construction, these structures are hydrated within an equilibrated water box. The details regarding all the constructed membranes in this study are presented in Table.7.1.

Table 7.1: Structural arrangements of cation intercalated GO membranes and their respective nomenclature.

Name of the membrane	Cation type	Structural arrangement
GOL-K	K^+	Lamellar
GONL-K	K^+	Non-lamellar
GOL-M	Mg^{2+}	Lamellar
GONL-M	Mg^{2+}	Non-lamellar

7.2.3 RO simulation setup

The RO simulation setup, shown in Figure.7.2 (c), contains three primary components: a feed section, a semipermeable membrane, and a permeate section, wherein the hydrated membrane is placed between the feed and permeate regions. This study considered 0.56 M NaCl solution as a feed solution, containing 108 Na^+ ions, 108 Cl^- ions, and 10000 water molecules. Additionally, the RO simulation system incorporates two rigid graphene sheets, serving as pistons, positioned at opposing extremities of the setup. Besides, a 30 Å vacuum is provided on the above and below of the simulation systems. Furthermore, a pressure of 10 MPa and 1 atm is applied to the feed and permeate pistons, respectively, to facilitate the external pressure-driven RO process.

7.2.4 Simulation Methodology

This study performed all molecular dynamics (MD) simulations using the LAMMPS package[212]. The prevalidated forcefield parameters of GO membranes are taken from the work of Williams et al[213]. For the remaining atomic species, the CHARMM forcefield parameters are applied[214]. The TIP3P water model is used to represent water molecules[162]. Following constructing the RO simulation system, an energy minimization step is executed, followed by equilibration of 0.5 ns at a constant temperature of 300 K. Subsequently, production runs of 60 ns are performed with a timestep of 1 fs, periodic boundary conditions in all three dimensions. The Nose-Hoover thermostat, with a damping factor of 50 fs, is used to maintain a constant temperature throughout the simulations. Van der Waals interactions are computed using the Lennard-Jones potential, with a cutoff distance of 12 Å. The particle-particle particle-mesh method is employed for the calculation of long-range electrostatic interactions. Atomic trajectories are saved at intervals of 20 ps. Moreover, a few selected carbon atoms (located at the corners of GO nanosheets and unbounded to any oxygen-containing functional groups) are fixed during the production runs to preserve the layered structure of the membrane[51, 198, 199]. The reported outcomes in the subsequent sections are averaged over three independent configurations[51, 71, 83, 119].

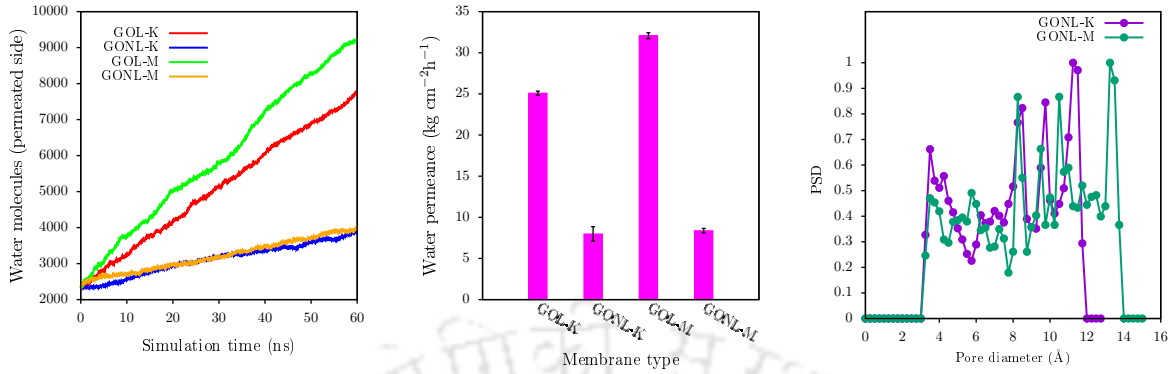

(a) (b) (c)

Figure 7.3: (a) Water molecules variations in the permeate region with the simulation time and (b) comparative water permeance of all membranes. (c) Pore size distrubution (PSD) of non-lamellar GO membranes.

7.3 Results and discussion

7.3.1 Water permeance

During the course of the simulations, this study monitored the number of water molecules that permeated from the feed region to the permeate region, aiming to examine the comparative water permeance of lamellar and non-lamellar membranes. The corresponding variations of water molecules in the permeate region over the simulation time and the comparative water permeance of all the membranes are depicted in Figure.7.3 (a) and (b), respectively. The results shown in Figures.7.3 (a) and (b) reveal that lamellar membranes exhibited significantly higher water permeance than non-lamellar membranes. This observation can be attributed to the distinct formation and structural characteristics of the nanochannels within the multilayered membranes, which directly influence water permeation. The pore size distribution (PSD) presented in Figure.7.3 (c) explains the heterogeneity of the interlayer galleries within non-lamellar GO membranes. As shown in Figure.7.3 (c), the GONL-K membrane has a pore size range of 3-12 Å, whereas GONL-M membranes have 3-14 Å. Specifically, lamellar GO membranes possess well-defined and uniform nanochannels throughout their structure, while non-lamellar GO membranes have irregular sizes and non-uniform nanochannels. Consequently, the presence of these well-defined and uniform nanochannels in lamellar GO membranes offers lower water resistance, resulting in higher water permeance as compared to non-lamellar membranes.

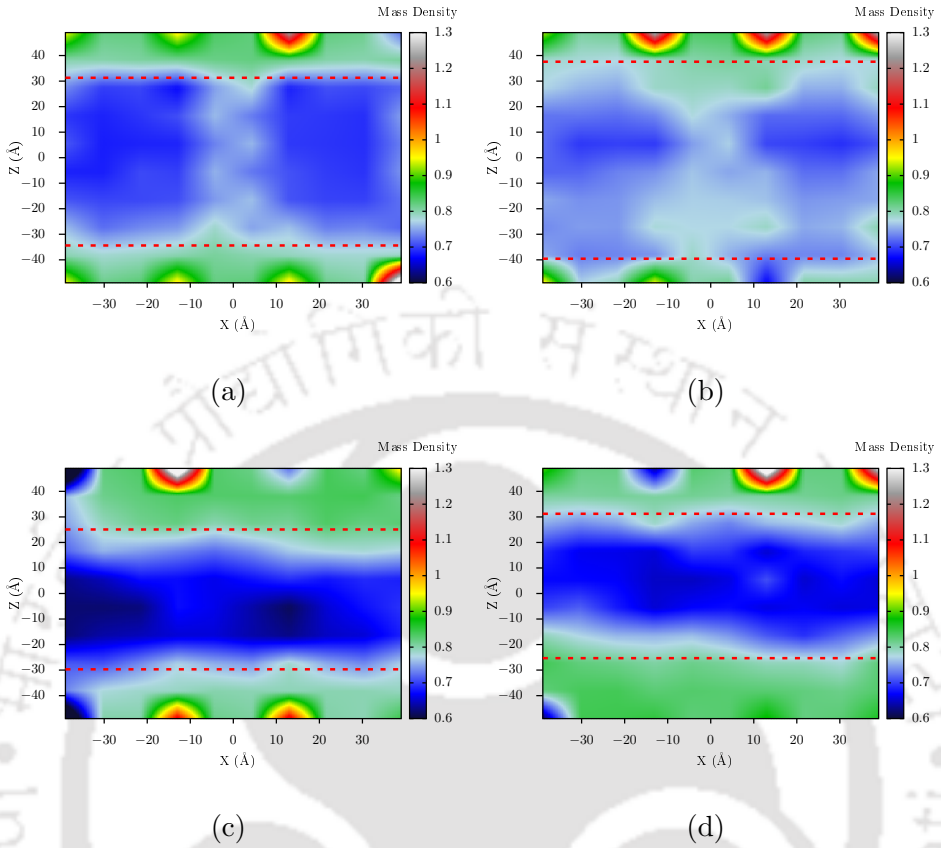

Figure 7.4: Two-dimensional (2D) mass density maps of water molecules in the XZ plane. (a) GOL-K, (b) GOL-M, (c) GONL-K, and (d) GONL-M membrane.

To gain deeper insights into water dynamics, we present two-dimensional (2D) mass density maps of water molecules in the XZ plane (Figure.7.4). The blue color region corresponds to the membrane position. These 2D maps demonstrate that lamellar GO membranes exhibit a higher density of water molecules within their layers compared to non-lamellar GO membranes. This disparity arises from the well-oriented nanochannels present in the lamellar GO membranes, facilitating enhanced water movement. Consequently, lamellar GO membranes exhibit superior water permeance compared to non-lamellar GO membranes. Furthermore, Figures.7.3 and 7.4 demonstrate that GO membranes intercalated with Mg^{2+} ions display higher water permeance than those with K^{+} ions. The reason could be that higher interlayer distance is observed in Mg^{2+} ion intercalated GO membranes compared to K^{+} ion intercalated GO membranes. The higher interlayer distance in Mg^{2+} ion intercalated GO membranes results in higher free pore volumes, drawing more water molecules into their layers and leading to higher water permeance.

Water permeance directly depends on nanochannels and interlayer distance of the multilayered membranes. However, the formation of the nanochannels has a direct relationship with several factors, such as the size of GO nanosheets, the concentration of the GO flakes, the oxygen-containing functional groups (OFGs) of the GO nanosheets, and the geometric parameters of the multilayered membranes.

According to the findings of Sun et al.[226], when GO membranes are stacked using nano-sized sheets exhibit a relatively smooth surface with minimal wrinkles. In contrast, membranes formed with microsized GO sheets display a corrugated structure with many wrinkles. This observation suggests that as the sheet size changes from nano to micro, the number of nanochannels available for water permeation decreases, consequently leading to reduced water permeance. Liu et al.[84] also examined the relative water permeance of membranes with different sizes of GO flakes. They also observed that smaller flakes results in more nanochannels for water transport, improving water permeance.

Another study by Liu et al.[47] reported that increasing the concentration of GO in the membrane preparation guided a decrease in the number of nanochannels for water permeation, resulting in reduced water permeance. Rajasekhar Reddy et al.[82] investigated the impact of OFGs on membrane performance. They noted that a decrease in the quantity of the functional groups of the membranes results in forming smaller pores (or nanochannels), causing resistance to water permeance. A few studies reported that increasing the pore offset of the multilayered membranes creates longer water transport nanochannels within their interlayer gallery, resulting in lower water permeance[51, 62, 71].

This study considered the same size and number of GO nanosheets and a constant number of OFGs. However, the geometric parameters of the membranes, specifically pore width and interlayer distance, differ among the membranes, and their effect on the water transport mechanism is already explained in detail. In contrast to nanochannels, the interlayer distance of the multilayered GO membranes depends on the strength of the electrostatic interaction of aromatic rings and OFGs of the GO nanosheets with intercalated cations and stability of the hydration sphere of the intercalated cations.

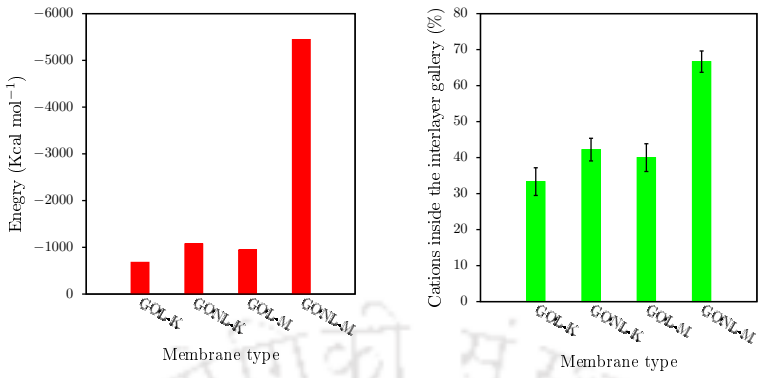

(a) (b)

Figure 7.5: (a) The combined average interaction energy of aromatic rings and oxygen-containing functional groups (OFGs) with intercalated cations (K^+, Mg^{2+}) and (b) the percentage of remaining intercalated cations inside the interlayer gallery of all membranes.

7.3.2 Membrane stability

Figure.7.5 (a) presents the electrostatic interaction energy of aromatic rings and OFGs with intercalated cations. These results reveal that non-lamellar membranes exhibit stronger interaction energies than lamellar GO membranes. This observation can be attributed to the structural configuration of nanochannels within the non-lamellar GO membrane layers, which effectively retain the majority of cations within the membrane layers during the simulation time. The percentage of intercalated cations within the interlayer gallery of the membranes is depicted in Figure.7.5 (b). The data indicate that non-lamellar GO membranes retain a higher percentage of intercalated cations within their interlayer gallery compared to lamellar GO membranes. In order to determine the percentage of intercalated cations that remained within GO laminates and estimate salt rejection in the following section, it is necessary to establish a reference time. This is because the structural features of the membranes influence water permeation, and the water flow rate directly impacts the mobility of cations and salt ions. Thus, the abovementioned percentages (i.e., intercalated cations and salt ions) are measured at the time when 30% of the feed water has permeated through the membrane layers.

Figure.7.5 also illustrate greater retention of Mg^{2+} cations within the GO channels than K^+ cations. In order to investigate the underlying reason, Figure.7.6 (a) presents the radial distribution function between the intercalated cations and water molecules. The data depicted in Figure.7.6 (a) indicate a stronger interaction between Mg^{2+} ions and water molecules com-

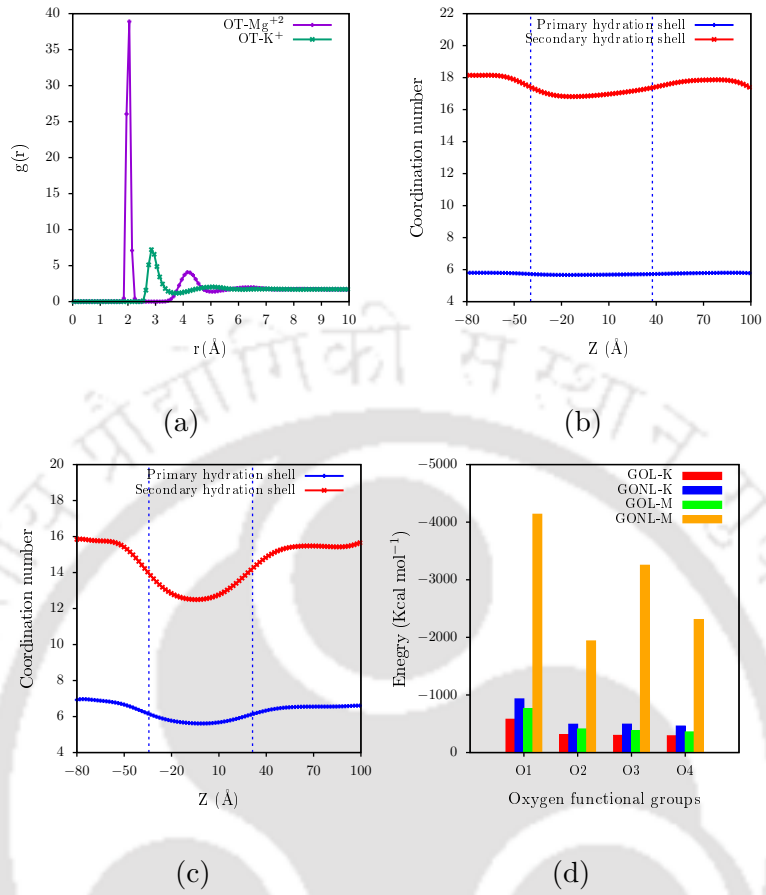

Figure 7.6: (a) The radial distribution function between the intercalated cations (K^+, Mg^{2+}) and water molecules (OT). The coordination number of (b) Mg^{2+} and (c) K^+ cations in their primary and secondary hydration shells along the Z-axis. (d) The average interaction energy between oxygen-containing functional groups (OFGs) and intercalated cations for all membranes. Here, the oxygen atoms of hydroxyl (-OH) and epoxy (-O-) groups are denoted as O1 and O2, respectively, while O3 and O4 represent the oxygen atoms of carboxyl groups (-COOH).

pared to K^+ ions. It suggests that the mobility of Mg^{2+} ions is comparatively slower, leading to a higher percentage of Mg^{2+} ions being retained within the GO channels. In addition to electrostatic interactions, the size of hydrated cations also influences the retention percentage of cations within the membrane layers. The impact of hydrated cation size is analyzed through coordination numbers of the primary and secondary hydration shells of both intercalated cations, as illustrated in Figures.7.6 (b) and (c).

Figures.7.6 (b) and (c) present the coordination numbers of Mg^{2+} and K^+ cations in the primary and secondary hydration shells, respectively. In the case of Mg^{2+} cations, the coordination numbers in both shells are invariant regardless of their position within the simulation

system. At the same time, the coordination numbers of K^+ cations decrease by 30% and 25% in the primary and secondary hydration shells, respectively, within the membrane layers. This indicates that Mg^{2+} cations maintain a stable and larger hydration shell compared to K^+ ions. Consequently, due to their larger hydration shells and stronger electrostatic interaction energies, Mg^{2+} cations are unable to migrate out of the membrane layers and exhibit higher retention within the GO channels than K^+ ions.

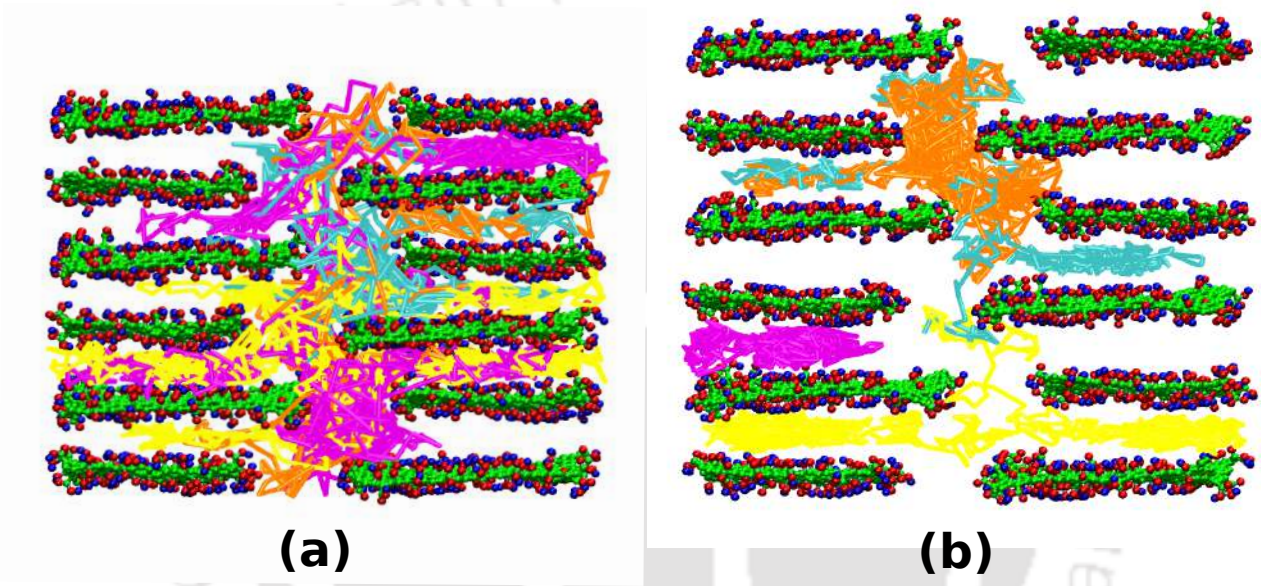

Figure 7.7: Pathways of four selected (a) K^+ and (b) Mg^{2+} cations within the interlayer gallery of lamellar GO membranes. Green color : carbon atoms; red color : oxygen atoms; blue color : hydrogen atoms, and the remaining colors represent the trajectories of selected intercalated cations.

Furthermore, we have analyzed the distribution of the cations within the interlayer gallery of the membranes by evaluating their interaction energies with OFGs and tracing their pathways. Figure.7.6 (d) displays the interaction energies of the intercalated cations with OFGs for all membranes. Here, the oxygen atoms of hydroxyl (-OH) and epoxy (-O-) groups are denoted as O1 and O2, respectively, while O3 and O4 represent the oxygen atoms of carboxyl groups (-COOH). The observed interaction energies suggest that both cations exhibit stronger interactions with hydroxyl groups compared to epoxy and carboxyl groups. This finding indicates that the cations mainly reside at the basal plane of the membranes, as hydroxyl functional groups are located in this region. The pathways depicted in Figure.7.7 also confirm that the cations

remain predominantly at the basal plane of the membranes. Furthermore, these trajectories also provide insight into the comparative diffusional dynamics of Mg^{2+} and K^+ ions within the GO layers. Notably, the mobility of Mg^{2+} ions is observed to be slower compared to K^+ ions. As a result, more Mg^{2+} cations are remained inside the GO laminates as compared to K^+ cations.

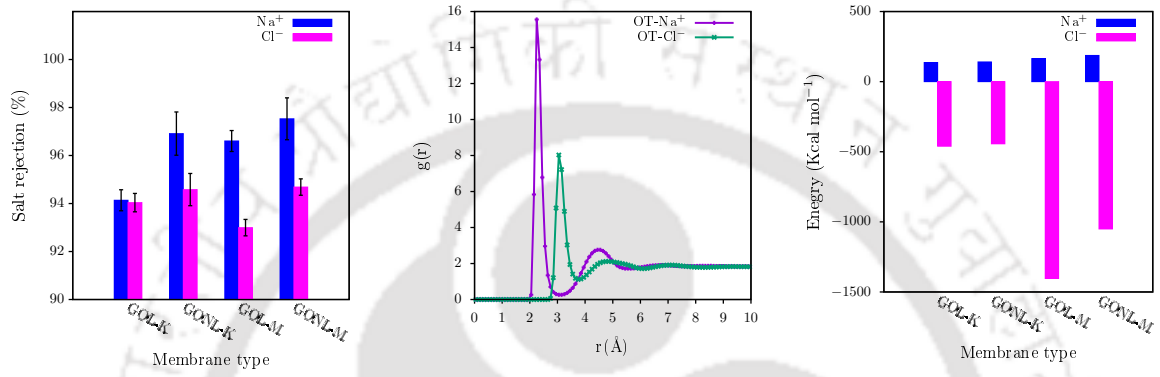

(a) (b) (c)

Figure 7.8: (a) Salt rejection percentage of all membranes. (b) The radial distribution function between the salt ions (Na^+, Cl^-) and water molecules (OT). (c) The average interaction energy between the salt ions and intercalated cations of all membranes.

7.3.3 Salt rejection

The comparative salt rejection of all membranes is presented in Figure.7.8 (a). The data reveals that the membranes exhibit higher rejection of Na^+ ions but poor rejection of Cl^- ions. This difference can be attributed to the mobility of ions within the GO channels and the electrostatic interactions between salt ions and intercalated cations. The radial distribution function (RDF) between salt ions and water molecules, depicted in Figure.7.8 (b), suggests that Na^+ ions interact more strongly with water molecules than Cl^- ions. It implies that the transport rate of Na^+ ions is slower compared to Cl^- ions. Furthermore, the RDF peaks demonstrate that Na^+ ions possess two hydration spheres, whereas Cl^- ions have only one. As a result, the size of hydrated Na^+ ions is bigger than the Cl^- ions, so membranes can also reject hydrated Na^+ ions via the size exclusion mechanism. Figure.7.8 also highlights that membranes with Mg^{2+} ion intercalation exhibit greater Na^+ rejection but poor Cl^- rejection, owing to the electrostatic interaction energies between salt ions and intercalated cations. As illustrated

in Figure.7.8 (c), Na^+ ions experience strong repulsion by Mg^{2+} cations, while Cl^- ions are strongly attracted, leading to the superior Na^+ rejection and poor Cl^- rejection performance of Mg^{2+} ion intercalated GO membranes.

7.4 Conclusions

In summary, this investigation performed MD simulations to explain the impact of geometric structural attributes on membrane performance and the dynamics of intercalated cations through the RO process using cation-intercalated GO membranes. Firstly, a comprehensive multistep simulation protocol has been employed to develop non-lamellar GO membrane models. Subsequently, lamellar GO membrane models have been assembled using VMD software. Our findings emphasized significant differences in performance between lamellar and non-lamellar GO membranes.

Specifically, lamellar GO membranes exhibit higher water permeance due to their homogeneous interlayer gallery structure that facilitates efficient water transport. On the other hand, non-lamellar GO membranes demonstrate greater salt rejection, attributed to their irregular interlayer gallery arrangement, which imposed resistance to salt transport. Moreover, the complex morphology of non-lamellar GO membranes causes more intercalated cations retention within the GO layers for a longer duration, which enhances stability under aqueous conditions.

Furthermore, a comprehensive analysis of membrane stability has been explored by introducing two distinct types of intercalated cations (K^+, Mg^{2+}) within the membrane layers. The results demonstrated that more Mg^{2+} cations resided within the interlayer galleries for a longer time, attributed to their strong interactions with GO membranes and larger, more stable hydration shells. Additionally, Mg^{2+} intercalated membranes displayed superior water permeance compared to K^+ intercalated membranes due to their higher interlayer distance. In conclusion, this study comprehensively explains the relationship between membrane structural configurations, cation intercalation, and performance attributes. These findings can be significant for membrane designs and cation selections to achieve optimized desalination efficiency and stability in water treatment applications.

Chapter 8

Conclusions and Future Scope

8.1 Conclusions

From the non-equilibrium MD simulations performed in this Ph.D dissertation study, following conclusions are made:

- In a multilayered GO membrane, the water and ion permeance through membrane layers strongly depend on the number of oxygen-containing functional groups (OFGs) of the membrane. Decreasing the number of OFGs leads to smaller pore sizes of the membranes, and it tends to lower water permeance. Reducing the number of OFGs in the membrane also leads to less intercalation of ions inside the interlayer gallery of the membrane. Moreover, these OFGs have a significant role in separating amoxicillin (AMX) from pharmaceutical industrial wastewater. AMX molecules interact more strongly with hydroxyl and epoxy functional groups than carboxyl functional groups. Consequently, the AMX molecules are more likely to retain on the basal plane of the membrane.

- One major problem with layered GO membranes is their tendency to swell in aqueous environments. Cation intercalation inside the interlayer gallery of layered GO membrane emerges as one of the promising solutions to mitigate this problem. However, the effect of cationic concentration inside the membrane layers on water permeance and the salt rejection mechanism needs to be addressed. We observed that more cations inside the GO laminates cause resistance to water mobility, leading to lower water permeance. This study also reveals that Mg^{2+} ions have stronger interactions with the GO nanosheets than

K^+ ions. Thus, Mg^{2+} ion intercalated GO membranes maintained a more stable interlayer distance than K^+ ion intercalated GO membranes. In contrast, increasing cation concentration inside the GO layers increases Na^+ rejection but decreases Cl^- rejection. Although higher concentrations of intercalated cations don't favor water permeance, the presence of the cations stabilizes the GO laminates. Our simulation results emphasize that the water permeance and salt rejection trade-off of GO-based membranes can be better understood by tuning the concentration of intercalated cations. This study suggests that membranes should maintain an optimum concentration of cations to resolve the water permeance and salt rejection trade-off. Besides the membrane performance, this study also explains the stability of crude oil aggregation, which is significant for shale gas wastewater treatment. The nature of the crude oil aggregation phenomena varies for different cation-intercalated GO membranes, which needs further investigation. In this study, crude oil aggregation is stable for K^+ ion intercalated GO membranes due to their weaker interactions of K^+ ions with crude oil. In contrast, crude oil aggregation forms closer to the surface of Mg^{2+} ion intercalated GO membranes owing to their higher water permeance and stronger interactions of Mg^{2+} ion with crude oil. Moreover, Aromatics are more concentrated at the surface of the crude oil-water mixture (for all membranes) due to the lower interfacial tension of aromatics-water.

- GO membranes, known for their efficacy in rejecting smaller molecules, face limitations due to undesirable swelling in aqueous environments. In this aspect, the potential of cation-intercalated GO membranes as RO membranes is investigated in boron removal via nonequilibrium MD simulations. The optimum pore size for boron rejection is proposed by constructing two types of cationic intercalated GO membranes (K^+ or Mg^{2+}) with different pore widths. Boron can be present in the form of boric acid or borate ion, depending on the pH of the solution; as a result, neutral boric acid and negatively charged borate ions are considered in this work to investigate the boron rejection mechanism. This study observed that all membranes reject borate ions effectively compared to boric acid. The reason is that borate ions hold a bigger hydration shell than boric acid and exhibit stronger electrostatic repulsions with GO membranes. Moreover, K^+ ion intercalated GO membranes favor boron rejection because K^+ ions showed weaker electrostatic attraction with boric acid (or borate ions) than Mg^{2+} ions. Further, the re-

sults demonstrated a directly proportional relationship between boron rejection and the intensity of interactions with OFGs of the GO membrane. Boric acid molecules interact strongly with hydroxyl and epoxy functional groups, whereas borate ions interact strongly with carboxyl functional groups. In addition, boric acid rejection decreases as the pore width of the membrane increases. However, these multilayered cationic intercalated GO membranes delivered better boric acid rejection for wider pores (12 Å) than nanoporous graphene and polymeric membranes. At the same time, all membranes exhibited superior borate ion rejection. Furthermore, compared to Mg^{2+} ion intercalated GO membranes, K^+ ion intercalated GO membranes exhibit greater Cl^- rejection, poor Na^+ rejection, and lower water permeance.

- Similarly, human urine, a rich source of valuable smaller compounds such as urea and ammonia (essential feedstock for urea production), requires efficient recovery methods to meet the increasing global demand for urea. Thus, this study uses non-equilibrium MD simulations to investigate the recovery of urea and ammonia from human urine using a cation-intercalated GO membrane in the FO separation process. This simulation study considers three distinct feed solutions based on nitrogen forms: urea, NH_3, and NH_4^+. Our findings reveal that GO membranes exhibit superior rejection of urea compared to NH_3 due to factors such as larger hydration size of urea, stronger attraction with GO nanosheets, and the formation of small urea aggregates. Furthermore, this study highlights that nitrogen in the form of NH_4^+ demonstrates greater rejection compared to NH_3, attributed to the stable hydration shell of positively charged NH_4^+ ions, stronger attraction with GO nanosheets, and electrostatic repulsion with intercalated cations in contrast to neutral NH_3 molecules. Additionally, the present study underscores that the hydroxyl and epoxy functional groups of the GO nanosheets significantly inhibit the permeation rates of urea and NH_4^+, resulting in substantial recovery. This research further demonstrates that GO membranes achieved higher water permeance with fresh human urine compared to hydrolyzed urine, attributed to a greater osmotic pressure gradient and salt rejection exceeding 94%.

- Although cation intercalation inside the GO membranes has emerged as a promising strategy to control the swelling tendency of GO membranes in aqueous environments, there is a need to address the longevity of the intercalated cations within the GO laminates, as

the stability of membranes relies on the interactions between these intercalated cations and GO nanosheets. Moreover, the retention of intercalated cations inside the interlayer gallery of GO membranes depends on the morphology and structural arrangement of interlayer galleries. Thus, this investigation performed MD simulations to explain the impact of geometric structural attributes on membrane performance and the dynamics of intercalated cations through the RO process using cation-intercalated GO membranes. Firstly, a comprehensive multistep simulation protocol has been employed to develop non-lamellar GO membrane models. Subsequently, lamellar GO membrane models have been assembled using VMD software. Our findings emphasized significant differences in performance between lamellar and non-lamellar GO membranes. Specifically, lamellar GO membranes exhibit higher water permeance due to their homogeneous interlayer gallery structure that facilitates efficient water transport. On the other hand, non-lamellar GO membranes demonstrate greater salt rejection, attributed to their irregular interlayer gallery arrangement, which imposed resistance to salt transport. Moreover, the complex morphology of non-lamellar GO membranes causes more intercalated cations retention within the GO layers for a longer duration, which enhances stability under aqueous conditions. Furthermore, a comprehensive analysis of membrane stability has been explored by introducing two distinct types of intercalated cations (K^+, Mg^{2+}) within the membrane layers. The results demonstrated that more Mg^{2+} cations resided within the interlayer galleries for a longer time, attributed to their strong interactions with GO membranes and larger, more stable hydration shells. Additionally, Mg^{2+} intercalated membranes displayed superior water permeance compared to K^+ intercalated membranes due to their higher interlayer distance.

8.2 Scope for Future Investigations

Continuing the research and observations outlined in the current study, it would be worthwhile to explore the following points in future investigations:

- **Exploration of GO membranes with diverse draw solutions:**

  Particularly in the FO process, beyond selecting the membrane material, a promising direction involves exploring diverse draw solutions with GO membranes and assessing

its anti-fouling properties in challenging feed environments. Furthermore, to ensure the sustainability of the FO process, it will be necessary to focus on the regeneration and reuse of draw solutions. Hence, integrating membrane distillation with FO systems will be essential. Therefore, future efforts will focus on developing and applying this composite simulation setup to diverse feed and draw solutions to evaluate membrane performance and draw solution regeneration.

- **Retention time of intercalated cations:**

  As discussed earlier, GO membranes tend to swell in aqueous environments, and cation intercalation shows promising results in mitigating this swelling nature. However, we have observed that some intercalated cations are migrating out of the membrane layers during FO and RO simulations. In this regard, exploring various simulation strategies to understand and extend the retention time of intercalated cations within GO membrane layers during FO and RO processes presents an exciting opportunity. This effort aims to maintain a consistent interlayer distance, ultimately enhancing membrane performance.

- **Modifying GO-based membrane strategies with polymeric materials:**

  Despite the significant progress of free-standing GO-based membranes in membrane separation applications, there is a need for GO membranes supported on suitable mechanical substrates for high-pressure applications. Furthermore, depositing GO layers onto specific polymeric or inorganic membrane surfaces could enhance the separation performance and antifouling properties of the GO-based membranes. Recent research has utilized GO nanosheets directly as active separation layers in free-standing and supported GO membranes. However, presently, researchers are directing their efforts toward modifying GO membranes with polymeric materials using various methods. In this aspect, two primary strategies have emerged: the direct incorporation of GO nanosheets into polymeric casting solutions during membrane fabrication and surface modification of GO nanosheets through crosslinking with polymeric materials. This exploration aims to enhance the chemical and mechanical stability of the membranes, ultimately enhancing the performance of GO-based membranes.

- **Assessing GO membranes under diverse driving gradients:**

  In the future, there is an exciting prospect in understanding and assessing GO membranes

under diverse driving gradients, including temperature and electric potential. Investigating the behavior of GO membranes under these conditions could provide valuable insights into their performance and potential applications in various separation processes. By exploring the effects of temperature and electric potential on GO membranes, researchers can optimize their design and operation for enhanced efficiency and selectivity. This research direction holds promise for advancing the field of membrane technology and expanding the applications of GO membranes in diverse industrial processes.

We hope that the findings presented in this study will serve as valuable insights for future research on GO membranes in desalination and wastewater treatment applications.

Appendix A

Research Output

Articles Published

- **P. Rajasekhar Reddy**, K. Anki Reddy, and Amit Kumar. "Comparative Retention Analysis of Intercalated Cations Inside the Interlayer Gallery of Lamellar and Nonlamellar Graphene Oxide Membranes in Reverse Osmosis Process: A Molecular Dynamics Study." **The Journal of Physical Chemistry B (ACS)** (2024).

- **P. Rajasekhar Reddy**, Amit Kumar, and K. Anki Reddy. "Understanding the boron rejection of cation intercalated multilayered graphene oxide (GO) membrane in reverse osmosis (RO) process: A molecular dynamics study." **Journal of Molecular Liquids (Elsevier)** 389 (2023): 122817.

- **P. Rajasekhar Reddy**, Abhijit Gogoi, and K. Anki Reddy. "Cationic stabilized layered graphene oxide (GO) membrane for shale gas wastewater treatment: An atomistic insight." **Desalination (Elsevier)** 559 (2023): 116621.

- **P. Rajasekhar Reddy**, Abhijit Gogoi, and K. Anki Reddy. "Effect of oxygen-containing functional groups of layered graphene oxide membrane on the removal of amoxicillin: a molecular dynamics study." **Molecular Simulation (Taylor & Francis)** 48.3 (2022): 185-196.

Manuscripts under review

- P. Rajasekhar Reddy, Amit Kumar, and K. Anki Reddy. "Urea and ammonia recovery from human urine by forward osmosis process using cation intercalated graphene oxide membrane: A molecular dynamics study"

Conferences

- Presented a research poster at the Outreach Symposium on "**Molecular Simulations: Advances and Applications**", organized by the **Department of Chemical Engineering, IIT Bombay** during 2^{nd} - 3^{rd} June, 2023.
- Presented a research poster in **SCIENTIFIQUE : POSTER PRESENTATION** under department of Chemical Engineering at "**Research & Industrial Conclave - Integration'23**" organized by the **Student's Academic Board, IIT Guwahati and IIT Guwahati Research Park** during 14-16^{th} May, 2023.

Collaborations

- Pathan, Shabnam, Sk Safikul Islam, Ria Sen Gupta, Barnali Maity, **P. Rajasekhar Reddy**, Samir Mandal, K. Anki Reddy, and Suryasarathi Bose. "Fundamental Understanding of Ultrathin, Highly Stable Self-Assembled Liquid Crystalline Graphene Oxide Membranes Leading to Precise Molecular Sieving through Non-equilibrium Molecular Dynamics." **ACS nano** 17 (2023): 7272-7284.
- Sk Safikul Islam, Anjali Kumari, Arya S, Shabnam Pathana, **P. Rajasekhar Reddy**, Ria Sen Guptaa, K. Anki Reddy and Suryasarathi Bose. "Precise molecular sieving by careful selection of solvent and functional motif in graphene oxide liquid crystal membranes" (**Under review**)

Appendix B

Supplementary Information for Specific Chapters

B.1 Supplementary information for Chapter 3

Graphene Oxide (GO) Nanosheet and different type of GO membranes

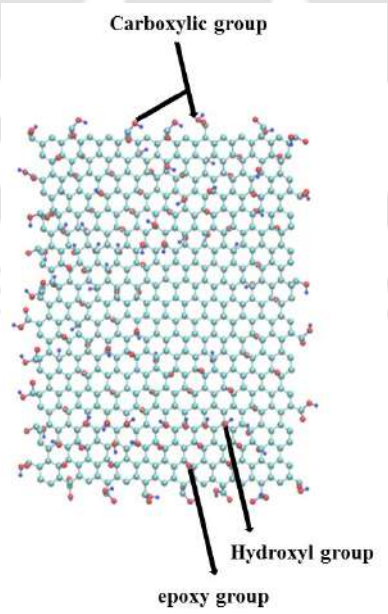

Figure B.1: Graphene Oxide sheet (50.0×49.0 Å^2) with oxygen functional groups. The blue color is for hydrogen atoms, the red color is for oxygen atoms and cyan color is for carbon atoms.

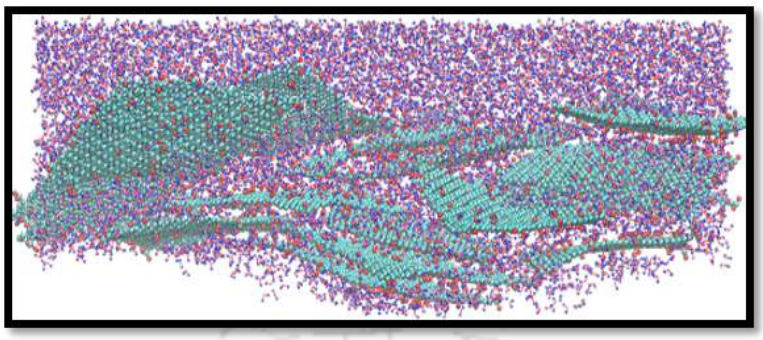

Figure B.2: rGO membrane. The blue color is for hydrogen atoms, the red color is for oxygen atoms and cyan color is for carbon atoms.

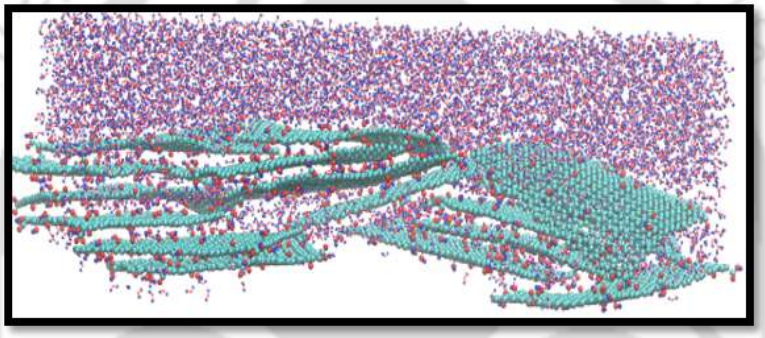

Figure B.3: ErGO membrane. The blue color is for hydrogen atoms, the red color is for oxygen atoms and cyan color is for carbon atoms.

Supporting results

The osmotic pressure gradient (which is a function of the draw solution concentration) drives the FO system. In the present work, a mixture of 3.0 M $MgCl_2$ and 0.05 M $Al_2(SO_4)_3$ solution is considered as the draw solution. We considered two more draw solutions concentrations [$MgCl_2$ (2M and 5M)]. The non-equilibrium MD simulations are performed for the GO membrane with these draw solutions using the same feed solution concentration to study the water permeance as a function of an osmotic pressure gradient. As shown in Figure.B.4, the water permeance increases with the increase in the concentration of the draw solution[172].

The movies are created to visualize how the water molecules (shown in magenta color) are permeated through the membranes, and link is provided underneath.

Link: Water permeance of three membranes.

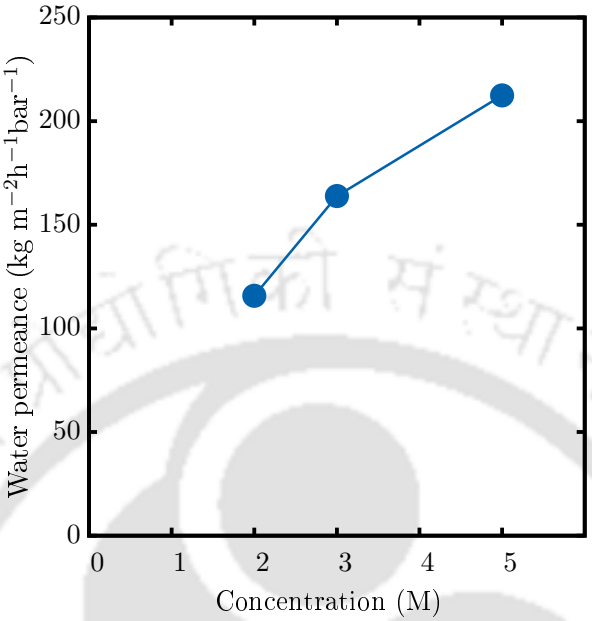

Figure B.4: Water permeance as a function of draw solution concentration.

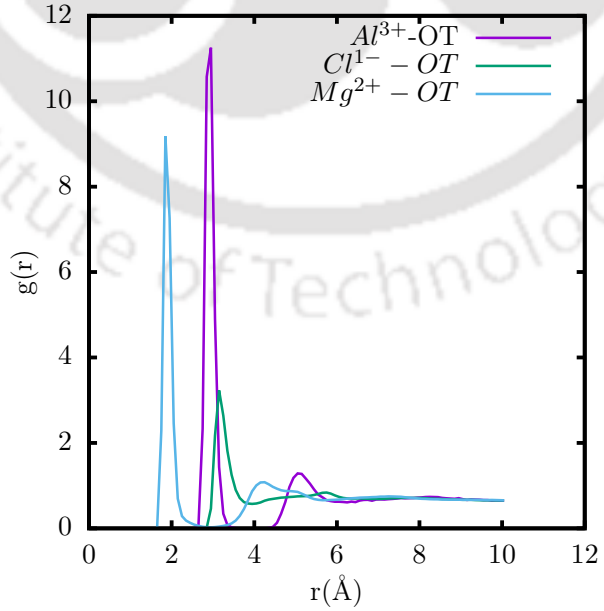

Figure B.5: RDF between the oxygen atom (OT) of the water molecule inside the GO membrane and ions of the draw solution.

B.2 Supplementary information for Chapter 4

The hydration shells of the Mg^{2+} ions of the GO-10-M, GO-15-M, and GO-20-M membranes at different times are presented in Fig. B.6, B.7, and B.8, respectively.

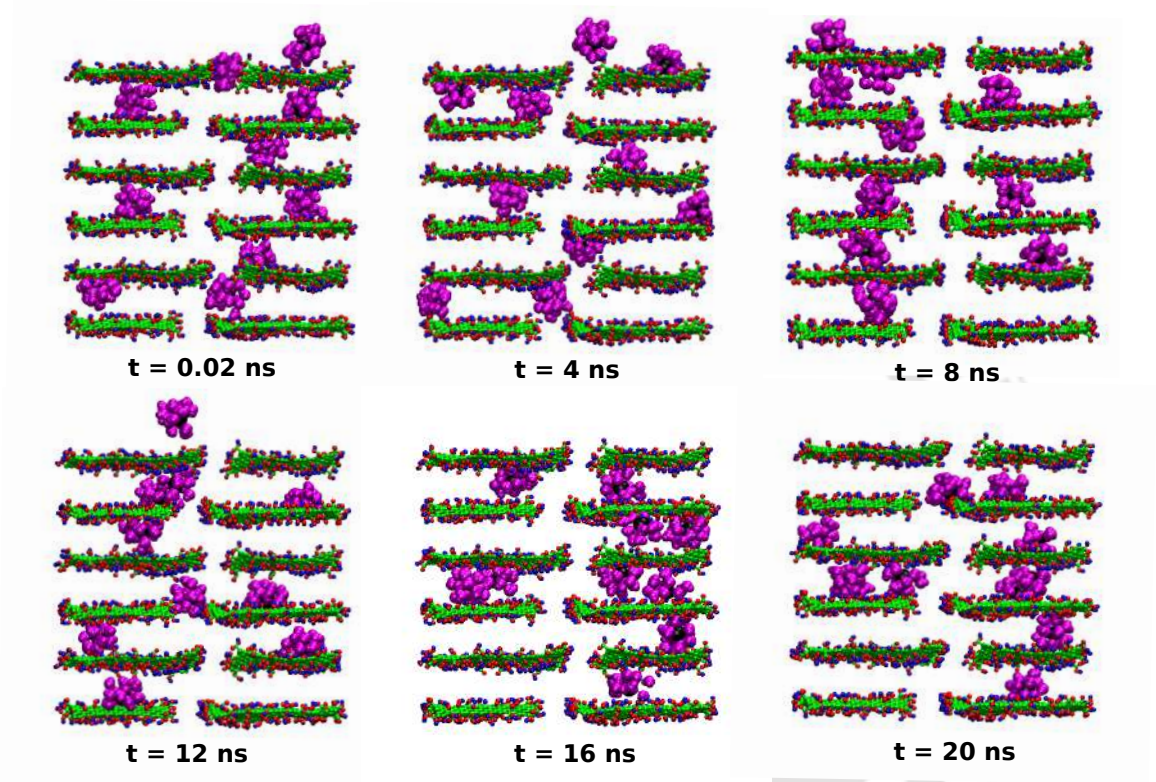

Figure B.6: The hydration shells of the Mg^{2+} ions of the GO-10-M membrane at different time. The blue color is for hydrogen atoms, the red color is for oxygen atoms and green color is for carbon atoms of the membrane. The black color is for Mg^{2+} ions and magenta color is for water molecules.

Water molecule coordination number (w(r))

Water molecule coordination number (w(r)) is defined as the integrals of the intercalated ions-water radial distribution function (g(r)) [227].The hydration shell of monovalent ions is lesser stable than the divalent ions, causing a frequent exchange of water molecules between the two hydration shells of monovalent ions. In other words, the hydration shell of K^+ ions is unstable, causing more significant interactions with the neighboring hydration shell of K^+ ions, leading to the formation larger hydration shell (after merging). In contrast, a stable hydration shell of Mg^{2+} ions yields lesser interactions with the adjacent hydration shell of Mg^{2+} ions, resulting

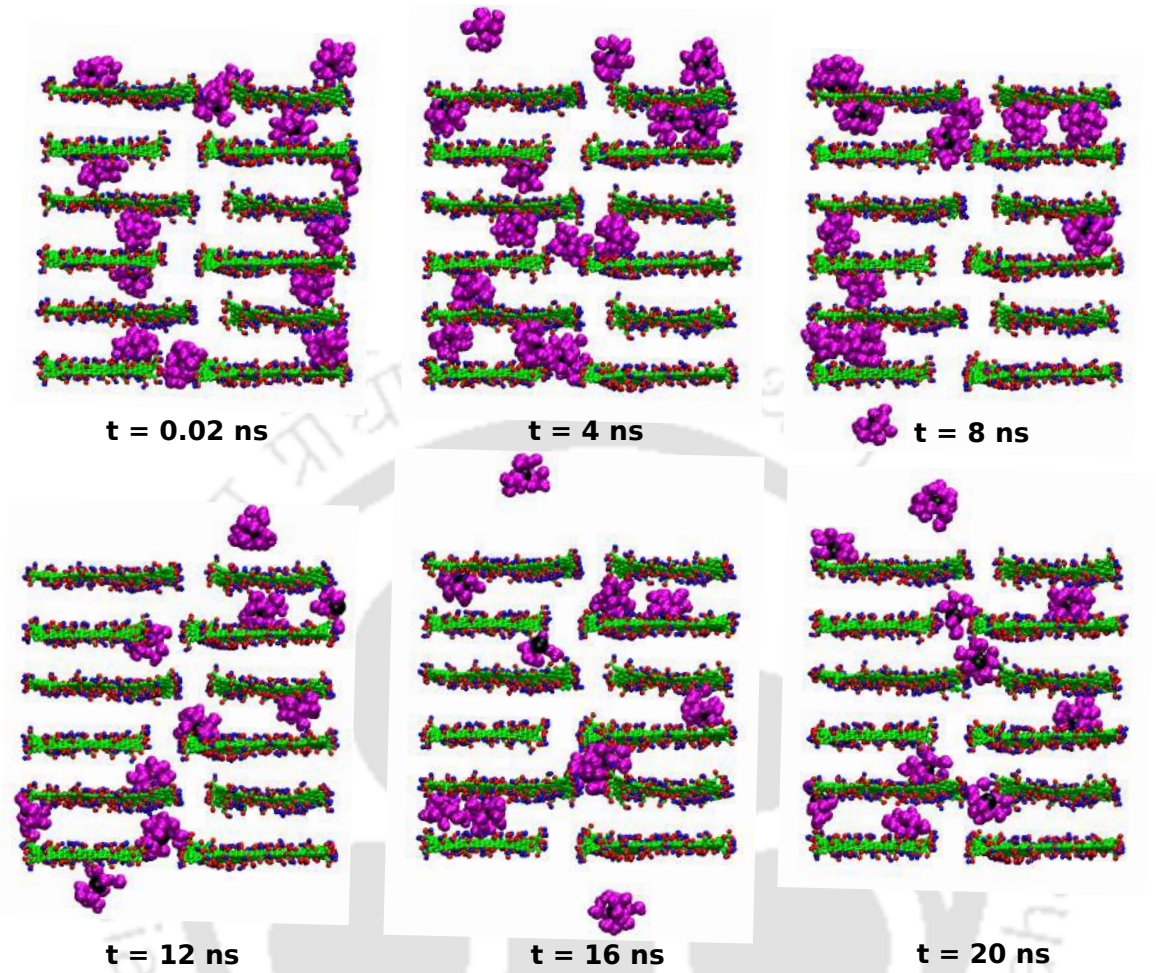

Figure B.7: The hydration shells of the Mg^{2+} ions of the GO-15-M membrane at different time. The blue color is for hydrogen atoms, the red color is for oxygen atoms and green color is for carbon atoms of the membrane. The black color is for Mg^{2+} ions and magenta color is for water molecules.

in a smaller hydration shell compared to K^+ ions (after merging). As shown in Fig. B.9, w(r) increases as the ionic concentration increases. It signifies that the number of water molecules in the hydration shell of intercalated ions increases as the ionic concentration increases due to the frequent merging of hydration shells which causes water resistance. Consequently, the movement of the water molecules through the membranes is impeded, resulting in lower water permeance as increasing the ionic concentration. The g(r) [82, 228, 229] defined,

$$g_{ij}(r) = \frac{P_{ij}(r, r + \Delta r)V}{4\Pi r^2 \Delta r P_i P_j} \tag{B.1}$$

In the above equation, r is the distance between a pair of particles i and j, V is the total

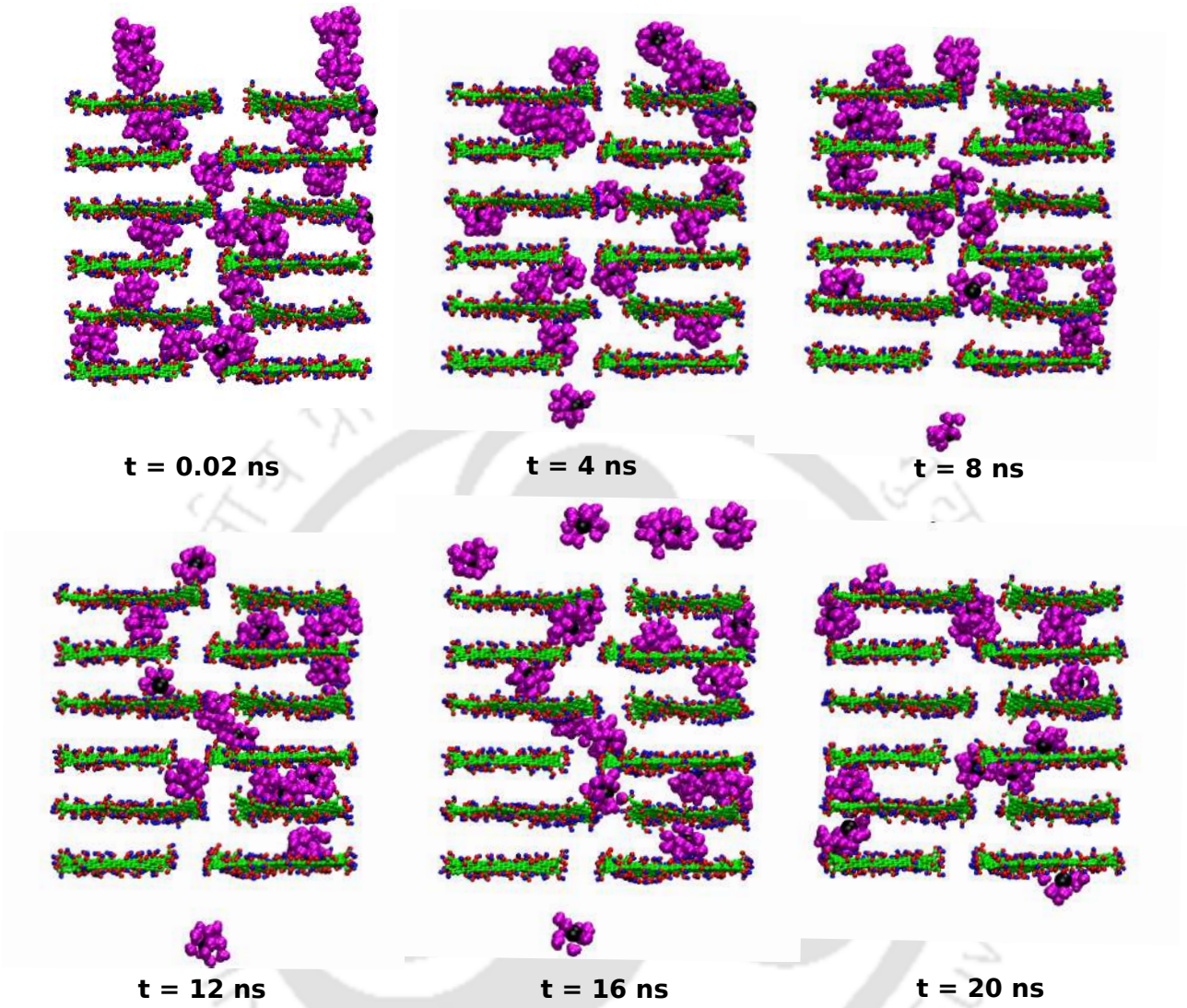

Figure B.8: The hydration shells of the Mg^{2+} ions of the GO-20-M membrane at different time. The blue color is for hydrogen atoms, the red color is for oxygen atoms and green color is for carbon atoms of the membrane. The black color is for Mg^{2+} ions and magenta color is for water molecules.

volume of the system, P_{ij}(r,r+Δr) is the number of atoms j around i within a shell from r to r+Δr, P_i and P_j indicates the number of atoms i and j, respectively.

Survival probability (SP)

The survival probability (SP) of water molecules within the membrane region is presented in Fig. B.10 to get further insights into the water diffusivity inside the membranes. Here, SP signifies the permeance time of the water molecules. The slower decay of SP indicates longer permeance

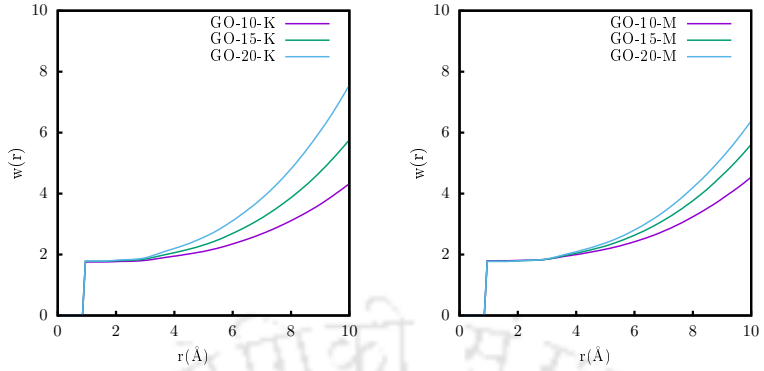

(a) (b)

Figure B.9: Water molecule coordination number (w(r)) of the intercalated ions. (a) K^+ ion intercalated and (b) Mg^{2+} ion intercalated GO membranes.

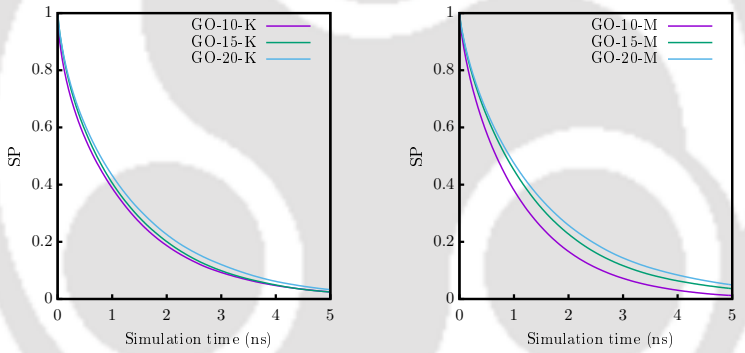

(a) (b)

Figure B.10: Survival probability (SP) of the water molecules in (a) K^+ ion intercalated and (b) Mg^{2+} ion intercalated GO membrane channels.

time, and the faster decay of SP indicates shorter permeance time. As shown in Fig. B.10(a), SP decays slowly for GO-20-K, followed by the GO-15-K and GO-10-K membranes. Likewsie, the GO-20-M membrane has slower decay of the SP, followed by the GO-15-M and GO-10-M membranes, as shown in Fig. B.10(b). In other words, the GO membranes containing a higher concentration of intercalated ions exhibit a slower SP decay. These SP results also indicate that membranes are exhibiting lower water permeance with an increase in the concentration of the intercalated ions.

The MD Analysis package[230, 231] is used to generate SP plots. The SP ($C_r(t)$) is defined

as [192, 232–234],

$$C_r(t) = \frac{1}{N_W} \sum_{j=1}^{N_W} \frac{\langle P_{Rj}(0) P_{Rj}(t) \rangle}{\langle P_{Rj}(0) \rangle^2} \tag{B.2}$$

In the above equation, P_{Rj} is a function that returns 1 if the j^{th} water molecule remains in an initially selected region at time t; otherwise, it returns zero. N_W is the total number of water molecules in the selected area.

Stability of the interlayer distance

For cationic intercalated GO membranes, the interlayer distance depends on the interactions between cations and oxygen-containing functional groups (OFGs), as well as cations and aromatic rings (AR). As shown in Fig. B.11 and B.12, the interactions between OFGs and cations are stronger than the interactions between AR and cations. In addition, the interaction energy between Mg^{2+} and OFGs is stronger than those between K^+ and OFGs, as shown in Fig. B.11 and B.12. It indicates that Mg^{2+} ions keep the interlayer distance between the GO layers more stable than K^+ ions.

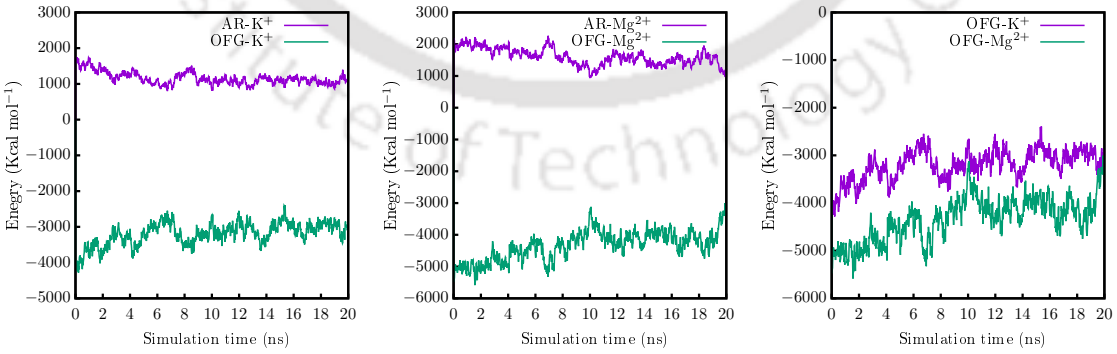

(a) (b) (c)

Figure B.11: Interaction energy of the oxygen-containing functional groups (OFGs) and aromatic rings (AR) with cations for (a) GO-15-K Membrane and (b) GO-15-M Membrane. (c) Comparative interaction energy (OFGs vs cations) of the GO-15-K and GO-15-M membranes.

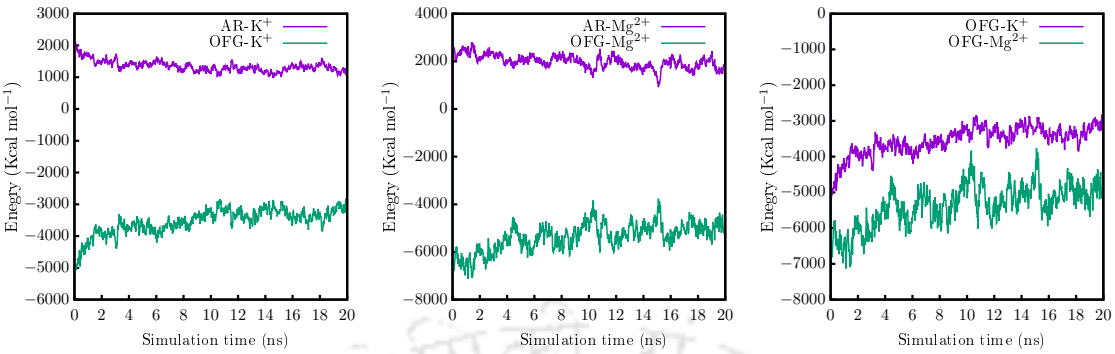

(a) (b) (c)

Figure B.12: Interaction energy of the oxygen-containing functional groups (OFGs) and aromatic rings (AR) with cations for (a) GO-20-K Membrane and (b) GO-20-M Membrane. (c) Comparative interaction energy (OFGs vs cations) of the GO-20-K and GO-20-M membranes.

Crude oil aggregation and rejection

Fig. B.13 (a),(b) shows the density profiles of the crude oil - water mixture for the GO-10-K and GO-10-M membranes. Fig. B.14 (a),(b) shows the density profiles of the crude oil - water mixture for the GO-20-K and GO-20-M membranes. It is observed that for the GO-10-K and GO-20-K membranes, crude oil forms one large aggregate. On the other hand, for the GO-10-M and GO-20-M membranes, crude oil forms two small aggregates. It indicates that crude oil aggregation is more stable for the K^+ ion intercalated membranes.

The interaction energies of hydrocarbons with oxygen atom of water (OT) for the GO-10-K and GO-10-M membranes are shown in Fig. B.13(c) and (d). The interaction energies of hydrocarbons with oxygen atom of water (OT) for the GO-20-K and GO-20-M membranes are shown in Fig. B.14(c) and (d). It shows that aromatics interact more strongly with water, which means aromatics are more concentrated at the crude oil-water interface for all membranes. The snapshots are shown in Fig. B.15 and B.16, confirming that crude oil aggregation is more stable in the K^+ ion intercalated membranes. The van der Waals (vdW) interaction energy of crude oil with intercalated ions is presented in Fig. B.17.

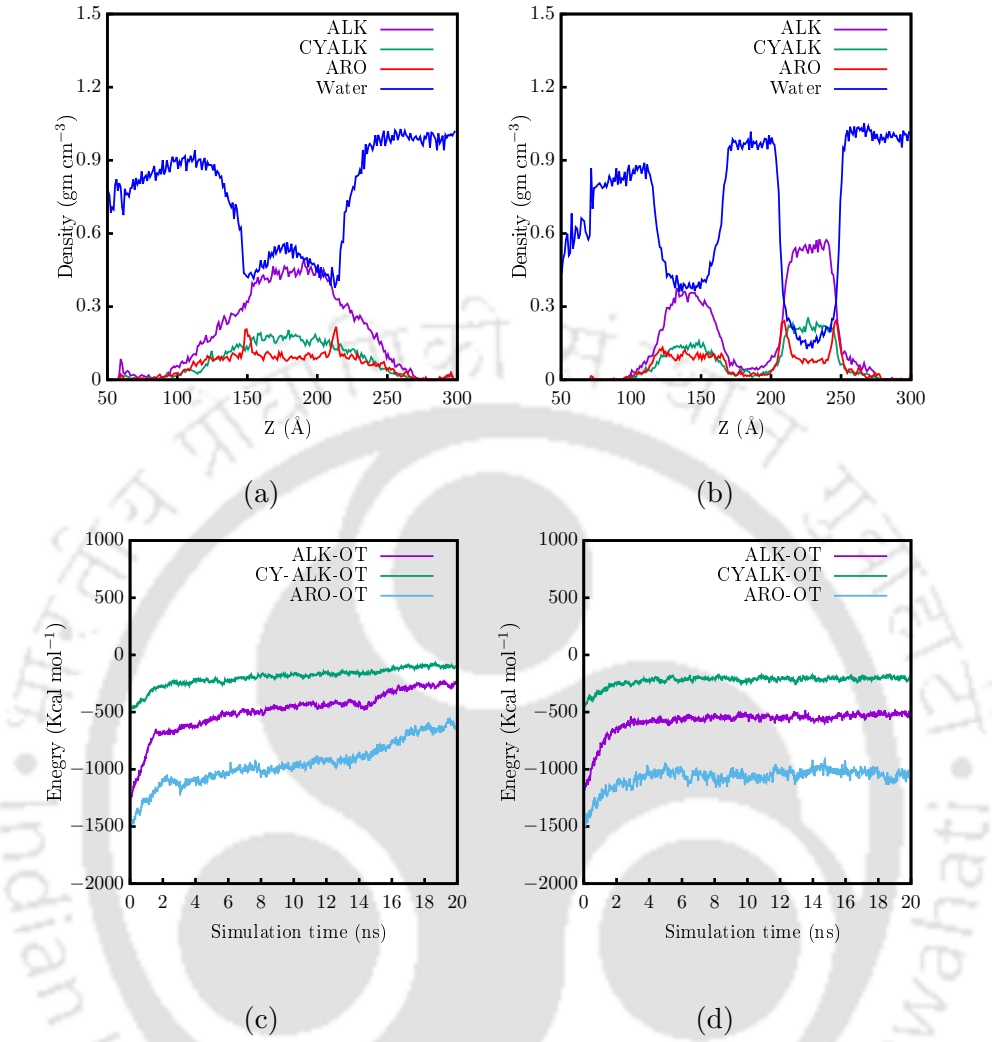

Figure B.13: The denisty profiles of the crude oil-water mixture [alkanes (ALK), cycloalkanes (CYALK), aromatics (ARO), water] along the Z direction for (a) GO-10-K membrane and (b) GO-10-M membrane. Interaction energy of the hydrocarbons with oxygen of water (OT) for (c) GO-10-K membrane and (d) GO-10-M membrane.

Salt rejection

The distribution of Na^+ and Cl^- ions in K^+ ion intercalated membranes at the end of the simulations are shown in Fig. B.18 and B.19, respectively. The distribution of Na^+ and Cl^- ions in Mg^{2+} ion intercalated membranes at the end of the simulations are shown in Fig. B.20 and B.21, respectively. The results of these membranes are similar to the K^+ ion intercalated membranes. Fig. B.22(a) and (b) illustrates the electrostatic interaction energies of K^+ ions with Na^+ and Cl^- ions, respectively.

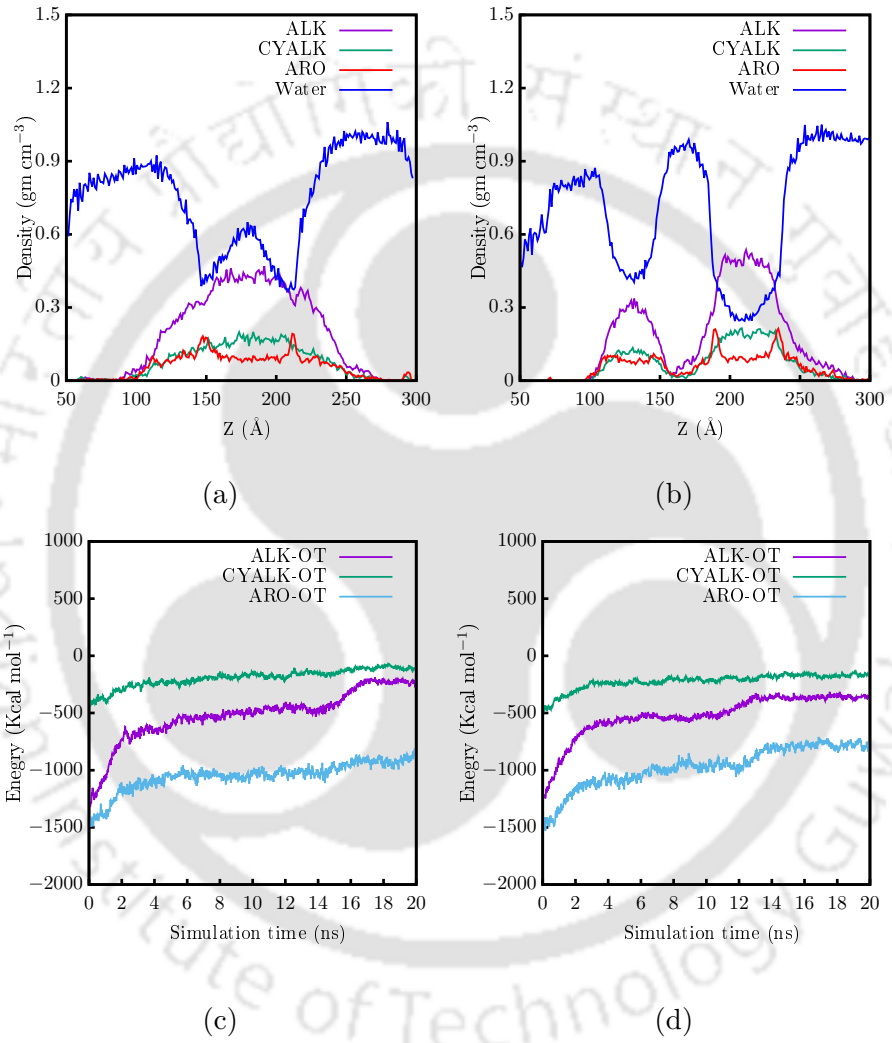

Figure B.14: The denisty profiles of the crude oil-water mixture [alkanes (ALK), cycloalkanes (CYALK), aromatics (ARO), water] along the Z direction for (a) GO-20-K membrane and (b) GO-20-M membrane. Interaction energy of the hydrocarbons with oxygen of water (OT) for (c) GO-20-K membrane and (d) GO-20-M membrane.

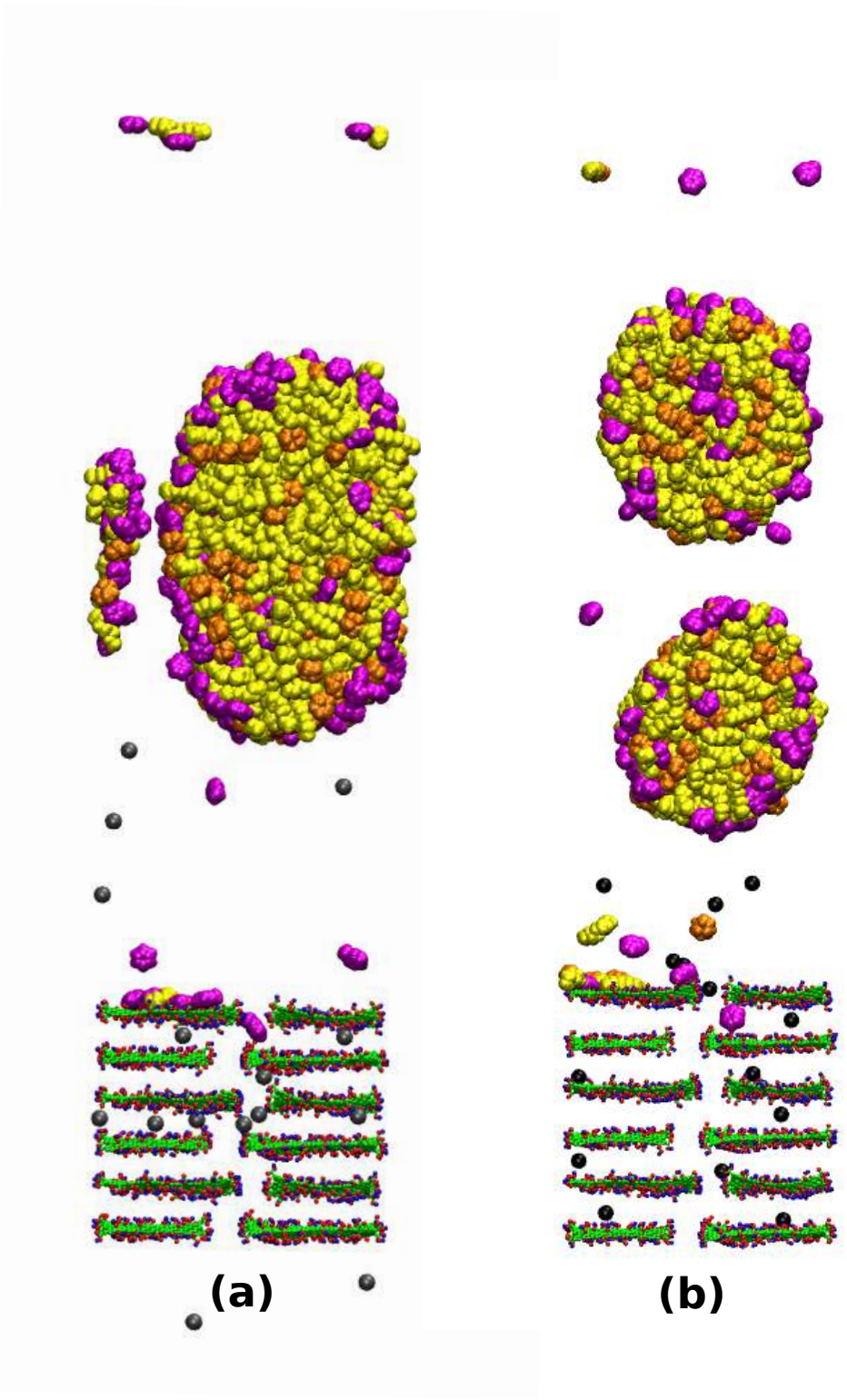

Figure B.15: Snapshot of crude oil aggregation in (a) GO-15-K membrane and (b) GO-15-M membrane. Green color is for carbon atoms, red color is for oxygen atoms, blue color is for hydrogen atoms, gray color is for K^+ ions, black color is for Mg^{2+} ions, yellow color is for alkanes, orange color is for cycloalkanes, and magenta color is for aromatics.

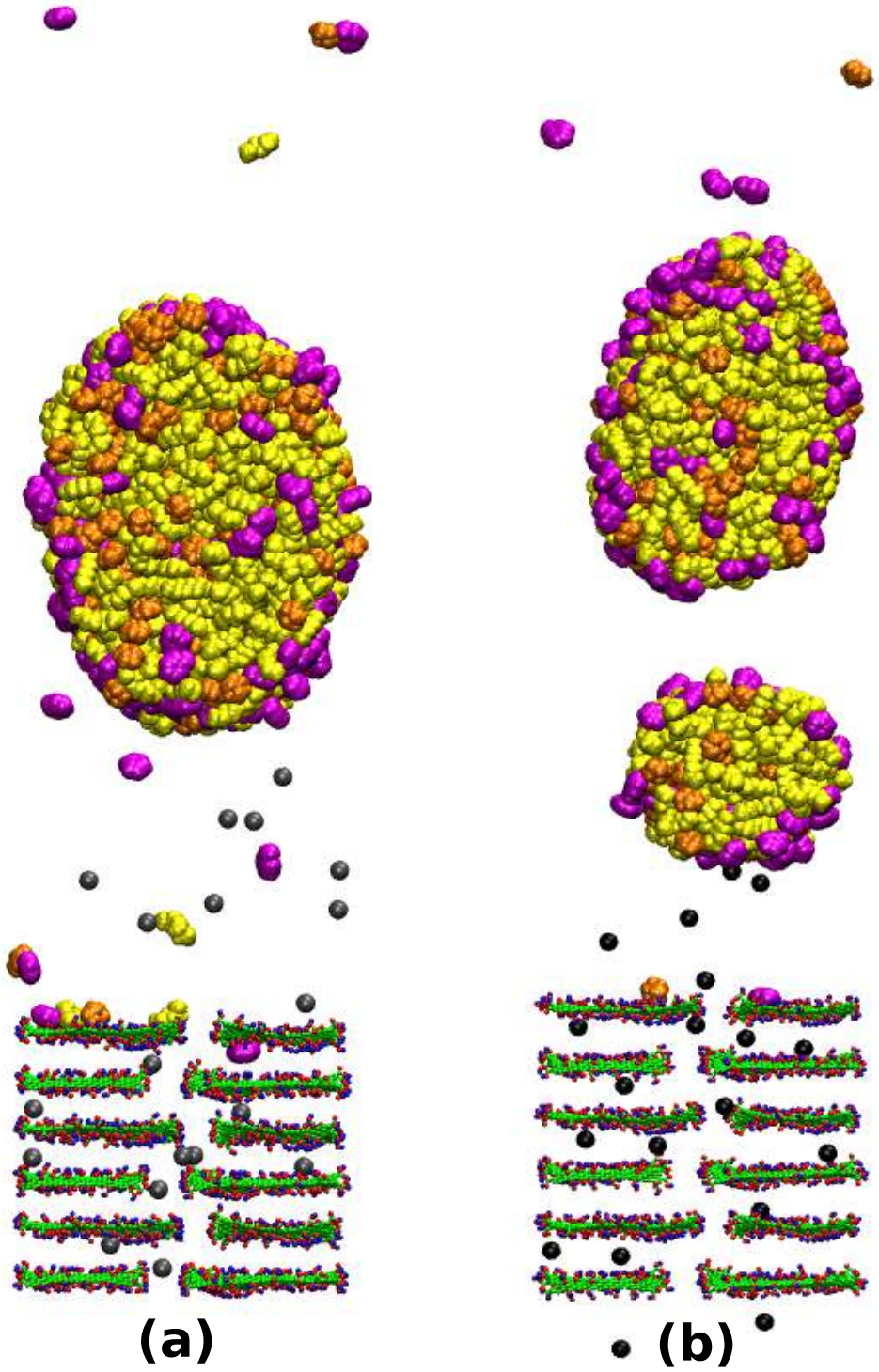

Figure B.16: Snapshot of crude oil aggregation in (a) GO-20-K membrane and (b) GO-20-M membrane. Green color is for carbon atoms, red color is for oxygen atoms, blue color is for hydrogen atoms, gray color is for K^+ ions, black color is for Mg^{2+} ions, yellow color is for alkanes, orange color is for cycloalkanes, and magenta color is for aromatics.

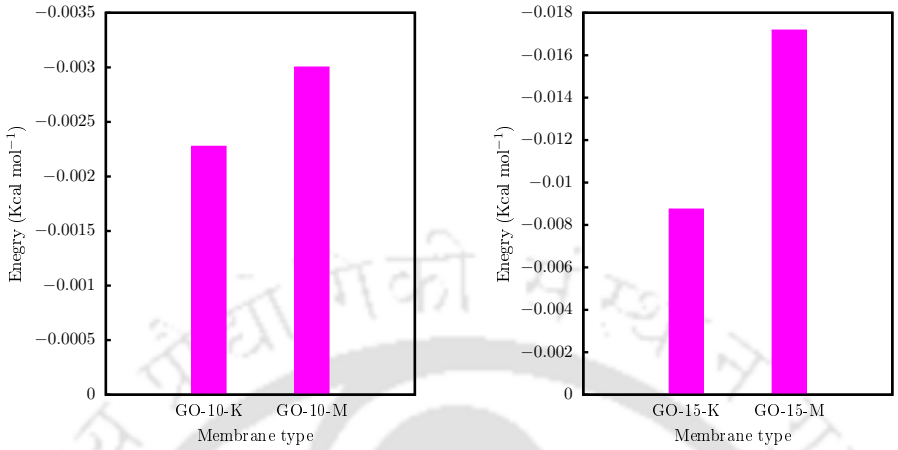

Figure B.17: Interaction energy of the crude oil with the intercalated ions (K^+, Mg^{2+}). (a) GO-10-K and GO-10-M membranes. (b) GO-20-K and GO-20-M membranes.

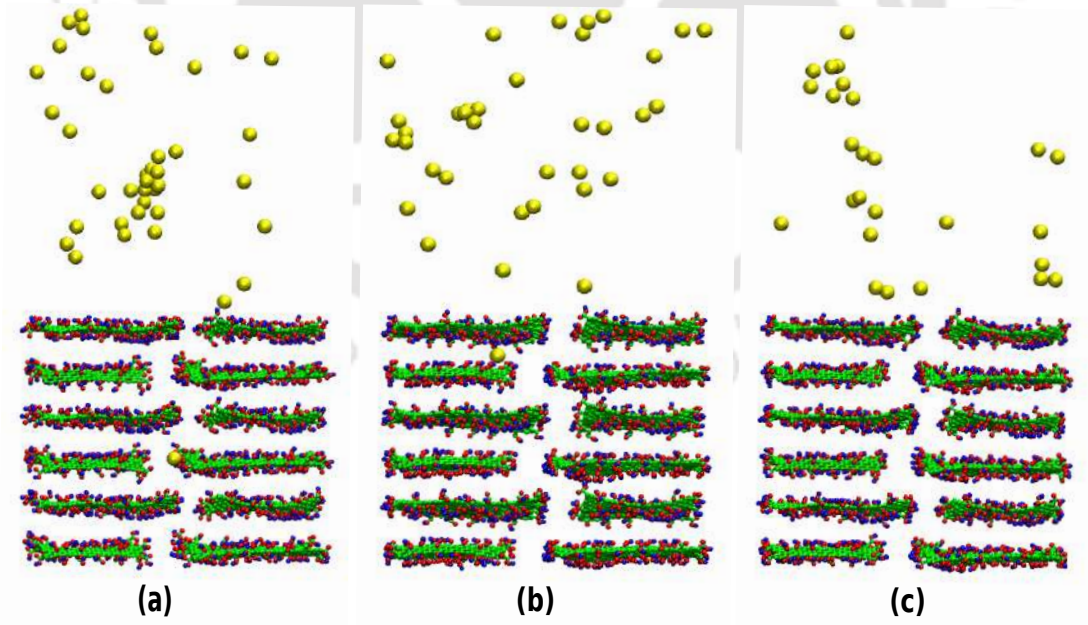

Figure B.18: Distribution of the Na^+ ions for (a) GO-10-K, (b) GO-15-K, and (c) GO-20-K membranes, at the end of the simulation. Green color is for carbon atoms, red color is for oxygen atoms, blue color is for hydrogen atoms, and yellow color is for Na^+ ions.

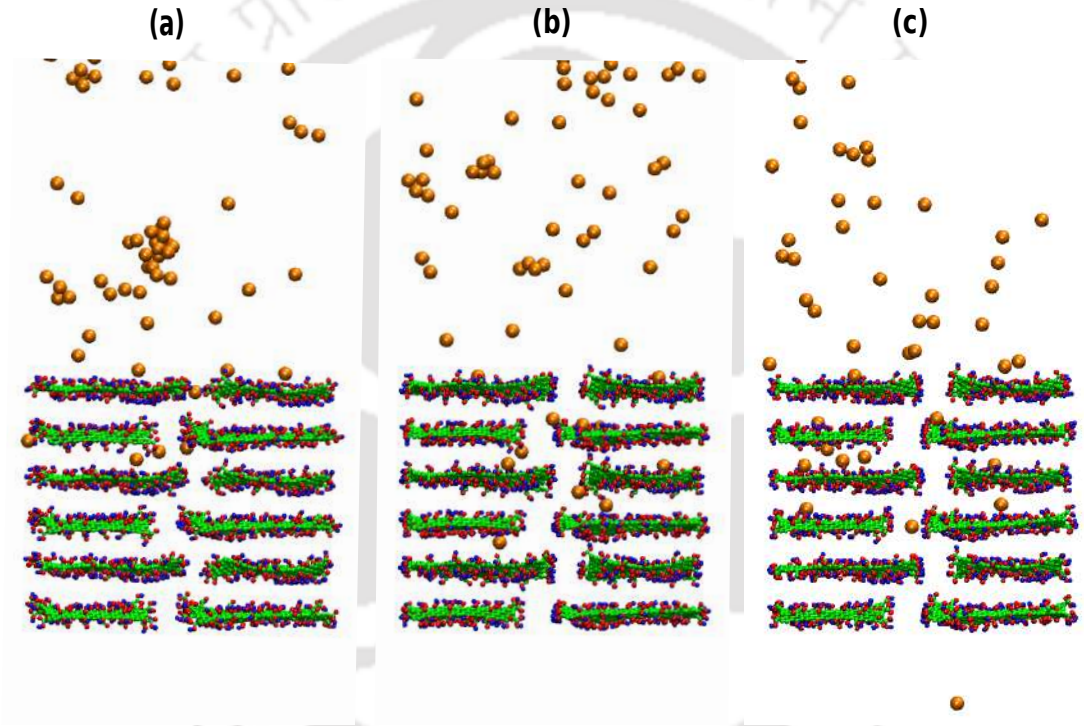

Figure B.19: Distribution of the Cl^- ions for (a) GO-10-K, (b) GO-15-K, and (c) GO-20-K membranes, at the end of the simulation. Green color is for carbon atoms, red color is for oxygen atoms, blue color is for hydrogen atoms, and orange color is for Cl^- ions.

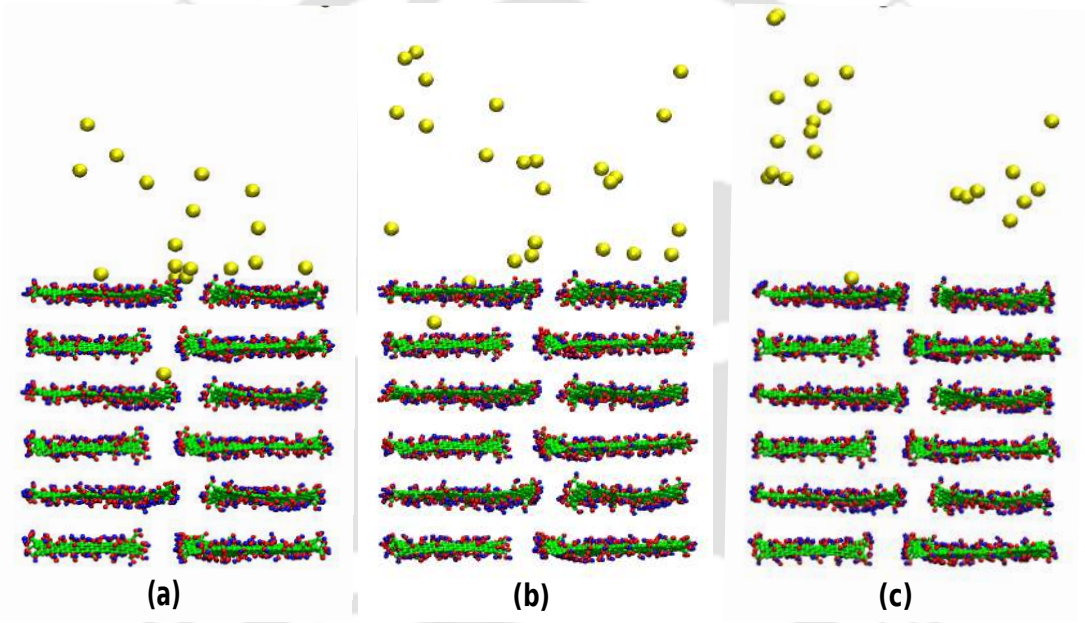

Figure B.20: Distribution of the Na^+ ions for (a) GO-10-M, (b) GO-15-M, and (c) GO-20-M membranes, at the end of the simulation. Green color is for carbon atoms, red color is for oxygen atoms, blue color is for hydrogen atoms, and yellow color is for Na^+ ions.

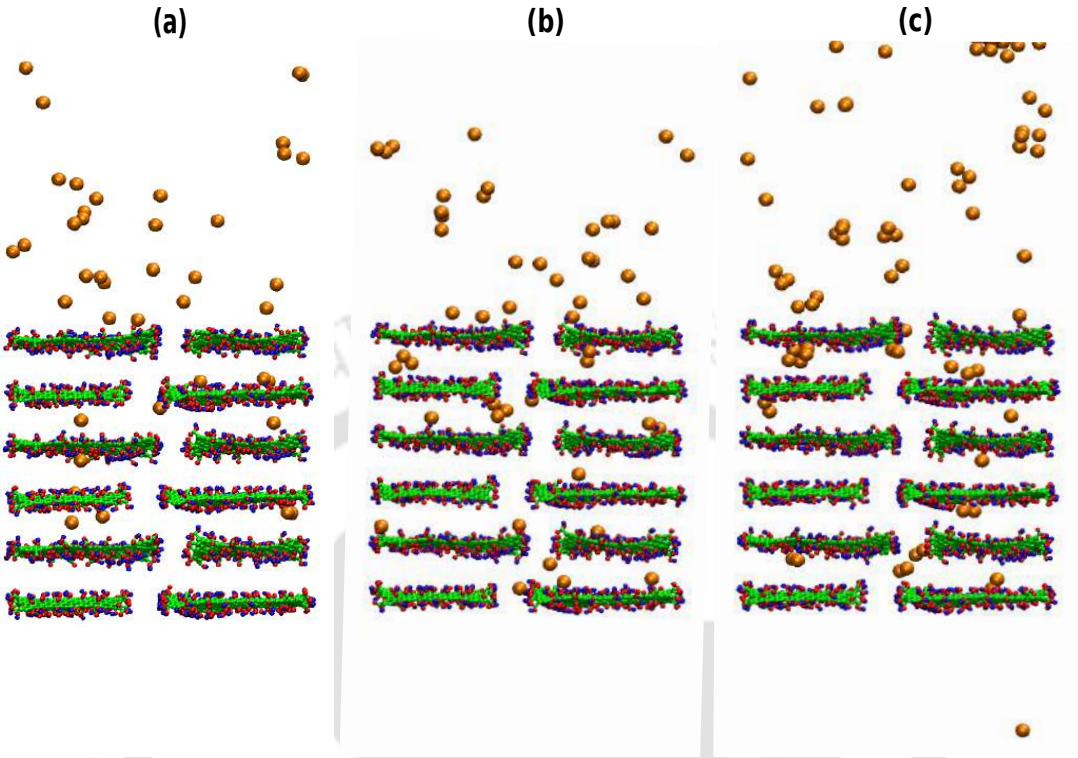

Figure B.21: Distribution of the Cl^- ions for (a) GO-10-M, (b) GO-15-M, and (c) GO-20-M membranes, at the end of the simulation. Green color is for carbon atoms, red color is for oxygen atoms, blue color is for hydrogen atoms, and orange color is for Cl^- ions.

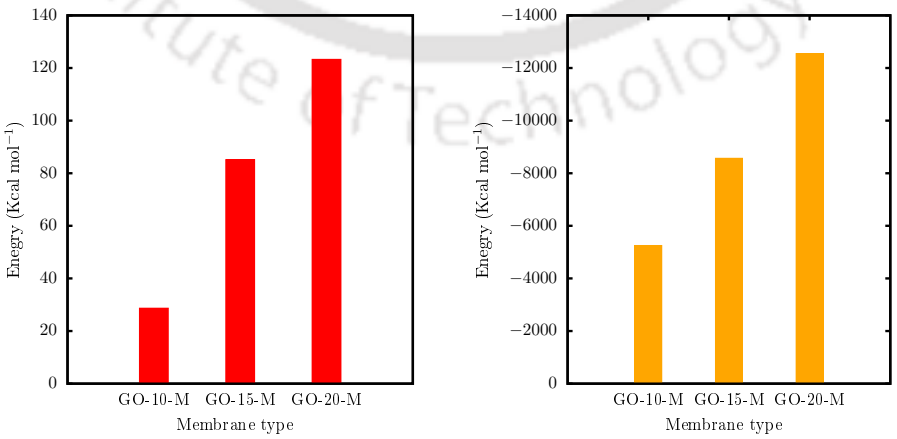

(a) (b)

Figure B.22: Average interaction energy of the Mg^{2+} ions with (a) Na^+ and (b) Cl^- ions.

Effect of the pore width (P)

Fig. B.23 and B.24 illustrate the distribution of Na^+ and Cl^- ions for K^+ ion intercalated membranes with different pore widths at the end of the simulations, respectively. Fig. B.25 and B.26 illustrate the distribution of Na^+ and Cl^- ions for Mg^{2+} ion intercalated membranes with different pore widths at the end of the simulations, respectively.

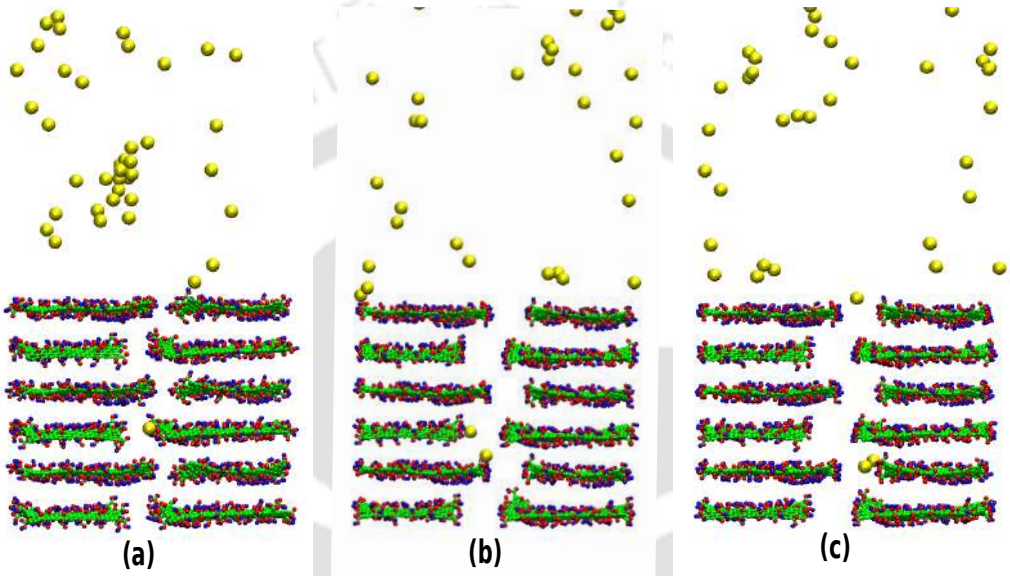

Figure B.23: Distribution of the Na^+ ions for (a) GO-10-K, (b) GO-10-K-10P, and (c) GO-10-K-12P membranes, at the end of the simulation. Green color is for carbon atoms, red color is for oxygen atoms, blue color is for hydrogen atoms, and yellow color is for Na^+ ions.

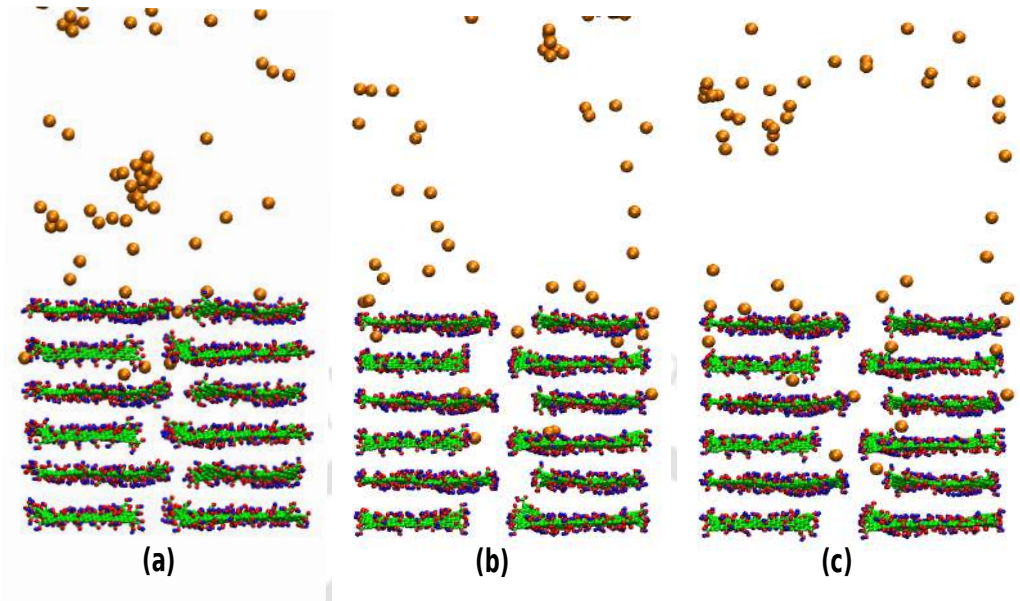

Figure B.24: Distribution of the Cl^- ions for (a) GO-10-K, (b) GO-10-K-10P, and (c) GO-10-K-12P membranes, at the end of the simulation. Green color is for carbon atoms, red color is for oxygen atoms, blue color is for hydrogen atoms, and orange color is for Cl^- ions.

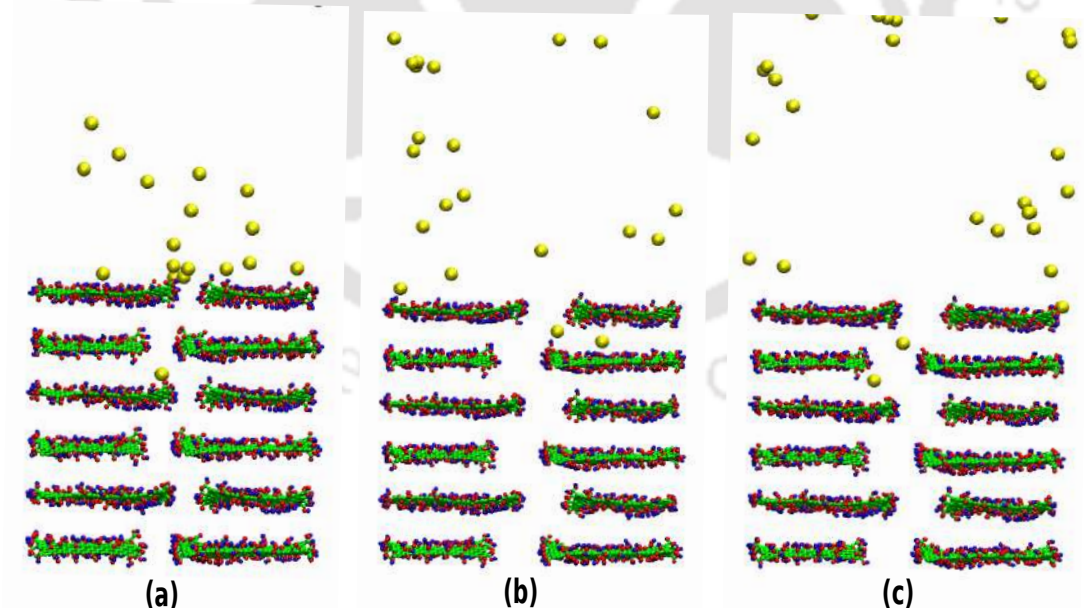

Figure B.25: Distribution of the Na^+ ions for (a) GO-10-M, (b) GO-10-M-10P, and (c) GO-10-M-12P membranes, at the end of the simulation. Green color is for carbon atoms, red color is for oxygen atoms, blue color is for hydrogen atoms, and yellow color is for Na^+ ions.

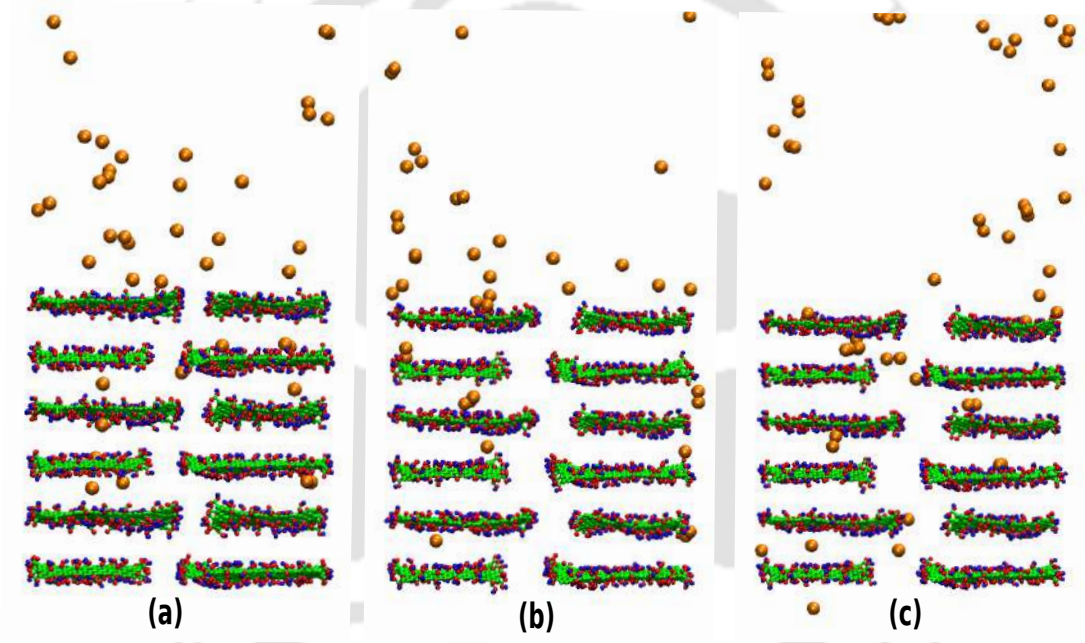

Figure B.26: Distribution of the Cl^- ions for (a) GO-10-M, (b) GO-10-M-10P, and (c) GO-10-M-12P membranes, at the end of the simulation. Green color is for carbon atoms, red color is for oxygen atoms, blue color is for hydrogen atoms, and orange color is for Cl^- ions.

Effect of the pore offset (O)

A few simulation studies show that water permeance decreases as the pore offset increases, and this is due to the multilayered GO membrane with a higher pore offset providing more water permeation resistance [62, 71]. Typically, water experiences three types of resistance during the permeation through the multilayered GO membranes: flow resistance at the entrance gap (R1), turning flow resistance at the entry gap into the interlayer gallery (R2), and interlayer flow resistance within channels (R3). A series combination of these three resistances is defined as the membrane's overall transport resistance (R). When the pore offset = 0; R = 2R1, when pore offset $\neq$ 0; R = 2R1 + R2 + R3. In other words, the addition of turning flow and interlayer flow resistance results in an increase in the total resistance of the membrane with an increase in pore offset. Additionally, this study performed simulations with a large pore offset of 16 Å to investigate the impact of pore offset on water permeance. As shown in figure.B.27, water permeance decreases as membrane pore offset increases.

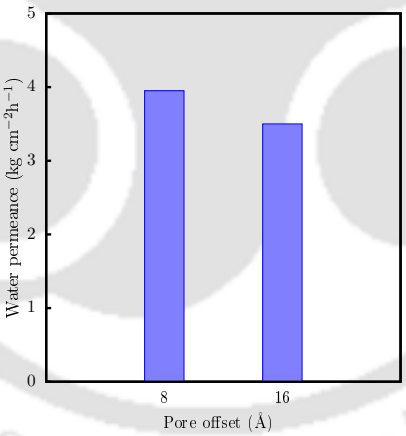

Figure B.27: Water permeance as a function of the pore offset.

Figures. B.28 and B.29 show the distribution of the salt ions (Na^+ and Cl^-) for membranes with different pore offsets (8 and 16 Å) at the end of the simulations. As shown in figure. B.28, when an offset is 8 Å, one Na^+ ion enters the membrane layers, but none does when the offset is 16 Å. Similarly, Cl^- ions move to the 5^{th} layer of the membranes when the offset is 8 Å but are restricted to the 4^{th} layer of the membranes when the offset is 16 Å, as shown in figure. B.29. Contrary to water permeance, the ability of salt rejection increases by increasing the offset of the membrane. However, salt rejection decreases with an increasing the interlayer distance of the membranes. Hence, improved salt rejection is achieved by enlarging the offset and smaller

the interlayer distance [62].

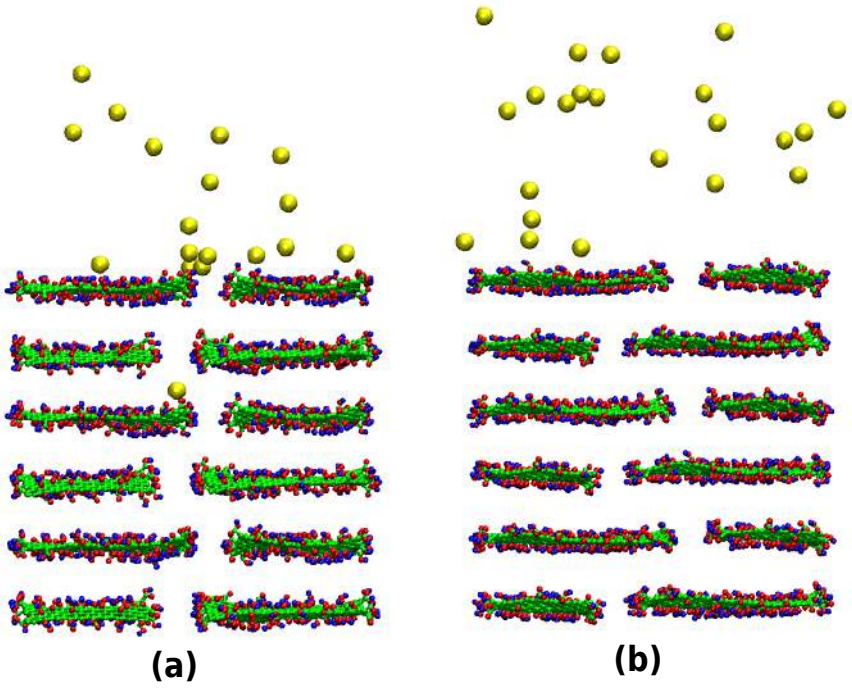

Figure B.28: Distribution of the Na^+ ions for membranes with different pore offsets at the end of the simulations. (a) 8 and (b) 16 Å. Green color is for carbon atoms, red color is for oxygen atoms, blue color is for hydrogen atoms, and yellow color is for Na^+ ions.

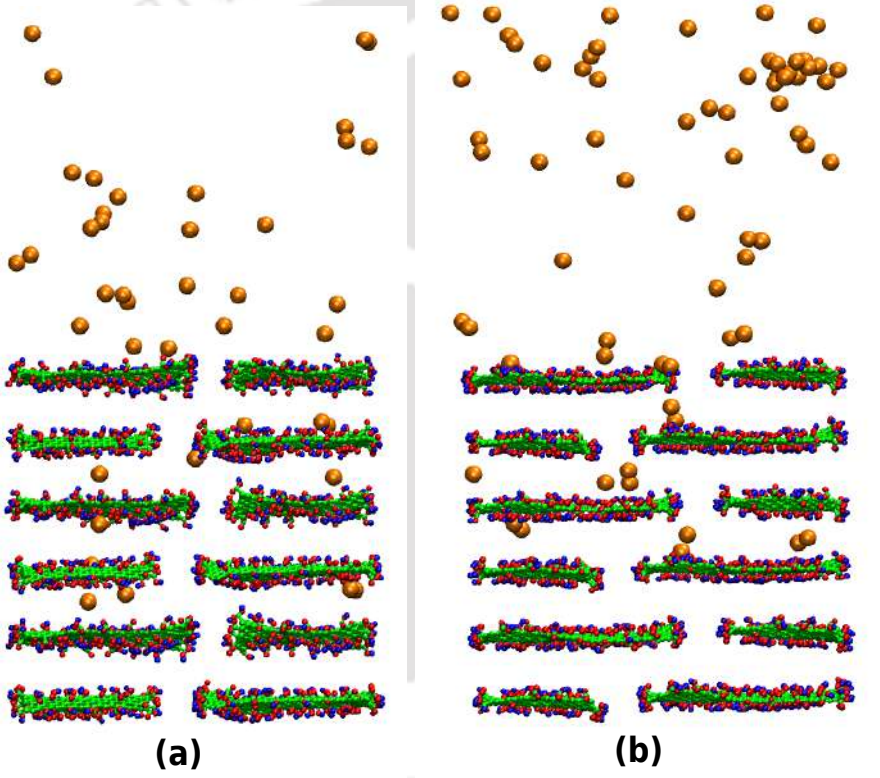

Figure B.29: Distribution of the Cl^- ions for membranes with different pore offsets at the end of the simulations. (a) 8 and (b) 16 Å. Green color is for carbon atoms, red color is for oxygen atoms, blue color is for hydrogen atoms, and orange color is for Cl^- ions.

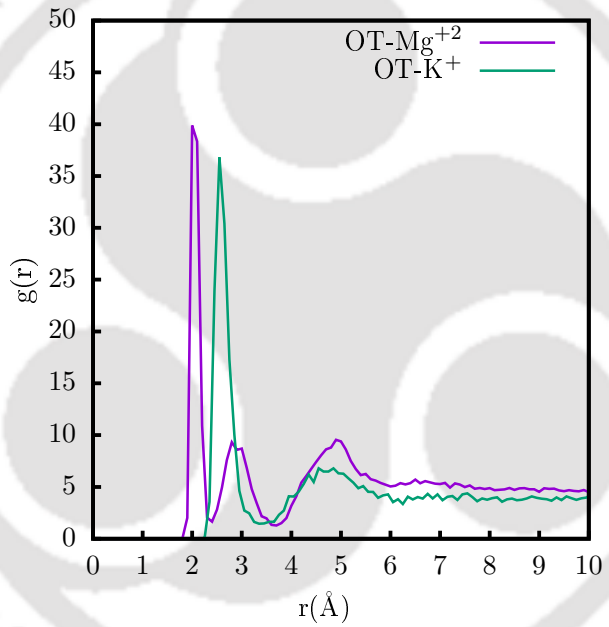

Figure B.30: Radial distribution function (g(r)) of the K^+ and Mg^{2+} ions with the oxygen atoms (OT) of the water inside the layers of the GO membrane.

B.3 Supplementary information for Chapter 5

The density of boric acid (BA) and borate ions (BI) along the Z-axis for both kinds of membranes presents in figure.B.31.

Figure.B.32 illustrates the intercalation percentages of BA and BI of the membranes (GO-K-10P and GO-M-10P) for the feed solution3.

The trajectories of a few selected BA and BI of the membranes (GO-K-10P and GO-M-10P) for the feed solution3 are depicted in the figure.B.33(a) and (b), respectively.

The changes in the number of water molecules (N_P) in the permeate region with the simulation time are presented in figure.B.34.

Figure.B.35 presents the density of water molecules along the Z-axis: (a) K^+ ion intercalated and (b) Mg^{2+} ion intercalated GO membranes.

Table.B.1 shows the comparative water permeance and boron rejection of a polymeric and graphene based membranes.

The 2D mass density of salt ions (Na^+ , Cl^- , and Mg^{2+}) and density profiles of the salt ions along the Z-axis for all membranes depicts in figures.B.36, B.37, and B.38.

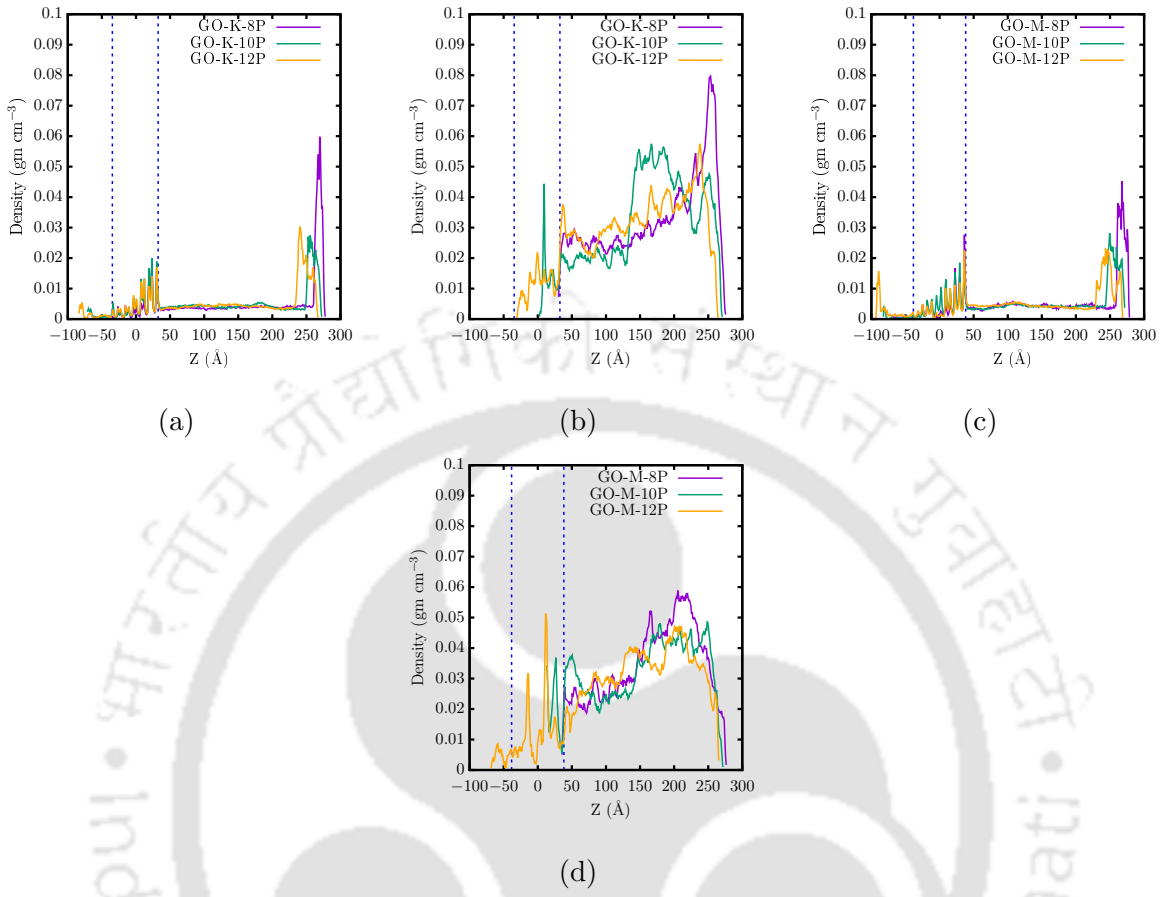

Figure B.31: The density of (a) boric acid (BA) and (b) borate ions (BI) along the Z-axis for K^+ ion intercalated GO membranes. The density of (c) BA and (d) BI along the Z-axis for Mg^{2+} ion intercalated GO membranes. Dotted lines indicate the position of the membrane.

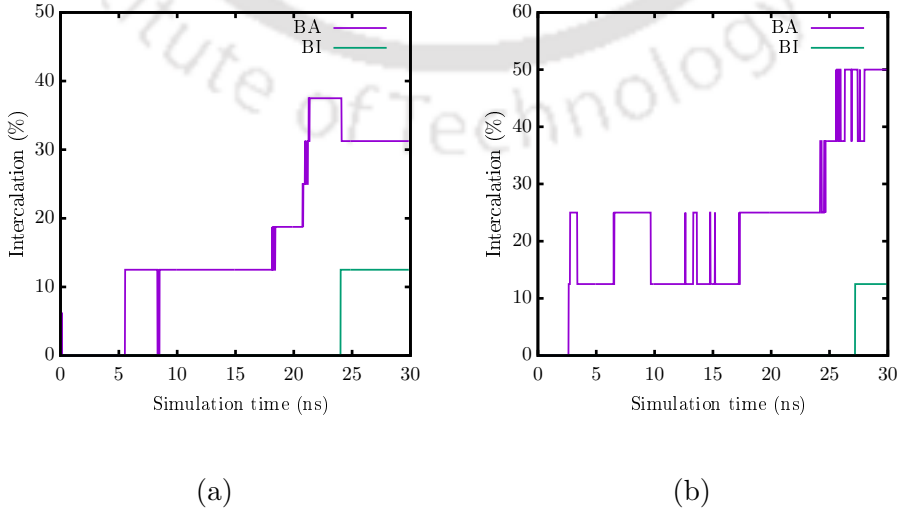

Figure B.32: The intercalation percentages of BA and BI for (a) GO-K-10P and (b) GO-M-10P membranes.

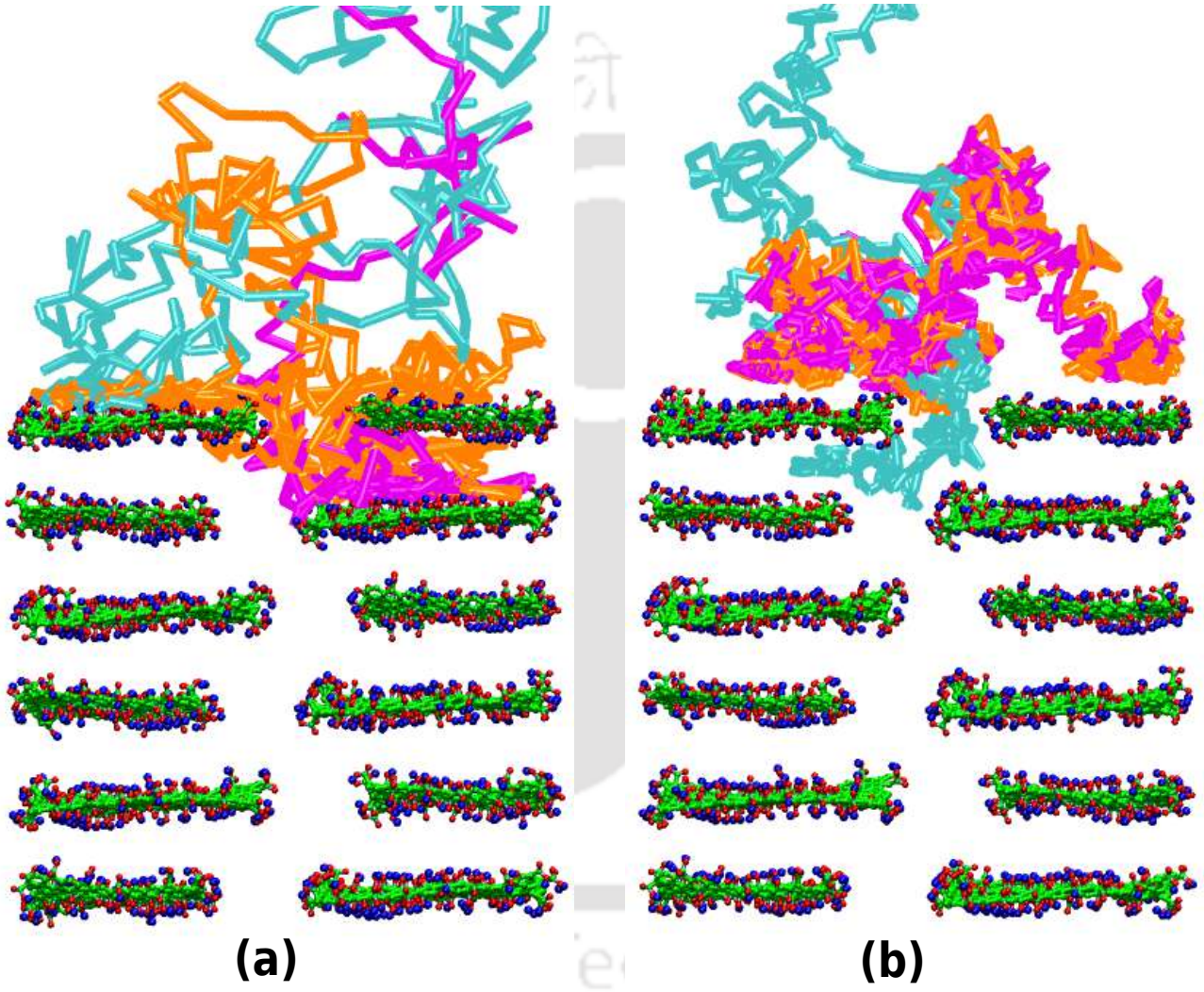

Figure B.33: Trajectories of (a) BA and (b) BI for feed solution3. Green color is for carbon atoms, red is for oxygen atoms, blue is for hydrogen atoms, and the remaining colors represent the trajectory of BA and BI.

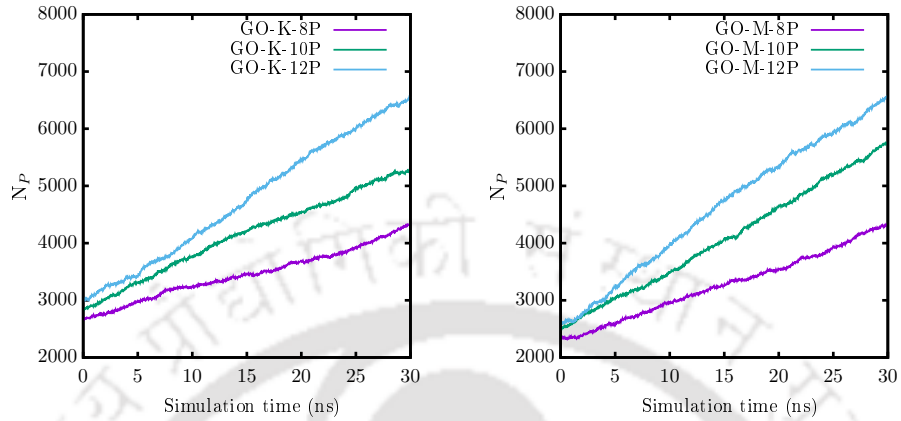

(a) (b)

Figure B.34: Changes in the number of water molecules (N_P) in the permeate region with the simulation time. (a) K^+ ion intercalated GO membranes and (b) Mg^{2+} ion intercalated GO membranes

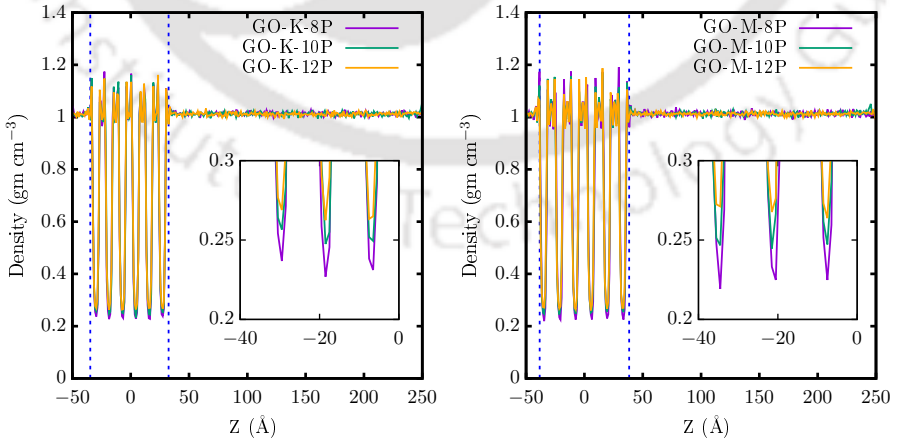

(a) (b)

Figure B.35: Density of water molecules along the Z-axis: (a) K^+ ion intercalated and (b) Mg^{2+} ion intercalated GO membranes.

Table B.1: The comparative water permeance and boron rejection of a polymeric and graphene based membranes.

Name of the membrane	Water permeance (Kg m^{-2} h^{-1})	Boric acid rejection (%)	Process
PA-PIB [116]	44.17	93.12	RO
PA-NBS [117]	16.89 ± 0.5	91.90 ± 0.082	RO
FTS H_2O^{TM} [122]	3.5	32–40	FO
Aquaporin Inside^{TM} [122]	11.25	20–30	FO
Fabricated PSU [122]	5.5	25–35	FO
PA-SR [124]	26.9	99.6	RO
PA-SWC4+ [124]	29.1	99.8	RO
PA-SW30 HR XLE [124]	38.3	99.7	RO
PA-SW30 HR LE [124]	32.0	99.75	RO
PA-TM820 [124]	28.1	99.75	RO
PA-TM820A [124]	25.5	99.75	RO
Nanoporous graphene [118]	82500	> 95	RO
Nanoporous graphene [118]	192500	80	RO
TpPa-COOH [119]	889000	93.4	RO
TpPa-NH_2 [119]	375000	100	RO
TpPa-OH [119]	127500	100	RO
TpPa-NO_2 [119]	85000	12.8	RO
TpPa-SH [119]	75000	19.8	RO
TpPa-CH_3 [119]	65000	0.1	RO
GO-K-8P	162438	100	RO
GO-M-8P	193058	100	RO

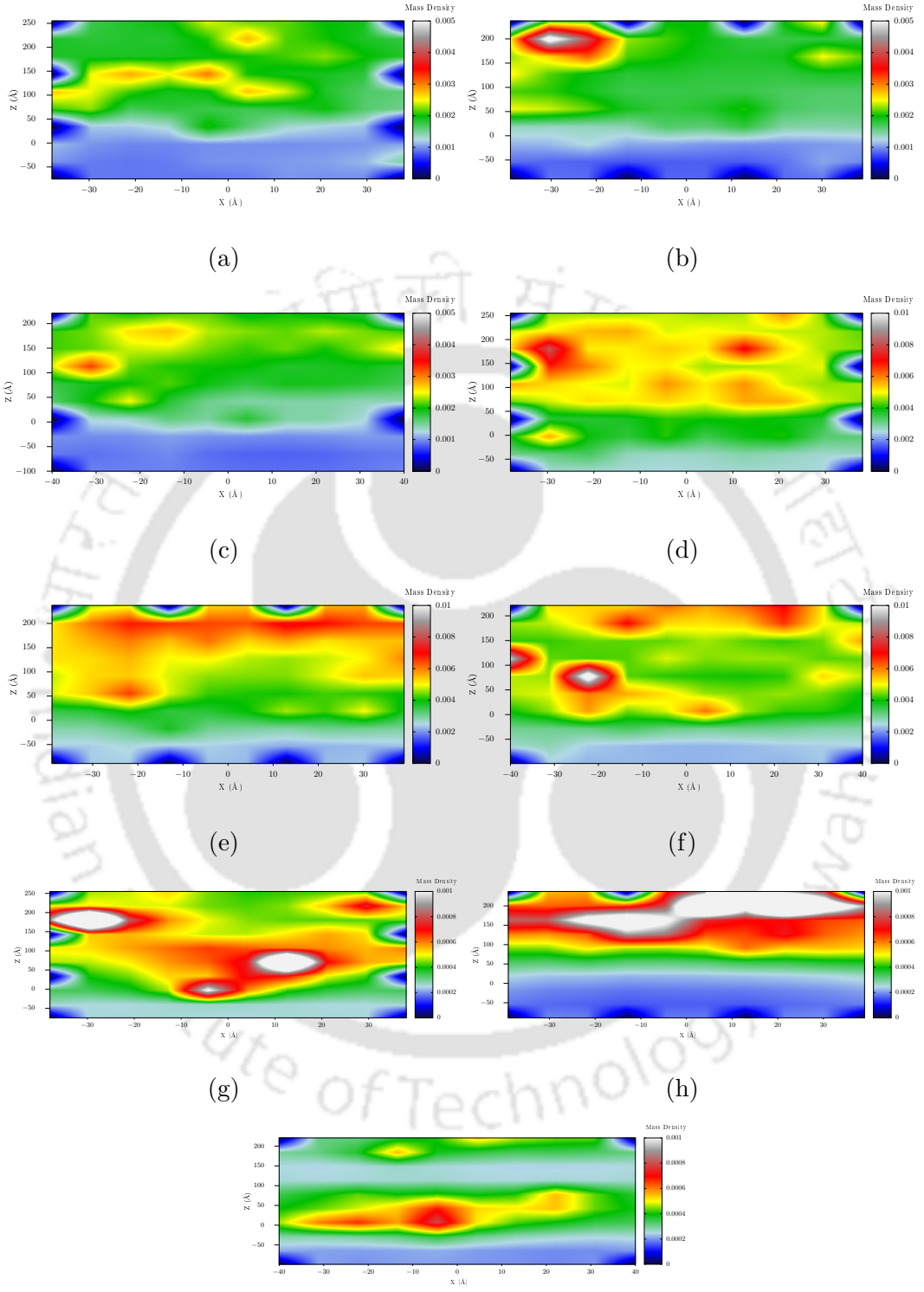

Figure B.36: The 2D mass density maps of Na^+ ions : (a) GO-K-8P , (b) GO-K-10P, and (c) GO-K-12P. The 2D density maps of Cl^- ions : (d) GO-K-8P, (e) GO-K-10P, and (f) GO-K-12P. The 2D density maps of Mg^{2+} ions : (g) GO-K-8P , (h) GO-K-10P, and (i) GO-K-12P. Dotted lines indicate the position of the membrane.

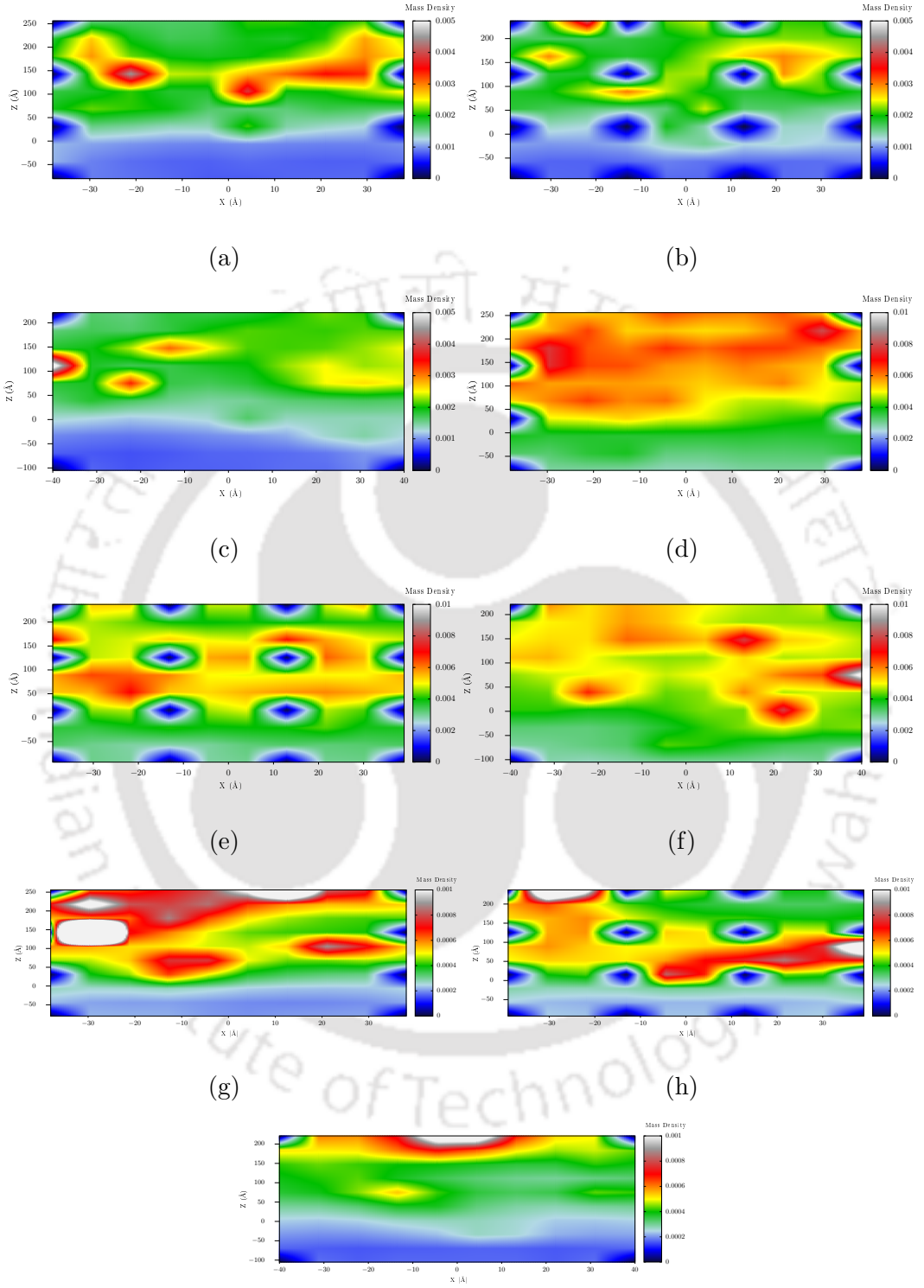

Figure B.37: The 2D mass density maps of Na^+ ions : (a) GO-M-8P , (b) GO-M-10P, and (c) GO-M-12P. The 2D density maps of Cl^- ions : (d) GO-M-8P, (e) GO-M-10P, and (f) GO-M-12P. The 2D density maps of Mg^{2+} ions : (g) GO-M-8P , (h) GO-M-10P, and (i) GO-M-12P. Dotted lines indicate the position of the membrane.

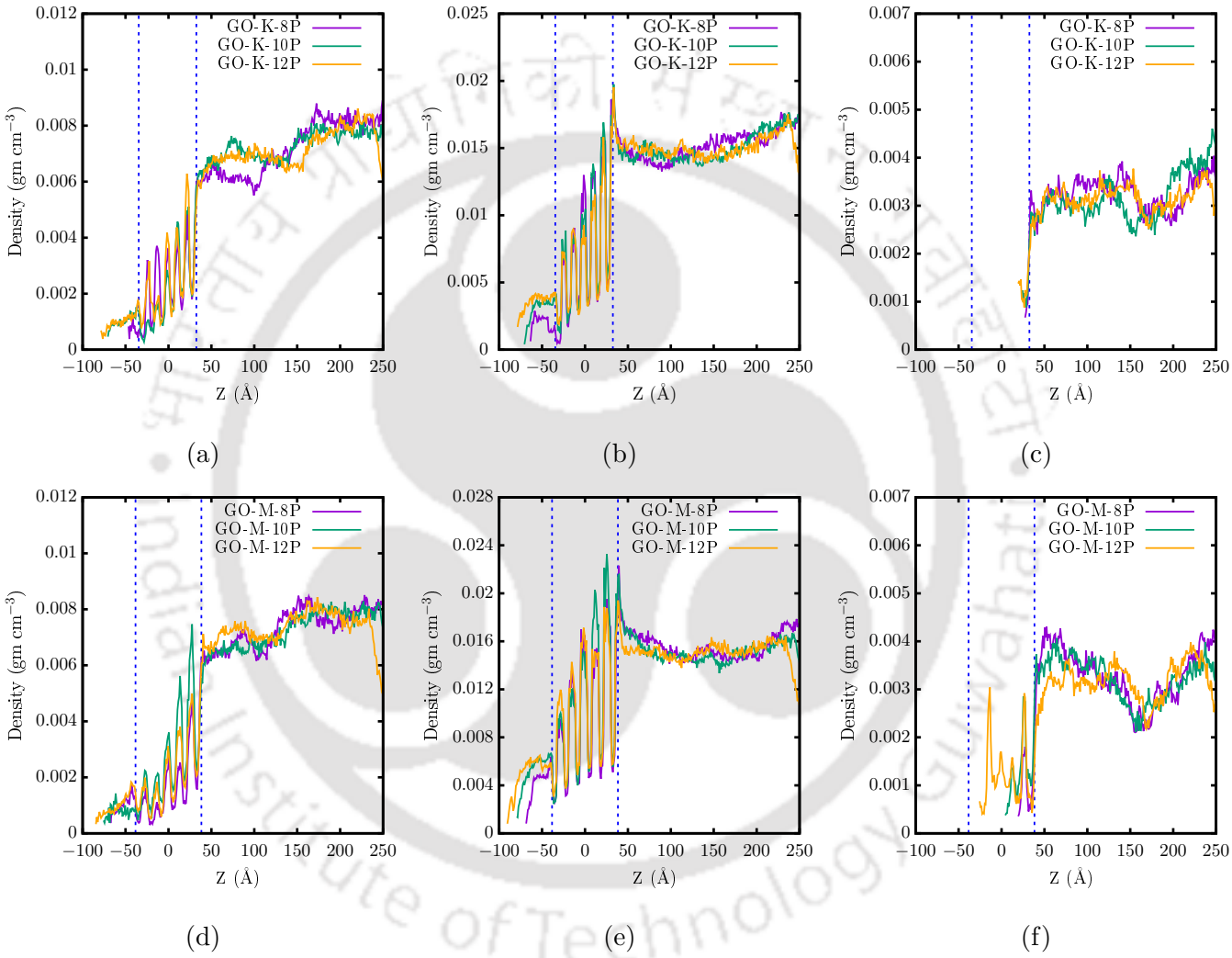

Figure B.38: The density of (a) Na^+ , (b) Cl^- , and (c) Mg^{2+} ions along the Z-axis for K^+ ion intercalated GO membranes. The density of (d) Na^+ , (e) Cl^- , and (f) Mg^{2+} ions along the Z-axis for Mg^{2+} ion intercalated GO membranes. Dotted lines indicate the position of the membrane.

Bibliography

[1] Elimelech M Phillip WA. The future of seawater desalination: Energy, technology, and the environment science 333712. elimelech, m., and phillip, wa (2011). the future of seawater desalination: Energy, technology, and the environment. *Science*, 333:712, 2011.

[2] Geoffrey M Geise, Hae-Seung Lee, Daniel J Miller, Benny D Freeman, James E McGrath, and Donald R Paul. Water purification by membranes: the role of polymer science. *J. Polym. Sci., Part B: Polym. Phys.*, 48(15):1685–1718, 2010.

[3] M Bassyouni, MH Abdel-Aziz, M Sh Zoromba, SMS Abdel-Hamid, and Enrico Drioli. A review of polymeric nanocomposite membranes for water purification. *J. Ind. Eng. Chem.*, 73:19–46, 2019.

[4] Irem Uluisik, Huseyin Caglar Karakaya, and Ahmet Koc. The importance of boron in biological systems. *J. Trace Elem. Med. Biol.*, 45:156–162, 2018.

[5] Ahmad Moarefian, Hossein Alizadeh Golestani, and Hooman Bahmanpour. Removal of amoxicillin from wastewater by self-made polyethersulfone membrane using nanofiltration. *Journal of Environmental Health Science and Engineering*, 12(1):127, 2014.

[6] Katanchalee Phadunghus, Aunnop Wongrueng, Pharkphum Rakruam, Suraphong Wattanachira, and Patiparn Punyapalakul. Efficiencies of nf and ro membranes on pharmaceutical removal and membrane fouling effects. *Engineering Journal*, 21(3):101–112, 2017.

[7] S Mompelat, B Le Bot, and O Thomas. Occurrence and fate of pharmaceutical products and by-products, from resource to drinking water. *Environment international*, 35(5):803–814, 2009.

[8] Long D Nghiem, Andrea I Schafer, and Menachem Elimelech. Pharmaceutical retention mechanisms by nanofiltration membranes. *Environmental science & technology*, 39(19):7698–7705, 2005.

[9] Xiuzhen Wei, Xiaoyan Bao, Jiawei Wu, Cuixia Li, Yingying Shi, Jinyuan Chen, Bosheng Lv, and Baoku Zhu. Typical pharmaceutical molecule removal behavior from water by positively and negatively charged composite hollow fiber nanofiltration membranes. *RSC advances*, 8(19):10396–10408, 2018.

[10] Paola Verlicchi, M Al Aukidy, A Galletti, M Petrovic, and D Barcelo. Hospital effluent: investigation of the concentrations and distribution of pharmaceuticals and environmental risk assessment. *Science of the total environment*, 430:109–118, 2012.

[11] Radisav D Vidic, Susan L Brantley, Julie M Vandenbossche, David Yoxtheimer, and Jorge D Abad. Impact of shale gas development on regional water quality. *science*, 340(6134), 2013.

[12] Brian G Rahm and Susan J Riha. Evolving shale gas management: water resource risks, impacts, and lessons learned. *Environ. Sci.: Processes Impacts*, 16(6):1400–1412, 2014.

[13] Andrew Kondash and Avner Vengosh. Water footprint of hydraulic fracturing. *Environ. Sci. Technol. Lett.*, 2(10):276–280, 2015.

[14] Fadhil Y Al-Aboosi and Mahmoud M El-Halwagi. A stochastic optimization approach to the design of shale gas/oil wastewater treatment systems with multiple energy sources under uncertainty. *Sustainability*, 11(18):4865, 2019.

[15] Namita Shrestha, Govinda Chilkoor, Joseph Wilder, Venkataramana Gadhamshetty, and James J Stone. Potential water resource impacts of hydraulic fracturing from unconventional oil production in the bakken shale. *Water Res.*, 108:1–24, 2017.

[16] Kyle E Murray. State-scale perspective on water use and production associated with oil and gas operations, oklahoma, us. *Environ. Sci. Technol.*, 47(9):4918–4925, 2013.

[17] Xuewei Du, Zuoyou Zhang, Kenneth H Carlson, Jongho Lee, and Tiezheng Tong. Membrane fouling and reusability in membrane distillation of shale oil and gas produced water: Effects of membrane surface wettability. *J. Membr. Sci.*, 567:199–208, 2018.

[18] Devin L. Shaffer, Laura H. Arias Chavez, Moshe Ben-Sasson, Santiago Romero-Vargas Castrillon, Ngai Yin Yip, and Menachem Elimelech. Desalination and reuse of high-salinity shale gas produced water: Drivers, technologies, and future directions. *Environ. Sci. Technol.*, 47(17):9569–9583, 2013.

[19] Emily Grubert and Saya Kitasei. How energy choices affect fresh water supplies: A comparison of us coal and natural gas. *Worldwatch Institute*, 2010.

[20] Sharon B Kausley, Chetan P Malhotra, and Aniruddha B Pandit. Treatment and reuse

of shale gas wastewater: Electrocoagulation system for enhanced removal of organic contamination and scale causing divalent cations. *J. Water Process. Eng.*, 16:149–162, 2017.

[21] Emile Zuckerkandl and Linus Pauling. Evolutionary divergence and convergence in proteins. In *Evolving genes and proteins*, pages 97–166. Elsevier, 1965.

[22] Tove A Larsen, Michel E Riechmann, and Kai M Udert. State of the art of urine treatment technologies: A critical review. *Water Research X*, 13:100114, 2021.

[23] F Volpin, L Chekli, S Phuntsho, N Ghaffour, Johannes S Vrouwenvelder, and Ho Kyong Shon. Optimisation of a forward osmosis and membrane distillation hybrid system for the treatment of source-separated urine. *Separation and Purification Technology*, 212:368–375, 2019.

[24] Federico Volpin, Laura Chekli, Sherub Phuntsho, Jaeweon Cho, Noreddine Ghaffour, Johannes S Vrouwenvelder, and Ho Kyong Shon. Simultaneous phosphorous and nitrogen recovery from source-separated urine: A novel application for fertiliser drawn forward osmosis. *Chemosphere*, 203:482–489, 2018.

[25] Tove A Larsen*, Alfredo C Alder, Rik IL Eggen, Max Maurer, and Judit Lienert. Source separation: will we see a paradigm shift in wastewater handling?, 2009.

[26] Tove A Larsen, Sabine Hoffmann, Christoph Luthi, Bernhard Truffer, and Max Maurer. Emerging solutions to the water challenges of an urbanizing world. *Science*, 352(6288):928–933, 2016.

[27] M Maurer, W Pronk, and TA Larsen. Treatment processes for source-separated urine. *Water research*, 40(17):3151–3166, 2006.

[28] Hannah Ray, Francois Perreault, and Treavor H Boyer. Ammonia recovery and fouling mitigation of hydrolyzed human urine treated by nanofiltration and reverse osmosis. *Environmental Science: Water Research & Technology*, 8(2):429–442, 2022.

[29] MHV Mulder. *Basic principles of membrane technology*. Kluwer Academic Press, 1991.

[30] Tzahi Y. Cath, Menachem Elimelech, Jeffrey R. McCutcheon, Robert L. McGinnis, Andrea Achilli, Daniel Anastasio, Adam R. Brady, Amy E. Childress, Isaac V. Farr, Nathan T. Hancock, Jason Lampi, Long D. Nghiem, Ming Xie, and Ngai Yin Yip. Standard methodology for evaluating membrane performance in osmotically driven membrane processes. *Desalination*, 312:31 – 38, 2013. Recent Advances in Forward Osmosis.

[31] Hannah Ray, Francois Perreault, and Treavor H Boyer. Ammonia recovery from hy-

drolyzed human urine by forward osmosis with acidified draw solution. *Environmental science & technology*, 54(18):11556–11565, 2020.

[32] Shahriar Habib and Steven T Weinman. Modification of polyamide reverse osmosis membranes for the separation of urea. *Journal of Membrane Science*, 655:120584, 2022.

[33] Zeynep Altintas, Iva Chianella, Gabriella Da Ponte, Sabine Paulussen, Soccorso Gaeta, and Ibtisam E Tothill. Development of functionalized nanostructured polymeric membranes for water purification. *Chemical Engineering Journal*, 300:358–366, 2016.

[34] Federico Volpin, Umakant Badeti, Chen Wang, Jiaxi Jiang, Jorg Vogel, Stefano Freguia, Dena Fam, Jaeweon Cho, Sherub Phuntsho, and Ho Kyong Shon. Urine treatment on the international space station: current practice and novel approaches. *Membranes*, 10(11):327, 2020.

[35] Gongping Liu, Wanqin Jin, and Nanping Xu. Graphene-based membranes. *Chemical Society Reviews*, 44(15):5016–5030, 2015.

[36] Andre Konstantin Geim. Graphene: status and prospects. *science*, 324(5934):1530–1534, 2009.

[37] ANDRE Geim and K Novoselov. Graphene calling. *Nat Mater*, 6(169):10–1038, 2007.

[38] Baoxia Mi. Graphene oxide membranes for ionic and molecular sieving. *Science*, 343(6172):740–742, 2014.

[39] Jihn Yih Lim, NM Mubarak, EC Abdullah, Sabzoi Nizamuddin, Mohammad Khalid, et al. Recent trends in the synthesis of graphene and graphene oxide based nanomaterials for removal of heavy metals. a review. *Journal of Industrial and Engineering Chemistry*, 66:29–44, 2018.

[40] Abedalkader Alkhouzaam and Hazim Qiblawey. Functional go-based membranes for water treatment and desalination: Fabrication methods, performance and advantages. a review. *Chemosphere*, 274:129853, 2021.

[41] Jesus Guerrero-Contreras and Felipe Caballero-Briones. Graphene oxide powders with different oxidation degree, prepared by synthesis variations of the hummers method. *Materials Chemistry and Physics*, 153:209–220, 2015.

[42] Yankai Chen and Xiaoning Yang. Molecular simulation of layered go membranes with amorphous structure for heavy metal ions separation. *J. Membr. Sci.*, 660:120863, 2022.

[43] RK Joshi, Paola Carbone, Feng-Chao Wang, Vasyl G Kravets, Ying Su, Irina V Grig-

orieva, HA Wu, Andre K Geim, and Rahul Raveendran Nair. Precise and ultrafast molecular sieving through graphene oxide membranes. *science*, 343(6172):752–754, 2014.

[44] Nor Farah Diana Aba, Jeng Yi Chong, Bo Wang, Cecilia Mattevi, and K Li. Graphene oxide membranes on ceramic hollow fibers–microstructural stability and nanofiltration performance. *J. Membr. Sci.*, 484:87–94, 2015.

[45] Pengzhan Sun, Feng Zheng, Miao Zhu, Kunlin Wang, Minlin Zhong, Dehai Wu, and Hongwei Zhu. Realizing synchronous energy harvesting and ion separation with graphene oxide membranes. *Sci. Rep.*, 4(1):1–5, 2014.

[46] L Paliotta, G De Bellis, A Tamburrano, F Marra, A Rinaldi, SK Balijepalli, S Kaciulis, and MS Sarto. Highly conductive multilayer-graphene paper as a flexible lightweight electromagnetic shield. *Carbon*, 89:260–271, 2015.

[47] Gonggang Liu, Hongqi Ye, Antai Li, Chenyuan Zhu, Heng Jiang, Yong Liu, Kai Han, and Yonghua Zhou. Graphene oxide for high-efficiency separation membranes: Role of electrostatic interactions. *Carbon*, 110:56–61, 2016.

[48] David Cohen-Tanugi and Jeffrey C Grossman. Water desalination across nanoporous graphene. *Nano Lett.*, 12(7):3602–3608, 2012.

[49] David Cohen-Tanugi, Li-Chiang Lin, and Jeffrey C Grossman. Multilayer nanoporous graphene membranes for water desalination. *Nano letters*, 16(2):1027–1033, 2016.

[50] David Cohen-Tanugi and Jeffrey C Grossman. Water permeability of nanoporous graphene at realistic pressures for reverse osmosis desalination. *J. Chem. Phys.*, 141(7):074704, 2014.

[51] P Rajasekhar Reddy, Abhijit Gogoi, and K Anki Reddy. Cationic stabilized layered graphene oxide (go) membrane for shale gas wastewater treatment: An atomistic insight. *Desalination*, 559:116621, 2023.

[52] P Rajasekhar Reddy, Amit Kumar, and K Anki Reddy. Understanding the boron rejection of cation intercalated multilayered graphene oxide (go) membrane in reverse osmosis (ro) process: A molecular dynamics study. *Journal of Molecular Liquids*, 389:122817, 2023.

[53] Yuan Gao, Yan Li, Liang Zhang, Hui Huang, Junjie Hu, Syed Mazhar Shah, and Xingguang Su. Adsorption and removal of tetracycline antibiotics from aqueous solution by graphene oxide. *Journal of Colloid and Interface Science*, 368(1):540 – 546, 2012.

[54] Yi Han, Zhen Xu, and Chao Gao. Ultrathin graphene nanofiltration membrane for water purification. *Advanced Functional Materials*, 23(29):3693–3700, 2013.

[55] R. R. Nair, H. A. Wu, P. N. Jayaram, I. V. Grigorieva, and A. K. Geim. Unimpeded permeation of water through helium-leak–tight graphene-based membranes. *Science*, 335(6067):442–444, 2012.

[56] Baoxia Mi. Graphene oxide membranes for ionic and molecular sieving. *Science*, 343(6172):740–742, 2014.

[57] Yi Wei, Yushan Zhang, Xueli Gao, Zhun Ma, Xiaojuan Wang, and Congjie Gao. Multi-layered graphene oxide membranes for water treatment: A review. *Carbon*, 139:964–981, 2018.

[58] Yu-Lei Xing, Guo-Rong Xu, Zi-Han An, Yan-Hui Liu, Ke Xu, Qian Liu, He-Li Zhao, and Rasel Das. Laminated go membranes for water transport and ions selectivity: Mechanism, synthesis, stabilization, and applications. *Separation and Purification Technology*, 259:118192, 2021.

[59] Jie Shen, Gongping Liu, Kang Huang, Zhenyu Chu, Wanqin Jin, and Nanping Xu. Subnanometer two-dimensional graphene oxide channels for ultrafast gas sieving. *ACS nano*, 10(3):3398–3409, 2016.

[60] Liang Huang, Miao Zhang, Chun Li, and Gaoquan Shi. Graphene-based membranes for molecular separation. *The journal of physical chemistry letters*, 6(14):2806–2815, 2015.

[61] Meng Hu and Baoxia Mi. Enabling graphene oxide nanosheets as water separation membranes. *Environ. Sci. Technol.*, 47(8):3715–3723, 2013.

[62] Bo Chen, Haifeng Jiang, Xiang Liu, and Xuejiao Hu. Molecular insight into water desalination across multilayer graphene oxide membranes. *ACS Appl. Mater. Interfaces*, 9(27):22826–22836, 2017.

[63] Ruosang Qiu, Shi Yuan, Jie Xiao, Xiao Dong Chen, Cordelia Selomulya, Xiwang Zhang, and Meng Wai Woo. Effects of edge functional groups on water transport in graphene oxide membranes. *ACS applied materials & interfaces*, 11(8):8483–8491, 2019.

[64] Ruosang Qiu, Jie Xiao, Xiao Dong Chen, Cordelia Selomulya, Xiwang Zhang, and Meng Wai Woo. Comparison of the effects of edge functionalized graphene oxide membranes on monovalent cation selectivity. *Journal of Membrane Science*, 620:118892, 2021.

[65] Chen Chen, Lingjie Jia, Jiachen Li, Li Zhang, Lijun Liang, Eryu Chen, Zhe Kong, Xinping Wang, Wei Zhang, and Jia-Wei Shen. Understanding the effect of hydroxyl/epoxy group on water desalination through lamellar graphene oxide membranes via molecular dynamics simulation. *Desalination*, 491:114560, 2020.

[66] Dmitriy A Dikin, Sasha Stankovich, Eric J Zimney, Richard D Piner, Geoffrey HB Dommett, Guennadi Evmenenko, SonBinh T Nguyen, and Rodney S Ruoff. Preparation and characterization of graphene oxide paper. *Nature*, 448(7152):457–460, 2007.

[67] Ge Shi, Qingshi Meng, Zhiheng Zhao, Hsu-Chiang Kuan, Andrew Michelmore, and Jun Ma. Facile fabrication of graphene membranes with readily tunable structures. *ACS applied materials & interfaces*, 7(25):13745–13757, 2015.

[68] Ayrat M Dimiev and James M Tour. Mechanism of graphene oxide formation. *ACS nano*, 8(3):3060–3068, 2014.

[69] Sunxiang Zheng, Qingsong Tu, Jeffrey J Urban, Shaofan Li, and Baoxia Mi. Swelling of graphene oxide membranes in aqueous solution: characterization of interlayer spacing and insight into water transport mechanisms. *ACS nano*, 11(6):6440–6450, 2017.

[70] Liang Chen, Guosheng Shi, Jie Shen, Bingquan Peng, Bowu Zhang, Yuzhu Wang, Fenggang Bian, Jiajun Wang, Deyuan Li, Zhe Qian, et al. Ion sieving in graphene oxide membranes via cationic control of interlayer spacing. *Nature*, 550(7676):380–383, 2017.

[71] Abhijit Gogoi, K Anki Reddy, and Pranab Mondal. Multilayer graphene oxide membrane in forward osmosis: molecular insights. *ACS Appl. Nano Mater.*, 1(9):4450–4460, 2018.

[72] Mohd Rafie Bin Shaharudin, Christopher D Williams, and Paola Carbone. The role of surface ionisation in the hydration-induced swelling of graphene oxide membranes. *J. Membr. Sci.*, 653:120489, 2022.

[73] Jijo Abraham, Kalangi S Vasu, Christopher D Williams, Kalon Gopinadhan, Yang Su, Christie T Cherian, James Dix, Eric Prestat, Sarah J Haigh, Irina V Grigorieva, et al. Tunable sieving of ions using graphene oxide membranes. *Nat. Nanotechnol.*, 12(6):546–550, 2017.

[74] Wanbin Li, Wufeng Wu, and Zhanjun Li. Controlling interlayer spacing of graphene oxide membranes by external pressure regulation. *Acs Nano*, 12(9):9309–9317, 2018.

[75] Khalid Hussain Thebo, Xitang Qian, Qing Zhang, Long Chen, Hui-Ming Cheng, and Wencai Ren. Highly stable graphene-oxide-based membranes with superior permeability. *Nat. Commun.*, 9(1):1–8, 2018.

[76] Ting Liu, Long Tian, Nigel Graham, Bing Yang, Wenzheng Yu, and Kening Sun. Regulating the interlayer spacing of graphene oxide membranes and enhancing their stability by use of pacl. *Environ. Sci. Technol.*, 53(20):11949–11959, 2019.

[77] Wei-Song Hung, Chi-Hui Tsou, Manuel De Guzman, Quan-Fu An, Ying-Ling Liu, Ya-

Ming Zhang, Chien-Chieh Hu, Kueir-Rarn Lee, and Juin-Yih Lai. Cross-linking with diamine monomers to prepare composite graphene oxide-framework membranes with varying d-spacing. *Chem. Mater.*, 26(9):2983–2990, 2014.

[78] Yizhou Yang, Liuhua Mu, Liang Chen, Guosheng Shi, and Haiping Fang. Precise control of the interlayer spacing between graphene sheets by hydrated cations. *Phys. Chem. Chem. Phys.*, 21(14):7623–7629, 2019.

[79] Yu Zhang, Sui Zhang, and TaiShung Chung. Nanometric graphene oxide framework membranes with enhanced heavy metal removal via nanofiltration. *Environ. Sci. Technol.*, 49(16):10235–10242, 2015.

[80] Sungjin Park, KyoungSeok Lee, Gulay Bozoklu, Weiwei Cai, SonBinh T Nguyen, and Rodney S Ruoff. Graphene oxide papers modified by divalent ions - enhancing mechanical properties via chemical cross-linking. *ACS nano*, 2(3):572–578, 2008.

[81] Shi Yuan, Yang Li, Yun Xia, Cordelia Selomulya, and Xiwang Zhang. Stable cation-controlled reduced graphene oxide membranes for improved nacl rejection. *Journal of Membrane Science*, 621:118995, 2021.

[82] P Rajasekhar reddy, Abhijit Gogoi, and K Anki Reddy. Effect of oxygen-containing functional groups of layered graphene oxide membrane on the removal of amoxicillin: a molecular dynamics study. *Mol. Simul.*, 48(3):185–196, 2022.

[83] Abhijit Gogoi, K Anki Reddy, and Pranab Kumar Mondal. Influence of the presence of cations on the water and salt dynamics inside layered graphene oxide (go) membranes. *Nanoscale*, 12(13):7273–7283, 2020.

[84] Song Liu, Guozhen Liu, Bojie Zhao, Yingxuan Deng, Haipeng Zhu, Gongping Liu, and Wanqin Jin. Methanol/dimethyl carbonate separation using graphene oxide membrane via cationic control of molecular transport channels. *J. Membr. Sci.*, page 120457, 2022.

[85] XiaoRong Li, FenYing Kong, Jing Liu, TongMing Liang, JingJuan Xu, and HongYuan Chen. Synthesis of potassium-modified graphene and its application in nitrite-selective sensing. *Adv. Funct. Mater.*, 22(9):1981–1988, 2012.

[86] Withita Cha-Umpong, Ehsan Hosseini, Amir Razmjou, Mohammad Zakertabrizi, Asghar Habibnejad Korayem, and Vicki Chen. New molecular understanding of hydrated ion trapping mechanism during thermally-driven desalination by pervaporation using go membrane. *J. Membr. Sci.*, 598:117687, 2020.

[87] KE Gmitrov, AA Eliseev, VA Brotsman, AA Poyarkov, IA Ryzhov, TA Zotov, AP Chu-

makov, and DI Petukhov. Pervaporation desalination with graphene oxide membranes: The influence of cation type and loading. *Desalination*, 547:116238, 2023.

[88] Guo-hai Yang, Dan-dan Bao, Da-qing Zhang, Cheng Wang, Lu-lu Qu, and Hai-tao Li. Removal of antibiotics from water with an all-carbon 3d nanofiltration membrane. *Nanoscale research letters*, 13(1):146, 2018.

[89] Angela L Batt, Ian B Bruce, and Diana S Aga. Evaluating the vulnerability of surface waters to antibiotic contamination from varying wastewater treatment plant discharges. *Environmental pollution*, 142(2):295–302, 2006.

[90] Hayet Mansouri, Rocio J Carmona, Alicia Gomis-Berenguer, Souad Souissi-Najar, Abdelmottaleb Ouederni, and Conchi O Ania. Competitive adsorption of ibuprofen and amoxicillin mixtures from aqueous solution on activated carbons. *Journal of colloid and interface science*, 449:252–260, 2015.

[91] Quanquan Yang, Guangcai Chen, Jianfeng Zhang, and Helian Li. Adsorption of sulfamethazine by multi-walled carbon nanotubes: effects of aqueous solution chemistry. *RSC advances*, 5(32):25541–25549, 2015.

[92] Fei Yu, Jie Ma, and Dongsu Bi. Enhanced adsorptive removal of selected pharmaceutical antibiotics from aqueous solution by activated graphene. *Environmental Science and Pollution Research*, 22(6):4715–4724, 2015.

[93] Yuan Zhuang, Fei Yu, Jie Ma, and Junhong Chen. Graphene as a template and structural scaffold for the synthesis of a 3d porous bio-adsorbent to remove antibiotics from water. *Rsc Advances*, 5(35):27964–27969, 2015.

[94] J. Radjenovic, M. Petrovic, F. Ventura, and D. Barcelo. Rejection of pharmaceuticals in nanofiltration and reverse osmosis membrane drinking water treatment. *Water Research*, 42(14):3601 – 3610, 2008.

[95] David Cohen-Tanugi, Li-Chiang Lin, and Jeffrey C. Grossman. Multilayer nanoporous graphene membranes for water desalination. *Nano Letters*, 16(2):1027–1033, 2016. PMID: 26806020.

[96] Jeffrey R. McCutcheon, Robert L. McGinnis, and Menachem Elimelech. A novel ammonia | carbon dioxide forward (direct) osmosis desalination process. *Desalination*, 174(1):1 – 11, 2005.

[97] Francois Zaviska, Patrick Drogui, Alain Grasmick, Antonin Azais, and Marc Héran.

Nanofiltration membrane bioreactor for removing pharmaceutical compounds. *Journal of membrane science*, 429:121–129, 2013.

[98] J.P.Ruparelia Sandip Sharma and Manish L.Patel. A general review on advanced oxidation processes for waste water treatment. *Nirma University International Conference, Ahmedabad, Gujarat*, pages 382 – 481, 2011.

[99] Kyoung Hoon Chu, Mahdi Fathizadeh, Miao Yu, Joseph RV Flora, Am Jang, Min Jang, Chang Min Park, Sung Soo Yoo, Namguk Her, and Yeomin Yoon. Evaluation of removal mechanisms in a graphene oxide-coated ceramic ultrafiltration membrane for retention of natural organic matter, pharmaceuticals, and inorganic salts. *ACS applied materials & interfaces*, 9(46):40369–40377, 2017.

[100] Ahmad Moarefian, Hossein Alizadeh Golestani, and Hooman Bahmanpour. Removal of amoxicillin from wastewater by self-made polyethersulfone membrane using nanofiltration. *Journal of Environmental Health Science and Engineering*, 12(1):127, Oct 2014.

[101] Yonggang Wang, Xu Wang, Mingwei Li, Jing Dong, Changhong Sun, and Guanyi Chen. Removal of pharmaceutical and personal care products (ppcps) from municipal waste water with integrated membrane systems, mbr-ro/nf. *International journal of environmental research and public health*, 15(2):269, 2018.

[102] Bofan Li, Yue Cui, Susilo Japip, Zhiwei Thong, and Tai-Shung Chung. Graphene oxide (go) laminar membranes for concentrating pharmaceuticals and food additives in organic solvents. *Carbon*, 130:503–514, 2018.

[103] Daniel Bahamon and Lourdes F. Vega. Pharmaceutical removal from water effluents by adsorption on activated carbons: A monte carlo simulation study. *Langmuir*, 33(42):11146–11155, Oct 2017.

[104] D. Bahamon and L. F. Vega. Molecular simulations of phenol and ibuprofen removal from water using multilayered graphene oxide membranes. *Molecular Physics*, 0(0):1–12, 2019.

[105] Peter Argust. Distribution of boron in the environment. *Biol. Trace Elem. Res.*, 66(1):131–143, 1998.

[106] Margaret Richold. Boron exposure from consumer products. *Biol. Trace Elem. Res.*, 66(1):121–129, 1998.

[107] Paul D Howe. A review of boron effects in the environment. *Biol. Trace Elem. Res.*, 66(1):153–166, 1998.

[108] Xue Jin, Chuyang Y Tang, Yangshuo Gu, Qianhong She, and Saren Qi. Boric acid permeation in forward osmosis membrane processes: modeling, experiments, and implications. *Environ. Sci. Technol.*, 45(6):2323–2330, 2011.

[109] Maria Polsia Princi, Antonio Lupini, Fabrizio Araniti, Caterina Longo, Antonio Mauceri, Francesco Sunseri, and Maria Rosa Abenavoli. Boron toxicity and tolerance in plants: Recent advances and future perspectives. *Plant metal interaction*, pages 115–147, 2016.

[110] Fyodor S Kot. Boron in the environment. *Boron Sep. Processes*, 1:33, 2015.

[111] Kha L Tu, Long D Nghiem, and Allan R Chivas. Boron removal by reverse osmosis membranes in seawater desalination applications. *Sep. Purif. Technol.*, 75(2):87–101, 2010.

[112] Joanna Kluczka, Wojciech Pudlo, and Katarzyna Krukiewicz. Boron adsorption removal by commercial and modified activated carbons. *Chem. Eng. Res. Des.*, 147:30–42, 2019.

[113] Bei Jiang, Xue Zhang, Xuan Zhao, and Fuzhi Li. Removal of high level boron in aqueous solutions using continuous electrodeionization (cedi). *Sep. Purif. Technol.*, 192:297–301, 2018.

[114] Danis Kartikaningsih, Yu-Jen Shih, and Yao-Hui Huang. Boron removal from boric acid wastewater by electrocoagulation using aluminum as sacrificial anode. *Sustainable Environ. Res.*, 26(4):150–155, 2016.

[115] Ran Zhang, Yingming Xie, Jianfeng Song, Lixin Xing, Dingfeng Kong, Xue-Mei Li, and Tao He. Extraction of boron from salt lake brine using 2-ethylhexanol. *Hydrometallurgy*, 160:129–136, 2016.

[116] Shuhao Wang, Yong Zhou, and Congjie Gao. Novel high boron removal polyamide reverse osmosis membranes. *J. Membr. Sci.*, 554:244–252, 2018.

[117] Yunhao Li, Shuhao Wang, Xiaoxiao Song, Yong Zhou, Hongmei Shen, Xingzhong Cao, Peng Zhang, and Congjie Gao. High boron removal polyamide reverse osmosis membranes by swelling induced embedding of a sulfonyl molecular plug. *J. Membr. Sci.*, 597:117716, 2020.

[118] Francesca Risplendi, Federico Raffone, Li-Chiang Lin, Jeffrey C Grossman, and Giancarlo Cicero. Fundamental insights on hydration environment of boric acid and its role in separation from saline water. *J. Phys. Chem. C.*, 124(2):1438–1445, 2019.

[119] Xin Zhang, Mingjie Wei, and Yong Wang. Designing sub-nanometer pores for efficient boron removal. *Desalination*, 533:115755, 2022.

[120] J Gilron, N Gara, and O Kedem. Experimental analysis of negative salt rejection in nanofiltration membranes. *J. Membr. Sci.*, 185(2):223–236, 2001.

[121] Gamze Artuug and Jobst Hapke. Characterization of nanofiltration membranes by their morphology, charge and filtration performance parameters. *Desalination*, 200(1-3):178–180, 2006.

[122] Nawaf Bin Darwish, Abdullah Alkhudhiri, Abdulrahman AlAlawi, Hamad AlRomaih, and Nidal Hilal. Experimental investigation of forward osmosis process for boron removal from water. *J. Water Process. Eng.*, 38:101570, 2020.

[123] Lifen Liu, Xin Xie, Saren Qi, Ruihan Li, Xiao Zhang, Xiaoxiao Song, and Congjie Gao. Thin film nanocomposite reverse osmosis membrane incorporated with uio-66 nanoparticles for enhanced boron removal. *J. Membr. Sci.*, 580:101–109, 2019.

[124] Hoon Hyung and Jae-Hong Kim. A mechanistic study on boron rejection by sea water reverse osmosis membranes. *J. Membr. Sci.*, 286(1-2):269–278, 2006.

[125] Hannah Ray, Francois Perreault, and Treavor H Boyer. Rejection of nitrogen species in real fresh and hydrolyzed human urine by reverse osmosis and nanofiltration. *Journal of Environmental Chemical Engineering*, 8(4):103993, 2020.

[126] Lucas Crane, Hannah Ray, Franccois Perreault, and Treavor H Boyer. Recovery of urea from human urine using nanofiltration and reverse osmosis. *ACS ES&T Water*, 2022.

[127] Arda Yapicioglu and Ibrahim Dincer. A review on clean ammonia as a potential fuel for power generators. *Renewable and sustainable energy reviews*, 103:96–108, 2019.

[128] Patricia M Glibert, John Harrison, Cynthia Heil, and Sybil Seitzinger. Escalating worldwide use of urea–a global change contributing to coastal eutrophication. *Biogeochemistry*, 77:441–463, 2006.

[129] Huazhang Liu. Ammonia synthesis catalyst 100 years: Practice, enlightenment and challenge. *Chinese journal of catalysis*, 35(10):1619–1640, 2014.

[130] Hannah Ray, Francois Perreault, and Treavor H Boyer. Urea recovery from fresh human urine by forward osmosis and membrane distillation (fo–md). *Environmental Science: Water Research & Technology*, 5(11):1993–2003, 2019.

[131] M Baker. Overview of industrial urea markets: Application and opportunities. In *TFI Fertilizer Technology and Outlook Conference, Philadelphia, PA*, 2012.

[132] Jose Jimenez, Charles Bott, Nancy Love, and John Bratby. Source separation of urine as

an alternative solution to nutrient management in biological nutrient removal treatment plants. *Water Environment Research*, 87(12):2120–2129, 2015.

[133] KM Udert and M Wachter. Complete nutrient recovery from source-separated urine by nitrification and distillation. *Water research*, 46(2):453–464, 2012.

[134] JA Wilsenach, CAH Schuurbiers, and MCM Van Loosdrecht. Phosphate and potassium recovery from source separated urine through struvite precipitation. *Water research*, 41(2):458–466, 2007.

[135] Jac A Wilsenach and Mark C van Loosdrecht. Integration of processes to treat wastewater and source-separated urine. *Journal of Environmental Engineering*, 132(3):331–341, 2006.

[136] M Maurer, P Schwegler, and TA Larsen. Nutrients in urine: energetic aspects of removal and recovery. *Water Science and technology*, 48(1):37–46, 2003.

[137] Kai M Udert, Tove A Larsen, Martin Biebow, and Willi Gujer. Urea hydrolysis and precipitation dynamics in a urine-collecting system. *Water research*, 37(11):2571–2582, 2003.

[138] Barbara Krajewska. Ureases i. functional, catalytic and kinetic properties: A review. *Journal of molecular catalysis B: Enzymatic*, 59(1-3):9–21, 2009.

[139] William A Tarpeh, Kai M Udert, and Kara L Nelson. Comparing ion exchange adsorbents for nitrogen recovery from source-separated urine. *Environmental science & technology*, 51(4):2373–2381, 2017.

[140] P Kuntke, KM8 Smiech, H Bruning, G Zeeman, M Saakes, THJA Sleutels, HVM Hamelers, and CJN Buisman. Ammonium recovery and energy production from urine by a microbial fuel cell. *Water research*, 46(8):2627–2636, 2012.

[141] Kangning Xu, Chi Zhang, Jiyun Li, Xiang Cheng, and Chengwen Wang. Removal and recovery of n, p and k from urine via ammonia stripping and precipitations of struvite and struvite-k. *Water Science and Technology*, 75(1):155–164, 2017.

[142] Neha Jagtap and Treavor H Boyer. Integrated, multi-process approach to total nutrient recovery from stored urine. *Environmental Science: Water Research & Technology*, 4(10):1639–1650, 2018.

[143] Shanqing Jiang, Xiaochang Wang, Shengjiong Yang, and Honglei Shi. Characteristics of simultaneous ammonium and phosphate adsorption from hydrolysis urine onto natural loess. *Environmental Science and Pollution Research*, 23:2628–2639, 2016.

[144] TL Chipako and DG Randall. Urine treatment technologies and the importance of ph. *Journal of Environmental Chemical Engineering*, 8(1):103622, 2020.

[145] Caitlin Courtney and Dyllon G Randall. A hybrid nanofiltration and reverse osmosis process for urine treatment: Effect on urea recovery and purity. *Water Research*, 222:118851, 2022.

[146] Bernard R Brooks, Robert E Bruccoleri, Barry D Olafson, David J States, S a Swaminathan, and Martin Karplus. Charmm: a program for macromolecular energy, minimization, and dynamics calculations. *Journal of computational chemistry*, 4(2):187–217, 1983.

[147] Alex D MacKerell Jr, Donald Bashford, MLDR Bellott, Roland Leslie Dunbrack Jr, Jeffrey D Evanseck, Martin J Field, Stefan Fischer, Jiali Gao, H Guo, Sookhee Ha, et al. All-atom empirical potential for molecular modeling and dynamics studies of proteins. *The journal of physical chemistry B*, 102(18):3586–3616, 1998.

[148] William L. Jorgensen, David S. Maxwell, and Julian Tirado-Rives. Development and testing of the opls all-atom force field on conformational energetics and properties of organic liquids. *Journal of the American Chemical Society*, 118(45):11225–11236, 1996.

[149] Wilfred F van Gunsteren, SR Billeter, AA Eising, PH Hünenberger, PKHC Krüger, AE Mark, WRP Scott, and IG Tironi. Biomolecular simulation: the gromos96 manual and user guide. *Vdf Hochschulverlag AG an der ETH Zürich, Zürich*, 86:1–1044, 1996.

[150] David A Pearlman, David A Case, James W Caldwell, Wilson S Ross, Thomas E Cheatham III, Steve DeBolt, David Ferguson, George Seibel, and Peter Kollman. Amber, a package of computer programs for applying molecular mechanics, normal mode analysis, molecular dynamics and free energy calculations to simulate the structural and energetic properties of molecules. *Computer Physics Communications*, 91(1-3):1–41, 1995.

[151] Loup Verlet. Computer" experiments" on classical fluids. i. thermodynamical properties of lennard-jones molecules. *Physical review*, 159(1):98, 1967.

[152] William C Swope, Hans C Andersen, Peter H Berens, and Kent R Wilson. A computer simulation method for the calculation of equilibrium constants for the formation of physical clusters of molecules: Application to small water clusters. *The Journal of chemical physics*, 76(1):637–649, 1982.

[153] Paul P Ewald. Die berechnung optischer und elektrostatischer gitterpotentiale. *Annalen der physik*, 369(3):253–287, 1921.

[154] Ulrich Essmann, Lalith Perera, Max L Berkowitz, Tom Darden, Hsing Lee, and Lee G Pedersen. A smooth particle mesh ewald method. *The Journal of chemical physics*, 103(19):8577–8593, 1995.

[155] H. J. C. Berendsen, J. P. M. Postma, W. F. van Gunsteren, A. DiNola, and J. R. Haak. Molecular dynamics with coupling to an external bath. *The Journal of Chemical Physics*, 81(8):3684–3690, 10 1984.

[156] Hans C Andersen. Molecular dynamics simulations at constant pressure and/or temperature. *The Journal of chemical physics*, 72(4):2384–2393, 1980.

[157] Shūichi Nosé. A molecular dynamics method for simulations in the canonical ensemble. *Molecular physics*, 52(2):255–268, 1984.

[158] William G Hoover. Canonical dynamics: Equilibrium phase-space distributions. *Physical review A*, 31(3):1695, 1985.

[159] Herman JC Berendsen, JPM van Postma, Wilfred F Van Gunsteren, ARHJ DiNola, and Jan R Haak. Molecular dynamics with coupling to an external bath. *The Journal of chemical physics*, 81(8):3684–3690, 1984.

[160] Shuichi Nosé and M.L. Klein. Constant pressure molecular dynamics for molecular systems. *Molecular Physics*, 50(5):1055–1076, 1983.

[161] William G. Hoover. Constant-pressure equations of motion. *Phys. Rev. A*, 34:2499–2500, Sep 1986.

[162] William L Jorgensen, Jayaraman Chandrasekhar, Jeffry D Madura, Roger W Impey, and Michael L Klein. Comparison of simple potential functions for simulating liquid water. *J. Chem. Phys.*, 79(2):926–935, 1983.

[163] Herman JC Berendsen, J Raul Grigera, and Tjerk P Straatsma. The missing term in effective pair potentials. *Journal of Physical Chemistry*, 91(24):6269–6271, 1987.

[164] C. D. Williams, P. Carbone, and F. R. Siperstein. Computational characterisation of dried and hydrated graphene oxide membranes. *Nanoscale*, 10:1946–1956, 2018.

[165] Anton Lerf, Heyong He, Michael Forster, and Jacek Klinowski. Structure of graphite oxide revisited. *The Journal of Physical Chemistry B*, 102(23):4477–4482, 1998.

[166] Huan Tang, Dongmei Liu, Ying Zhao, Xiaonan Yang, Jing Lu, and Fuyi Cui. Molecular dynamics study of the aggregation process of graphene oxide in water. *The Journal of Physical Chemistry C*, 119(47):26712–26718, 2015.

[167] Chih-Jen Shih, Shangchao Lin, Richa Sharma, Michael S. Strano, and Daniel

Blankschtein. Understanding the ph-dependent behavior of graphene oxide aqueous solutions: A comparative experimental and molecular dynamics simulation study. *Langmuir*, 28(1):235–241, 2012. PMID: 22039913.

[168] James C. Phillips, Rosemary Braun, Wei Wang, James Gumbart, Emad Tajkhorshid, Elizabeth Villa, Christophe Chipot, Robert D. Skeel, Laxmikant Kale, and Klaus Schulten. Scalable molecular dynamics with namd. *Journal of Computational Chemistry*, 26(16):1781–1802, 2005.

[169] Supriyo Bhattacharya and Keith E Gubbins. Fast method for computing pore size distributions of model materials. *Langmuir*, 22(18):7726–7731, 2006.

[170] Quan Liu, Mingqiang Chen, Yangyang Mao, and Gongping Liu. Theoretical study on janus graphene oxide membrane for water transport. *Frontiers of Chemical Science and Engineering*, pages 1–9, 2020.

[171] Quan Liu, Long Cheng, and Gongping Liu. Enhanced selective hydrogen permeation through graphdiyne membrane: A theoretical study. *Membranes*, 10(10), 2020.

[172] Madhavi Dahanayaka, Bo Liu, Zhongqiao Hu, Qing-Xiang Pei, Zhong Chen, Adrian Wing-Keung Law, and Kun Zhou. Graphene membranes with nanoslits for seawater desalination via forward osmosis. *Physical Chemistry Chemical Physics*, 19(45):30551–30561, 2017.

[173] Maryam Omidvar, Seyed Mahmoud Mousavi, Mohammad Soltanieh, and Ali Akbar Safekordi. Preparation and characterization of poly (ethersulfone) nanofiltration membranes for amoxicillin removal from contaminated water. *Journal of Environmental Health Science and Engineering*, 12:1–10, 2014.

[174] Reza Derakhsheshpoor, Maryam Homayoonfal, Ahmad Akbari, and Mohammad Reza Mehrnia. Amoxicillin separation from pharmaceutical wastewater by high permeability polysulfone nanofiltration membrane. *Journal of Environmental Health Science and Engineering*, 11:1–10, 2013.

[175] Yasamin Pesaran Afsharian, Mehrab Hedayatpour, and Sona Jamshidi. Amoxicillin separation from aqueous solution by negatively charged silica composite membrane. *Journal of Environmental Health Science and Engineering*, 19:121–131, 2021.

[176] Hanieh Karimnezhad, Amir H Navarchian, Touraj Tavakoli Gheinani, and Sirus Zinadini. Amoxicillin removal by fe-based nanoparticles immobilized on polyacrylonitrile

membrane: Individual nanofiltration or fenton reaction, vs. engineered combined process. *Chemical Engineering Research and Design*, 153:187–200, 2020.

[177] Mohammad Shakak, Reza Rezaee, Afshin Maleki, Ali Jafari, Mahdi Safari, Behzad Shahmoradi, Hiua Daraei, and Seung-Mok Lee. Synthesis and characterization of nanocomposite ultrafiltration membrane (psf/pvp/sio2) and performance evaluation for the removal of amoxicillin from aqueous solutions. *Environmental Technology & Innovation*, 17:100529, 2020.

[178] Rohit Goyat, Joginder Singh, Ahmad Umar, Yajvinder Saharan, Ahmed A Ibrahim, Sheikh Akbar, and Sotirios Baskoutas. Synthesis and characterization of nanocomposite based polymeric membrane (pes/pvp/go-tio2) and performance evaluation for the removal of various antibiotics (amoxicillin, azithromycin & ciprofloxacin) from aqueous solution. *Chemosphere*, 353:141542, 2024.

[179] Kamalpreet Kaur, Gagandeep Singh, Navneet Kaur, and Narinder Singh. Polyether sulfone-based organic nanoparticle coupled membrane for detection and purification of amoxicillin antibiotic from wastewater. *ACS ES&T Water*, 3(10):3387–3397, 2023.

[180] William Humphrey, Andrew Dalke, and Klaus Schulten. Vmd: visual molecular dynamics. *Journal of molecular graphics*, 14(1):33–38, 1996.

[181] Marcus D Hanwell, Donald E Curtis, David C Lonie, Tim Vandermeersch, Eva Zurek, and Geoffrey R Hutchison. Avogadro: an advanced semantic chemical editor, visualization, and analysis platform. *J. Cheminf.*, 4(1):1–17, 2012.

[182] Anton Lerf, Heyong He, Michael Forster, and Jacek Klinowski. Structure of graphite oxide revisited. *J. Phys. Chem. B .*, 102(23):4477–4482, 1998.

[183] Huan Tang, Dongmei Liu, Ying Zhao, Xiaonan Yang, Jing Lu, and Fuyi Cui. Molecular dynamics study of the aggregation process of graphene oxide in water. *J. Phys. Chem. C .*, 119(47):26712–26718, 2015.

[184] Eunyoung Jang, Seongpil Jeong, and Eunhyea Chung. Application of three different water treatment technologies to shale gas produced water. *Geosyst. Eng.*, 20(2):104–110, 2017.

[185] Mustafa Al-Furaiji, Nieck Benes, Arian Nijmeijer, and Jeffrey R McCutcheon. Use of a forward osmosis–membrane distillation integrated process in the treatment of high-salinity oily wastewater. *Ind. Eng. Chem. Res.*, 58(2):956–962, 2018.

[186] Nasim Esmaeilirad, Ken Carlson, and Pinar Omur Ozbek. Influence of softening sequenc-

ing on electrocoagulation treatment of produced water. *J. Hazard. Mater.*, 283:721–729, 2015.

[187] James Rosenblum, E Michael Thurman, Imma Ferrer, George Aiken, and Karl G Linden. Organic chemical characterization and mass balance of a hydraulically fractured well: from fracturing fluid to produced water over 405 days. *Environ. Sci. Technol.*, 51(23):14006–14015, 2017.

[188] Mahdi Mohammadi Ghaleni, Abdullah Al Balushi, Shayan Kaviani, Elham Tavakoli, Mona Bavarian, and Siamak Nejati. Fabrication of janus membranes for desalination of oil-contaminated saline water. *ACS Appl. Mater. Interfaces*, 10(51):44871–44879, 2018.

[189] Seongyun Kim, Pinar Omur Ozbek, Ashwin Dhanasekar, Adam Prior, and Ken Carlson. Temporal analysis of flowback and produced water composition from shale oil and gas operations: Impact of frac fluid characteristics. *J. Pet. Sci. Eng.*, 147:202–210, 2016.

[190] Yohei Mikami, Yunfeng Liang, Toshifumi Matsuoka, and Edo S Boek. Molecular dynamics simulations of asphaltenes at the oil–water interface: from nanoaggregation to thin-film formation. *Energy Fuels*, 27(4):1838–1845, 2013.

[191] Makoto Kunieda, Kennichi Nakaoka, Yunfeng Liang, Caetano R Miranda, Akira Ueda, Satoru Takahashi, Hiroshi Okabe, and Toshifumi Matsuoka. Self-accumulation of aromatics at the oil- water interface through weak hydrogen bonding. *J. Am. Chem. Soc.*, 132(51):18281–18286, 2010.

[192] Shenghan Song, Heng Zhang, Lixin Sun, Jing Shi, Xulong Cao, and Shiling Yuan. Molecular dynamics study on aggregating behavior of asphaltene and resin in emulsified heavy oil droplets with sodium dodecyl sulfate. *Energy Fuels*, 32(12):12383–12393, 2018.

[193] Hui Yan and Shiling Yuan. Molecular dynamics simulation of the oil detachment process within silica nanopores. *J. Phys. Chem. C*, 120(5):2667–2674, 2016.

[194] Lucas S de Lara, Mateus F Michelon, and Caetano R Miranda. Molecular dynamics studies of fluid/oil interfaces for improved oil recovery processes. *J. Phys. Chem. B*, 116(50):14667–14676, 2012.

[195] Xuejiao Chen, Lei Hou, Wenchao Li, Shiyao Li, and Yujie Chen. Molecular dynamics simulation of magnetic field influence on waxy crude oil. *J. Mol. Liq.*, 249:1052–1059, 2018.

[196] William L Jorgensen, David S Maxwell, and Julian Tirado-Rives. Development and

testing of the opls all-atom force field on conformational energetics and properties of organic liquids. *J. Am. Chem. Soc.*, 118(45):11225–11236, 1996.

[197] JC Phillips, R Braun, W Wang, J Gumbart, E Tajkhorshid, and E Villa. and schulten, k. 2005. *Scalable molecular dynamics with NAMD. J. Comput. Chem.*, 26(16):1781–1802, 2005.

[198] Yang Song, Fang Xu, Mingjie Wei, and Yong Wang. Water flow inside polamide reverse osmosis membranes: A non-equilibrium molecular dynamics study. *J. Phys. Chem. B .*, 121(7):1715–1722, 2017.

[199] Meng Shen, Sinan Keten, and Richard M Lueptow. Dynamics of water and solute transport in polymeric reverse osmosis membranes via molecular dynamics simulations. *J. Membr. Sci.*, 506:95–108, 2016.

[200] Yong Long, Kai Wang, Guolei Xiang, Kai Song, Gang Zhou, and Xun Wang. Molecule channels directed by cation-decorated graphene oxide nanosheets and their application as membrane reactors. *Adv. Mater.*, 29(16):1606093, 2017.

[201] Karin Ching, Boyue Lian, Greg Leslie, Xianjue Chen, and Chuan Zhao. Metal-cation-modified graphene oxide membranes for water permeation. *Carbon*, 170:646–657, 2020.

[202] Kerri L Hickenbottom, Nathan T Hancock, Nathan R Hutchings, Eric W Appleton, Edward G Beaudry, Pei Xu, and Tzahi Y Cath. Forward osmosis treatment of drilling mud and fracturing wastewater from oil and gas operations. *Desalination*, 312:60–66, 2013.

[203] Phuoc HH Duong and Tai-Shung Chung. Application of thin film composite membranes with forward osmosis technology for the separation of emulsified oil–water. *J. Membr. Sci.*, 452:117–126, 2014.

[204] Sui Zhang, Peng Wang, Xiuzhu Fu, and Tai-Shung Chung. Sustainable water recovery from oily wastewater via forward osmosis-membrane distillation (fo-md). *Water Res.*, 52:112–121, 2014.

[205] Abhijit Gogoi, Aditya Koneru, and K Anki Reddy. Effect of graphene oxide (go) nanosheet sizes, pinhole defects and non-ideal lamellar stacking on the performance of layered go membranes: an atomistic investigation. *Nanoscale Adv.*, 1(8):3023–3035, 2019.

[206] Hubiao Huang, Yiyin Mao, Yulong Ying, Yu Liu, Luwei Sun, and Xinsheng Peng. Salt concentration, ph and pressure controlled separation of small molecules through lamellar graphene oxide membranes. *Chem. Commun.*, 49(53):5963–5965, 2013.

[207] Zhongying Wang, Qingsong Tu, Sunxiang Zheng, Jeffrey J Urban, Shaofan Li, and Baoxia Mi. Understanding the aqueous stability and filtration capability of mos2 membranes. *Nano Lett.*, 17(12):7289–7298, 2017.

[208] Chih-Jen Shih, Shangchao Lin, Richa Sharma, Michael S Strano, and Daniel Blankschtein. Understanding the ph-dependent behavior of graphene oxide aqueous solutions: a comparative experimental and molecular dynamics simulation study. *Langmuir*, 28(1):235–241, 2012.

[209] Ch W Bielawski, DR Dreyer, S Park, and RS Ruoff. The chemistry of grapheme oxide. *Chem. Soc. Rev*, 39(1):228–240, 2010.

[210] Francois Perreault, Andreia Fonseca De Faria, and Menachem Elimelech. Environmental applications of graphene-based nanomaterials. *Chem. Soc. Rev*, 44(16):5861–5896, 2015.

[211] Hyunwoo Kim, Ahmed A Abdala, and Christopher W Macosko. Graphene/polymer nanocomposites. *Macromolecules*, 43(16):6515–6530, 2010.

[212] Steve Plimpton. Fast parallel algorithms for short-range molecular dynamics. *J. Comput. Phys.*, 117(1):1–19, 1995.

[213] Christopher D Williams, Paola Carbone, and FR Siperstein. Computational characterisation of dried and hydrated graphene oxide membranes. *Nanoscale*, 10(4):1946–1956, 2018.

[214] Kenno Vanommeslaeghe, Elizabeth Hatcher, Chayan Acharya, Sibsankar Kundu, Shijun Zhong, Jihyun Shim, Eva Darian, Olgun Guvench, P Lopes, Igor Vorobyov, et al. Charmm general force field: A force field for drug-like molecules compatible with the charmm all-atom additive biological force fields. *J. Comput. Chem.*, 31(4):671–690, 2010.

[215] Axel D Becke. Density-functional exchange-energy approximation with correct asymptotic behavior. *Physical review A*, 38(6):3098, 1988.

[216] C Lee. W. yang and rg parr. *Phys. Rev. B*, 37(2):785, 1988.

[217] J Stephen Binkley, John A Pople, and Warren J Hehre. Self-consistent molecular orbital methods. 21. small split-valence basis sets for first-row elements. *Journal of the American Chemical Society*, 102(3):939–947, 1980.

[218] Michelle M Francl, William J Pietro, Warren J Hehre, J Stephen Binkley, Mark S Gordon, Douglas J DeFrees, and John A Pople. Self-consistent molecular orbital methods. xxiii. a polarization-type basis set for second-row elements. *The Journal of Chemical Physics*, 77(7):3654–3665, 1982.

[219] U Chandra Singh and Peter A Kollman. An approach to computing electrostatic charges for molecules. *Journal of computational chemistry*, 5(2):129–145, 1984.

[220] Brent H Besler, Kenneth M Merz Jr, and Peter A Kollman. Atomic charges derived from semiempirical methods. *Journal of computational chemistry*, 11(4):431–439, 1990.

[221] Christopher G Mayne, Jan Saam, Klaus Schulten, Emad Tajkhorshid, and James C Gumbart. Rapid parameterization of small molecules using the force field toolkit. *Journal of computational chemistry*, 34(32):2757–2770, 2013.

[222] MJ Frisch, GW Trucks, HB Schlegel, GE Scuseria, MA Robb, JR Cheeseman, JA Montgomery Jr, T Vreven, KN Kudin, JC Burant, et al. Gaussian 03. pittsburgh pa: Gaussian. *Inc.[Google Scholar]*, 2003.

[223] Laura J Banasiak and Andrea I Schafer. Removal of boron, fluoride and nitrate by electrodialysis in the presence of organic matter. *J. Membr. Sci.*, 334(1-2):101–109, 2009.

[224] Nitzan Geffen, Raphael Semiat, Moris S Eisen, Yael Balazs, Ilan Katz, and Carlos G Dosoretz. Boron removal from water by complexation to polyol compounds. *J. Membr. Sci.*, 286(1-2):45–51, 2006.

[225] Shabnam Pathan, Sk Safikul Islam, Ria Sen Gupta, Barnali Maity, P Rajasekhar Reddy, Samir Mandal, K Anki Reddy, and Suryasarathi Bose. Fundamental understanding of ultrathin, highly stable self-assembled liquid crystalline graphene oxide membranes leading to precise molecular sieving through non-equilibrium molecular dynamics. *ACS nano*, 17(8):7272–7284, 2023.

[226] Pengzhan Sun, Feng Zheng, Miao Zhu, Zhigong Song, Kunlin Wang, Minlin Zhong, Dehai Wu, Reginald B Little, Zhiping Xu, and Hongwei Zhu. Selective trans-membrane transport of alkali and alkaline earth cations through graphene oxide membranes based on cation- π interactions. *Acs Nano*, 8(1):850–859, 2014.

[227] Thomas Carey, Christopher D Williams, Daniel J McArthur, Tammie Malkinson, Olivia R Thompson, Aliaksandr Baidak, Laura Murtagh, Gyorgyi Glodan, Sean P Morgan, and Anthony W Banford. Removal of cs, sr, u and pu species from simulated nuclear waste effluent using graphene oxide. *J. Radioanal. Nucl. Chem.*, 317(1):93–102, 2018.

[228] Quan Liu, Long Cheng, and Gongping Liu. Enhanced selective hydrogen permeation through graphdiyne membrane: A theoretical study. *Membranes*, 10(10):286, 2020.

[229] Quan Liu, Mingqiang Chen, Yangyang Mao, and Gongping Liu. Theoretical study on

janus graphene oxide membrane for water transport. *Front. Chem. Sci. Eng.*, 15(4):913–921, 2021.

[230] Richard J Gowers, Max Linke, Jonathan Barnoud, Tyler John Edward Reddy, Manuel N Melo, Sean L Seyler, Jan Domanski, David L Dotson, Sebastien Buchoux, Ian M Kenney, et al. Mdanalysis: a python package for the rapid analysis of molecular dynamics simulations. Technical report, Los Alamos National Lab.(LANL), Los Alamos, NM (United States), 2019.

[231] Naveen Michaud-Agrawal, Elizabeth J Denning, Thomas B Woolf, and Oliver Beckstein. Mdanalysis: a toolkit for the analysis of molecular dynamics simulations. *J. Comput. Chem.*, 32(10):2319–2327, 2011.

[232] Shivam Tiwari, Abhijit Gogoi, and K Anki Reddy. Effect of an ionic environment on membrane fouling: a molecular dynamics study. *Phys. Chem. Chem. Phys.*, 23(8):5001–5011, 2021.

[233] Jason C Hower, Yi He, Matthew T Bernards, and Shaoyi Jiang. Understanding the nonfouling mechanism of surfaces through molecular simulations of sugar-based self-assembled monolayers. *J. Chem. Phys.*, 125(21):214704, 2006.

[234] Qing Shao, Yi He, Andrew D White, and Shaoyi Jiang. Difference in hydration between carboxybetaine and sulfobetaine. *J. Phys. Chem. B*, 114(49):16625–16631, 2010.